Challenging Conventional Approaches to Energy Storage: Direct Integration of Energy Storage into Solar Cells, the Use of Scrap Metals to Build Batteries, and the Development of Multifunctional Structural Energy Storage Composites

By

Andrew S. Westover

Dissertation

Submitted to the Faculty of the

Graduate School of Vanderbilt University

in partial fulfillment of the requirements

for the degree of

DOCTOR OF PHILOSOPHY

in

Interdisciplinary Materials Science and Engineering

December, 2016

Nashville, Tennessee

Approved:

Cary Pint, Ph.D.
Douglas Adams, Ph.D.
Shihong Lin, Ph.D.
Jason Valentine, Ph.D.
Amrutur Anilkumar, Ph.D.

ACKNOWLEDGEMENTS

My biggest thanks must first and foremost go out to Dr. Cary Pint my adviser and mentor. My success throughout this dissertation has been because of his hard work support and training.

Next I want to thank my wife Jaymee Westover who has been a constant support throughout the process and my Dad Kerry Westover and who has always been completely interested in what I have been doing and always listen to me drone on about all my projects, and my mother Shannon Westover who has always believed in me.

Next I need to give a big thanks to my fellow group members, Landon Oakes, Adam Cohn, Rachel Carter, Nitin Muralidharan, Anna Douglas, Keith Share, Mengya Li, Shahana Chatterjee and Kate Moyer and most especially to all of the undergraduate and high school students who have contributed greatly to this success: Thomas Metke, John W. Tian, Robert Edwards, Haotian Sun, Babatunde Bello, Jeremiah Afolabi, Shiva Bernath, Farhan Shabob, Nicholas Galioto, Daniel Freudiger, Zarif S Gani and Eric Speer.

Some of my most heartfelt thanks must go to the labs of Dr. Shigeo Maruyama at the University of Tokyo, Japan and Dr. Daniel Nessim of Bar Ilan University in Israel both of which hosted me for summer research experiences and where some of the most critical research for this dissertation was performed. I would also like to thank all the members of their labs who contributed so much to my projects. From the University of Tokyo: Naoki Hayakawa (Tsuchiya Lab) , Dr. Kehang Cui, Dr. Xiang Rong, Dr. Kensuke Tsuchiya (Tsuchiya Lab), Dr. Taiki Inoue, Dr. Shohei Chiashi, Dr. Junho Choi (Kato-Choi lab), Takumi Ishikawa (Kato-Choi lab) Dr. Takahisa Kato (Kato-Choi lab). From Bar Ilan University: Eti Teblum, Anat Yitzhak and Merav Muallem.

I would also like to express appreciation for all of the support from additional faculty, staff and graduate students at Vanderbilt University including, Dr. Leon Bellan, Dr. Rizia Bardhan, Dr. Amrutur Anilkumar, Dr. Douglas Adams, Dr. Jason Valentine, Dr. Shihong Lin, Will Erwin, Bradly Baer, Shane Finn, Sarah Satterwhite, Ben Schmidt and Tony Hmelo.

Lastly I would like to give a big thanks to my funding sources throughout the years including NSF grant EPS 1004083 and CMMI 1334269, NASA EPSCoR grant NNX13AB26A, BSF Grant Number – 2014041, the Prof. Rahamimoff Travel Grant Program 2016, the East Asia and Pacific Summer Institute 2015 award number 1515541, the Japan Society for the Promotion of Science's summer program 2015, a Ralph E. Powe Junior Faculty Enhancement Award, and Vanderbilt Start-up funds.

TABLE OF CONTENTS

LIST OF TABLES AND FIGURES

Chapter 1

Figures Page #

Chapter 2

Chapter 3

Chapter 4

Chapter 5

Chapter 6

Chapter 7

Chapter 8

Chapter 9

Chapter 10

Chapter 11

Chapter 12

Chapter 13

LIST OF ABBREVIATIONS

ACCVD – Alcohol Catalytic Chemical Vapor Deposition

ALD – Atomic Layer Deposition

BMIBF$_4$ - 1-Butyl-3-Methyl Imidazolium Tetrafluoroborate

CD – Charge/Discharge

CDI – Capacitive Deionization

CF – Carbon Fiber

CNT – Carbon Nanotube

CV – Cyclic Voltammetry

CVD – Chemical Vapor Deposition

EDLC – Electric Double Layer Capacitance

EIS – Electron Impedance Spectroscopy

EMIBF$_4$ - 1-Ethyl-3-Methyl Imidazolium Tetrafluoroborate

ESR – Equivalent Series Resistance

FESEM – Field Emission Scanning Electron Miscroscopy

FFT – Fast Fourier Transform

HiPEN PV - High Penetration Photovoltaic

HRTEM – High Resolution Transmission Electron Microscopy

IL – Ionic Liquid

LED – Light Emitting Diode

MWCNT – Multi-walled Carbon Nanotube

PANI – Polyanaline

PAN - Polyacrylonitrile

PC – Propylene Carbonate

PEGDGE – Poly Ethylene Glycol Di-Glycidyl Ether

PEO – Polyethylene Oxide

PSi – Porous Silicon

PV – Photovoltaic

PVA – Polyvinyl Alcohol

PVdF - Polyvinylidene Fluoride

RACNT – Randomly Aligned Carbon Nanotube

SCE – Saturated Calomel Electrode

SEM – Scanning Electron Microscopy

SWCNT – Single Walled Carbon Nanotube

TBP – Tetrabutylpyrridine

TEM – Transmission Electron Microscopy

UAV – Unmanned Autonomous Vehicle

VACNT – Vertically Aligned Carbon Nanotubes

XRD – X-ray Diffraction

LIST OF PUBLICATIONS

Portions of this dissertation have been drawn from the following publications:

1) **Andrew S. Westover**, Eti Teblum, Deanna Schauben, Anat Yitzhak, Nitin Muralidharan, Merav Muallem, Gilbert Nessim, Cary L. Pint "Carbon Nanotube Reinforced Multifunctional Energy Storage Composites", *In preparation.*

2) **Andrew S. Westover**, Naoki Hayakawa, Kehang Cui, Xiang Rong, Kensuke Tsuchiya, Taiki Inoue, Shohei Chiashi, Esko I. Kauppinen, Cary L. Pint, and Shigeo Maruyama, "The effect of interfacial contact on the adhesion of single walled carbon nanotube films to surfaces", *In submission.*

3) **Andrew S. Westover**, Thomas Metke, Nitin Muralidharan, Jeremiah Afolabi, and Cary L. Pint, "Room temperature passivation of porous Si with Ag and polyaniline for integratable pseudocapacitor electrodes", *In submission.*

4) **Andrew S. Westover**,* Nitin Muralidharan,* Haotian Sun, Nicholas Galioto, Rachel E. Carter, Adam P. Cohn, Landon Oakes and Cary L. Pint, "From the Junkyard to the Power Grid: Ambient Processing of Scrap Metals into Nanostructured Electrodes for Ultrafast Rechargeable Batteries", *ACS Energy Letters*, 1, 1034–1041, Oct. 2016.

5) **Andrew S. Westover**, Junho Choi, Kehang Cui, Takumi Ishikawa, Taiki Inoue, Rong Xiang, Shohei Chiashi, Takahisa Kato, Shigeo Maruyama, and Cary L. Pint, "Load Dependent Frictional Response of Vertically Aligned Single-Walled Carbon Nanotube Films", *Scripta Materialia* 125, 63-67, Aug. 2016.

6) **Andrew S. Westover**, * Thomas Metke*, Rachel Carter, Landon Oakes, Anna Douglas, Cary L. Pint, "Particulate-free porous silicon networks for efficient capacitive deionization water desalination", *Scientific Reports* 6, 24680, Apr. 2016.

7) **Andrew S. Westover**, Bradly Baer, Babatunde H Bello, Haotian Sun, Landon Oakes, Leon M Bellan, Cary L Pint, "Multifunctional high strength and high energy epoxy composite structural supercapacitors with wet-dry operational stability", *Journal of Materials Chemistry A*, 3 (40), 20097-20102, Sep. 2015.

8) **Andrew S. Westover,** Daniel Freudiger, Zarif S Gani, Keith Share, Landon Oakes, Rachel E Carter, Cary L. Pint, "On-Chip High Power Porous Silicon Lithium Ion Batteries with Stable Capacity over 10000 Cycles", *Nanoscale* 7 (1), 98-103, Nov. 2014.

9) **Andrew S. Westover**, John W Tian, Shivaprem Bernath, Landon Oakes, Rob Edwards, Farhan N Shabab, Shahana Chatterjee, Amrutur V Anilkumar, Cary L Pint, "A multifunctional load-bearing solid-state supercapacitor", *Nano Letters*, 14 (6), 3197–3202, May 2014. (Highlighted by NSF)

10) **Andrew S. Westover**, Keith Share, Rachel Carter, Adam P Cohn, Landon Oakes, Cary L. Pint, "Direct integration of a supercapacitor into the backside of a silicon photovoltaic device", *Applied Phys. Lett.* 104, 213905, May 2014

11) **Andrew S. Westover**, Farhan N. Shabab, John W. Tian, Shiva Bernath, Landon Oakes, William R. Erwin, Rachel Carter, Rizia Bardhan, and Cary L. Pint, “Stretching ion conducting polymer electrolytes: In-situ correlation of mechanical, ionic transport, and optical properties”, *Journal of The Electrochemical Society,* 161, E112-E117, Apr. 2014.

CHAPTER 1

INTRODUCTION

1.1 Paradigm Shifts in Energy Storage

The field of energy storage has been defined by a series of giant leaps in innovation that have spurred complete paradigm shifts in the way we use energy. Some examples of these include the first development of batteries by Edison and Volta[1-3] and the switch from the moderate energy densities of aqueous based battery systems to the 4V Li ion batteries enabled by Sony and the research in $LiCoO_2$ by Goodenough.[4] This last development has led to a fundamental change in our society, as it has enabled the development of portable electronics and made electrical vehicles a practical reality.[5-8] With this increased demand for batteries with greater and greater energy density there have been several paradigm shifts toward Li-S,[9, 10] Li-air,[11, 12] and Li metal[30, 31] batteries all of which exhibit significantly higher energy densities than Li ion batteries. The fear of climate change and the subsequent push for renewable energy sources, which require coupling with energy storage,[13, 14] has also spurred two additional innovations: the development of liquid-based redox flow batteries[15, 16] and the development of alternative Na[17, 18] and K[19-21] ion battery technologies. These have again completely changed the paradigm of energy storage research. The future of energy storage will continue to be defined by such paradigm shifts into non-conventional energy storage designs. This dissertation presents three such possible paradigm shifts: 1) the direct integration of energy storage into Si photovoltaics, 2) the use of scrap metals to develop batteries using simple manufacturing, and 3) the development of multifunctional structural energy storage composites.

1.2 Direct Integration of Energy Storage into Si Photovoltaics

One of the most critical areas of research in energy storage is the development of high penetration systems that can be paired with photovoltaics, are relatively inexpensive, and can be produced in a large volume.[22-24] This is highlighted by the current model for the deployment of photovoltaics. The prevailing approach typically involves the installation of solar cells on the roofs of homes and businesses, where the solar cells are tied to the grid and the homeowner or business gets a discount on their energy bill based on the energy production of their solar cells. While this works very well for low penetration of photovoltaics, it does not overcome the problem of intermittent energy generation for high penetration deployment of photovoltaics. In some places, energy companies have had to curtail their energy production due to financial losses resulting from the photovoltaics.

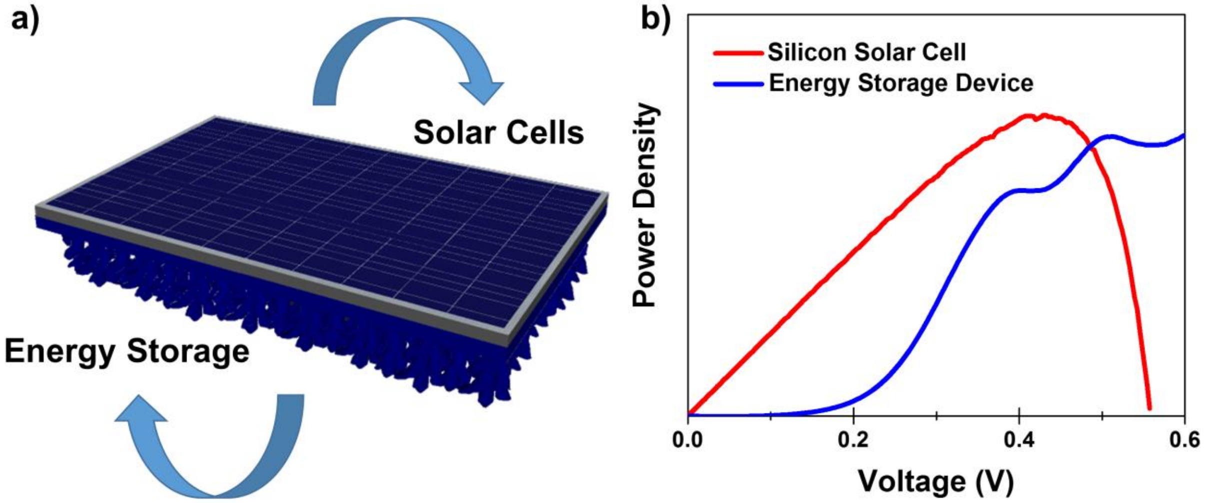

Figure 1.1 (a) Schematic showing the concept of direct integration of energy storage into silicon solar cells. (b) Initial data showing the concept of power matching the performance of a solar cell with the power performance of an energy storage device.

There have been several efforts to combat this; the most publicized have been Tesla's Powerwall,[25] a Li ion battery capable of being installed in homes in conjunction with photovoltaics, and the test development of large scale energy storage facilities using flow cell batteries.[26] Although still in the early stages of research, one of the most interesting possibilities for developing solar energy storage devices with paired energy storage is the direct integration of energy storage with solar cells (**Figure 1.1a**).[27-35] This has the potential to multipurpose material, simplify the overall manufacturing, and, most importantly, give the possibility of directly matching the energetics and power profile of the solar cells with that of the energy storage devices (**Figure 1.1b**). Initial work on this system has focused on integrating supercapacitors and batteries directly into the backs of polymer,[29, 33] dye-sensitized,[30-33] and perovskite based solar cells.[34, 35] Despite the promise of these systems there has been essentially zero work in directly integrating energy storage with the most common and commercially available type of solar cell – silicon solar cells. Furthermore, although there has been a significant amount of initial work in developing fully integrated systems, one aspect has been completely neglected in the field and is absolutely critical to integrated functionality: power matching the function of the solar cell and that of the energy storage device. One prime example of this is the work by Guo et al.[30] In order to match a solar cell with the Li ion battery they had to pair 3 solar cells in series to reach an appropriate operating voltage. The first part of my work presents initial proof of concept integrating energy storage onto the back of Si based photovoltaics (Chapter 2). I also present several possibilities for the development of high power battery systems onto the back of Si photovoltaics for ideal power matching and energy matching, a requirement for an integrated system (Chapter 3-4). Finally, I show the potential for the direct integration of capacitive deionization with solar cells using a similar porous Si system (Chapter 5).

1.3 Scrap Metals to Batteries

Another possibility in the provision of a large-scale energy storage system that can enable the high penetration of solar cells into the grid is the development of batteries with simple manufacturing that could even be done in a do-it-yourself format that uses simple and easily obtainable chemicals and processes. The flow cell battery concept has been developed for this purpose.[15, 26, 36] There have been a few other developments that are also extremely intriguing; one of these is the development of energy storage systems from waste tires that were once used for cars.[37] Additional methods that both use simpler processing and more common materials are extremely desirable to meet this need. The second part of my dissertation presents a novel and innovative

Figure 1.2 Concept of using scrap metals for batteries is depicted with pictures of scrap brass and scrap steel on the left and the picture of a full cell scrap metal battery charging an LED on the right.

approach to developing batteries from scrap metals (**Figure 1.2**) using inexpensive materials and simple processing techniques in addition to motivating additional recycling and reuse of our materials (Chapter 6).

1.4 Multifunctional Structural Energy Storage Composites

In the area of energy storage, there is always a push to develop improved batteries that have more energy and power per unit of volume and weight. Although the most popular strategies have involved developing new materials and battery chemistries, one of the most intriguing routes to achieve this end is the development of multifunctional structural energy storage systems.[38-40] Within any device that uses energy storage in addition to the functional components, there are additional components that fulfill only a structural or cosmetic purpose, such as the doors of a car or the cases of laptops and cell phones. If this non-critical material could be multipurposed for multifunctional use as an energy storage system, it presents another possibility for improving the amount of energy storage and power available in these devices without increasing the overall weight or volume. This remains the most elegant solution for the future of energy storage. I envision a future where the roofs and walls of buildings store the energy generated by solar cells which power our houses and the doors and frames of vehicles power cars and unmanned autonomous vehicles (UAVs).

Although research in this field started several years ago, there has been very little progress. Initial efforts have primarily involved embedding full batteries into a larger material, such as a backpack, UAV wing, etc.[38, 41-43] More recent work has focused on the development of multifunctional structural energy storage composites following the design of a traditional fiberglass or carbon fiber composite. On the battery side, the most impressive work was that of Ping Liu et al.[44] who developed a multifunctional battery with an ultimate tensile strength of 12 MPa and an energy density of 35 Wh/kg. Their design modified a traditional Li ion battery design using a solid state polymer electrolyte and conductive carbon fibers as the electrode material. The biggest weaknesses of this design is that the mechanical properties are limited by the random carbon fiber network used and the polymer electrolyte which lacked the stiffness and strength of the traditional epoxy used in composite design. Furthermore, although the energy storage was significant, it still had poor cyclability and did not fulfill the potential of a battery-based multifunctional design.

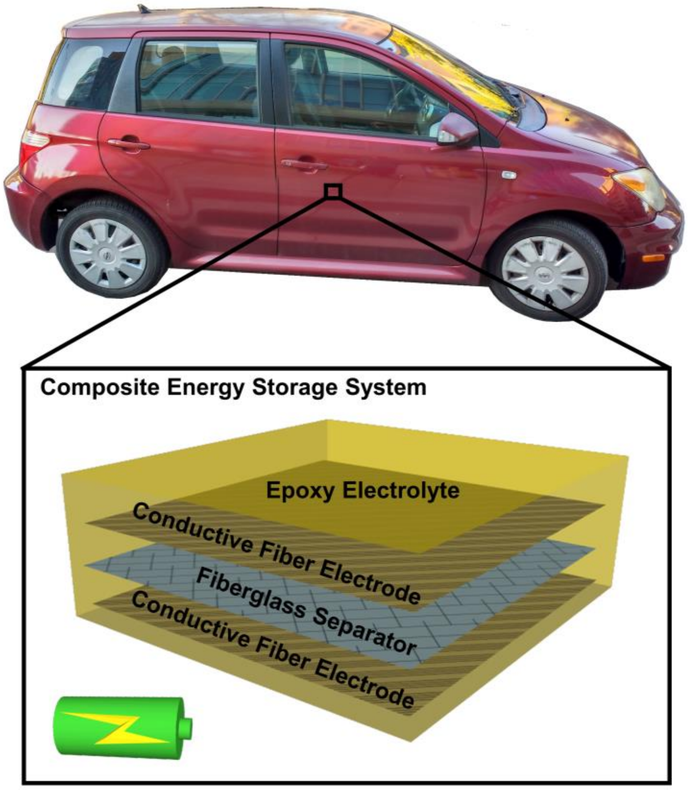

Figure 1.3 Schematic showing the concept of multifunctional structural energy storage devices.

The most impressive work to date in developing structural energy storage systems has been that of the Greenhalgh's group at the imperial college of London.[45-49] Following traditional composite manufacturing design principles, they have developed structural supercapacitors that can be manufactured in the traditional manner of carbon fiber composites. Their design consists of modifying carbon fibers (CF) using a variety of methods, including etching the surface, attaching single walled carbon nanotubes (CNT), inserting a carbon aerogel pressed onto the CF for electrodes, and using a fiberglass separator. Their best performance resulted in a composite material that could hold ~10 MPa of tensile stress with a specific energy of ~ 0.1 mWh/kg.[45] Despite the impressive progress of the Greenhalgh's group, critical challenges remain that must be overcome before such a multifunctional structural supercapacitor can be implemented. In particular, when considering the ultimate target of such a multifunctional structural energy storage system, the goal is to produce a composite that has mechanical performance on par with a commercial composite material (>200MPa tensile strength) and an energy storage on par with commercial supercapacitors (~1 Wh/kg). Furthermore, whereas all multifunctional architectures to date focus on the ability to independently measure the structural and energy storage characteristics of composites, they do not measure the simultaneous performance of the energy and structural properties. The third part of my dissertation focuses first on the development of techniques showing the effect of static and dynamic mechanical forces on energy storage characteristics of both solid state polymer electrolytes and on full cell supercapacitors (Chapter 7-8). Second, it focuses on developing environmentally-resistant epoxy-ionic liquid (IL) structural electrolytes that can act as the matrix for structural composite supercapacitors (Chapter 9). Third, I show initial work investigating the adhesion of CNT to substrates which is one critical factor for simultaneous structural and electrochemical performance (Chapter 10-12). Finally, I show the development of full structural energy storage composites with CNT grown on stainless steel electrodes, fiberglass and Kevlar separators, and an epoxy-IL electrolyte (Chapter 13).

1.A Appendix - Electrochemical Energy Storage Systems

1.A.1 Key components of electrochemical energy storage systems

In order to understand the field of energy storage, it is important to understand the different types of electrochemical energy storage systems and the different components that make up an energy storage system. As can be seen in **Figure 1.A1** the main components of electrochemical energy storage systems consist of two electrodes (a positively charted *anode* and a negatively charged *cathode*), the *electrolyte*, the *separator,* and the *current collector*. Most commercial *anodes* and *cathodes* consist of an active material that is mixed with conductive carbon additives within a structural polymer matrix. The second major component is the *electrolyte* which needs to be an ion-conducting medium. Traditionally the *electrolyte* is a liquid consisting of a solvent with ions dissolved in it, although more recent *electrolytes* are often gel or solid state where the ions move along the polymer chain or within an ion-conducting ceramic. In order to maintain the minimum possible separation between the electrodes, they are sandwiched together with an insulative membrane called a *separator* that is typically made of polyethylene, polyurethane, or a similar polymer that allows ion transfer but is insulated, preventing shorting between the electrodes. The final key component of a battery is the *current collector*; in Li ion batteries these consist of copper or aluminum foil that acts as a base to collect the charges generated by the chemical reactions of the *anode* and the *cathode*.

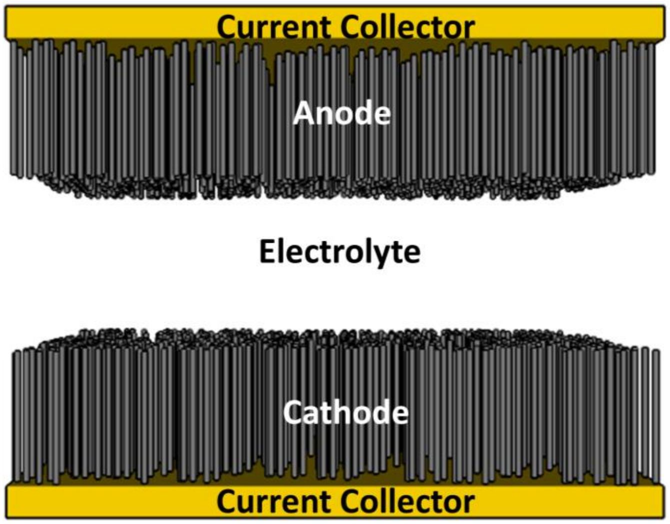

Figure 1.A1 Schematic showing the different parts of an electrochemical energy storage device including the current collectors, anode, cathode and the electrolyte.

1.A.2 Types of electrochemical energy storage systems

Electrochemical energy storage systems are made up of two different types of energy storage mechanisms. The first type is non-faradic energy storage that relies on the buildup of an ionic double layer on the surface of the electrode called ‘electric double layer capacitance’ (EDLC), and the second type is faradaic energy storage that relies on chemical reactions at the surface and in the bulk of electrodes to store energy. As electrochemical devices require two electrodes typically labeled the *anode* and the *cathode*. There are three different types of devices that are primarily used in energy storage: *electric double layer capacitors* which consist of the pairing of two electrodes that both exhibit ELDC, *hybrid capacitors* or *hybrid batteries* that rely on the pairing of a single electrode that relies on EDLC and a single electrode that exhibits a faradaic chemical reaction, and *batteries* that consist of two electrodes that exhibit faradaic chemical reactions. A more detailed explanation is given in the training module in the appendix of Chapter 6.

1.A.3 Function of electrochemical energy storage systems

In order to store energy in an electrochemical device, a current is applied between the anode and cathode that causes a voltage buildup on the electrode surface due to the accumulation of charge on either surface. In the case of electric double layer capacitors, this buildup of charge causes an increase in voltage, which forces the ions in the electrolyte to migrate to either the cathode or anode and form an electric double layer. The motion of the ions and the formation of the double layer allows for the storage of electrochemical energy. In a battery, this buildup of charge, in addition to causing ion migration from the electrolyte to the surface of the electrodes, causes electrochemical reactions that either result in the alloying/de-alloying or intercalation/de-intercalation of ions into the electrodes where the energy is stored via these chemical reactions. The amount of energy depends on the relative energetics of the respective chemical reactions at the cathode and the anode. In a hybrid system where an electric double layer electrode is paired with an electrode that exhibits an electrochemical reaction, the buildup of charge causes a chemical reaction at one electrode and the buildup up of an electric double layer at the other electrode. The energy stored is then released by discharging with an inverse current to the charging current, allowing for the reversal of chemical reactions and for the ions in the double layer to return to the electrolyte.

1.A.4 Two electrode vs. three electrode measurements

When doing energy storage research we primarily rely on two different types of electrochemical setups. The first is the most common and is used for full cell devices where the anode and the cathode are measured with reference to each other in a two-electrode setup; it measures the performance of full cell electrochemical energy storage systems. The second is the use of a three electrode setup, which is used to explore the performance of a single electrode. In a three electrode setup, the working electrode is the active electrode whose performance is being studied and could be an anode or a cathode; the counter electrode is used as the second electrode that acts as an electron source for the chemical reaction of the working electrode. The reference electrode exhibits a well-known and stable chemical reaction. The reaction voltage and the charge storage capacity of the working electrode is measured with respect to the chemical reaction of the reference electrode (typically saturated calomel or $Ag/AgNO_3$), allowing for the determination of the isolated performance of individual electrodes. In this work, both two cell and three cell electrode measurement setups are used. The difference between these setups is depicted in **Figure 1.A2**.

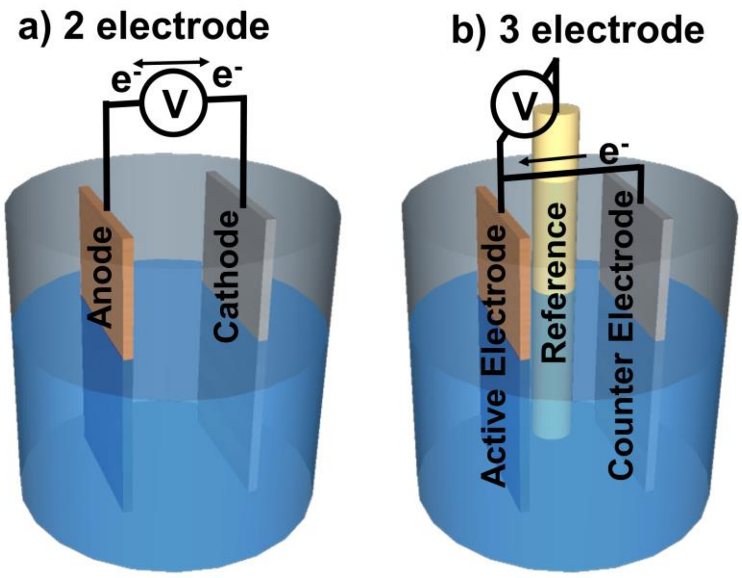

Figure 1.A2 Schematic showing the difference between a 2 electrode measurement and a 3 electrode measurement. It also depicts how a full cell architecture probes a full battery device but a 3 electrode architecture probes the performance of a single active electrode.

1.A.5 Types of electrochemical measurements

In order to assess the full cell performance of difference electrochemical energy systems, several different measurement techniques are employed. The first consists of galvanostatic charge-discharge measurements (CD curves) where a constant current is applied and the voltage changes as the devices charges or discharges. For EDLC, this results in a triangular looking curve, as can be seen in **Figure 1.A3a.** For batteries and electrodes exhibiting distinct faradaic reactions, the CD curves have an initial increase/decrease in voltage followed by a voltage plateau corresponding to the chemical reactions as can be seen in **Figure 1.A3b.** CD measurements are perhaps the most crucial form of electrochemical measurement as the energy and power of a device can be calculated by integrating the area under the charge or discharge curves according to the equation $E = \int_0^t IV dt$ and the average power can be calculated by dividing the energy by the charge or discharge time. The most common method of comparing electrochemical devices is a Ragone plot where the power is plotted in comparison to the energy performance. An example Ragone plot with the performance of different types of devices denoted is depicted in **Figure 1.A4.**

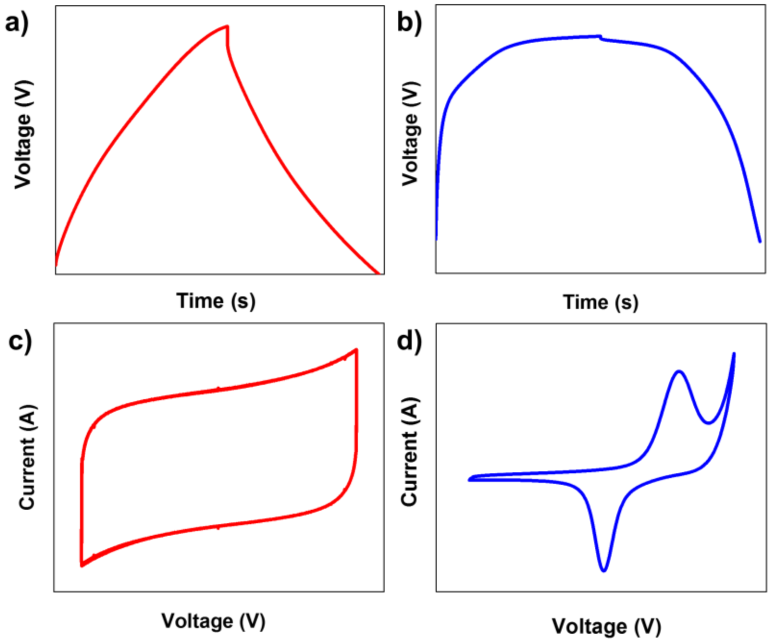

Figure 1.A3 (a) CD curve for an EDLC. (b) CD curve for a battery. (c) CV curve for an EDLC. (d) CV curve for a battery.

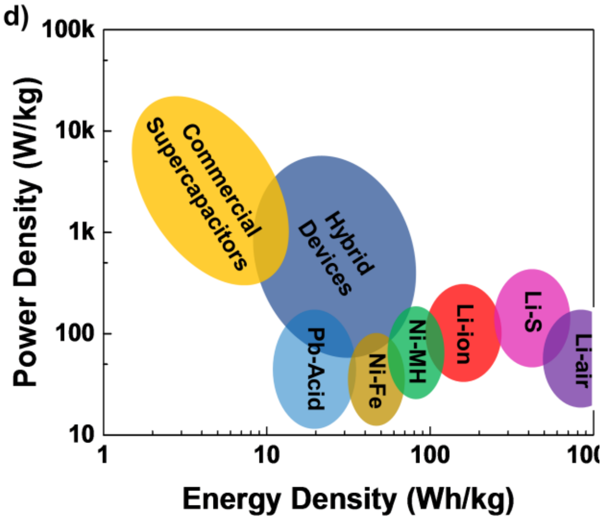

Figure 1.A4 Ragone plot showing the different energy and power performance of different energy storage architectures including supercapacitors, Li ion batteries and advanced Li-air and Li-S batteries.

The second type of measurement that is employed is called a cyclic voltammetry measurement (CV). In this measurement, the voltage is scanned and the current is measured. For EDLC this results in a box-like curve where the hysteresis is proportional to the amount of charge and energy stored, as seen in **Figure 1.A3c**. At a certain point, the CV curve of an EDLC will increase exponentially. This corresponds to unwanted chemical reactions with the electrolyte and is called the electrochemical window. Having a large electrochemical window is critical in developing systems with a large amount of energy storage. In a battery system, there are distinct peaks that correspond to the reduction and oxidation peaks of the chemical reactions, as seen in **Figure 1.A3d**. In a perfectly ideal world, these peaks would occur at the exact same voltage in the positive and negative scan, but in reality they are separated by a small potential called the over-potential that results in a small amount of energy lost in each energy storage cycle.

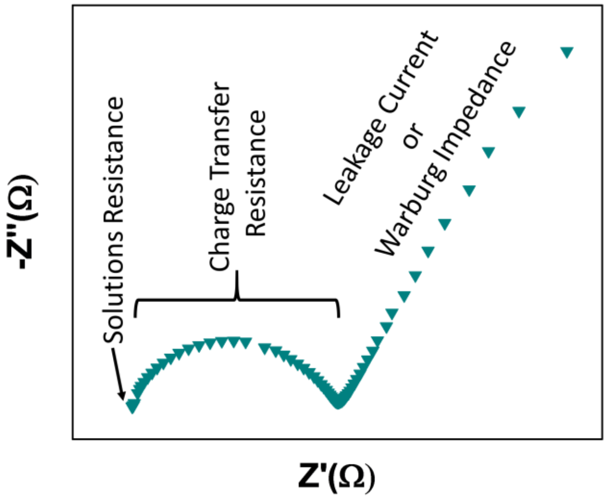

Figure 1.A5 Representative Nyquist plot showing the key elements including the solution resistance, the charge transfer resistance and the impedeance corresponding to the leakage current or Warburg impedance depending on whether or not it is a battery or as supercapacitor

The final type of measurement that is commonly used is that of electron impedance spectroscopy (EIS) where a small AC voltage oscillation is supplied around a given voltage (often 0V or the reaction voltage). In this measurement the frequency of the voltage oscillation is typically varied within the frequency range of 1MHz to .01Hz. Through this measurement, one can determine the various resistances in the system by fitting the resulting data to an equivalent circuit, giving information about the different layers and thin films in the system. An example measurement is presented in **Figure 1.A5.**

1.A.6 Battery design

In an ELDC, the primary design considerations are the conductivity of the electrodes, the electrochemical window of the electrode/electrolyte combination, and the surface area of the system. In order to maximize energy storage, the surface area needs to be increased and the electrochemical window should be maximized. For this purpose the most common EDLC materials are carbon nanomaterial electrodes including activated carbon, carbon nanotubes, and graphene paired with an organic solvent electrolyte or an ionic liquid which exhibit superior electrochemical windows from 2-4V.

Battery design is significantly more involved than traditional EDLC design. Whereas the electrodes in EDLC are identical, in a battery system two different electrodes must be employed in a full cell architecture. In a full cell device, energy is stored in the pairing of two different electrochemical reactions,

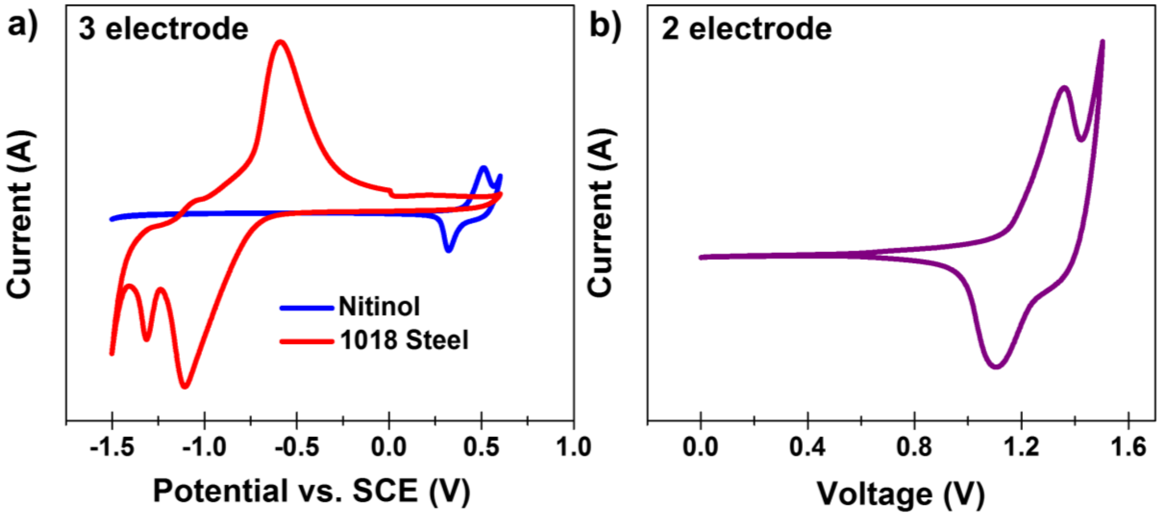

Figure 1.A6 a) CV curves of two three electrode measurements one on anodized steel one on anodized nitinol with the Voltage V plotted versus SCE. b) Paired system for the electrodes represented in a) with the full cell voltage between 0.9 and 1.4V.

one at the cathode and one at the anode. The energy stored in a battery is maximized by maximizing the voltage separation between the absolute reaction voltages of both the anode and the cathode. The second most important consideration in maximizing the voltage of a battery is the charge storage capacity of both the cathode and the anode (see equation for energy above). An example of a battery design is presented in **Figure 1.A6** where an anodized NiTi electrode is paired with an anodized steel electrode in a 1M NaOH electrolyte. **Figure 1.A6a** shows the CV curves of the individual electrodes from 3 electrode measurements on the same graph and **Figure 1.A6b** shows the CV curve for the combined 2 electrode battery system.

References

1. Pancaldi, G. *Historical studies in the physical and biological sciences* **1990,** 21, (1), 123-160.

2. Salkind, A. J.; Israel, P. *J Power Sources* **2004,** 136, (2), 356-365.

3. Kurzweil, P. *J Power Sources* **2010,** 195, (14), 4424-4434.

4. Goodenough, J. B.; Park, K.-S. *J. Am. Chem. Soc.* **2013,** 135, (4), 1167-1176.

5. Armand, M.; Tarascon, J.-M. *Nature* **2008,** 451, (7179), 652-657.

6. Palencia, J. C. G.; Furubayashi, T.; Nakata, T. *Energy* **2012,** 48, (1), 548-565.

7. Palencia, J. C. G.; Araki, M.; Shiga, S. *Applied Energy* **2016,** 181, 96-109.

8. Oshiro, K.; Masui, T. *Energy Policy* **2015,** 81, 215-225.

9. Carter, R.; Ejorh, D.; Share, K.; Cohn, A. P.; Douglas, A.; Muralidharan, N.; Tovar, T. M.; Pint, C. L. *J Power Sources* **2016,** 330, 70-77.

10. Oakes, L. Controlling Nanomaterial Assembly to Improve Material Performance in Energy Storage Electrodes. Vanderbilt University, **2016**.

11. Bruce, P. G.; Freunberger, S. A.; Hardwick, L. J.; Tarascon, J.-M. *Nature materials* **2012,** 11, (1), 19-29.

12. Carter, R.; Oakes, L.; Cohn, A. P.; Holzgrafe, J.; Zarick, H. F.; Chatterjee, S.; Bardhan, R.; Pint, C. L. *The Journal of Physical Chemistry C* **2014,** 118, (35), 20137-20151.

13. Hoffert, M. I.; Caldeira, K.; Benford, G.; Criswell, D. R.; Green, C.; Herzog, H.; Jain, A. K.; Kheshgi, H. S.; Lackner, K. S.; Lewis, J. S. *science* **2002,** 298, (5595), 981-987.

14. Baruch, J. J. *Technology in Society* **2008,** 30, (2), 111-121.

15. Alotto, P.; Guarnieri, M.; Moro, F. *Renewable and Sustainable Energy Reviews* **2014,** 29, 325-335.

16. Weber, A. Z.; Mench, M. M.; Meyers, J. P.; Ross, P. N.; Gostick, J. T.; Liu, Q. *Journal of Applied Electrochemistry* **2011,** 41, (10), 1137-1164.

17. Cohn, A. P.; Share, K.; Carter, R.; Oakes, L.; Pint, C. L. *Nano letters* **2015,** 16, (1), 543-548.

18. Share, K.; Lewis, J.; Oakes, L.; Carter, R. E.; Cohn, A. P.; Pint, C. L. *RSC Advances* **2015,** 5, (123), 101262-101267.

19. Cohn, A. P.; Muralidharan, N.; Carter, R.; Share, K.; Oakes, L.; Pint, C. L. *Journal of Materials Chemistry A* **2016,** 4, (39), 14954-14959.

20. Share, K.; Cohn, A. P.; Carter, R. E.; Pint, C. L. *Nanoscale* **2016,** 8, (36), 16435-16439.

21. Share, K.; Cohn, A. P.; Carter, R.; Rogers, B.; Pint, C. L. *ACS nano* **2016**.

22. Hill, C. A.; Such, M. C.; Chen, D.; Gonzalez, J.; Grady, W. M. *IEEE Transactions on smart grid* **2012,** 3, (2), 850-857.

23. Dunn, B.; Kamath, H.; Tarascon, J.-M. *Science* **2011,** 334, (6058), 928-935.

24. Lund, H. *Energy* **2005,** 30, (13), 2402-2412.

25. Motors, T. *URL: http://www. teslamotors. com/powerwall (accessed: May 2, 2015)* **2015**.

26. Skyllas-Kazacos, M.; Chakrabarti, M.; Hajimolana, S.; Mjalli, F.; Saleem, M. *J Electrochem Soc* **2011,** 158, (8), R55-R79.

27. Cohn, A. P.; Erwin, W. R.; Share, K.; Oakes, L.; Westover, A. S.; Carter, R. E.; Bardhan, R.; Pint, C. L. *Nano letters* **2015,** 15, (4), 2727-2731.

28. Miyasaka, T.; Murakami, T. N. *Applied Physics Letters* **2004,** 85, (17), 3932-3934.

29. Zhang, Z.; Chen, X.; Chen, P.; Guan, G.; Qiu, L.; Lin, H.; Yang, Z.; Bai, W.; Luo, Y.; Peng, H. *Advanced Materials* **2014,** 26, (3), 466-470.

30. Guo, W.; Xue, X.; Wang, S.; Lin, C.; Wang, Z. L. *Nano letters* **2012,** 12, (5), 2520-2523.

31. Chen, T.; Qiu, L.; Yang, Z.; Cai, Z.; Ren, J.; Li, H.; Lin, H.; Sun, X.; Peng, H. *Angewandte Chemie International Edition* **2012,** 51, (48), 11977-11980.

32. Yang, Z.; Deng, J.; Sun, X.; Li, H.; Peng, H. *Advanced Materials* **2014,** 26, (17), 2643-2647.

33. Chen, T.; Yang, Z.; Peng, H. *ChemPhysChem* **2013,** 14, (9), 1777-1782.

34. Xu, J.; Ku, Z.; Zhang, Y.; Chao, D.; Fan, H. J. *Advanced Materials Technologies* **2016**, 1, (5), 1600074 .

35. Zhou, F.; Ren, Z.; Zhao, Y.; Shen, X.; Wang, A.; Li, Y. Y.; Surya, C.; Chai, Y. *ACS nano* **2016**, 10, (6), 5900-5908.

36. Wang, W.; Luo, Q.; Li, B.; Wei, X.; Li, L.; Yang, Z. *Advanced Functional Materials* **2013,** 23, (8), 970-986.

37. Boota, M.; Paranthaman, M. P.; Naskar, A. K.; Li, Y.; Akato, K.; Gogotsi, Y. *ChemSusChem* **2015,** 8, (21), 3576-3581.

38. Thomas, J.; Qidwai, S.; Pogue, W.; Pham, G. *Journal of Composite Materials* **2013,** 47, (1), 5-26.

39. Roberts, S. C.; Aglietti, G. S. *Acta Astronautica* **2010,** 67, (3), 424-439.

40. Snyder, J. F.; Carter, R. H.; Wetzel, E. D. *Chemistry of materials* **2007,** 19, (15), 3793-3801.

41. Roberts, S.; Aglietti, G. *Proceedings of the Institution of Mechanical Engineers, Part G: Journal of Aerospace Engineering* **2008,** 222, (1), 41-51.

42. Thomas, J. P.; Qidwai, M. A. *Acta Materialia* **2004,** 52, (8), 2155-2164.

43. Thomas, J. P.; Qidwai, M. A. *JOM Journal of the Minerals, Metals and Materials Society* **2005,** 57, (3), 18-24.

44. Liu, P.; Sherman, E.; Jacobsen, A. *J Power Sources* **2009,** 189, (1), 646-650.

45. Qian, H.; Kucernak, A. R.; Greenhalgh, E. S.; Bismarck, A.; Shaffer, M. S. *ACS applied materials & interfaces* **2013,** 5, (13), 6113-6122.

46. Javaid, A.; Ho, K.; Bismarck, A.; Shaffer, M.; Steinke, J.; Greenhalgh, E. *Journal of Composite Materials* **2014,** 48, (12), 1409-1416.

47. Shirshova, N.; Qian, H.; Shaffer, M. S.; Steinke, J. H.; Greenhalgh, E. S.; Curtis, P. T.; Kucernak, A.; Bismarck, A. *Composites Part A: Applied Science and Manufacturing* **2013,** 46, 96-107.

48. Qian, H.; Diao, H.; Shirshova, N.; Greenhalgh, E. S.; Steinke, J. G.; Shaffer, M. S.; Bismarck, A. *Journal of colloid and interface science* **2013,** 395, 241-248.

49. Asp, L. E.; Greenhalgh, E. S. *Composites science and technology* **2014,** 101, 41-61.

CHAPTER 2

DIRECT INTEGRATION OF A SUPERCAPACITOR INTO THE BACKSIDE OF A SILICON PHOTOVOLTAIC DEVICE[1]

Andrew S. Westover,[1,2] *Keith Share,*[1,2] *Rachel Carter,*[2] *Adam P. Cohn,*[2] *Landon Oakes,*[1,2] *and Cary L. Pint*[1,2]

[1]Interdisciplinary Material Science and Engineering Program, Vanderbilt University, Nashville, TN 37235, USA

[2]Department of Mechanical Engineering, Vanderbilt University, Nashville, TN 37235, USA

Abstract: We demonstrate a route to integrate active material for energy storage directly into a silicon photovoltaic (PV) device, and the synergistic operation of the PV and storage systems for load leveling. Porous silicon supercapacitors with 84% Coulombic efficiency are etched directly into the excess absorbing layer material in a commercially available polycrystalline silicon PV device and coupled with solid-state polymer electrolytes. Our work demonstrates the simple idea both that the PV device can charge the supercapacitor under an external load and that a constant current load can be maintained through periods of intermittent illumination, demonstrating the concept of an all-silicon integrated solar supercapacitor.

This work was originally published in **Applied Phys. Lett. 104, 213905, May 2014** and is reproduced with permission. © *Applied Physics Letters (2014)*. http://dx.doi.org/10.1063/1.4880211

2.1 Introduction

High penetration photovoltaic (HiPen PV) solar power integration into the electric grid requires temporal coordination between solar energy harvesting and power delivery.[2, 3] The intermittency of solar power in a HiPen PV model leads to the inability to facilitate a constant grid load, which ultimately leads to energy curtailment and lower economic value of PV systems.[4, 5] However, the coupling of energy storage with PV systems to temporally manage power generation and delivery solves this problem, despite the short lifetime and high cost of conventional secondary batteries that steeply increases the cost per watt of solar-storage.[6] Furthermore, power transmission to a centralized battery source will require subsequent power inversion that lowers the total system efficiency. Therefore, the most attractive scheme for solar-storage is to have storage capability integrated at the point of energy generation, with minimum added cost to the native solar cell. Conventional PV devices make use of less than 5% of the total silicon in the device for power generation, and are produced in wafers with thicknesses > 100 μm due to the extreme high cost of producing ultra-thin silicon.[7] The premise of our approach is that the unused silicon can be directly converted to a medium for energy storage using a one-step route compatible with current manufacturing processes. This is unique from other recent efforts focused on electrochemical solar devices where nanostructured materials can be grown or fabricated on a common metal or conductive electrode that can enable dual function for conversion and storage operation.[8-15] In our case, we are transforming an existent, commercially available silicon PV cell into a solar storage material by transforming existent material already contained in the solar device.

2.2 Experimental Methods

To achieve integration into an existent silicon PV device, the as-received commercial polycrystalline silicon solar cell panel (Silicon Solar, 400mA, .22W, Polycrystalline, 14.8% efficiency) was placed in a 1 M KOH solution for 40 minutes to dissolve the aluminum current collector from the silicon absorbing layer. Following this, electrochemical etching for 360 seconds was performed using a current

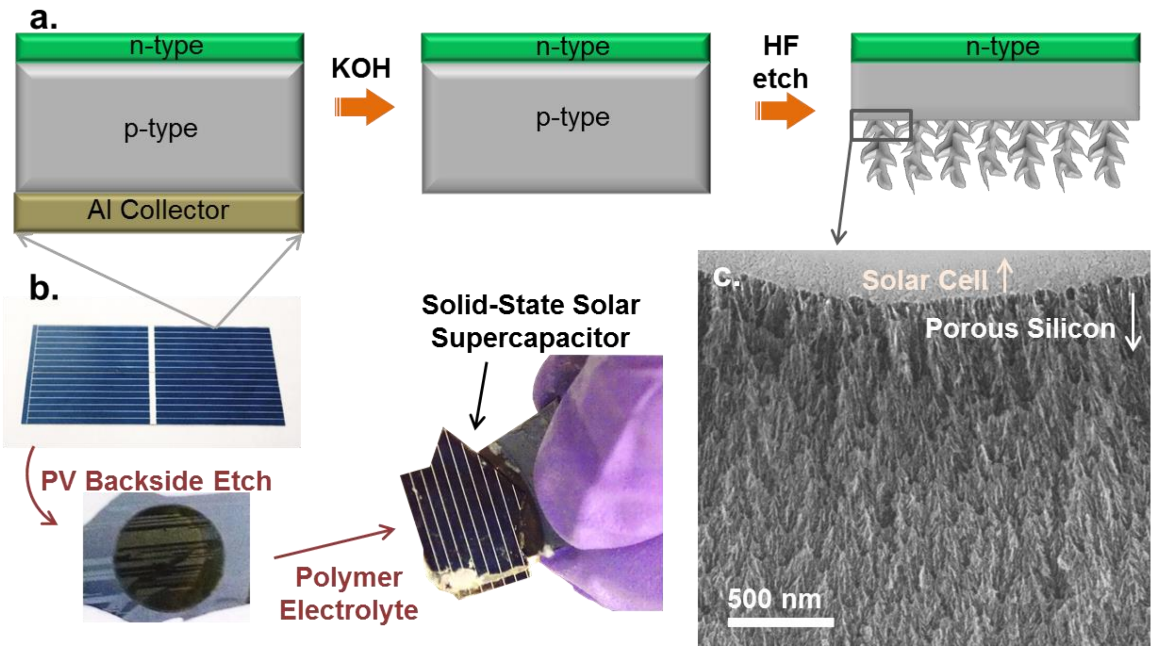

Figure 2.1 (a) Scheme demonstrating key steps for fabrication of a solar supercapacitor based on a commercial PV device, including KOH dissolution of the Al collector material, and HF electrochemical etching to produce porous silicon. (b) Photographs of the PV cell after HF etching showing the dark circular porous silicon material, and the final solid-state integrated device following polymer electrolyte infiltration, (c) SEM image of the interface between the high surface area porous silicon energy storage material and the absorbing layer of the solar cell.

density of 45 mA/cm^2 in a 3:7 v/v HF (50% H_2O by volume) and ethanol solution directly into the backside of the solar cell (**Figure 2.1 a-b**) in accordance with our previous efforts to fabricate porous silicon supercapacitors.[16] SEM imaging (**Figure 2.1c**) of the porous silicon-PV device interface demonstrates an electrically addressable high-surface area porous silicon material[17] with a thickness of ~ 4.8 μm that can enable electric double-layer energy storage as a supercapacitor. To develop a solid-state architecture that sustains mechanical integrity and requires no external electrolyte packaging, we mixed (on a hot plate at 50˚ C) polyethylene oxide (PEO) (Sigma Aldrich, 100,000 M.W.), 1-ethyl-3-methyl imidazolium tetrafluoroborate (EMIBF$_4$, Sigma 98%), and propylene carbonate (PC) in a 1:1:8 ratio by weight,[18, 19] cast this onto the PV supercapacitor electrode, and sandwiched this with an equivalently prepared single crystalline porous silicon counterelectrode. This entire device is then left in a vacuum oven for 24 hours at 50ºC to remove PC and produce an integrated solid-state solar supercapacitor (**Figure 2.1b**). To test operation of the integrated system, the solar cell was wired to the bottom of the supercapacitor counterelectrode, and the supercapacitor was individually tested by attaching wires to the bottom of the solar cell and to the bottom of the counterelectrode.

2.3 Results and Discussion

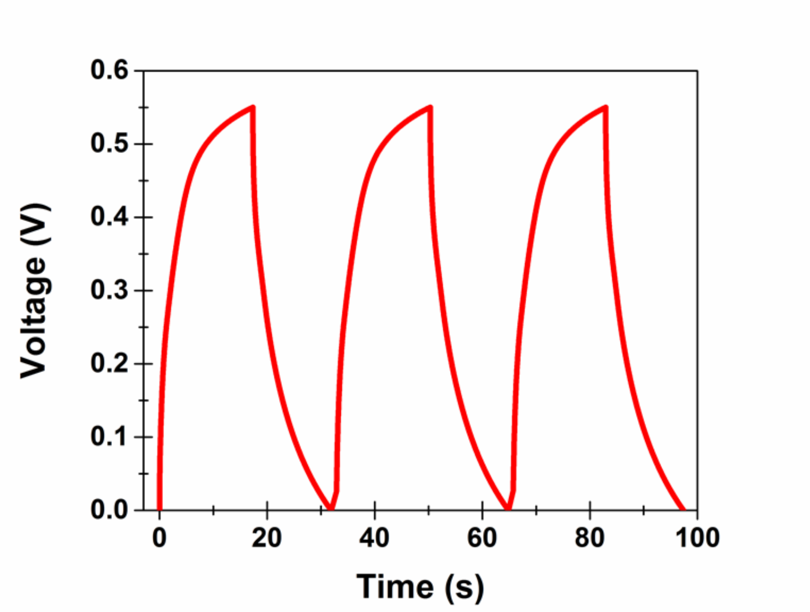

Figure 2.2 Three consecutive Galanostatic charge-discharge cycles on the supercapacitor integrated into the solar cell, but charged and discharged electrically as an isolated system.

To characterize the device performance of the supercapacitor integrated into the backside of the PV device, we performed Galvanostatic charge-discharge measurements at a current of I_c = 0.4 µA/cm^2 to a cutoff voltage of 0.55 V, to match the specified output voltage of the PV device (**Figure 2.2**). From these curves, we calculate a total Coulombic efficiency of 84%, and total capacitance of 0.14 F/m^2 normalized to the area of the electrode and based on the relationship $C = I_c(dV/dt)^{-1}$, where dV/dt is the slope of the discharge curve.[20, 21] This indicates for a PV device operating with 14.8% efficiency and under ideal operation of the supercapacitor, 84% of the charge generated by the PV device can be effectively stored by the supercapacitor.

In order to further elucidate the coordinated performance of the integrated solar supercap device, we performed experiments where 0.65 suns (65 mA/cm^2) of solar illumination was utilized to charge the integrated supercapacitor using an Oriel 200 W solar simulator, and the supercapacitor was then electrically discharged Galvanostatically at a current density of 0.4 µA/cm^2 (**Figure 2.3a**). Here, the PV-supercap was illuminated for 20 seconds, at which time the lights were turned off, the electrical path between the counterelectrode and PV device was disconnected, and the device was Galvanostatically discharged. In order to clearly demonstrate the effect of the incident solar illumination as the mechanism for charging the supercapacitor, we compared this to an identical control measurement involving the same PV device, except wired across the solar cell as opposed to wired across the solar supercapacitor integrated system. As can be expected from the PV device independently, the voltage drops almost instantaneously when an electric current load is applied in the dark following 20 seconds of illumination. However, the solar supercapacitor integrated device exposed to the same conditions exhibits an electrical discharge of several seconds with this current load, emphasizing the ability to discharge energy under dark conditions that is enabled by the integrated supercapacitor.

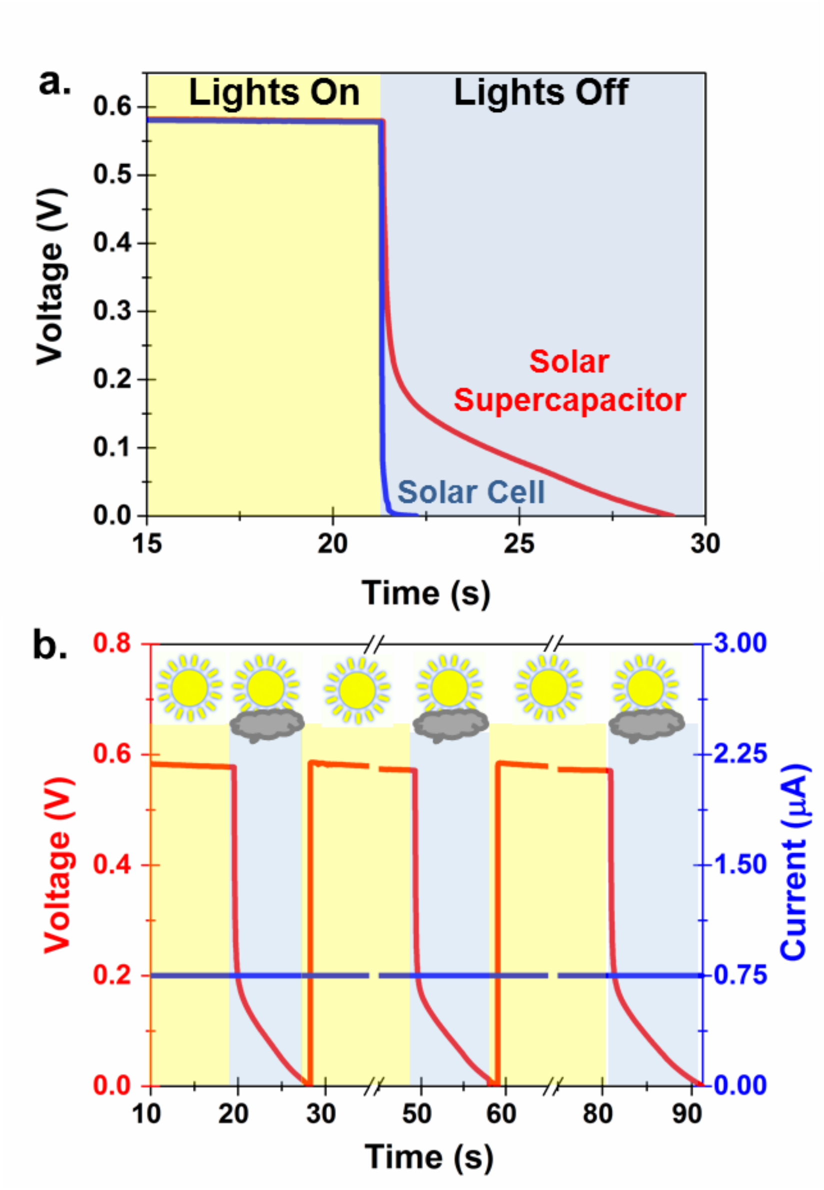

Figure 2.3 (a) Charging of the solar supercap with AM 1.5 solar illumination at 0.65 mW/cm^2, and electrical discharging of the device at 0.4 μA/cm2. To emphasize the synergistic performance of the integrated supercapactor, a control was performed on the same device except wired only across the solar cell (blue). (b) three consecutive cycles of illuminated and dark states under a constant current load of 0.75 μA to demonstrate the constant current output from the solar supercapacitor device.

One of the key challenges of isolated PV cells is the notion that intermittent changes in climate, such as a cloud passing overhead, can lead to temporary load-shifting onto the electrical grid, and this can be problematic in HiPen PV models. However, we demonstrate that under a constant electric current load (0.4 µA/cm^2, or 0.75 µA), that the integration of the PV device and supercapacitor can yield a constant current output despite a cyclic intermittent variation between dark and illuminated states, measured over three cycles. As illustrated in **Figure 2.3b**, this simulates the effect of a cloud passing overhead, and without the integrated supercapacitor with the PV device the resulting discontinuous current output would be unable to maintain a constant current load, thus requiring either an externally situated battery or load-shifting to the grid.

2.4 Conclusion

Whereas this work demonstrates the feasibility of this integration approach, numerous routes can be taken to optimize this system, such as deeper etches into the PV device to improve the total active material,[17] low-temperature surface passivation of the porous silicon to improve charge storage,[16] and other device platforms that utilize the porous silicon that can improve energy density while still retaining a cycle longevity commensurate with a potential 30 year solar cell lifetime, which supercapacitors are capable of matching.[20] Our results give promise to the synergistic integration of energy storage directly into PV devices, and provide a route to improve the viability of PV for the electrical grid with no additional materials cost to current PV systems and etch processes consistent with current semiconductor manufacturing routes. The underlying basis of this work is a system where an energy storage medium is remotely charged by sunlight, which could extend beyond grid-scale solar applications to remote, cordless charging routes for a variety of next-generation technologies such as mobile electronics, electric vehicles, and aerospace systems, for example.

Acknowledgements

The authors would like to acknowledge the support of W. Erwin and R. Bardhan for experimental and literature guidance, S. Weiss for partial use of facilities for etching, and D. Gardner for early discussions on this idea. This work was supported in part by the National Science Foundation CMMI 1334269, and Vanderbilt start-up funds with support for A.W. provided by NSF grant EPS 1004083.

References:

1. Westover, A. S.; Share, K.; Carter, R.; Cohn, A. P.; Oakes, L.; Pint, C. L. *Applied Physics Letters* **2014,** 104, (21), 213905.

2. Brinkman, G.; Denholm, P.; Drury, E.; Margolis, R.; Mowers, M. *IEEE Power Energy M.* **2011,** 9, (3), 24-32.

3. Katiraei, F.; Aguero, J. R. *IEEE Power Energy M.* **2011,** 9, (3), 62-71.

4. Denholm, P.; Margolis, R. M. *Energ. Policy* **2007,** 35, (5), 2852-2861.

5. Zhao, J. Y.; Kucuksari, S.; Mazhari, E.; Son, Y. J. *Appl. Energ.* **2013,** 112, 35-51.

6. Denholm, P.; Margolis, R. M. *Energ. Policy* **2007,** 35, (9), 4424-4433.

7. Shah, A.; Torres, P.; Tscharner, R.; Wyrsch, N.; Keppner, H. *Science* **1999,** 285, (5428), 692-698.

8. Guo, W. X.; Xue, X. Y.; Wang, S. H.; Lin, C. J.; Wang, Z. L. *Nano Lett.* **2012,** 12, (5), 2520-2523.

9. Zhang, X.; Huang, X. Z.; Li, C. S.; Jiang, H. R. *Adv. Mater.* **2013,** 25, (30), 4093-4096.

10. Huang, X. Z.; Zhang, X.; Jiang, H. R. *J. Power Sources* **2014,** 248, 434-438.

11. Zhang, Z.; Chen, X.; Chen, P.; Guan, G.; Qiu, L.; Lin, H.; Yang, Z.; Bai, W.; Luo, Y.; Peng, H. S. *Adv. Mater.* **2014,** 26, 466-470.

12. Chen, T.; Yang, Z. B.; Peng, H. S. *Chemphyschem* **2013,** 14, (9), 1777-1782.

13. Song, T.; Sun, B. Q. *Chemsuschem* **2013,** 6, (3), 408-410.

14. Xia, X. H.; Luo, J. S.; Zeng, Z. Y.; Guan, C.; Zhang, Y. Q.; Tu, J. P.; Zhang, H.; Fan, H. J. *Sci. Rep.* **2012,** 2, 981.

15. Wee, G.; Salim, T.; Lam, Y. M.; Mhaisalkar, S. G.; Srinivasan, M. *Energ. Environ. Sci.* **2011,** 4, (2), 413-416.

16. Oakes, L.; Westover, A.; Mares, J. W.; Chatterjee, S.; Erwin, W. R.; Bardhan, R.; Weiss, S. M.; Pint, C. L. *Sci. Rep.* **2013,** 3, 3020.

17. Granitzer, P.; Rumpf, K. *Materials* **2010,** 3, (2), 943-998.

18. Ketabi, S.; Lian, K. *Solid State Ionics* **2012,** 227, 86-90.

19. Lewandowski, A.; Swiderska, A. *Solid State Ionics* **2004,** 169, (1-4), 21-24.

20. Simon, P.; Gogotsi, Y. *Nat. Mater.* **2008,** 7, (11), 845-854.

21. Gogotsi, Y.; Simon, P. *Science* **2011,** 334, (6058), 917-918.

CHAPTER 3

ON-CHIP HIGH POWER POROUS SILICON LITHIUM ION BATTERIES WITH STABLE CAPACITY OVER 10000 CYCLES[1]

Andrew S. Westover[1,2], Daniel Freudiger[1], Zarif S. Gani[1], Keith Share[1,2], Landon Oakes[1,2], Rachel E. Carter[1], and Cary L. Pint[1,2]

[1]Department of Mechanical Engineering, Vanderbilt University, Nashville TN 37235

[2]Interdisciplinary Material Science and Engineering Program, Vanderbilt University, Nashville, TN 37235, USA

Abstract: We demonstrate the operation of a graphene-passivated on-chip porous silicon material as a high rate lithium battery anode with over 50X power density, and 100X energy density improvement compared to identically prepared on-chip supercapacitors. We demonstrate this Faradaic storage behavior to occur at fast charging rates (1-10 mA/cm^2) where lithium locally intercalates into the nanoporous silicon, preventing the degradation and poor cycling performance attributed to deep storage in the bulk silicon. This device exhibits cycling performance that exceeds 10000 cycles with capacity above 0.1 mAh/cm^2 without notable capacity fade. This demonstrates a practical route toward high power, high energy, and long lifetime all-silicon on-chip storage systems relevant toward integration into electronics, photovoltaics, and other silicon-based platforms.

This work was originally published in **Nanoscale 7 (1), 98-103, Nov. 2014** and is reproduced with permission. © *Nanoscale (2014)* DOI: 10.1039/C4NR04720F

3.1 Introduction

From portable electronics to solar cells, power delivery systems that can be integrated into unused components in devices are critical to meet the increasing power requirements of future applications. In electronics, as the number of transistors per unit area increases, so do the corresponding power requirements for operation. For solar cells, as residential solar usage becomes more prominent, integrated energy storage allows continuous power generation amidst intermittent periods of sunshine.[2-4] In both of these cases, as well as in other silicon-based on-chip applications, a key differentiating factor for integration is the notion that energy storage must be developed on a two-dimensional, planar substrate that must concurrently support operation of the component on the front side of the device. Unlike conventional energy storage systems that are packaged into three-dimensional architectures with performance assessed relative to mass or volume,[5] on-chip devices must be assessed for their ability to store charge that scales with the total available chip area, or footprint. This has led to the development of on-chip devices called micro-supercapacitors or micro-batteries,[6-9] which are most practical when the native chip material is used as real estate for energy storage with minimal additional manufacturing steps. Silicon is an ideal choice due to its relevance to batteries, supercapacitors, and its broad application in electronics, MEMS, solar energy conversion, and sensing.

Specifically for lithium storage applications, silicon exhibits the highest known storage capacities (up to 4200 mAh/g), but exhibits rapid capacity fade upon cycling associated with the large volume expansion in silicon during lithiation.[10-12] Whereas elegant routes have been developed to combat such degradation in nanoparticle electrodes, such as yolk-shell structures[13] and pomegranate-like architectures,[14] seamless integration of these techniques to on-chip platforms is not straightforward. Previous studies which have demonstrated on-chip storage using porous silicon build upon a native architecture that enables efficient volumetric expansion of the silicon during cycling, but exhibit limitations in cycle lifetime due to the porous silicon/silicon interface,[15-17] even though some studies indicate some intercalation control through modulating the rates or capacities.[17, 18] This has motived the development of superior macroparticle silicon particle networks.[19] Therefore, despite the promise of large energy densities, the bottleneck for on-chip silicon batteries is the low power density and short cycle lifetime of these materials. On the other hand, electrochemical supercapacitors exhibit the power capability sought for on-board electronics, and are often rated for up to a million consecutive cycles, but are limited to energy densities at best 10X lower than conventional batteries due to the physical double layer charge storage mechanism.[20-22] However, porous silicon materials used for supercapacitors have demonstrated unique integration capability with applications,[23-25] such as the ability to form supercapacitors to store energy directly in the unused material in solar cells.[26]

In this work, we demonstrate hybrid performance bridging these two device platforms based on carbon-passivated porous silicon material etched into bulk silicon wafers and cycled as a lithium-ion battery electrode at high currents. Using identically structured supercapacitors as a control comparison, we demonstrate over 50X improved power density, and over 100X improved energy density in this high rate porous silicon battery which operates over 10000 cycles with no significant capacity fade and stores more *total* energy on chip than both an ideal deeply intercalated battery anode, or an electrochemical supercapacitor operating for 250 and a million cycles, respectively. This unique operation mode provides ideal characteristics of power, energy, and lifetime sought for on-chip integration.

3.2 Experimental Methods

In order to prepare electrodes, B-doped silicon wafers (0.01 – 0.02 Ωcm) were electrochemically etched using a 3:7 v/v HF (50% H_2O by volume) and ethanol solution at 45 mA/cm^2 for 180 seconds in either a home-built etching cell or an AMMT porous silicon etching system. This yields porous Si with 75% porosity and a ~ 4 µm depth (**Figure 3.1a**). To passivate the porous silicon from the effects of electrochemical degradation or inhibitory solid electrolyte interphase layer formation, we used chemical vapor deposition using a ramp procedure described previously[23, 24] that is known to generate few-layer coatings of graphene-like carbon on the surface of the porous silicon material. Briefly, this involves consecutive temperature ramps from 650-750ºC, and 750-850ºC for 10 minutes each, with a 1:20:100 ratio of C_2H_2:H_2:Ar gas mixture carried out under atmospheric conditions. A representative TEM image of the carbon passivated silicon material used in these experiments is shown in **Figure 3.1c.** In order to assess the storage performance of these materials, we constructed lithium-ion batteries using the passivated porous silicon as an electrode combined with Li foil, a Celgard battery separator, and electrolyte consisting of 1 M $LiPF_6$ dissolved in ethylene carbonate/dimethyl carbonate, sealed in a coin cell assembly. One general observation is that the charging rate dictates the penetration depth of the intercalation process, and a transition exists between what we indicate as “high-rate” behavior, where the current is high enough to only allow intercalation into the nanoporous active material, and “deep-charge” behavior where lower charging currents allow the slower bulk intercalation kinetics into bulk silicon material underneath the porous silicon layer. In order to assess the non-Faradaic (surface) storage per unit footprint in a material with an identical porous structure (thickness, porosity, *etc.*), we utilized an electrochemical supercapacitor as an ideal control experiment. Here, a supercapacitor only stores energy by the assembly

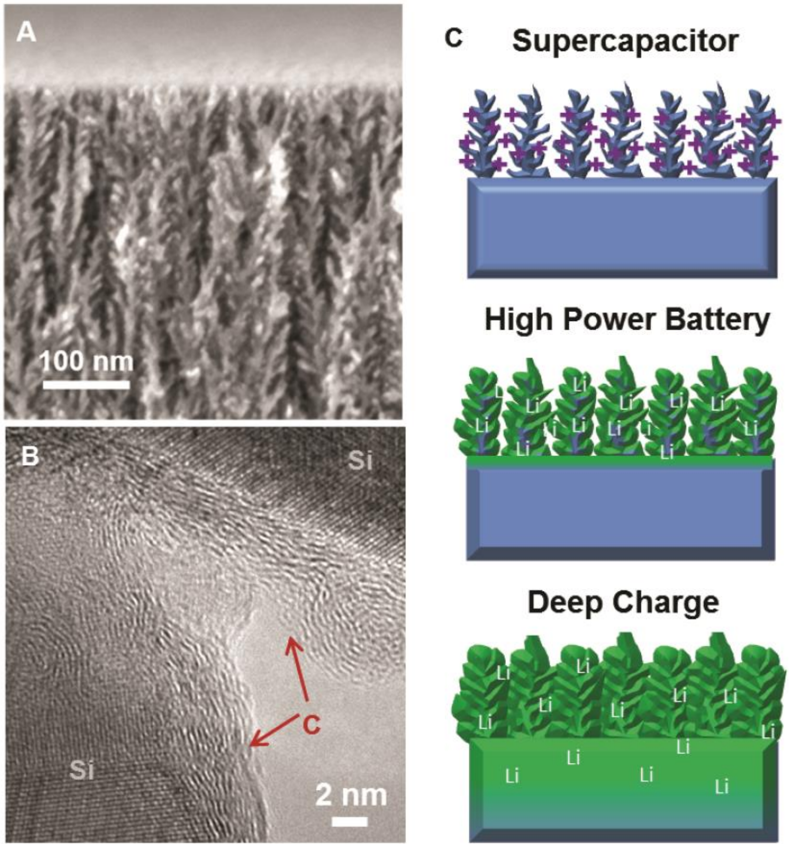

Figure 3.1. (a) Side-view SEM image of carbon-passivated porous silicon materials utilized in this work, (b) High resolution TEM image of the carbon passivated silicon material that indicates the quality of the carbon and crystalline nature of the silicon nanomaterials, and (c) Scheme visually depicting the three modes of energy storage in carbon-passivated porous silicon materials explored and discussed in this work including supercapacitors, high-power batteries, and deep intercalation batteries.

of a double-layer of ions at the surface of the porous silicon, allowing a robust comparison to Faradaic, bulk redox storage in batteries using an identical material. Supercapacitors were made in a manner reported elsewhere[23, 24] by sandwiching two symmetric porous silicon electrodes with a Celgard separator and 1-ethyl-3-methylimidazolium tetraflouroborate ($EMIBF_4$) ionic liquid electrolyte. A visual comparison of these three different storage modes in the same material are shown in **Figure 3.1c** representing (top) double-layer storage of ions in a supercapacitor, (middle) fast lithium intercalation into the nanoscale porous active material, and (bottom) deep intercalation at slow rates into both the porous layer and the bulk silicon wafer.

3.3 Results and Discussion

In order to assess the performance of these on-chip devices, we performed both Galvanostatic charge-discharge measurements and cyclic voltammetry analysis. With this specific porous silicon material employed in a Li-ion battery, we observe a distinct transition near charging currents of 1.2 mA/cm^2 separating the "high rate" and "deep-intercalation" processes. Above 1.2 mA/cm^2, we observe reversible storage capacities up to ~ 0.1 mAh/cm^2, with energy stored at voltages vs. Li/Li+ above the energy of intercalation into bulk silicon (*e.g.* above 0.6 V vs Li/Li+) extending up to ~ 3 V (**Figure 3.2a**). In comparison to a device charged at 1 mA/cm^2 (inset, **Figure 3.2a**), signatures of deep Li bulk intercalation (below 0.6 V) and Li intercalation into the passivated porous silicon layer (0.6 V – 3 V) are observed, distinguishing these two intercalation processes. To better understand this, we performed CV measurements of high-rate devices at rates of 5, 10, and 20 mV/s (**Figure 3.2b**). Evident from these curves is the lack of a bulk intercalation signature below 0.5 V, and a redox couple for insertion/deinsertion at voltages centered around ~ 1.6 V and ~ 1.2 V vs. Li/Li+, respectively. CV curves taken at the same rates, but without the carbon passivation layer indicate similar intercalation and deintercalation kinetics, emphasizing that this behavior is not due to the graphene passivation (**Figure 3.A2**). Furthermore, we performed control experiments where freestanding layers of identical porous silicon were isolated on Ti substrates and assessed at high rates, with similar cyclic voltammetry profiles observed in comparison to on-chip integrated devices emphasizing the porous material as being responsible for the lithium storage.

The high rate intercalation behavior is distinguished from that observed in CV scans taken at slow rates of 0.1 and 0.5 mV/s, respectively (**Figure 3.2c**), where sharp intercalation peaks are observed at 0.36 V and 0.56 V and a deintercalation peak is observed at 0.14 V that emphasizes the redox couples associated with bulk Li storage in silicon.[27-29] Furthermore, whereas high-rate Galvanostatic measurements indicate less distinctly defined Faradaic storage energies, we can distinguish this storage from capacitive double-layer

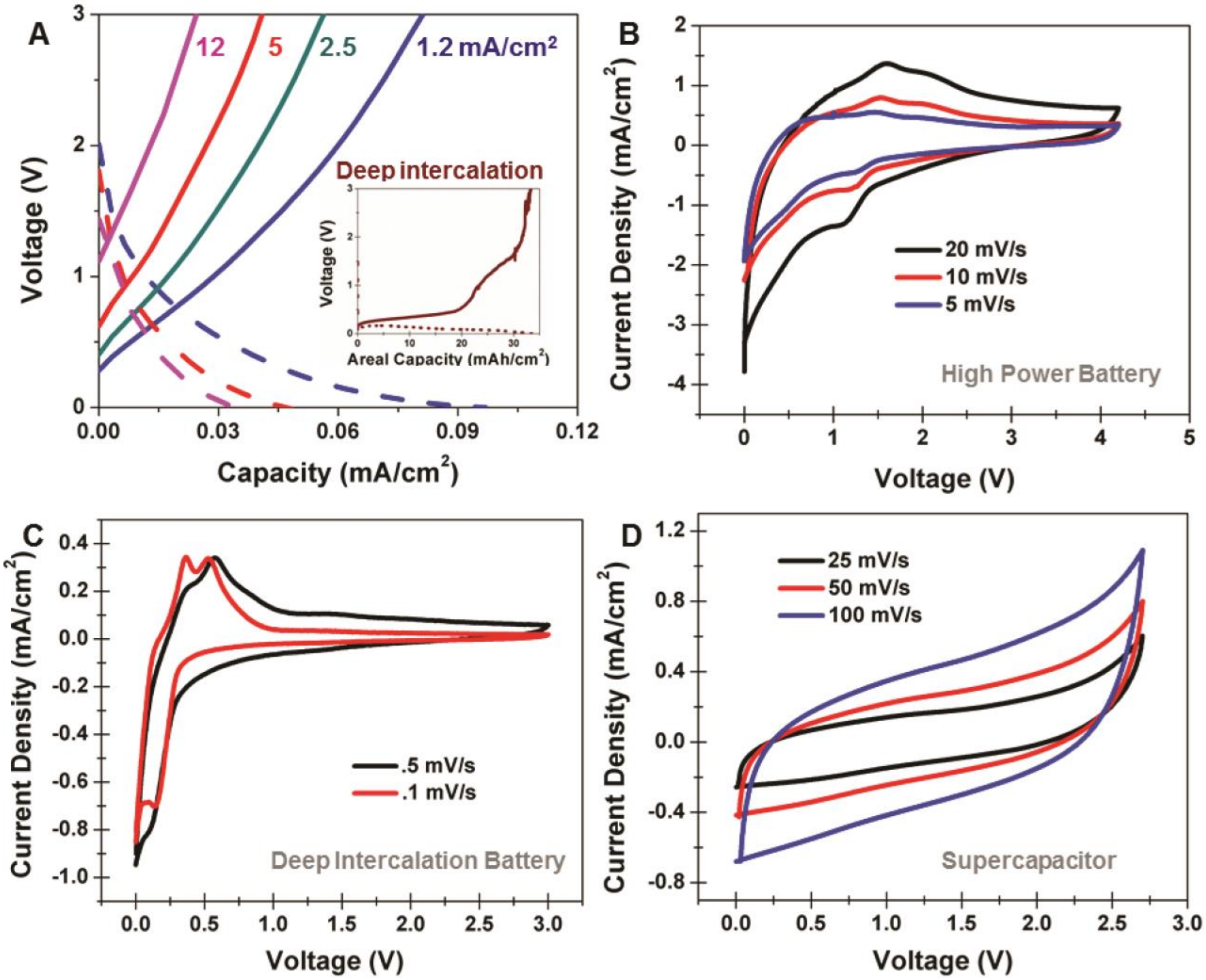

Figure 3.2 (a) Galvanostatic charge-discharge curves taken for carbon-passivated porous silicon high power batteries at rates between 1.2 – 12 mA/cm^2. A corresponding deep intercalation battery charge-discharge curve is inset in order to distinguish bulk Si intercalation versus high power storage in the nanoscale carbon-passivated porous silicon material. (b) Cyclic voltammetry (CV) curves of carbon-passivated porous silicon batteries at fast scan rates of 5, 10, and 20 mV/s demonstrating the high power storage behavior of the porous silicon. (c) CV curves for carbon-passivated porous silicon batteries at slow scan rates of 0.1 and 0.5 mV/s indicating standard Si bulk intercalation behavior. (d) CV curves for carbon passivated porous silicon supercapacitors with EMIBF4 electrolytes at 50 mV/s to demonstrate charge storage through a surface double layer formation.

storage by direct comparison to supercapacitors formed from identical carbon passivated porous silicon. CV measurements for supercapacitors (**Figure 3.2d**) indicate smooth, featureless curves representative of non-Faradaic storage processes, in comparison to CV curves for high-rate batteries, which implies storage through Faradaic chemical redox processes. This indicates the high-rate storage energetics and process for carbon-passivated porous silicon electrodes is distinguished both from bulk Li storage observed in conventional silicon battery electrodes and the surface double-layer storage behavior observed in electrochemical supercapacitors.

One of the key challenges in utilizing silicon materials in batteries is the poor cycling lifetime of the active materials. Our work demonstrates that we can overcome this limitation for an on-chip carbon passivated porous silicon battery by operation in the high power mode, thus inhibiting deep bulk intercalation that leads to irreversible capacity fade. **Figure 3.3** shows the capacity measured as a function of the number of cycles for an on-chip porous silicon Li ion battery charged and discharged at 3 mA/cm^2, following 3000 preliminary cycles for stabilization at 3 mA/cm^2. We speculate that the preliminary 3000 cycles represents a continuous activation of the porous silicon electrical conductivity by formation of a Li-Si alloy, which has been observed to improve conductivity of amorphous silicon by over 3 orders of magnitude.[30] As porous silicon exhibits high resistance after electrochemical etching, we anticipate that lowering the resistance of the active material in combination with the high surface area for the electrode-electrolyte interface that leads to low cell resistance, allows this device to overcome the resistance polarization that

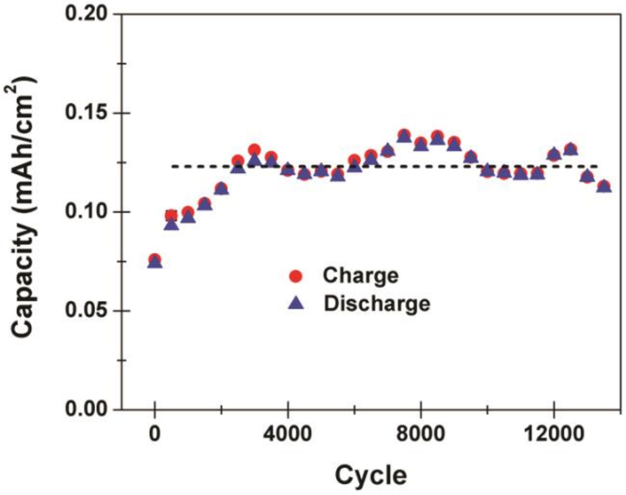

Figure 3.3 Footprint capacity as a function of cycle number over more than 13000 consecutive cycles with charge and discharge capacities plotted separately to indicate the ~ 100% Coulombic efficiency achieved. A straight line is included to guide the eye.

ultimately limits conventional batteries from high power cycling behavior. After capacity stabilization, the device shows excellent cycling capability, with a slightly fluctuating but constant capacity that exceeds 13,000 cycles. This result is in direct contrast to the slow charged porous Si anodes which rapidly degrade over 10-30 cycles with the capacity fade showing an exponential decay upon cycling (**Figure 3.A1, 3.A3**). Whereas the best silicon nanoparticle electrode materials have demonstrated cycling lifetime up to 1000 cycles,[13, 14] these materials must be combined with binders and cast into coatings applied to a conductive charge collector. In our case, the electrode active material is mechanically integrated directly into a silicon wafer with no binder materials, resulting in deep intercalation processes that inhibit cyclability as observed in other studies with porous silicon materials.[11, 12, 15] However, by using the Galvanostatic charging conditions to control the intercalation depth to only penetrate the nanoscale active layer, we observe this battery to exhibit exemplary cycling stability that significantly exceeds the capability of other Si materials. This mechanism and the device lifetime is similar to that exhibited in a conventional pseudocapacitor, except with significantly improved capacities and using conventional carbonate electrolytes. To support this concept, we performed SEM imaging of porous Si materials cycled both at high power conditions, and under deep intercalation conditions. For the deep intercalation (~ 20 cycles), significant cracking that extends up to ~ 40 microns into the surface is observed. However, for the high power cycling experiments, the porous structure after cycling is clearly in-tact, with no evident damage to the silicon material residing underneath the porous layer. This confirms, in agreement with cycling data performed on freestanding porous silicon films, that the high rate cycling is correlated to storage in the porous material (**Figure 3.A4**). To further emphasize this point, normalizing the capacity of the deep intercalation battery to only the material in the porous layer yields ~ 124,600 mAh/g, which is clearly well above the maximum capacity of Si for Li storage. Similar assessment of the high rate storage normalized to the porous layer indicates a capacity of ~ 570 mAh/g, which is a reasonable capacity for silicon materials at high charge-discharge cycling rates, and still respectable in comparison to conventional anodes such as bulk carbons (maximum capacity of 372 mAh/g).

Additionally, it is important to assess the energy and power capability of these devices based on their available chip-based footprint. For devices produced using identical carbon-passivated porous silicon materials, we compared the energy and power performance of supercapacitors, high power batteries, and deep intercalation batteries (**Figure 3.4a**). These curves were each assessed by direct integration of Galvanostatic discharge curves at different cycling rates, and analysis of the average power that is represented by the total energy divided by the discharge duration. A distinguishing factor between the high-power Li-ion battery and the electrochemical supercapacitor is that the high power battery can exhibit up to 100X the power density per footprint of the supercapacitor, and exhibit energy densities up to almost 250X greater than the supercapacitor per unit footprint. We anticipate this is due to the greater electrode-electrolyte surface area interface that minimizes electrode resistance polarization losses that inhibit bulk materials from high power storage. These relative values significantly distinguish the bulk storage in the nanoscale porous layer from the surface double-layer storage in a supercapacitor

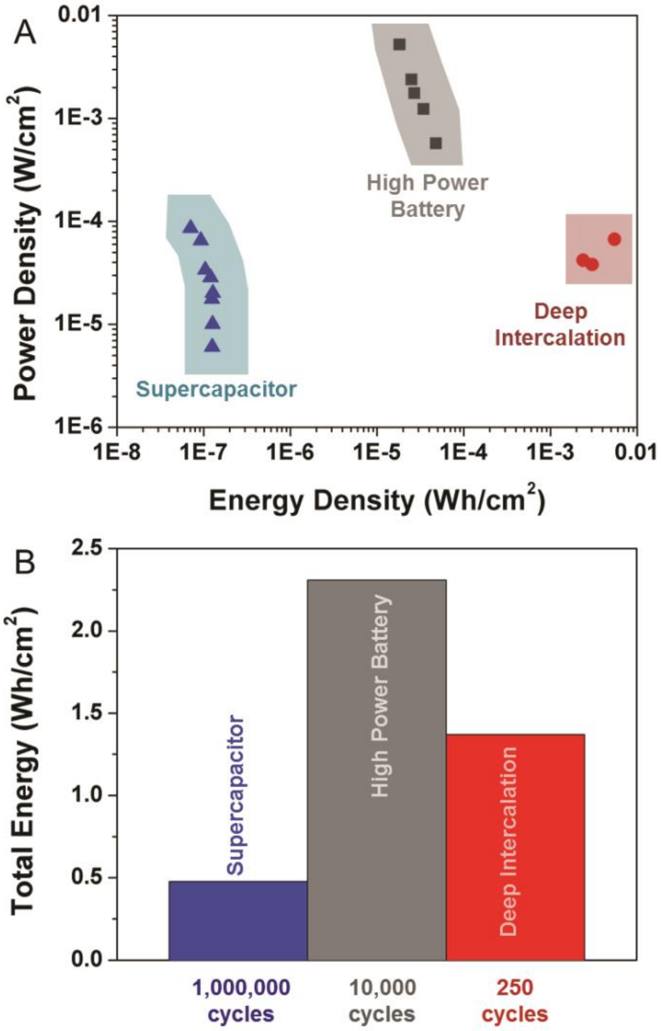

Figure 3.4 (a) Energy-power analysis based on the integration of discharge curves from devices prepared with identical carbon-passivated porous silicon materials, including supercapacitors, high-power lithium-ion batteries, and deep-intercalation lithium-ion batteries. (b) Total energy stored over the measured or extrapolated lifetime of the three devices studied in this work. For supercapacitors, the cycle lifetime is extrapolated to 1 million cycles, and for deep-intercalation batteries the cycle lifetime is extrapolated to 250 cycles. As both of these are optimistic and ideal extrapolations, the total energy for the high power device is based on the measured stored energy over 10000 cycles conducted in this study.

since both materials have the exact same structure. Comparing the power and energy storage capability measured in these high rate devices to the best state-of-the-art 3D graphene supercapacitors per unit active mass (40-85 Wh/kg, 25 kW/kg),[31] the specific power and energy capability, scaled to the porous active material, still exhibits comparable power density of ~ 20 kW/kg, and much greater energy density of ~ 220 Wh/kg. It should further be noted that higher power carbon supercapacitors are usually realized from ultrathin highly porous electrodes, and the energy and power performance is known to decrease or change with electrode thickness making the comparison of such materials challenging.[4] This means thick active layers of storage material, such as graphene, are likely to both inhibit good areal on-chip performance, in addition to being poorly suited for integration due to a heterogeneous van der Waals interface with a collector material – in contrast to the directly integrated high power porous silicon battery electrode. Further, comparison of the high power battery to a slow-charged, deep intercalation battery indicates a 100-150X lower energy density, but a power density that remains between 10-100X improved per unit footprint.

The unique nature of a secondary battery emphasizes that both the energy stored per cycle and the total stored energy over the lifetime of the device are important metrics for device performance. In order to compare the total energy stored, we provide an optimistic comparison between the electrochemical supercapacitor and deep intercalation battery performance, compared to the measured performance of the high power battery. The total energy stored by the supercapacitor, over the lifetime of the device was estimated by multiplying the maximum energy stored by the supercapacitor times the anticipated supercapacitor lifetime of 1,000,000 cycles. For the deep intercalation battery, we assess the maximum capacity and optimistically assume this capacity to be achievable for 250 cycles, despite our experimental measurements of ~ 60% capacity fade for the first 10 cycles, emphasizing the highly conservative nature of this estimate. Finally, we calculated the total energy stored in the high power Li ion battery based on experimental analysis of the 10,000 active cycles that were experimentally measured and assessed. Whereas this device is still active after 10,000 cycles and our cycling experiments extend beyond 13,000 cycles, we observe this high rate battery platform to exhibit significantly more total energy stored in comparison to both a conservatively estimated ideal deep intercalation battery and an ideal supercapacitor that operates based on an identical electrode structure. Furthermore, the higher power capability of the fast-rate porous silicon battery that is enabled by Li metal stored in the nanoscale silicon material enables it to exhibit better power capability in storing its energy over the course of its lifetime.

3.4 Conclusion

Finally, whereas our results emphasize that the on-chip porous layer is responsible for the high power, long lifetime cycling capability that we demonstrate here, we emphasize that modifications of the porous silicon porosity, pore structure, thickness, and passive layer composition are all factors that could lead to improved and controllable performance relevant to a spectrum of long-term integrated applications. As an example, for energy storage directly integrated into photovoltaics, a concept we recently demonstrated as being feasible for porous silicon supercapacitors,[26] most respectable photovoltaic devices exhibit current densities greater than 5 mA/cm^2 and are rated for between 20-30 years of stable operation. Such charging currents kinetically inhibit deep bulk intercalation storage in silicon (**Figure 3.2**), requiring asymmetry in power generation and power storage footprint areas, which makes integration challenging in addition to the large mismatch between storage and generation lifetimes. For a high-power silicon battery device that can operate at the native photogenerated current density of a silicon solar cell exposed to 1 sun of illumination, and charged and discharged once per day, the ability to achieve 10,000 cycles without noticeable capacity loss indicates the capability to be charged and discharged once per day through a period of almost 30 years – which is the maximum rated lifetime of a solar cell.[2] Beyond this unique integration scheme for solar cells, integration of on-chip high power, long-lifetime silicon-based energy storage into other applications such as silicon-based integrated circuits and electronics, MEMS devices, and sensors, provides a unique pathway to provide on-board energy storage in excess silicon material real estate in these devices.

Appendix 3.A

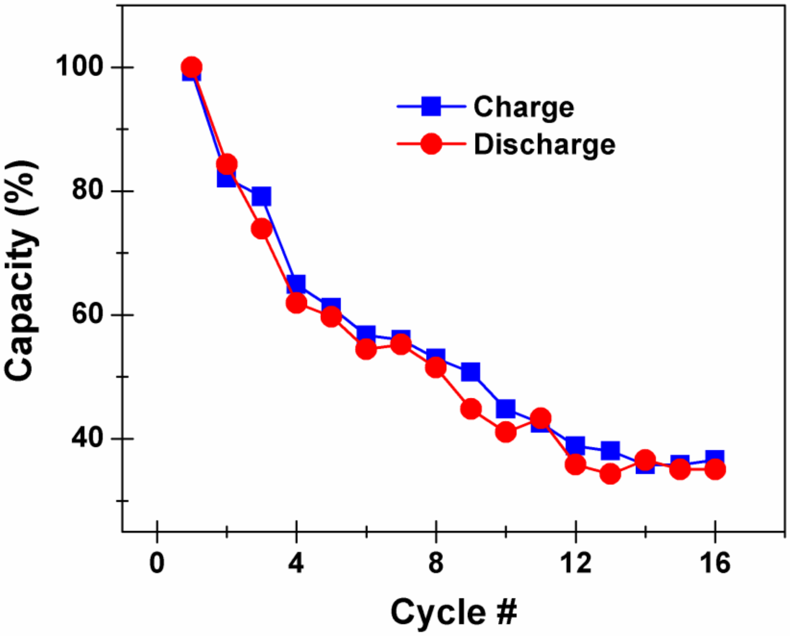

Figure 3.A1 Capacity as a function of cycle number for carbon passivated porous silicon anodes cycled at 1 mA/cm^2, where intercalation deep into the silicon bulk is observed. Notably, the capacity fades rapidly with ~ 60% capacity loss over the first 16 cycles.

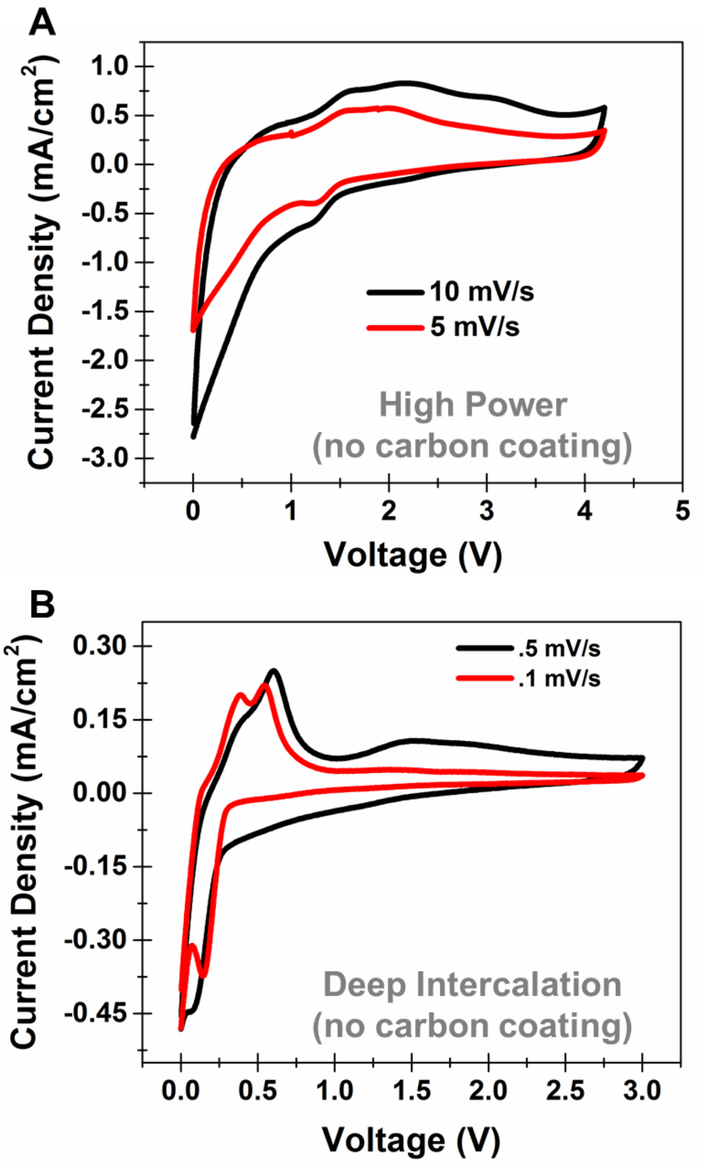

Figure 3.A2 CV curves showing both (a) high power lithium storage and (b) standard deep intercalation storage in porous silicon materials not passivated with carbon. Notably, in (c), we observe a charge-discharge redox pair similar to that observed in carbon passivated porous silicon materials, indicating the charge storage observed in **Figure 3.2** is associated with storage in the silicon material.

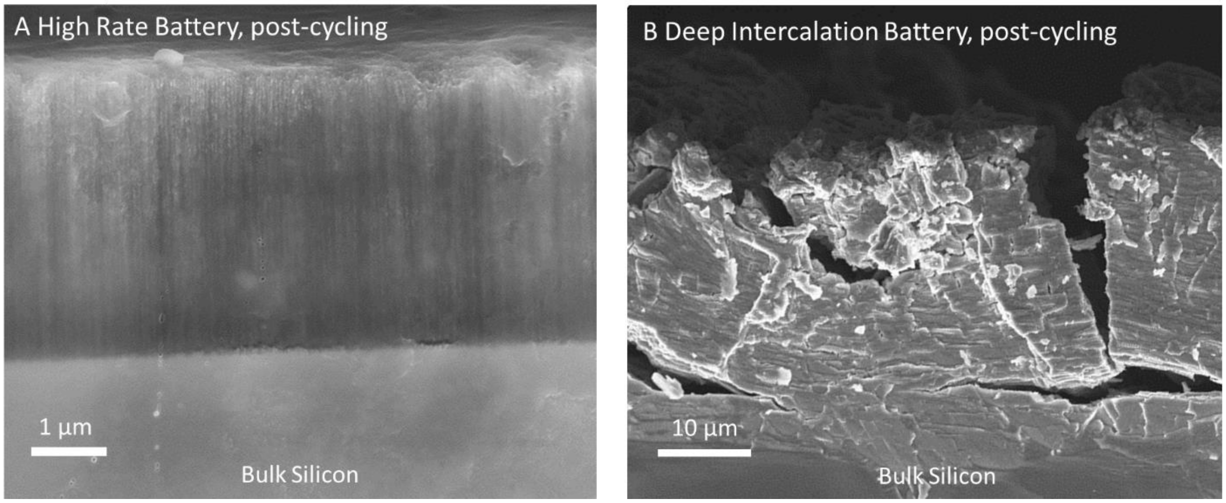

Figure 3.A3 Cross sectional scanning electron microscope (SEM) images of two porous Si batteries after 3000 cycles at high rate (a) and after 20 cycles at slow charging rates (b). Evident from (a) is the in-tact nature of the porous silicon material. In this sample, no damage or degradation was observed in the silicon material underneath the porous layer, and the nanostructured silicon in the porous layer exhibits no significant structural modifications. From (b), lithium evidently intercalates deep into the bulk of the silicon material, causing the bulk silicon to pulverize and the capacity to rapidly fade.

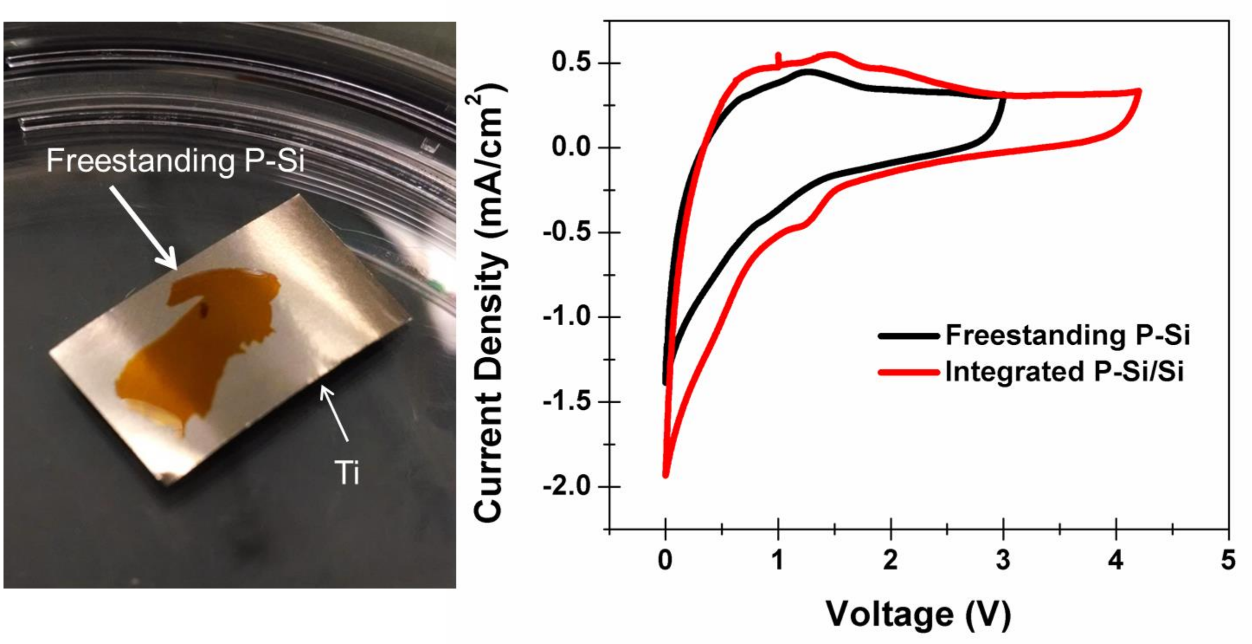

Figure 3.A4 Comparison of lithium storage characteristics of freestanding P-Si layers. (left panel) Photograph of the substrate utilized, where the orange-colored material is a freestanding porous silicon layer produced by an electropolishing step following electrochemical etching as described in the main text. In the electropolishing step, a current density of 200 mA/cm^2 was pulsed for 15 seconds, and the porous layer was partially removed. The sample was then placed in an ethanol solution and agitated until a freestanding layer was isolated, and this was then dried on a Ti foil substrate as a battery electrode, and carbonized using an identical CVD process as that described in the main text. This electrode Li storage performance was then assessed using cyclic voltammetry (right panel) at a rate of 5 mA/cm^2, and normalized to the area of the porous silicon. Notably, due to the shape of the freestanding layer, and some delaminated regions during CVD treatment, we anticipate between 10 - 50% error in the absolute values of the current density. In comparison to the integrated P-Si/Si sample, the general high power behavior is the same – with no apparent bulk-like storage characteristics, and a redox couple at higher voltages. This indicates that the general high rate performance observed for integrated samples is due to the porous layer, clearly emphasized by the isolated freestanding porous layer showing the same Li storage behavior.

Acknowledgements

We thank Adam Cohn for useful discussions, Jeremy Mares for insight on electropolishing, and Sharon Weiss for early use of facilities for porous silicon etching. This work was supported by National Science Foundation (NSF) CMMI grant # 1334269, and A.S.W. was supported by NSF grant EPS 1004083.

References

1. Westover, A. S.; Freudiger, D.; Gani, Z. S.; Share, K.; Oakes, L.; Carter, R. E.; Pint, C. L. *Nanoscale* **2015,** 7, (1), 98-103.
2. Lewis, N. S. *Science* **2007,** 315, (5813), 798-801.
3. Lund, H.; Andersen, A. N.; Ostergaard, P. A.; Mathiesen, B. V.; Connolly, D. *Energy* **2012,** 42, (1), 96-102.
4. Dunn, B.; Kamath, H.; Tarascon, J. M. *Science* **2011,** 334, (6058), 928-935.
5. Gogotsi, Y.; Simon, P. *Science* **2011,** 334, (6058), 917-918.
6. Baggetto, L.; Niessen, R. A. H.; Roozeboom, F.; Notten, P. H. L. *Advanced Functional Materials* **2008,** 18, (7), 1057-1066.
7. Chmiola, J.; Largeot, C.; Taberna, P. L.; Simon, P.; Gogotsi, Y. *Science* **2010,** 328, (5977), 480-483.
8. Pikul, J. H.; Zhang, H. G.; Cho, J.; Braun, P. V.; King, W. P. *Nature Communications* **2013,** 4.
9. Zhang, H. G.; Braun, P. V. *Nano Letters* **2012,** 12, (6), 2778-2783.
10. Szczech, J. R.; Jin, S. *Energ Environ Sci* **2011,** 4, (1), 56-72.
11. Lee, S. J.; Lee, J. K.; Chung, S. H.; Lee, H. Y.; Lee, S. M.; Baik, H. K. *J Power Sources* **2001,** 97-8, 191-193.
12. Bourderau, S.; Brousse, T.; Schleich, D. M. *J Power Sources* **1999,** 81, 233-236.
13. Liu, N.; Wu, H.; McDowell, M. T.; Yao, Y.; Wang, C. M.; Cui, Y. *Nano Letters* **2012,** 12, (6), 3315-3321.

14. Liu, N.; Lu, Z. D.; Zhao, J.; McDowell, M. T.; Lee, H. W.; Zhao, W. T.; Cui, Y. *Nature Nanotechnology* **2014,** 9, (3), 187-192.

15. Thakur, M.; Isaacson, M.; Sinsabaugh, S. L.; Wong, M. S.; Biswal, S. L. *J Power Sources* **2012,** 205, 426-432.

16. Shin, H. C.; Corno, J. A.; Gole, J. L.; Liu, M. L. *J Power Sources* **2005,** 139, (1-2), 314-320.

17. Sun, X. D.; Huang, H.; Chu, K. L.; Zhuang, Y. *Journal of Electronic Materials* **2012,** 41, (9), 2369-2375.

18. Quiroga-Gonzalez, E.; Carstensen, J.; Foll, H. *Electrochimica Acta* **2013,** 101, 93-98.

19. Thakur, M.; Sinsabaugh, S. L.; Isaacson, M. J.; Wong, M. S.; Biswal, S. L. *Scientific Reports* **2012,** 2, 795.

20. Simon, P.; Gogotsi, Y. *Nature Materials* **2008,** 7, (11), 845-854.

21. Chu, A.; Braatz, P. *J Power Sources* **2002,** 112, (1), 236-246.

22. Hadjipaschalis, I.; Poullikkas, A.; Efthimiou, V. *Renew Sust Energ Rev* **2009,** 13, (6-7), 1513-1522.

23. Chatterjee, S.; Carter, R.; Oakes, L.; Erwin, W. R.; Bardhan, R.; Pint, C. L. *Journal of Physical Chemistry C* **2014,** 118, (20), 10893-10902.

24. Oakes, L.; Westover, A.; Mares, J. W.; Chatterjee, S.; Erwin, W. R.; Bardhan, R.; Weiss, S. M.; Pint, C. L. *Scientific Reports* **2013,** 3, 3020.

25. Westover, A. S.; Tian, J. W.; Bernath, S.; Oakes, L.; Edwards, R.; Shabab, F. N.; Chatterjee, S.; Anilkumar, A. V.; Pint, C. L. *Nano Lett.* **2014,** 14, 3197-3202.

26. Westover, A. S.; Share, K.; Carter, R.; Cohn, A. P.; Oakes, L.; Pint, C. L. *Appl. Phys. Lett.* **2014,** 104, 213905.

27. Yao, Y.; McDowell, M. T.; Ryu, I.; Wu, H.; Liu, N. A.; Hu, L. B.; Nix, W. D.; Cui, Y. *Nano Letters* **2011,** 11, (7), 2949-2954.

28. Zhou, X. S.; Yin, Y. X.; Wan, L. J.; Guo, Y. G. *Chem Commun* **2012,** 48, (16), 2198-2200.

29. Jiang, T.; Zhang, S. C.; Qiu, X. P.; Zhu, W. T.; Chen, L. Q. *Electrochem Commun* **2007,** 9, (5), 930-934.

30. Pollak, E.; Salitra, G.; Baranchugov, V.; Aurbach, D. *Journal of Physical Chemistry C* **2007,** 111, (30), 11437-11444.

31. Choi, B. G.; Yang, M.; Hong, W. H.; Choi, J. W.; Huh, Y. S. *Acs Nano* **2012,** 6, (5), 4020-4028.

CHAPTER 4

ROOM TEMPERATURE PASSIVATION OF POROUS SI WITH AG AND POLYANILINE FOR INTEGRATABLE PSEUDOCAPACITOR ELECTRODES

Andrew S. Westover,[a,b] Thomas Metke,[b] Nitin Muralidharan,[a,b] Jeremiah Afolabi,[b] and Cary L. Pint[a,b]

[a] Interdisciplinary Materials Science Program, Vanderbilt University, Nashville, TN 37235

[b] Department of Mechanical Engineering, Vanderbilt University, Nashville, TN 37235

Abstract: We present here our work in developing room temperature processes to coat porous Si with electrochemically active polyaniline (PANI) as faradaic electrochemical electrodes. Best performance was achieved by first immersion coating porous Si in silver nitrate to passivate the porous Si surface with Ag, followed by potentiostatic deposition of PANI at .75V vs. SCE giving exceptional volumetric capacitance up to 110 F/cm^3 with excellent cyclability up to 700 cycles. This work lays the foundation for developing fully integrated devices where faradaic energy storage is directly coupled with solar cells and silicon microelectronics.

4.1 Introduction

The possibility of directly integrating energy storage devices into microelectronics and solar cells is one of the most promising enabling technologies for next generation electronics.[1-5] Initial work in this field has focused on the ability to utilize the excess material necessitated for structural stability in solar cells and microelectronics and multipurpose it as an energy storage medium. One of the most promising candidates for direct integration of energy storage with both microelectronics and solar cells has been the development of surface passivated high surface area porous Si.[6-11] Because silicon is the material of choice both for solar cells and for microelectronics further improvements that bring integrated porous Si energy storage one step closer to implementation is extremely desirable.

In the case of microelectronics, the most promising integrated porous Si electrodes have consisted of the surface passivation of porous Si with carbon via high temperature chemical vapor deposition (CVD)[6, 7, 12] or the surface passivation of the porous Si using atomic layer deposition (ALD) of conductive materials such as TiN.[10, 13, 14] These routes have shown excellent stable double layer non-faradaic energy storage performance on porous Si, but because of the limitations of non-faradaic energy storage the performance has been limited to ~10 F/g or ~20 F/cm^3. More recently Douglass and Muralidharan et al.[15] showed that an ALD coating of V_2O_5, which is redox active with Li ions, enabled faradaic high power pseudocapacitance of up to 20 F/g. Unfortunately due to the difficulty in depositing large amounts of active material, and the limitations with using ALD to penetrate deeply into the Porous Si with deep depths over about 10 microns, this approach has also been limited in the overall charge storage performance.

In the case of direct integration into solar cells, there has recently been a surge in studies showing how direct integration of supercapacitors and in some cases Li ion batteries with dye sensitized solar cells and other organic solar cells has shown much promise.[3, 4, 16-18] However because Si based solar cells are the most prevalent and one of the most efficient solar cells the ability to directly integrate into Si would be the optimal scenario.[19, 20] Our previous research efforts[21] showed that we can indeed directly integrate porous Si supercapacitors onto the back of solar cells. Unfortunately however the use of CVD and ALD coating on porous Si require temperatures greater than 600 °C for CVD and 200 °C for ALD both of which destroy the P-N junction of Si solar cells[22] which limits our integrated solar energy storage devices to the extremely low capacitance of porous Si alone. Furthermore although indirect integration into solar cells does not depend on the voltage profile of the solar cell, in the case of direct integration it is important that the voltage for charge storage be matched to the optimal power regime of the solar cell where the maximum power point is at about 0.45V.[23, 24] This is impossible with non-faradaic energy storage, but in the case of faradaic energy storage where a given reaction occurs over a small range of voltages the system can be designed to indeed match the power profile of the solar cell. Thus the optimal route for the practical implementation of porous Si energy storage both for integration with microelectronics and for integration with solar cells necessitates the development of room temperature passivation coatings on porous Si with redox active materials that have a significantly larger capacitance when compared to simple carbon and TiN passivation and can match the power profile of Si solar cells.

Polyanaline (PANI) has recently emerged as an excellent energy storage material that can be easily coated onto carbon nanomaterials at room temperature to greatly improve the specific capacitance of carbon based supercapacitors.[25-28] Furthermore it has been shown that by varying the deposition methods it is possible to tailor the voltage of the chemical reactions for possible voltage and power matching with solar cells.[25, 29, 30] Although this simple process has been shown in the past on Si materials, it has never been implemented on porous Si materials for energy storage applications. In this light our work highlights the first room temperature deposition of PANI onto porous Si with faradaic charge storage capacitance of 62 F/cm^3. Furthermore we show that limitations in the charge transfer process due to lack of conductivity in the PANI and porous Si can be improved by using the room temperature electroless deposition of Ag onto porous Si prior to the coating of the electrode with PANI to passivate the surface traps in the porous Si with conductive Ag allowing for a decreased overpotential and an improved capacitance of up to 110 F/cm^3.

4.2 Experimental Methods

4.2.1 Fabrication of porous Si

Porous Si was fabricated using an AMMT electrochemical etching system with a current density of 45 mS/cm^2 in a 3:7 v/v HF/ethanol electrolyte to develop a porous Si material with an approximate porosity of 75%.[6, 7, 21] The Si wafers used were p doped with a resistivity of 0.01-0.05 Ω/cm (Ultrasil). For the Ag coated porous Si, the initial electrochemical etching was then followed by immersion of the Porous Si into a 1 M $AgNO_3$ solution for 30 minutes to allow time for the $AgNO_3$ solution to fully penetrate the pores.[31-33] The Ag coated porous Si turned the porous Si yellow-green. Throughout the paper porous Si is labeled as PSi and Ag coated porous Si is denoted as Ag/PSi.

4.2.2 PANI coating

In order to make the electrolyte for PANI deposition we mixed 0.5M analine (Sigma Aldrich) and 0.5 M H_2SO_4 (Sigma Aldrich) in ultrapure water. Deposition was performed using a 3 electrode setup with a gold counter electrode and a saturated calomel reference electrode (SCE). PANI was deposited by first immersing the porous Si electrodes in the electrolyte for 30 minutes to allow the electrolyte to penetrate the pores followed by applying a voltage of 0.75 V vs SCE to the electrodes for an additional 30 min.[25, 28] This process resulted in a visual change of the porous Si surface from dark brown or the yellow-green for the Ag coated porous Si to a dark blue consistent with pernigranaline. It is important to note that the PANI deposition process is extremely sensitive to the presence of an oxide layer on the surface of the porous Si. **Figure 4.A1** shows the deposition profile of PANI coating on porous Si and Ag coated porous Si for freshly etched porous Si and for older porous Si. We observed that when using fresh PSi or Ag/PSi we have excellent deposition curves with high currents in the range of mA. However when old porous Si which has had a chance to oxidize is used, (even when stored in a glove box) we get no deposition of PANI and observe an extremely low current density. We have also observed that after extended exposure to oxygen an additional HF wash can also enable PANI deposition.

4.2.3 Characterization

Raman measurements were performed using a Renishaw inVia MicroRaman system with 535 nm laser excitation. Electrochemical tests were performed using a Metrohm Autolab Multichannel Analyzer with a FRA attachment. Electron impedance spectroscopy was performed using frequencies ranging from 1,000,000 Hz to 0.1 Hz with an amplitude of 10 mV around 0V vs SCE. All measurements were performed in a 3 electrode setup with a gold counter electrode and a saturated calomel reference electrode. The mass of the active material used for normalization was calculated by massing the porous Si electrodes before and after PANI deposition.

4.3 Results and Discussion

Figure 4.1a shows a schematic illustration of the steps used to develop PANI porous Si with the possibility of being integrated into solar cells or silicon microelectronics. This consists of an initial electroless deposition of Ag onto porous Si followed by potentiodynamic deposition of PANI at 0.75V vs. SCE.. In order to confirm that we could indeed conformably coat the porous Si nanostructure with PANI we performed cross sectional SEM imaging on the border of where the porous Si was immersed in the electrolyte solution and the portion of the porous Si that was not immersed. The portion that was immersed in solution shows a clear conformal PANI coating of the porous Si nanostructure without clogging the pores allowing for the full PANI active material to be utilized for energy storage (**Figure 4.1b**). The coating of the PANI was further confirmed using cross sectional Raman of the material showing the Si peak at 513 nm^{-1} the porous Si shoulder at 477 nm^{-1} and a clear PANI signature with a number of Raman modes ranging from 1100-1650 nm^{-1} which correspond to C-C, C-O, and C-N bonds (**Figure 4.1c**).

In order to ascertain the effect of adding the intermediate electroless deposition of Ag onto the porous Si surface we performed additional SEM imaging, Raman microscopy and electron impedance spectroscopy (EIS). A comparison of the Raman of the PANI coated porous Si (hereafter denoted as PSi) and the PANI coated Ag passivated porous Si (hereafter denoted as Ag/PSi) showed that the PANI deposited on the plain PSi and the Ag/PSi was essentially the same (**Figure 4.1d**) except for minor variations in some of the relative peak intensities that can one would expect from deposition to deposition. SEM imaging (**Figure 4.A2**) shows that the Ag immersion coating followed by the PANI deposition also shows a conformal coating of the PANI with a small number of Ag nanoparticles scattered throughout the PANI.

Although Raman and SEM showed the electroless deposition of the Ag had no adverse effects on the deposition of PANI, in order to confirm whether or not the Ag had successfully passivated the surface traps

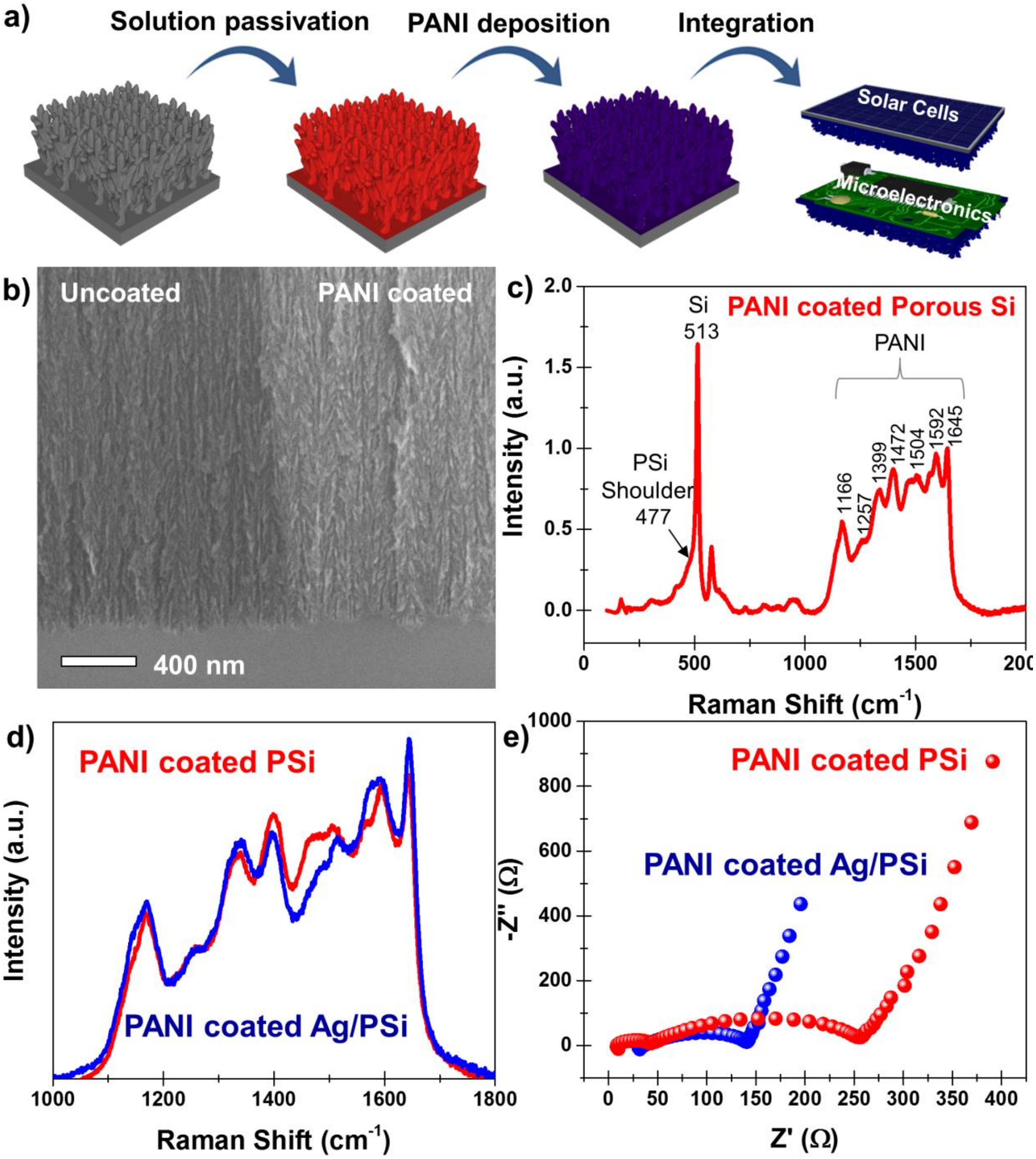

Figure 4.1 (a) Schematic illustrating Ag immersion coating, the PANI deposition onto porous Si and the possibility for integration into solar cells and microelectronics. (b) SEM image of the border region between the coated and uncoated porous Si. (c) Raman spectra of the PANI coated porous Si at a wavelength of 535 nm^{-1}**.** **(**d) Comparison of PANI signature for PANI coated PSi and PANI coated Ag/PSi. (e) EIS of PANI coated PSi and PANI coated Ag/PSi.

on the surface of the porous Si we performed EIS. Fitting of the EIS data showed that we have several different components in our system (**Figure 4.A3**). First the solution resistance, second the charge transfer resistance for charge transfer from the solution to the PANI, third the charge transfer resistance for charge transfer from PANI to the PSi or Ag/PSi and finally the resistance due to leakage current in the system. For the assessment of the effect of the Ag layer, the most relevant terms are the charge transfer resistance from the solution to the PANI and the PANI to the PSi or Ag/PSi denoted as $R_{CT\text{-}PANI}$ and $R_{CT\text{-}PSi}$ respectively. We observe that the $R_{CT\text{-}PANI,}$ for the Ag/PSi was 18Ω compared to 34Ω for the plain PSi, and the $R_{CT\text{-}PSi}$ was 90Ω for the Ag/PSi as opposed to 217Ω for the PSi. For both charge transfer processes the resistance is reduced by approximately half, emphasizing the impact of the Ag layer in reducing the resistance to charge transfer in our system.

After confirming both surface passivation with the Ag coating and the conformal coating of the PANI we performed electrochemical tests to prove the energy storage capability of the electrodes. **Figure 4.2a** shows cyclic voltammetry of uncoated porous Si and PANI coated PSi and PANI coated Ag/PSi in 1 M H_2SO_4 electrolyte. We see that the uncoated porous Si has virtually negligible energy storage in this electrolyte. The PANI coated PSi has a very distinct redox couple centered at 0.6V vs SCE corresponding to the protonation of emeraldine to pernigranaline and an overpotential of ~0.4V. When the PANI is coated on the Ag/PSi however we see a very significant improvement in the electrochemical properties, with a significantly higher current density at any given scan rate and a significantly reduced overpotential down to ~0.1V at a scan rate of 100 mV/s (**Figure 4.2a**). Although some reports show the doping of PANI with Ag to improve the conductivity of PANI and the subsequent performance[29, 30], the nearly identical Raman signature (**Figure 4.1d**) and the universal decrease in the charge transfer resistance suggest that the bulk of the improvement indeed comes from the passivation of the porous Si surface. Furthermore a comparison to the electrochemical performance of the Ag/PSi by itself (**Figure 4.A4**) shows that although there is a redox

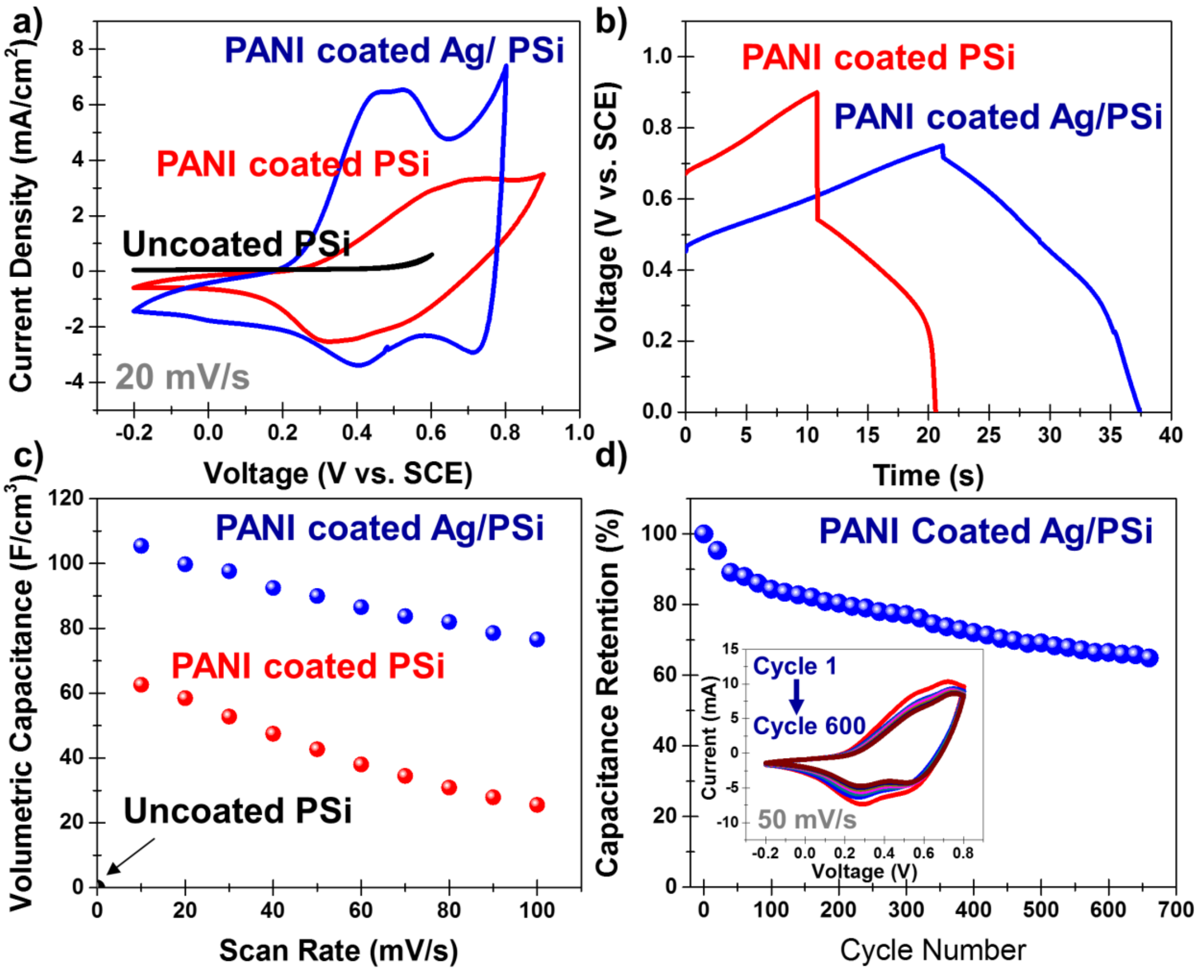

Figure 4.2 (a) Cyclic voltammetry comparison of the plain, PANI coated porous Si, and PANI coated Ag/PSi. (b) Charge discharge measurement of the PANI coated PSi and PANI coated Ag/PSi. (c) Comparison of the volumetric capacitance as a function of scan rate for the PANI coated PSi and PANI coated Ag/PSi. (d) Cycling performance for the PANI coated Ag/PSi, inset is the CV curves used for the cycling analysis.

couple for the Ag passivating layer the capacitance in also negligible in comparison to the PANI redox couple on PANI coated Ag/PSi suggesting that the improved performance is not due to an additional redox couple but due to surface passivation of the porous Si. Charge discharge measurements matched the cyclic voltammetry with the same charging current per unit area giving a significantly improved capacity as evidenced by the greater charge/discharge time (nearly double) for the PANI coated Ag/PSi and with a significantly reduced equivalent series resistance voltage drop consistent with the decreased charge transfer resistance. A comparison across scan rates (**Figure 4.2c** and **Figure 4.A5**) shows that the PANI coated Ag/PSi has nearly double the capacitance of the plain PANI coated PSi for all scan rates with a maximum capacitance of 110 F/cm^3 at 5 mV/s and a high rate capacitance of 80 F/cm^3 at a scan rate of 100 mV/s. Mass estimates obtained by measuring the PSi before and after deposition give a specific capacitance of ~72 F/g for the PANI coated PSi and a volumetric capacitance of 65 mAh/g at slow rates and 25 F/cm^3 at 100 mV/s. Comparing both the volumetric and specific capacitance of the PANI coated Ag/PSi to previous reports we observe that these electrodes have capacitances more than 3-5X that of the best volumetric and specific capacitances from previous studies using ALD of TiN and V_2O_5 on porous Si.[13, 15] Furthermore **Figure 4.2d** shows extended cycling of the PANI coated Ag/PSi showing that it maintains about 70% of its initial performance after least 600 cycles.

Together the exceptional volumetric and specific performance coupled with the stable cycling of these pseudocapacitor electrodes strongly motivates their use for integrated applications such as solar cells and microelectronics. This is even more apparent when considering that The reaction voltage for the PANI coated Ag/PSi is notably centered around 0.45V which means if it were paired with the proper counter electrode this could easily accommodate the voltage range and maximum power regime around 0.45V for silicon photovoltaics, which is a feature lacking in practically every other integrated solar and energy storage device. In addition the nature of both the Ag passivation and the electrodeposition of the PANI at room temperature emphasizes the ability to integrate both with silicon photovoltaics and silicon microelectronics without damaging the p-n junction or the circuitry of the microelectronics.

4.4 Conclusion

In summary we have demonstrated the ability to coat porous Si with redox active PANI at room temperature to enable it as a high performance pseudocapacitor. We further show that using electroless deposition of Ag onto the porous Si prior to PANI deposition allows us to passivate the porous Si surface traps decreasing the charge transfer resistance at the interface and enabling decreased overpotential and leading to a 2X improvement in the capacitance over plain PANI coated PSi. These findings and the room temperature nature of the processes motivate the possibility of direct integration of high energy density pseudocapacitors into microelectronics and the possible integration of PANI coated porous Si into solar cells with the ability to match the maximum power and operating voltage of the solar cell around 0.45V.

Appendix 4.A

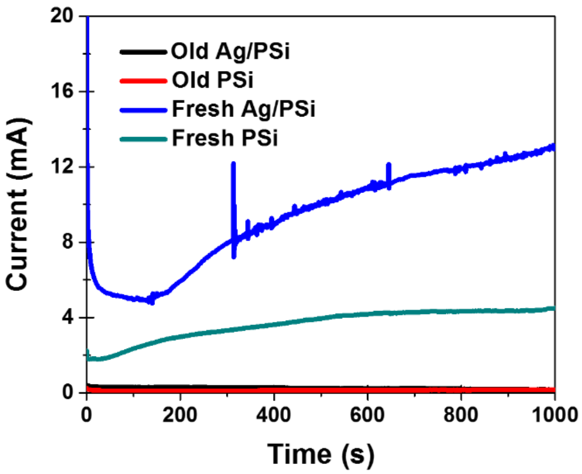

Figure 4.A1 Current vs. time deposition curves for PANI on fresh Ag/PSi, fresh PSi, old Ag/PSi and old PSi.

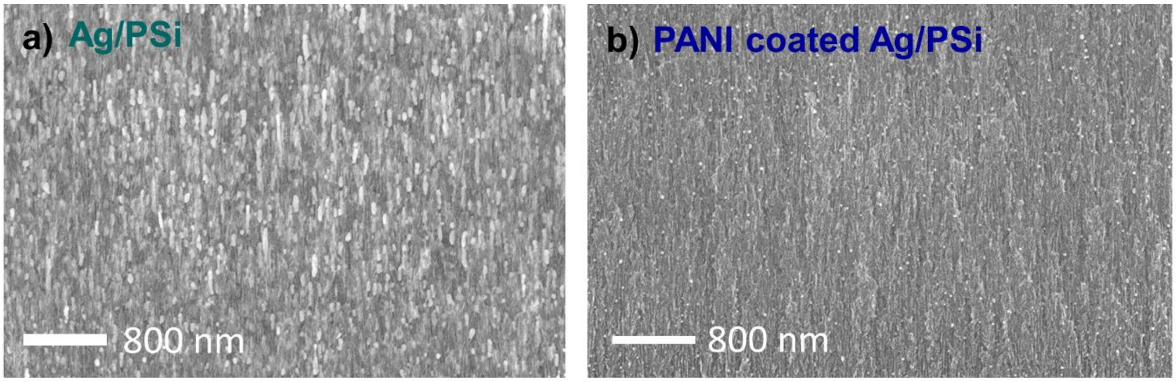

Figure 4.A2 (a) SEM image of the Ag coated porous Si. (b) SEM image of the PANI coated Ag/PSi.

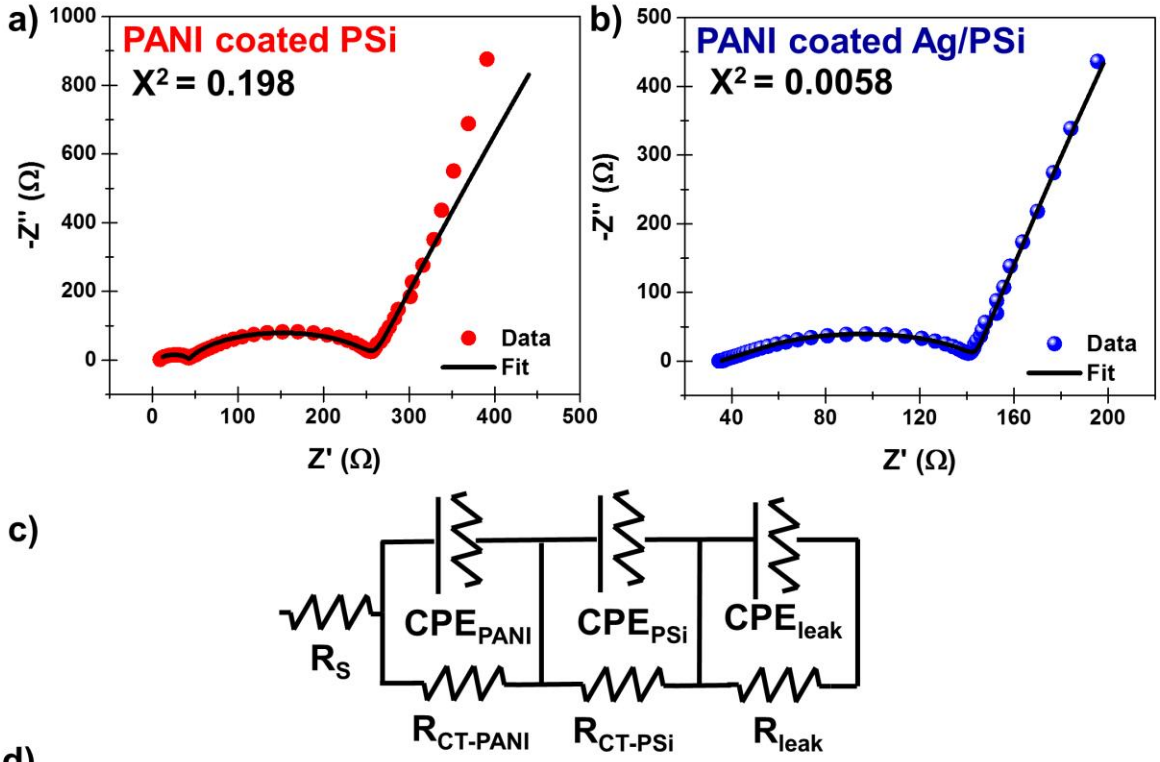

d)

	R_S	PANI		Porous Si		Leakage	
	R_S	$R_{CT-PANI}$	CPE_{PANI}	R_{CT-PSi}	CPE_{PSi}	R_{leak}	CPE_{leak}
PANI PSi	**8.10 Ω**	**34.0 Ω**	**77.4 n℧** **n = 0.936**	**217 Ω**	**66.6 µ℧** **n = 0.8**	**66.0 kΩ**	**13.1 m℧** **n = .871**
PANI Ag/PSi	**35.4 Ω**	**18 Ω**	**612 µ℧** **n = 0.606**	**90 Ω**	**173 µ℧** **n = 0.877**	**46.1 kΩ**	**29.7 m℧** **n = 0.926**

Figure 4.A3 (a) Comparison of EIS data and fit for PANI coated PSi. (b) Comparison of EIS data and fit for PANI coated Ag/PSi. (c) Equivalent circuit used for fitting for PANI coated PSi and Ag/PSi. (d) Table showing the different fitting parameters for the PANI coated PSi and Ag/PSi.

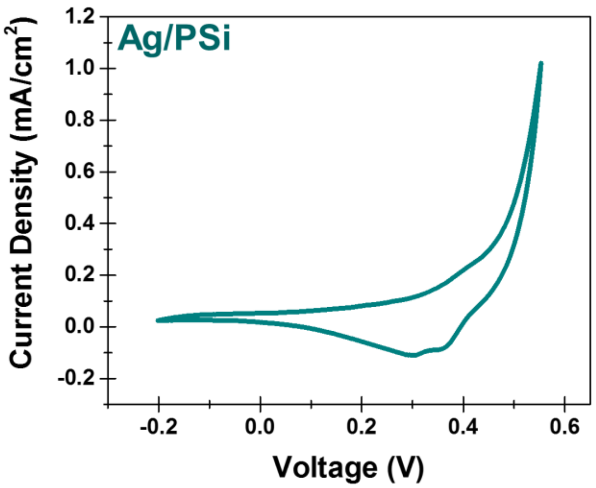

Figure 4.A4 Cyclic voltammetry of the Ag coated porous Si at 100 mV/s.

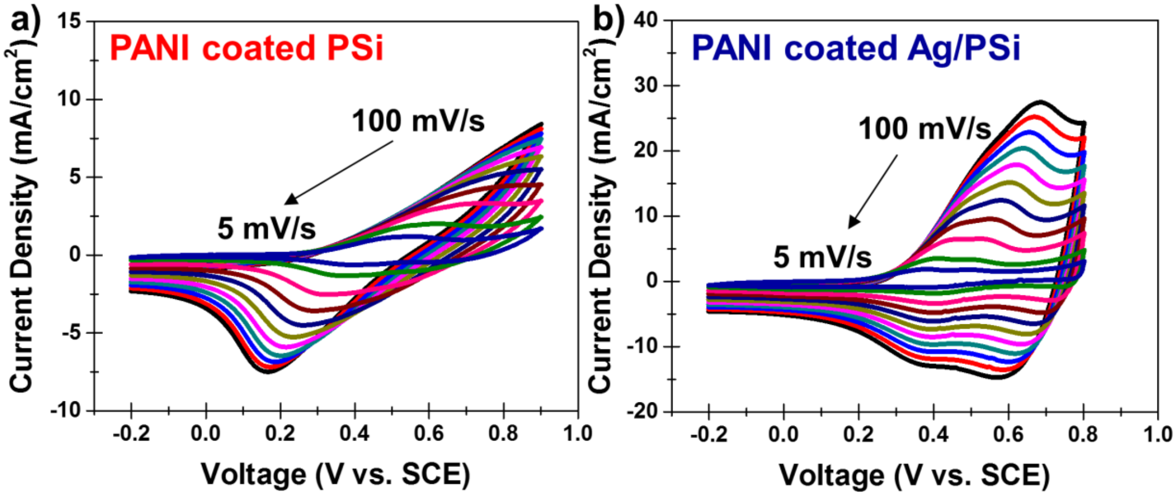

Figure 4.A5 (a) Cyclic voltammetry at scan rates ranging from 5-100 mV/s for PANI coated PSi. (b) Cyclic voltammetry at scan rates ranging from 5-100 mV/s for PANI coated Ag/PSi.

Acknowledgements

Funding for this project and for A.S.W. was provided by NSF grant CMMI 1334269. The authors would also like to thank Rizia Bardhan for the use of Raman microscropy and the Vanderbilt Institute for Nanoscale Science and Engineering (VINSE) for use of SEM.

References

1. El-Kady, M. F.; Kaner, R. B. *Nat. Commun.* **2013,** 4, 1475.

2. Beidaghi, M.; Gogotsi, Y. *Energy Environ. Sci.* **2014,** 7, (3), 867-884.

3. Cohn, A. P.; Erwin, W. R.; Share, K.; Oakes, L.; Westover, A. S.; Carter, R. E.; Bardhan, R.; Pint, C. L. *Nano Lett.* **2015,** 15, (4), 2727-2731.

4. Guo, W.; Xue, X.; Wang, S.; Lin, C.; Wang, Z. L. *Nano Lett.* **2012,** 12, (5), 2520-2523.

5. Thekkekara, L. V.; Jia, B.; Zhang, Y.; Qiu, L.; Li, D.; Gu, M. *Appl. Phys. Lett.* **2015,** 107, (3), 031105.

6. Oakes, L.; Westover, A.; Mares, J. W.; Chatterjee, S.; Erwin, W. R.; Bardhan, R.; Weiss, S. M.; Pint, C. L. *Sci. Rep.* **2013,** 3, 3020.

7. Chatterjee, S.; Carter, R.; Oakes, L.; Erwin, W. R.; Bardhan, R.; Pint, C. L. *J. Phys. Chem. C* **2014,** 118, (20), 10893-10902.

8. Share, K.; Westover, A.; Li, M.; Pint, C. L. *Chemical Engineering Science* **2016,** 154, 3-19.

9. Li, M.; Westover, A. S.; Carter, R. E.; Oakes, L.; Muralidharan, N.; Boire, T. C.; Sung, H.-J.; Pint, C. L. *ACS Applied Materials & Interfaces* **2016,** 8, 19558–19566.

10. Lu, P.; Ohlckers, P.; Müller, L.; Leopold, S.; Hoffmann, M.; Grigoras, K.; Ahopelto, J.; Prunnila, M.; Chen, X. *Electrochem Commun* **2016,** 70, 51-55.

11. Devarapalli, R. R.; Szunerits, S.; Coffinier, Y.; Shelke, M. V.; Boukherroub, R. *ACS applied materials & interfaces* **2016,** 8, (7), 4298-4302.

12. Salonen, J.; Kaasalainen, M.; Rauhala, O.-P.; Lassila, L.; Hakamies, M.; Jalkanen, T.; Hahn, R.; Schmuki, P.; Mäkilä, E. *ECS Transactions* **2015,** 69, (2), 167-176.

13. Grigoras, K.; Keskinen, J.; Grönberg, L.; Yli-Rantala, E.; Laakso, S.; Välimäki, H.; Kauranen, P.; Ahopelto, J.; Prunnila, M. *Nano Energy* **2016,** 26, 340-345.

14. Gardner, D. S.; Holzwarth, C. W.; Liu, Y.; Clendenning, S. B.; Jin, W.; Moon, B.-K.; Pint, C.; Chen, Z.; Hannah, E. C.; Chen, C. *Nano Energy* **2016,** 25, 68-79.

15. Douglas, A.; Muralidharan, N.; Carter, R.; Share, K.; Pint, C. L. *Nanoscale* **2016,** 8, (14), 7384-7390.

16. Xu, J.; Ku, Z.; Zhang, Y.; Chao, D.; Fan, H. J. *Adv. Mater. Technol.* **2016**, 1600074.

17. Ng, C.; Lim, H.; Hayase, S.; Harrison, I.; Pandikumar, A.; Huang, N. *J. Power Sources* **2015,** 296, 169-185.

18. Schmidt, D.; Hager, M. D.; Schubert, U. S. *Adv. Energy Mater.* **2016,** 6, (1), 1500369.

19. Jayawardena, K. I.; Rozanski, L. J.; Mills, C. A.; Silva, S. R. P. *Nat. Photonics* **2015,** 9, (4), 207-208.

20. Hosenuzzaman, M.; Rahim, N.; Selvaraj, J.; Hasanuzzaman, M.; Malek, A.; Nahar, A. *Renewable Sustainable Energy Rev.* **2015,** 41, 284-297.

21. Westover, A. S.; Share, K.; Carter, R.; Cohn, A. P.; Oakes, L.; Pint, C. L. *Appl. Phys. Lett.* **2014,** 104, (21), 213905.

22. Wysocki, J. J.; Rappaport, P. *J. Appl. Phys.* **1960,** 31, (3), 571-578.

23. Chung, H. S.-H.; Tse, K.; Hui, S. R.; Mok, C.; Ho, M. *IEEE Trans. Power Electron.* **2003,** 18, (3), 717-724.

24. Shockley, W.; Queisser, H. J. *J. Appl. Phys.* **1961,** 32, (3), 510-519.

25. Tran, C.; Singhal, R.; Lawrence, D.; Kalra, V. *J. Power Sources* **2015,** 293, 373-379.

26. Wu, Q.; Xu, Y.; Yao, Z.; Liu, A.; Shi, G. *ACS Nano* **2010,** 4, (4), 1963-1970.

27. Cheng, Q.; Tang, J.; Ma, J.; Zhang, H.; Shinya, N.; Qin, L.-C. *J. Phys. Chem. C* **2011,** 115, (47), 23584-23590.

28. Wang, D.-W.; Li, F.; Zhao, J.; Ren, W.; Chen, Z.-G.; Tan, J.; Wu, Z.-S.; Gentle, I.; Lu, G. Q.; Cheng, H.-M. *ACS Nano* **2009,** 3, (7), 1745-1752.

29. Sawangphruk, M.; Suksomboon, M.; Kongsupornsak, K.; Khuntilo, J.; Srimuk, P.; Sanguansak, Y.; Klunbud, P.; Suktha, P.; Chiochan, P. *J. Mater. Chem. A* **2013,** 1, (34), 9630-9636.

30. Patil, D. S.; Shaikh, J.; Pawar, S.; Devan, R.; Ma, Y.; Moholkar, A.; Kim, J.; Kalubarme, R.; Park, C.; Patil, P. *Phys. Chem. Chem. Phys.* **2012,** 14, (34), 11886-11895.

31. Tsuboi, T.; Sakka, T.; Ogata, Y. H. *J. Appl. Phys.* **1998,** 83, (8), 4501-4506.

32. Harraz, F.; Tsuboi, T.; Sasano, J.; Sakka, T.; Ogata, Y. *J. Electrochem. Soc.* **2002,** 149, (9), C456-C463.

33. Chan, S.; Kwon, S.; Koo, T. W.; Lee, L. P.; Berlin, A. A. *Adv. Mater.* **2003,** 15, (19), 1595-1598.

CHAPTER 5

PARTICULATE-FREE POROUS SILICON NETWORKS FOR EFFICIENT CAPACITIVE DEIONIZATION WATER DESALINATION[1]

Andrew S. Westover,[1,2,^] Thomas Metke[1,^], Rachel Carter[1], Landon Oakes[1,2], Anna Douglas[1,2], and Cary L. Pint[1,2,]*

[1]Department of Mechanical Engineering, Vanderbilt University, Nashville, TN 37235, USA

[2]Interdisciplinary Materials Science Program, Vanderbilt University, Nashville, TN 37235, USA

^equally contributing first authors

Abstract: Energy efficient water desalination processes employing low-cost and earth-abundant materials is a critical step to sustainably manage future human needs for clean water resources. Here we demonstrate that porous silicon – a material harnessing earth abundance, cost, and environmental/biological compatibility is a candidate material for water desalination. With appropriate surface passivation of the porous silicon material to prevent surface corrosion in aqueous environments, we show that porous silicon templates can enable salt removal in capacitive deionization (CDI) ranging from 0.36% by mass at the onset from fresh to brackish water (10 mM, or 0.06% salinity) to 0.52% in ocean water salt concentrations (500 mM, or ~ 0.3% salinity). This is on par with reports of most carbon nanomaterial based CDI systems based on particulate electrodes and covers the full salinity range required of a CDI system with a total ocean-to-fresh water required energy input of ~ 1.45 Wh/L. The use of porous silicon for CDI enables new routes to directly couple water desalination technology with microfluidic systems and photovoltaics that natively use silicon materials, while mitigating adverse effects of water contamination occurring from nanoparticulate-based CDI electrodes.

This work was originally published in **Scientific Reports 6, 24680, Apr. 2016** and is reproduced with permission. © *Scientific Reports (2016)* DOI: 10.1038/srep24680

5.1 Introduction

Water desalination is a key challenge facing human sustainability in coming decades.[5] Ninety-eight percent of all the water on earth is salt water, leaving only two percent of water usable for society.[6] Increasing population density and rapid consumption of fresh water resources will cause major water shortages in coming years from overuse and contamination.[5] Desalination methods can transform salt water reserves to usable freshwater sources, but require significant amounts of energy input to be successful.[7,8,9,10] Despite advances in desalination technology, the cost and scale of currently available routes for water desalination remain too expensive for use in developing countries, where water shortage is already a current problem.[11] Therefore, new techniques that can lead to low-cost materials and energy efficient processes for water desalination are of critical importance to a sustainable future.

Currently, the most commonly used methods of desalination include multi-stage flash distillation and reverse osmosis.[8, 9, 10] Flash distillation is the most energy expensive, requiring ~ 25 Wh/L of energy that is lost upon condensation.[12, 13] Reverse osmosis is more energy efficient than flash distillation (5 Wh/L), but utilizes membranes most often made from cellulose or polyamides, and used to remove salt or contaminants under a very large applied pressure.[12-15] As a result, this requires costly centralized infrastructure that is not straight-forward to scale-down. Capacitance Deionization (CDI) has the potential to be more efficient than either of these techniques with a total energy consumption of as little as 1.1 Wh/L,[13, 16] and promise for system development at small scales relevant to families or individuals. Capacitance deionization operates on the principle of a low-voltage (< 2 V) electric bias applied across electrodes immersed in salt water to assemble the dissolved salt on the electrode surface.[17] The formation of this salt layer in the form of an electrochemical double layer on materials with ultra-high surface areas, such as many forms of carbons, can lead to the complete extraction of salt ions from water. Furthermore, when the electrodes are discharged to expel the ions back into another medium, a significant portion of the energy that is utilized for desalination can be recycled in the process, greatly improving the efficiency of capacitive deionization.[18] Recent efforts have most notably demonstrated materials such as metal organic porous Carbon frameworks and three dimensional graphene architectures with measured capacitive desalination that gives promise to practical CDI technology.[2, 19-21] At the current time however there are still several key challenges for CDI technologies including achieving high efficiency for water desalination, maintaining electrodes compatible with large-scale manufacturing, and controlling the electrode structure to inhibit fouling or deactivation.[22] High performance materials for these applications, such as single-walled carbon nanotubes or 3D graphene foams,[2] result in the best performance but rely on small-scale processing that remains expensive and research-centered, generate particulates that can contaminate the water source, and provide highly porous networks prone to fouling.[23,24] Activated carbon is the most cost-viable option for CDI electrodes, but bring many of the same challenges as other carbons for practical use and require expensive processing to cast particulates into robust templates resistant to salt water flow environments.

Here we demonstrate that porous silicon – a material exhibiting earth abundance,[25] low cost,[26] environmental/biological compatibility[27, 28] and readily adaptable into the already well developed Si manufacturing infrastructure,[26] as a candidate material for water desalination. Unlike the assembly of carbon-based particulates, porous silicon templates can be etched into bulk silicon using processes central to semiconductor manufacturing and dating back over 6 decades of material development and building on raw materials with cost as little as $2/kg.[26, 29] Additionally the widespread use of Si has led to very well developed silicon processing infrastructure[26] which is in contrast to carbon based devices where the necessary infrastructure for large scale processing has yet to be developed, even though carbon is an earth abundant and attractive material. The porosity, thickness, and feature size (surface area) can be varied over orders of magnitude,[30-32] enabling a level of control that can mitigate fouling, optimize durability under flow, and efficiently enable salt removal without the release of free particulates into the flow. As this material has promise to overcome many of the key problems facing current CDI technology, our results indicate salt removal performance up to 0.52% by mass with performance maintained across the whole range of brackish water conditions, which is comparable or better than other state-of-the-art carbon particulate-based electrodes. This not only gives promise to this material for CDI applications, but opens new routes for integration into systems such as microfluidics[33] or solar cells,[34] that are synergistic with desalination technology and rooted in silicon processing architectures.

5.2 Experimental Methods

5.2.1 Porous Silicon Fabrication

Porous silicon etching was performed in a commercial AMMT electrochemical system using full 4” boron-doped silicon wafers. The etch process was carried out using a 3:8 v/v HF (50% H_2O by volume) and ethanol etch solution, and durations of 540 s, 1080 s, and 1800 s to produce different depths. Based on previous analysis, this technique yields a porous silicon material with ~ 75% porosity.[35, 36] To modify the porosity to 35%, the etch current was modified to 10 mA/cm^2. Following the P-Si etch process, the samples were washed in ethanol and stored in an Ar glove box until gas phase carbonization.

5.2.2 Porous Silicon Surface Passivation

Carbon coatings were applied to the porous silicon materials in order to both prevent oxidation of the silicon in aqueous environments and reverse the effect of trap states at the surface. Porous silicon materials were loaded into a 1” Lindberg-Blue tube furnace and placed in the center the tube furnace. The sample was then flushed with Ar (1 slm) and H_2 (200 sccm) during heating up to 650^{o}C. At a temperature of 650^{o}C, 10 sccm of C_2H_2 were included in the gas mixture, and the temperature was sequentially ramped to 750^{o}C and 850^{o}C over durations of 10 minutes in both cases. This route has been observed to produce conformal coatings of carbon that retain the structure of the porous silicon and yield significant corrosion resistance of the silicon in even the most aggressive electrochemical environments.[35, 37] Material analysis of this surface passivated porous silicon was performed using scanning electron microscopy (Zeiss, Merlin) and transmission electron microscopy (FEI Osiris). Carbon mass was determined by weighing the porous Si before and after carbonization using a semi-microbalance.

5.2.3 Capacitive Deionization Testing

Capacitive deionization testing was performed using two separate routes. The first route involves testing of electrodes in a two-electrode configuration using an MTI split flat cell. The second route involves the development of a cell involving four pairs of CDI electrodes in a square configuration that was continuously stirred or circulated for the duration of experiments (**Figures 5.1c, 5.1d**). In the latter case, the total salt removal from the water was characterized based on a conductivity meter (Thermo Scientific, Orion Star A212) that was inserted into the cell following potentiostatic salt removal. For cyclic voltammetry tests, which were primarily tested in a two-electrode configuration, a voltage range of 0 – 1 V was utilized to inhibit hydrolysis of water. For potentiostatic tests, which were primarily carried out in the CDI cell, the current was monitored as a 1 V potential is applied to the cell (salt removal). In all cases, electrochemical tests were performed using a Metrohm autolab multichannel workstation. The energy analysis was performed based on galvanostatic charge discharge curves used for the cycling analysis in **Figure 5.3c**, where the total charge absorbed was measured with the current and time and then translated into grams of NaCl, and the energy was calculated by integrating the charge and discharge curves respectively and multiplying by the charging current according to the following equation. $E = \int IVdt$. The effect of fouling was determined by galvanostatically cycling the electrodes in an NaCl solution (1000 ppm) and similarly NaCl solution (1000 ppm) with the addition of 3 ppm of humic acid salts (Sigma Aldrich) similar to the procedure used by M. Mossad et al.[38] The fouling resistance used for the inset in **Figure 5.3c.** was calculated by comparing the performance of the Porous Si electrodes of 35 and 75% porosities after a steady state absorption capacity was reached with the performance after the full 24 hours of testing.

5.3 Results

Porous silicon was produced by electrochemically etching full 4” Si wafers in an AMMT commercial etching system to create a porous silicon material with ~75% porosity and depth that varies with etch time. Whereas porous silicon is natively poorly suited for operation in aqueous environments, surface passivation of the porous silicon material with carbon[35, 36, 39, 40] was used to effectively transform the highly porous material into an electrochemically stable template for water desalination. The ability to fine tune the porous Si structure allows for optimization of the desalination performance and antifouling capability, and the carbon coating presents an electrode interface capturing the properties of carbon that lead to highly efficient salt electrosorption. Electron microscopy analysis shows representative images confirming both the porous network that is integrated onto the silicon wafer (**Figure 5.1a**) as well as a

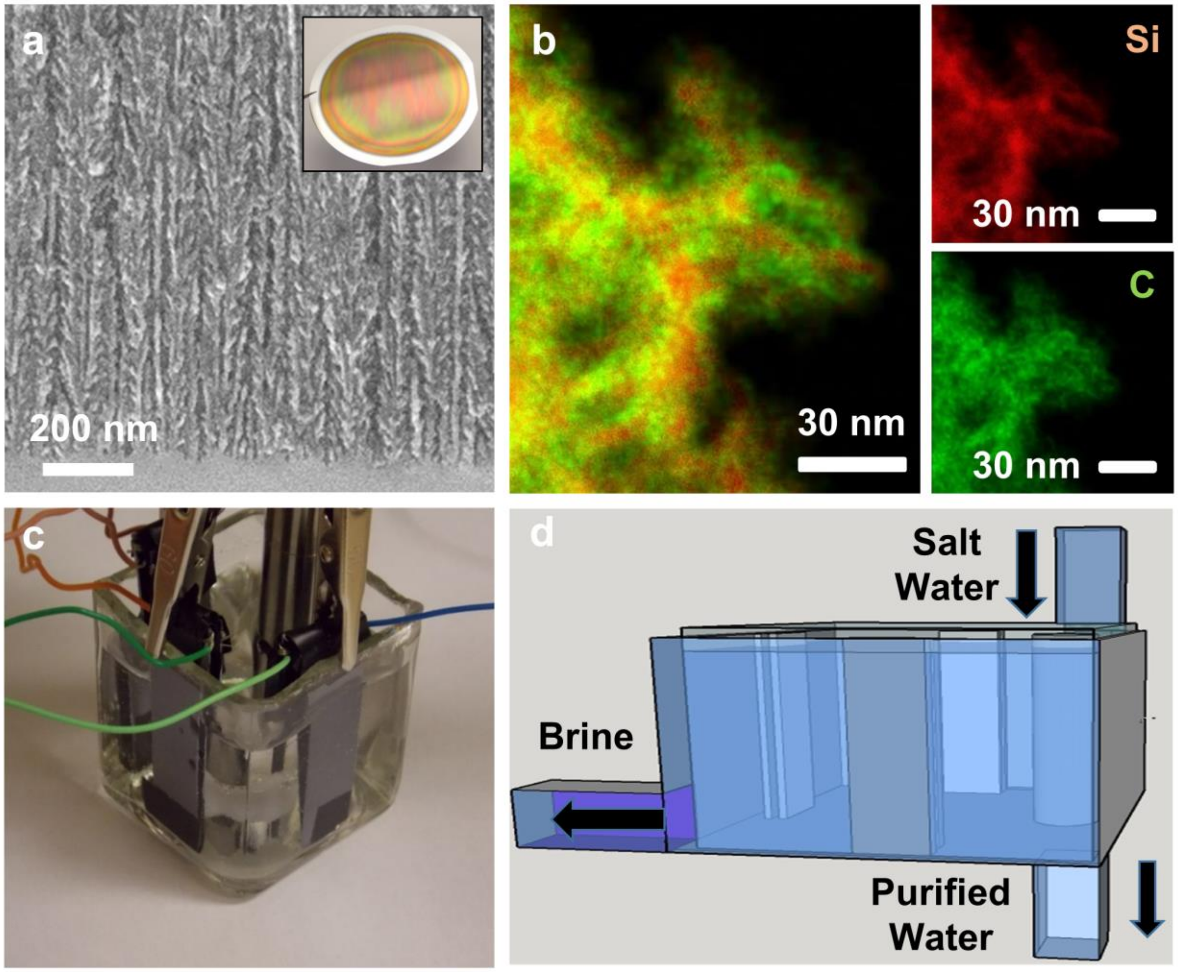

Figure 5.1 (a) Cross-sectional SEM image of a carbon passivated porous silicon electrode for water desalination. (b) Analytical elemental TEM analysis a carbon passivated porous silicon material showing uniform carbon passivation on the material. (c) Photograph of the CDI testing cell combining 4 pairs of silicon-based electrodes, and (d) illustration of a CDI module in the context of the testing apparatus for continuous flow-through CDI water desalination using porous silicon.

nanostructured material that is conformally passivated with carbon **(Figure 5.1b)**. Unlike other routes to produce CDI electrodes, this material has a pore architecture controlled by the silicon electrochemical etching process, a structure that is tethered to a solid surface to inhibit particulate removal, and a stable interface for salt removal that is mediated by the carbon passivation layer. This gives a level of controllability in electrode design that can be modulated based on the electrochemical etching process, leading to routes to produce integrated materials that can overcome challenges of fouling and flow-resistance critical for CDI electrode systems.

In order to generate measureable changes in the salinity of aqueous solutions, a test cell was designed that involves four parallel sets of electrode pairs assigned to each face of a square container filled with salt water with a circulator in the center to maintain an equilibrium salinity of the water during experiments. (**Figure 5.1c)** This design is envisioned to be a modular component of an engineered CDI desalination cell that can sequentially purify salt water until a tolerable fresh water concentration is achieved. (**Figure 5.1d**) In the flow cell employed for this study, the electrodes were separated by ~1.1 cm to allow ample water flow between the electrodes and a conductivity meter was utilized to assess the change in salinity of the aqueous solution in the cell. Although a full process scale design for continuous desalination is beyond the present study, it is anticipated this could be carried out using two routes at two different scales. First, a modular CDI cell composed of a series of cells similar to that illustrated in **Figure 5.1d** would involve a sequence where salt water and brine were sequentially cycled through the modular series of cells to lead to fresh water and concentrated brine. An alternative to this that would be effective at small scales is the incorporation of porous silicon into microfluidic flow channels whose channel dimensions and flow rate would be optimized for salt electrosorption, and salt water and brine could similarly be repetitively cycled. Notably the efficient recovery of the brine in both cases can lead to the recovery of the majority of the initial energy input into the system.

To first assess the ability of this material for salt removal, cyclic voltammetry (CV) measurements were performed in 500 mM NaCl. (**Figure 5.2a**) CV measurements confirm the stable electrochemical interface between salt water and the porous silicon material in the voltage range relevant for CDI experiments, between 0 V and 1 V. The total width of the box in the CV curve in **Figure 5.2a** corresponds to the total charge associated with both salt absorption and salt desorption from the porous silicon electrode, appropriately labeled. In the CV curves it is apparent that the majority of the ions stored can be released from the electrodes effectively rejuvenating them to allow for continuous cycles and recovery of a significant portion of the energy input. To further characterize this system, and to understand the ability to both remove ions and then rejuvenate the electrodes we performed potentiostatic testing to porous silicon CDI electrodes immersed in salt water with varying NaCl concentration ranging from high concentrations relevant to salt concentrations in ocean water (500 mM) to lower concentrations representing moderately brackish water (10 mM). (**Figures 5.2b, 5.2c**) Salt removal is associated with a large spike in current that is due to the rapid assembly of salt ions onto the porous silicon surface, with a current tail that exponentially decays over time. This potentiostatic testing indicates that this passivated porous silicon material can yield salt removal at high salt concentrations of up to 5.2 mg NaCl per gram of porous silicon material (5.2 mg/g),

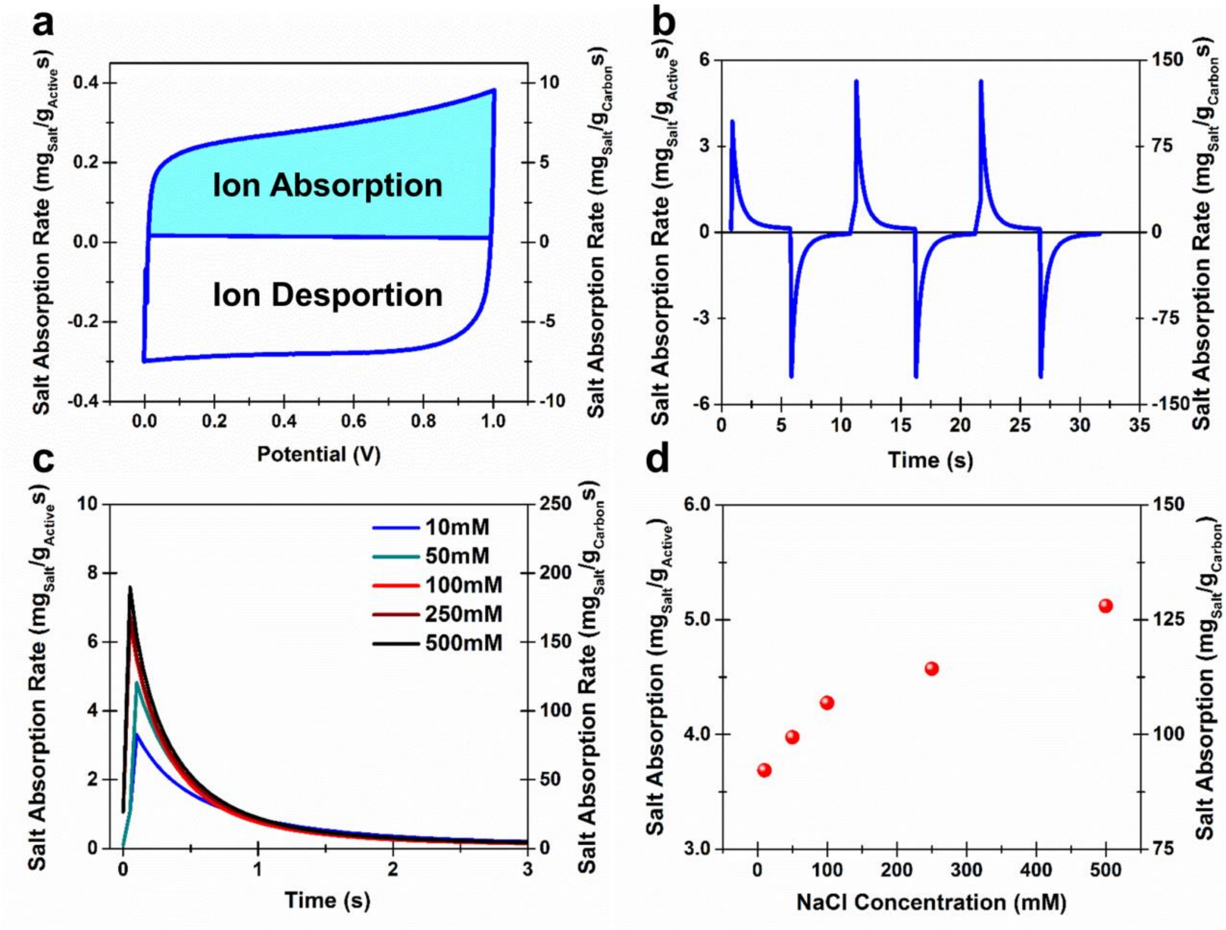

Figure 5.2 (a) Cyclic voltammetry analysis at 100 mV/s scan rate in 500 mM NaCl salt water solution, with labeled salt absorption and desorption segments. (b) Current profile for 3 cycles of potentiostatic desalination cycling in 500 mM NaCl solutions with porous silicon CDI electrodes, (c) Potentiostatic salt removal profiles for NaCl solutions ranging from 10 mM (near-fresh) to 500 mM (near-ocean water concentration) NaCl. (d) Specific salt removal capacity as a function of water concentration based on results in part (c).

and can still maintain salt removal of 3.8 mg/g at low salt concentrations that border the transition from brackish to fresh water. (**Figure 5.2d)**. Importantly, these results are normalized to the combined mass of the porous silicon and the carbon interface, which forms the skeleton and passivating interface for this electrode system, respectively. Isolating only the performance of the active carbon material interface, our results indicate that ion removal capacity could be as high as ~125 mg/g_{carbon} if the optimal performance could be implemented in a flow electrode setup. Whereas such an ultrathin porous carbon material would likely not have the native mechanical integrity to be a practical self-supporting CDI flow electrode, the combined function of the carbon and porous silicon give promise to a tunable architecture to mitigate fouling, high electrosorption properties, and a material that can be seamlessly integrated with silicon-based applications.

In order to assess how these electrodes compare to RO and Flash distillation we used the electrosorption results to calculate the net energy required by the system to desalinate ocean and brackish water. Coulombic efficiency of ~95-98% and an energy efficiency of ~85% was measured in our system. Based on these values, the net amount of energy it would take to desalinate salt water from either ocean water concentrations (35000 ppm) or brackish water concentrations (30000-5000 ppm) to fresh drinkable water (<500ppm) was calculated. Our results indicate that it would take ~1.45 Wh/L to purify ocean water to fresh water and 0.25-1.25 Wh/L to purify brackish water to fresh water emphasizing the ability of these electrodes to provide a significant energy advantage over RO (>5 Wh/L) and Flash Distillation (~30 Wh/L).[12]

One unique feature of porous silicon materials is the ability to control the porous silicon thickness, the porosity and pore size based on the total duration of electrochemical etching and the etching current density. In order to show the advantages that come from this ability to fine-tune the porous Si depth and structure we first performed CDI experiments on porous Si electrodes of differing pore depths and showed the effect of pore depth on the overall salt removal capability of porous silicon CDI electrodes. The specific salt removal measured as a function of the footprint area of porous silicon material (**Figure 5.3a**) exhibits a linear correlation with porous silicon depth, with depths ranging up to ~ 50 µm in thickness. The use of deeper pores allows for the removal of more salt for a single, planar electrode. This emphasizes the possibility to easily develop significant amounts of active material integrated into a single electrode and enabling more CDI active material produced in any one given etch process, yielding a versatile approach to developing functional electrodes for CDI operation. Furthermore, the thickest porous silicon layer used as a CDI electrode (~ 50 µm) was subjected to subsequent salt extraction cycles to demonstrate its longevity for stable CDI performance (**Figure 5.3b**). The slight increasing baseline in **Figure 5.3b** is associated with water evaporation in a module open to ambient conditions. Notably, whereas these results were obtained using low-concentration salt water due to the ease of resolving the total salt removal, this trend is consistent across the whole range of brackish water concentrations relevant for a CDI system.

One additional advantage that comes from the ability to fine tune the porosity of the porous Si is the potential to design a pore structure that can mitigate the effect of fouling. **Figure 5.3c** and inset shows the fouling

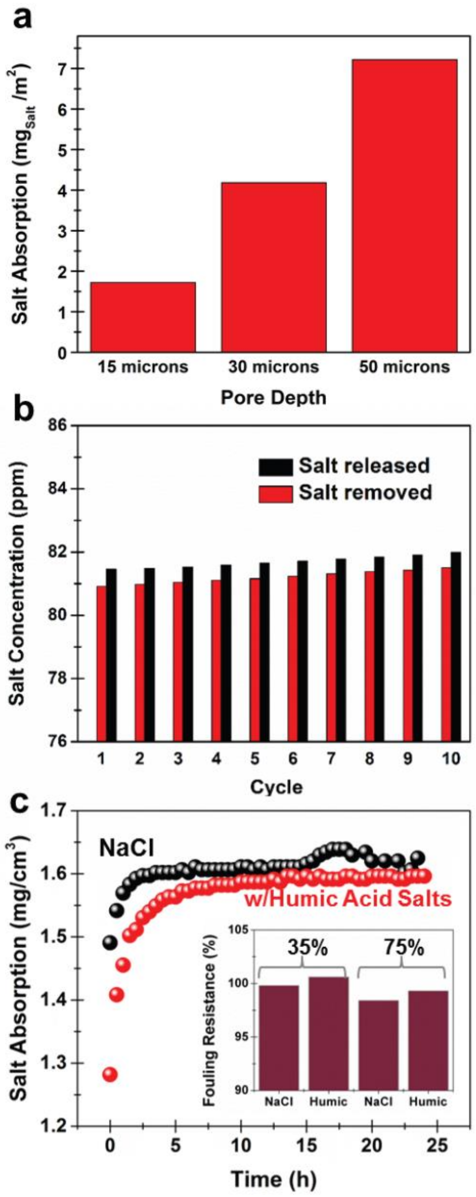

Figure 5.3 (a) Average salt removal capacity per CDI electrode area over 10 cycles based on porous silicon layers with thickness of ~ 15, 30, and 50 µm, respectively. (b) Salt removal cycling in low-concentration (fresh) water showing salt absorption (red) and salt desorption back into water (black). (c) Galvanostatic salt absorption/desorption curves in pure NaCl (black) and with humic acid salt fouling additives (red). Inset shows fouling resistance comparing porous silicon electrodes with 35% and 75% porosity with and without fouling agent.

performance of the porous Si CDI electrodes with 75% porosity and a comparison of 75% porosity and 35% porosity (inset). In order to simulate the effect of fouling we compared the long term cycling performance of the porous Si electrodes in the pure NaCl solution (1000ppm-1g/L) and compared that to the performance with an additional 3ppm of humic acid salts.[38] Despite slightly different response of the electrodes in the first few hours of cycling, the stable long-term performance over a 24 hour period reaches a steady state performance that is relatively invariant with regard to the fouling agent. This implies that due to the ideal structure of porous silicon combining deep pore channels and pockets of electrosorption sites along the channels (**Figure 5.1a**), fouling does not appear to present a significant challenge. This is further emphasized by comparing the fouling resistance, or the modification of the steady-state electro-sorption/desorption properties, in the latter (steady-state) 15 hours of cycling at two different porosities of 75% and 35% as inset in **Figure 5.3c** that does not indicate a significant effect of fouling in these electrodes.

5.4 Discussion

The results presented in **Figures 5.1-5.3** support the principle that porous silicon networks are practical scaffolds for CDI applications over a wide range of practical salt concentrations ranging from ocean water to fresh water. Based on the accepted standards of the United States Office of Naval Research (ONR) and the Groundwater Foundation (GF), fresh water contains salt concentrations < 500 ppm (salinity < 0.05%) and brackish water involves concentrations ranging from 500 – 30,000 ppm (0.05 – 3% salinity). Ocean water has salinity near ~ 3.5%. In this spirit, the tests in **Figures 5.2** and **5.3** range from saline water with salt concentrations near that of ocean water (~ 2.9% salinity, 500 mM) to near-fresh water concentrations (~ 0.06% salinity, 10 mM). The performance of porous-silicon based CDI electrodes over this range of concentrations supports the principle of a multi-cell CDI system based on porous silicon materials that can maintain high efficiency in converting ocean water to fresh water.

To further highlight the performance measured for porous silicon CDI electrodes, we compare the performance measured in this study against that reported for CDI electrodes produced with different carbon electrode materials.[2,3, 4] (**Figure 5.4a**) To compare to these materials we report the average salt removal measured across the entire range of concentrations. This compares the integrated carbon coated porous

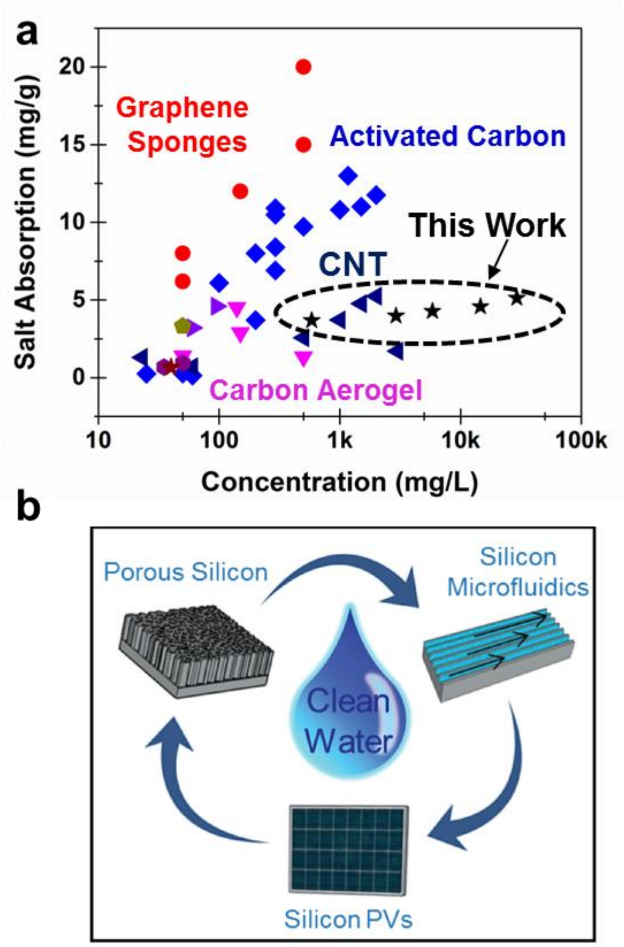

Figure 5.4. (a) Comparison of average specific salt removal capacity for porous silicon electrodes compared to other notable forms of carbon, such as 3D graphene sponges, carbon aerogels (CA), activated carbons (AC), and carbon nanotubes (CNTs).[2,3, 4] (b) Scheme emphasizing the vision of porous silicon integration with microfluidics and/or solar cells for technological water desalination platforms.

silicon CDI electrodes against 3D Graphene foams, carbon aerogels (CA), activated carbon (AC), carbon nanotubes (CNTs), carbon nanofibers (CNFs), and mesoporous carbons (MC) and other carbon based CDI electrodes. Notably, the majority of these materials involve nanoscale carbon materials with either nano- or micro-particulates that are pressed into a CDI electrode. The results we report are comparable to salt removal capacity of many of these state-of-the-art carbon materials and better than the general range of salt removal capacities of these different materials. Although our measured performance still lags behind the highest performing graphene-based electrode assemblies, our results indicate that routes to isolate mechanically robust free-form carbon electrodes from the porous silicon networks can potentially achieve such high performance. However, in contrast to stand-alone carbon CDI electrodes, the use of porous silicon templates for CDI opens up routes to directly couple CDI active materials into silicon platforms relevant to microfluidic flow systems or even such flow systems integrated on the backside of silicon photovoltaic cells. (**Figure 5.4b**) Recent efforts have emphasized the capability to etch porous silicon into the back-side of unused silicon in photovoltaic cells to enable the dual function of energy storage and energy conversion in a silicon solar cell.[34] The coupling of CDI technology into silicon can lead to even the more exciting prospect of integrating solar and desalination systems into directly coupled systems that, in contrast to reverse osmosis systems that require large-footprint infrastructure for operation, could be powered by cheap solar cells and operated at small scales in low-income families or communities for water purification.

5.5 Conclusion

In summary, building from the 2nd most abundant element on earth, leveraging scalable processing routes, and producing controllable materials not involving free-formed particulates, as in other techniques, we show specific salt removal ranging from 3.8 mg/g to 5.2 mg/g ranging from fresh to ocean water salt concentrations, requiring energy input as little as 1.45 Wh/L to convert ocean water to drinking water. This is comparable or better in many cases to particulate carbon-based electrodes, with a tunable pore morphology and structure that can optimize CDI performance in different flow architectures and mitigate the effect of fouling. Unlike carbon-based particulate materials, this route leads to straightforward directions to seamlessly integrate CDI materials into silicon-based microfluidics or photovoltaic cells. This inspires a vision of cheap, local water desalination platforms powered by silicon photovoltaics that can be employed in low-income or developing countries without the necessity of external power input or high cost infrastructure.

Acknowledgements

We would like to thank Shahana Chatterjee, Rizia Bardhan, Jeremy Mares, and Sharon Weiss for early assistance with materials and facilities in this study. This work was supported by NSF grant CMMI 1335269.

References

1. Metke, T.; Westover, A. S.; Carter, R.; Oakes, L.; Douglas, A.; Pint, C. L. *Scientific reports* **2016,** 6, 24680.

2. Xu, X.; Sun, Z.; Chua, D. H.; Pan, L. *Scientific reports* **2015,** 5.

3. Liu, Y.; Nie, C.; Liu, X.; Xu, X.; Sun, Z.; Pan, L. *RSC Advances* **2015,** 5, (20), 15205-15225.

4. Shi, W.; Li, H.; Cao, X.; Leong, Z. Y.; Zhang, J.; Chen, T.; Zhang, H.; Yang, H. Y. *Scientific reports* **2016,** 6.

5. Shannon, M. A.; Bohn, P. W.; Elimelech, M.; Georgiadis, J. G.; Marinas, B. J.; Mayes, A. M. *Nature* **2008,** 452, (7185), 301-310.

6. Hem, J. D., *Study and interpretation of the chemical characteristics of natural water*. Department of the Interior, US Geological Survey: 1985; Vol. 2254.

7. Karagiannis, I. C.; Soldatos, P. G. *Desalination* **2008,** 223, (1), 448-456.

8. Wade, N. M. *Desalination* **2001,** 136, (1), 3-12.

9. Borsani, R.; Rebagliati, S. *Desalination* **2005,** 182, (1), 29-37.

10. Tian, L.; Guo, J.; Tang, Y.; Cao, L. *Desalination* **2005,** 183, (1), 317-325.

11. Miller, J. E. *Sandia National Labs Unlimited Release Report SAND-2003-0800* **2003**.

12. Darwish, M.; Al Asfour, F.; Al-Najem, N. *Desalination* **2003,** 152, (1), 83-92.

13. AlMarzooqi, F. A.; Al Ghaferi, A. A.; Saadat, I.; Hilal, N. *Desalination* **2014,** 342, 3-15.

14. Peñate, B.; García-Rodríguez, L. *Desalination* **2012,** 284, 1-8.

15. Kang, G.-d.; Cao, Y.-m. *Water research* **2012,** 46, (3), 584-600.

16. Anderson, M. A.; Cudero, A. L.; Palma, J. *Electrochimica Acta* **2010,** 55, (12), 3845-3856.

17. Oren, Y. *Desalination* **2008,** 228, (1), 10-29.

18. Biesheuvel, P. *Journal of colloid and interface science* **2009,** 332, (1), 258-264.

19. Dykstra, J.; Zhao, R.; Biesheuvel, P.; van der Wal, A. *Water research* **2016,** 88, 358-370.

20. Liu, Y.; Xu, X.; Wang, M.; Lu, T.; Sun, Z.; Pan, L. *Chem Commun* **2015,** 51, (60), 12020-12023.

21. Jia, B.; Zhang, W. *Nanoscale research letters* **2016,** 11, (1), 1.

22. Welgemoed, T.; Schutte, C. *Desalination* **2005,** 183, (1), 327-340.

23. Choucair, M.; Thordarson, P.; Stride, J. A. *Nature Nanotechnology* **2009,** 4, (1), 30-33.

24. Simon, P.; Gogotsi, Y. *Nature Materials* **2008,** 7, (11), 845-854.

25. Taylor, S. *Geochimica et cosmochimica acta* **1964,** 28, (8), 1273-1285.

26. Baehr-Jones, T.; Pinguet, T.; Guo-Qiang, P. L.; Danziger, S.; Prather, D.; Hochberg, M. *Nature Photonics* **2012,** 6, (4), 206-208.

27. Park, J. G.; Smithyman, J.; Lin, C. Y.; Cooke, A.; Kismarahardja, A. W.; Li, S.; Liang, R.; Brooks, J. S.; Zhang, C.; Wang, B. *J. Appl. Phys.* **2009,** 106, (10), 104310.

28. Chiappini, C.; Liu, X. W.; Fakhoury, J. R.; Ferrari, M. *Advanced Functional Materials* **2010,** 20, (14), 2231-2239.

29. Chau, R.; Doyle, B.; Datta, S.; Kavalieros, J.; Zhang, K. *Nature materials* **2007,** 6, (11), 810-812.

30. Loni, A.; Canham, L. T.; Defforge, T.; Gautier, G. *Ecs Journal of Solid State Science and Technology* **2015,** 4, (8), P289-P292.

31. Foll, H.; Christophersen, M.; Carstensen, J.; Hasse, G. *Mater. Sci. Eng. R-Rep.* **2002,** 39, (4), 93-141.

32. Granitzer, P.; Rumpf, K. *Materials* **2010,** 3, (2), 943-998.

33. Whitesides, G. M. *Nature* **2006,** 442, (7101), 368-373.

34. Westover, A. S.; Share, K.; Carter, R.; Cohn, A. P.; Oakes, L.; Pint, C. L. *Applied Physics Letters* **2014,** 104, (21), 213905.

35. Chatterjee, S.; Carter, R.; Oakes, L.; Erwin, W. R.; Bardhan, R.; Pint, C. L. *Journal of Physical Chemistry C* **2014,** 118, (20), 10893-10902.

36. Oakes, L.; Westover, A.; Mares, J. W.; Chatterjee, S.; Erwin, W. R.; Bardhan, R.; Weiss, S. M.; Pint, C. L. *Scientific Reports* **2013,** 3, 3020.

37. Carter, R.; Chatterjee, S.; Gordon, E.; Share, K.; Erwin, W. R.; Cohn, A. P.; Bardhan, R.; Pint, C. L. *Nanoscale* **2015,** 7, (40), 16755-16762.

38. Mossad, M.; Zou, L. *Journal of hazardous materials* **2013,** 244, 387-393.

39. Cohn, A. P.; Erwin, W. R.; Share, K.; Oakes, L.; Westover, A. S.; Carter, R. E.; Bardhan, R.; Pint, C. L. *Nano letters* **2015,** 15, (4), 2727-2731.

40. Westover, A. S.; Freudiger, D.; Gani, Z. S.; Share, K.; Oakes, L.; Carter, R. E.; Pint, C. L. *Nanoscale* **2015,** 7, (1), 98-103.

CHAPTER 6

FROM THE JUNKYARD TO THE POWER GRID: AMBIENT PROCESSING OF SCRAP METALS INTO NANOSTRUCTURED ELECTRODES FOR ULTRAFAST RECHARGEABLE BATTERIES

Andrew S. Westover,[1,2^] ,Nitin Muralidharan,[1,2,^] Haotian Sun,[2] Nicholas Galioto,[2] Rachel E. Carter,[2] Adam P. Cohn,[2] Landon Oakes[1,2] and Cary L. Pint[1,2]

[1]Interdisciplinary Materials Science Program, Vanderbilt University, Nashville, TN 37235, USA

[2]Department of Mechanical Engineering, Vanderbilt University, Nashville, TN 37235, USA

^equally contributing first authors

Abstract: Here we present the first full-cell battery device that is developed entirely from scrap metals of brass and steel – two of the most commonly used and discarded metals. A room temperature chemical process is developed to convert brass and steel into functional electrodes for rechargeable energy storage that transforms these multicomponent alloys into redox-active iron-oxide and copper-oxide materials. The resulting steel-brass battery exhibits cell voltages up to 1.8 V, energy density up to 20 Wh/kg, power density up to 20 kW/kg, and stable cycling over 5000 cycles in alkaline electrolytes. Further, we show the versatility of this technique to enable processing of steel and brass materials of different shapes, sizes, and purity, such as screws and shavings, to produce functional battery components. The simplicity of this approach, building from commonly available chemicals enables a simple pathway to the local recovery, processing, and assembly of storage systems based on materials that would otherwise be discarded.

This work was originally published in **ACS Energy Lett., 1, 1034-1041, Oct. 2016**, and is reproduced with permission. © *ACS Energy Letters (2016)* DOI: 10.1021/acsenergylett.6b00295

6.1 Introduction

The complexity of modern battery systems that involve highly processed and purified materials, air sensitive materials, and/or flammable electrolytes sustain a multi-billion dollar battery industry devoted to delivering safe, high energy density, and portable energy storage solutions.[1-3] However, the early development of the first known batteries hinged on a much different rationale, where readily accessible (bulk) materials were combined at local scales to store energy. An early example of this is the first (speculated) development of a battery known as the ‘Baghdad Battery’[4] dating back to the 1st century BC that consists of a terracotta (ceramic) pot with a copper sheet and iron rod. More recent examples include the copper zinc system discovered by Volta[5] and the nickel iron battery developed by Edison,[6-8] both where common metals are immersed in simple electrolytes for local energy storage. Today, whereas bulk materials are readily available, achieving competitive high performing battery materials requires processing control and materials not commonly available in a residential or household setting.

In this spirit, stationary (grid-scale) storage of energy presents a critical solution to the intermittency of a future power grid that builds from a high penetration of renewable power generation such as wind and solar.[9, 10] However, a critical barrier to energy storage on the grid is the infrastructure needed for (low-cost) centralized storage systems, such as redox flow batteries, or pathways to implement high cost metal ion batteries for distributed storage.[9, 11] Other routes such as liquid metal batteries show promise,[12] but any route that significantly modifies the current centralized grid architecture poses a large barrier for practical incorporation to a future renewable grid system. On this note, as emerging manufacturing routes such as 3-D printing are aiming to transplant centralized industries onto local scales,[13-15] one may consider the feasibility for this vision to impact the future of stationary storage, especially given the historical framework in which batteries were developed. Could future consumers or communities have the capability to cost-effectively and safely produce batteries for stationary storage applications?

On this front, the side-effect of consumer-driven large-scale manufacturing is the depreciation of manufactured systems and eventual disposal of the material as waste. Scrap metals represent over 130 million tons of waste each year, with steels representing 84 million tons, aluminum representing 7.3 million tons, and brass (copper) representing 1.38 million tons a year.[16, 17] Although scrap metal recycling is active in the United States and worldwide today,[18] there are still enormous amounts of scrap metal waste that are not recycled each year including an estimated 17.5 million tons of steel,[19] and an estimated 1.15 million tons of copper/brass.[17] This is in part due to the lack of consumer benefits for scrap recycling and the high cost of single-stream recycling infrastructure. As steel and brass exist as multicomponent alloys and are present in nearly every household, a critical barrier to repurposing these materials rather than discarding them is the availability to carry out material processing in a common household environment. In this manner, chemical processing using anodization is particularly attractive since this technique requires low voltages, often builds from water-based environments, and can be leveraged to produce controllable nanostructured materials ideally suited for applications such as energy storage.[20-22] The anodization process for multicomponent alloys utilizes a voltage applied in a reactive electrolyte to electrochemically remove (and/or oxidize) one or more elemental species, and has been demonstrated for a wide range of materials and applications. Specifically for energy storage applications, anodization has been shown as an excellent tool to process binary metal alloys, and especially NiTi alloys, into porous or nanotubular nickel-oxide or titanium-oxide materials with high specific storage capability compared to bulk metal oxides.[22, 23] However, as of yet, anodization of complex multicomponent alloys such as steels or brass for the purpose of energy storage applications has never been explored. Unlike high purity metals, these manufacturing alloys involve elemental additives that act to improve the material properties, but complicate processing into a target metal-oxide functional material. Nonetheless, the abundance of these metals from manufactured products makes these materials excellent scaffolds for practical investigations leading to energy storage materials.

In this work, we draw inspiration from the rationale and working materials of the original Baghdad battery, and demonstrate a route where otherwise discarded scrap metals of brass and steels can be processed and combined to yield ultrafast rechargeable batteries. This builds upon an anodization process producing nanostructured electrodes from brass and cheap low-carbon steels that, when paired in aqueous electrolytes, exhibit nominal voltage ranging from 1V-1.8V, energy densities upwards of 20 Wh/kg, and power densities up to 20 kW/kg. Further, we show this idea can be transferred to scraps with various shapes, sizes, and purity, such as screws and shavings, that motivates the use of this processing strategy at local scales to generate functional energy storage capability from otherwise discarded metal objects.

6.2 Experimental Methods

6.2.1 Development of iron oxide nanorods and copper oxide nanothorns

The obtained scrap carbon steel (1010 steel) and brass sheets (Yellow brass, 67% Cu/33% Zn) were cut into small squares and subjected to ultrasonic cleaning using acetone, ethanol and water for 10 min each. For the preparation of iron oxide nanorods, the steel samples were subjected to potentiostatic anodization at 40 V for 900 seconds using a Keithley sourcemeter. The electrolyte used in this case contained 0.05M NH_4F in 3 vol% of water with ethylene glycol. The anodized steel samples were washed with water and dried in air. To stabilize the surface oxide, an annealing step was added where the sheets were subjected to a temperature of 350 ^oC for 1 hour under Ar(1SLM)/H_2 (200 sccm) flow. To prepare copper oxide nanothorns, the ultrasonically cleaned brass sheets were soaked in HCl where the initial solution (37%) HCl (sigma aldrich) was diluted down in a ratio of 10mL of ultrapure water to 5 mL of 37% (HCl). This allowed for removal of the native oxide. Anodization was then performed in a 2M KOH electrolyte using 100 cyclic voltammetric sweeps between 0 V and 0.6 V using a Metrohm Autolab controller. To truly demonstrate the versatility of the anodization process, brass sheets were anodized galvanostatically as well using a current density of 1 mA/cm^2 for 300 seconds. The counter electrode and the reference electrode in these set ups were a Pt foil and saturated calomel electrode respectively. The anodized brass sheets were washed with water and dried in air. Similar anodization and post treatment conditions were followed for the scrap screws, pipes and trimmings.

In order to assess the active mass, the active materials on the surface were mechanically separated from the electrodes. This technique was judged in comparison to other techniques we considered and tested for active mass assessment such as the dissolution of active oxides in liquid media and corresponding mass assessment. The mechanical separation approach, albeit very simple, errors on the side of overestimating the active mass due to the potential removal of some inactive material, providing an underestimate of the actual electrode performance. Thus mechanical separation is more appropriate than relying on a technique where the error in the mass measurement is skewed toward the incomplete removal of all active mass, and hence inflation of the results.

6.2.2 Microstructural and Compositional Analysis

Microstructural analysis and Energy Dispersive Spectroscopy (EDS) elemental analysis were performed on the anodized and treated steel and brass surfaces using a Zeiss Merlin Scanning Electron Microscope. Compositional analysis of the anodized brass and steel surfaces were also performed using Renishaw Raman Microscope using 532 nm Laser excitations to determine the surface species corresponding to the different nanostructures.

6.2.3 Electrochemical Characterization

The anodized steel and brass samples were subjected to electrochemical testing individually in a .1M or 1M KOH electrolyte with a Pt counter and SCE reference electrode in a beaker type electrochemical cell. For the scrap metal battery, the steel electrode was made the anode and the brass electrode the cathode, the electrolyte used was 1 M KOH. A jar type battery was made using the same electrode configuration in a glass vial sealed with a rubber septa forming a full cell. Two such jar batteries were connected in series to reach the required voltage to power a blue LED. The jar battery system was galvanostatically charged and then a blue LED was connected to the jar battery which allowed for the jar battery to discharge thereby lighting the LED. All electrochemical characterization was performed using a Metrohm Autolab Multichannel Analyzer. All full cells were cycled a 100 CV cycles for conditioning and to obtain reproducible voltammograms.

Specific capacity was calculated from CV curves using the equation $Capacity_{sp} = \frac{\int IdV}{m*dV/dt}$ and from discharge curves using the equation $Capacity_{sp} = \frac{I*t}{m}$. Specific Capacitance was calculated from CV curves using the equation $Capacitance_{sp} = \frac{\int IdV}{V*m*dV/dt}$. In all cases I represents the current, V is the voltage, m is the mass, and dV/dt is the scan rate. Specific energy was calculated from the discharge curves according to the equation $Energy_{sp} = \frac{\int IVdt}{m}$ and the specific power was calculated according to the following equation. $Power = \frac{Energy_{sp}}{\Delta t}$.

Figure 6.1 Schematic representation of the process of developing the scrap metal battery with a photograph of one of two scrap metal jar batteries powering a blue LED.

6.3 Results and Discussion

A general scheme that elucidates the approach to transform scrap metals into ultrafast rechargeable batteries is shown in **Figure 6.1**. Importantly, the primary consideration when assembling two electrodes into a battery assembly is the total resulting operation voltage, which is dictated by the relative potential of the redox couples at the anode and the cathode. In this manner, the original Ni-Fe battery system developed by Edison has reemerged in the research arena due to the moderate voltage (~ 1.5 V), and capability to produce nanostructured $Ni(OH)_2$ and Fe_xO_y structures readily from bulk materials.[7, 24-26] However, whereas brass has never been studied as the basis for a battery electrode, CuO_x active materials (Cu is the primary component of brass) exhibit redox couples ranging from +0.2-0.6V vs. SCE in aqueous KOH, which are very close to those for NiOH.[27, 28] Compared to nickel metal electrodes, brass is significantly less toxic, more abundant as a metal, and cheaper (~$1.1 per lb. versus ~ $3.6 per lb, United States Scrap Register).[29] This led us to envision using low carbon steel – the most abundant scrap metal, as a source of iron oxide, and brass – the third most abundant scrap metal, as a source of copper oxide and combined with aqueous KOH electrolyte to produce a full cell battery with appropriate electrode potential pairing to produce a competitive energy storage platform. To generally demonstrate the function of this battery system, **Figure 6.1** shows one of two scrap metal batteries wired in series used to light up a blue LED where the anodized brass and anodized steel electrodes can be clearly seen.

In this effort, the use of anodization is critical to transforming scrap metal into electrodes with a low environmental impact, and additionally yields a self-contained electrode structure that can operate in the absence of binders or additives.[30, 31] **Figure 6.2a** demonstrates the experimental configuration for the anodization process that is universally applied to both steel and brass. This setup involves and low cost processing in electrolytes using low voltages that can be achieved in a household setting (see methods). To guide efforts in processing steel and brass materials into electrodes containing redox active materials, Raman spectroscopy (532 nm excitation, **Figure 6.2b**) and scanning electron microscopy (SEM, **Figure 6.2c-d**) were used to assess the chemical and physical characteristics of the resulting materials, respectively.

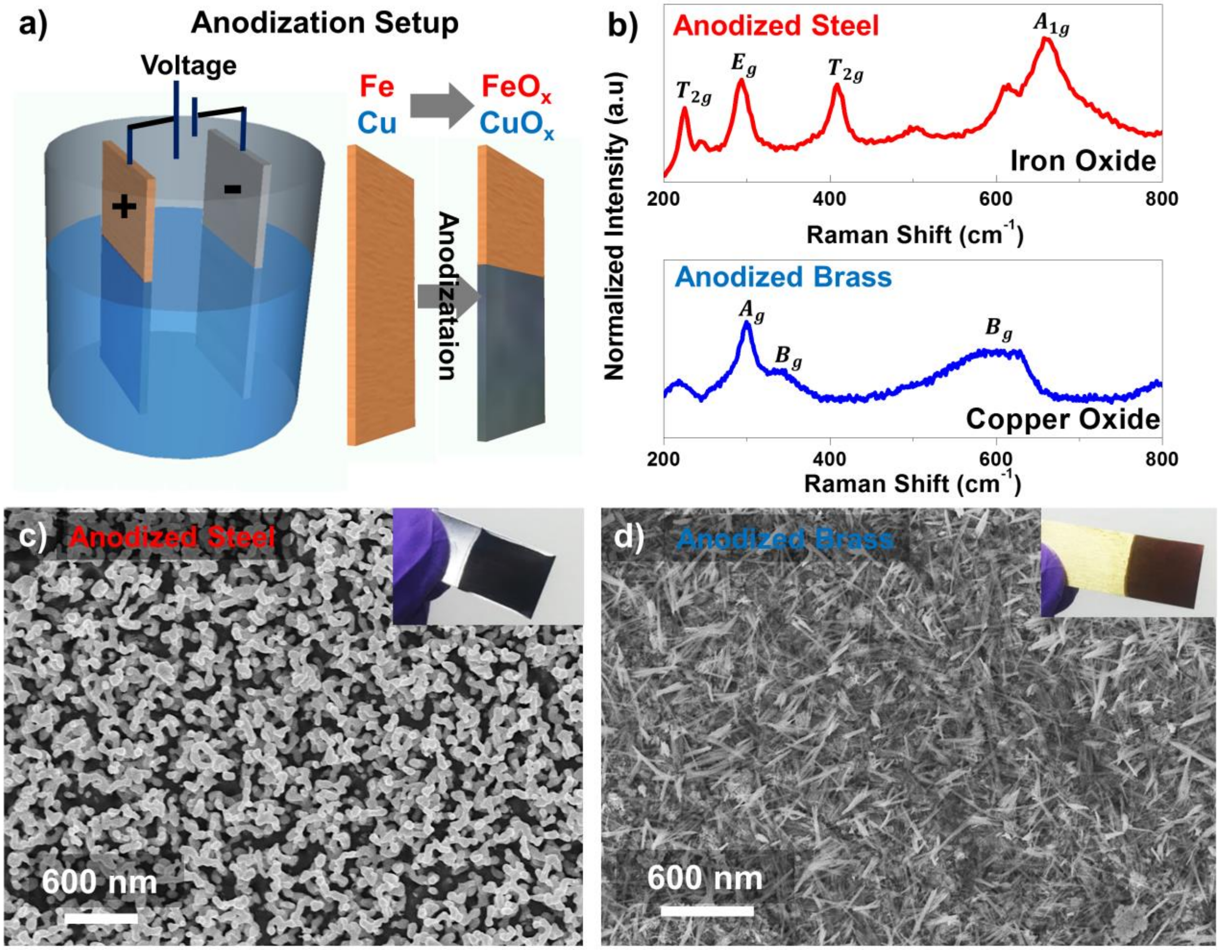

Figure 6.2 (a) Schematic representation of the anodization process applicable to both steel and brass electrodes. (b) Raman spectra of the treated steel and brass surfaces showing the Raman signatures of iron oxide and copper oxide. (c) SEM micrograph showing iron oxide nanorods developed on the steel surface, inset- photograph of treated steel electrode. (d) SEM micrograph showing copper oxide nanothorns developed on the steel surface, inset- photograph of treated brass electrode.

Elemental analysis using energy dispersive spectroscopy (EDS) of the processed steel and brass (**Figure 6.S1** and **Figure 6.A2** respectively) revealed the presence of oxygen on the surface indicating the surface of both electrodes have been oxidized through the processing. Following anodization, distinct Raman signatures corresponding to T_{2g} (225 cm^{-1}, 409 cm^{-1}), E_g (290 cm^{-1}) and A_g (660 cm^{-1}) modes are observed in the case of anodized steel.[32, 33] For anodized brass, one A_g (300 cm^{-1}) mode and two B_g (337 cm^{-1}, 600 cm^{-1}) modes are observed.[34-37] This assessment confirms the capability of the anodization processes to result in the formation of iron oxide and copper oxide on the treated steel and brass respectively. SEM micrographs shown in **Figure 6.2c** and **6.2d** for the treated steel and brass surfaces indicate the presence of a nanostructured surface oxide in nanorod and nanothorn architectures respectively. These nanostructured surface oxides are in direct contact with the metallic steel and brass surfaces which function as effective current collectors to facilitate redox reactions of the respective oxides. As supported by recent studies,[7, 24] this electrode morphology is well-suited for ultrafast cycling performance.

To individually assess the electrochemical performance of each electrode, we performed electrochemical measurements in a three electrode configuration with the anodized scrap steel and brass as the working electrodes against a platinum or gold counter with a saturated calomel electrode (SCE) reference (see methods). **Figure 6.3a** shows the cyclic voltammograms of the surface activated steel electrode at scan rates of 10 mV/s to 500 mV/s. The voltammograms show clear anodic and cathodic peaks centered around -0.7V and -1.1V respectively which correspond to the Fe^{3+}/Fe^{2+} redox couple according to the following reaction[38]

$$Fe(OH)_2 + OH^- \leftrightarrow FeOOH + H_2O + e^- \tag{1}$$

This redox couple operating at negative potentials with respect to SCE, is an ideal candidate for consideration as an anode for the scrap metal battery. As the voltammograms show distinct Faradaic reactions which contribute to most of the energy stored, the performance of the electrde can be assessed by determining the specific capacity (mAh/g) as shown in **Figure 6.3b**. The anodized steel electrode boasts a capacity of 270 mAh/g based on the mass of the active material. At scan rates 20 times higher, the electrode maintains a capacity of 100 mAh/g. Owing to the ultrafast nature of this redox reaction, the anodized steel electrode can also be treated as a pseudocapacitor offering possibilities of developing asymmetric supercapacitors through combinations with traditional electric double layer (EDL) capacitors. The specific capacitance (**Figure 6.3b**) of these electrodes ranged from 770 F/g at slow rates of 10 mV/s to 300 F/g at fast rates of 500 mV/s. In contrast to the iron oxide redox reactions of the steel electrode, the voltammograms of the brass (**Figure 6.3c**) reveal the redox electrochemistry of copper oxide at positive

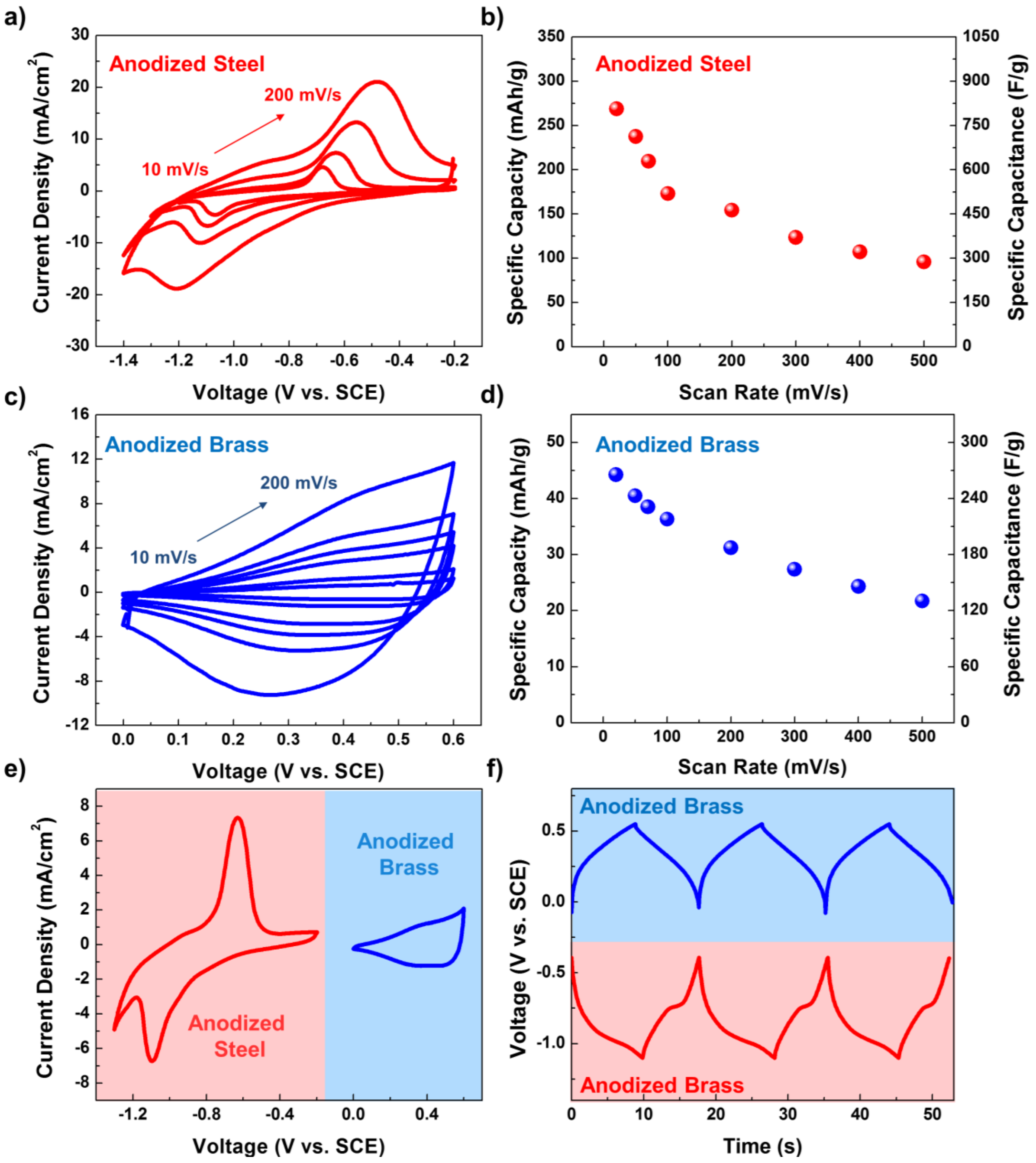

Figure 6.3 (a) Cyclic voltammograms of anodized steel electrode at scan rates of 10 mV/s to 200 mV/s. (b) Specific capacitance and specific capacity for anodized steel calculated from cyclic voltammograms. (c) Cyclic voltammograms of anodized brass electrode at scan rates of 10 mV/s to 200 mV/s. (d) Specific capacitance and specific capacity for anodized brass calculated from cyclic voltammograms. (e) Cyclic voltammograms of the anodized steel and brass electrode showing the pairing possibility of the Fe-Cu redox couples. (f) Galvanostatic charge discharge curves of anodized steel and anodized brass electrodes plotted vs. SCE.

potentials with respect to SCE ranging from .2 to .8V vs. SCE suggesting ideally suited pairing for the anodized steel electrodes. Due to the broad nature of the electrochemical peak(s) seen in **Figure 6.3c**, this is expected to represent an envelope of electroactive surface species comprising of CuO, Cu_2O, CuOH and $Cu(OH)_2$.[28] The anodized brass electrode had a specific capacity of 45 mAh/g at low scan rates of 10 mV/s and 20 mAh/g at scan rates of 500 mV/s as represented in **Figure 6.3d**. Similar to the steel electrodes, we estimated the specific capacitance of the anodized brass electrodes showing 270 F/g (10 mV/s) to 130 F/g (500 mV/s) as shown in **Figure 6.3d**. One significant advantage of both of the steel and brass electrodes is the ability to maintain >40% of the capacity at high rates even up to 500 mV/s. In both cases, this can be attributed to the nanoscale structure of the active materials that mitigates the necessity of fillers or conductive additives and enables intimate contact between the active material and the current collector. The redox peak potentials of the anodized steel and brass electrode indicate the possibility of pairing these reactions in a full cell architecture with steel anodes and brass cathodes (**Figure 6.3e**). To support the potentiodynamic cyclic voltammetry data, **Figure 6.3f** shows the galvanostatic charge discharge curves of the steel and brass electrodes where a comparison of the redox potentials indicate an overall potential window of 0.8V - 1.8V when paired in a full cell architecture.

Leveraging the relative location of the redox couples in each nanostructured electrode, we used the same electrolyte system to successfully pair the iron oxide/copper oxide redox couples in a full cell battery architecture, thus producing the first ever entirely scrap metal derived battery as well as the first instance of pairing steel and brass materials into a battery system. Cyclic voltammetry measurements (**Figure 6.4a)** indicate reversible charge storage in the voltage window of 0.8 V to 1.8 V in the battery. Increasing the scan rate up to 500 mV/s also demonstrates that the battery system maintains the ultrafast storage properties addressed in half-cell assessments (**Figure 6.3**). Assessing the discharge curves shown in **Figure 6.4b**, we observe a discharge capacitance of 110 F/g (discharge capacity 16 mAh/g) at a current density of 0.5 A/g with a discharge time >100 s.

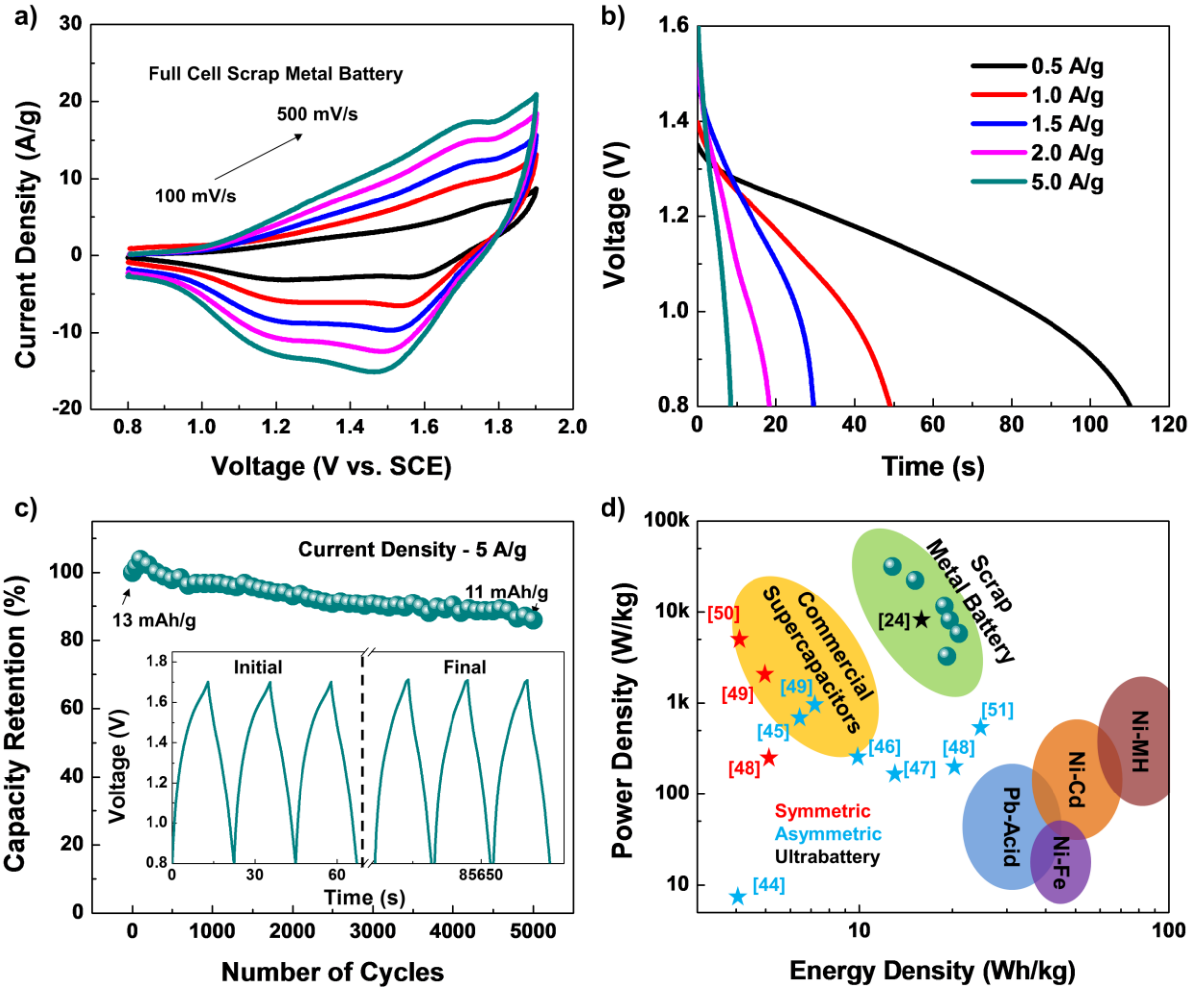

Figure 6.4. (a) Cyclic voltammograms of the scrap metal battery with steel anode and brass cathode at scan rates from 100 mV/s to 500 mV/s. (b) Galvanostatic discharge curves of the scrap metal battery at current densities from 0.5 A/g to 5 A/g. (c) Cycling behavior of the scrap metal battery up to 5000 charge discharge curves at a current density of 5 A/g, inset- initial and near final galvanostatic charge discharge performance. (d) Ragone plot comparing the performance of the scrap metal battery to commercial supercapacitors and other aqueous based battery systems along with specific references to symmetric (red stars) and asymmetric devices (blue stars) and ultrabatteries (black star) reported in literature.

Following the precedent set by similar paired high rate nanomaterial batteries in the recent years especially the case of ultrafast nickel-iron batteries, for the half cell characterizations we provided both the specific capacity and specific capacitance values for each of our individual electrode materials. Whereas when these electrodes are paired together in the same manner as a battery these clearly should be classified as a battery, the individual electrodes could also be paired with traditional electric double layer electrodes to form hybrid capacitor devices. Thus our reporting of both specific capacity and specific capacitance allows for easy comparison with traditional battery electrodes and with traditional supercapacitor or pseudocapacitor electrodes. A more in depth discussion of where our electrodes and full cell devices fit in the broader view of energy storage is provided in Appendix 6.A. (**Figure 6.A3** and **Table 6.A4**)[7, 24, 39, 40]

To illustrate the stability of this paired anodized steel and brass system we performed galvanostatic charge discharge tests over 5000 cycles at a current density of 5 A/g (**Figure 6.4c**). After an initial electrode stabilization phase of 100 cycles, the full cell reached a stable discharge capacity. For this ultrafast scrap metal battery, the paired electrodes retained 85% of the initial capacity of 13 mAh/g even after charging and discharging the device for 5000 cycles.

EIS measurements were performed on the full cell to understand the nature of the electrical connectivity of the active materials in the developed nanostructured electrodes (**Figure 6.A5**). Testing in a full cell configuration, gives a better estimate of the equivalent series resistance of the solution resistance when compared to a half cell in the presence of a reference electrode. The scrap metal battery had an equivalent series resistance of 6.23Ω indicating comparably good electrical connectivity of these iron oxide nanorods and copper oxide nanothorns on the steel and brass electrodes respectively.

Further, to compare the performance of the ultrafast scrap metal battery to other traditional battery systems we construct a Ragone plot from galvanostatic charge discharge curves in **Figure 6.4d**. Our scrap metal battery has an energy density of 20 Wh/kg while functioning in the ultrafast high power regime from 5-20 kW/kg. The operating voltage window of this scrap metal battery is dictated by the aqueous electrolyte used which limits the energy density when compared to traditional Li-ion batteries.[3] Whereas, the energy density approaches traditional Pb acid and Ni-Fe battery systems, the ability to maintain this energy performance at high rates similar or better than that of supercapacitors makes this an attractive energy storage system.[41-43] We note that for commercial battery systems the reported performance is optimized to have ~50% of the reported weight from the active mass. Taking this into consideration, the combination of energy and power performance of our system still highlights a unique area of energy storage with the capability to store energy as a battery but operate in the same high power regime as that used by solar cells and other renewable energy sources and can likely be improved with further optimization. To further illustrate the performance of this scrap metal battery we compared our results to some existing literature works on hybrid devices (asymmetric and symmetric capacitors) (**Figure 6.4d**) in these cases our devices outperform both symmetric and asymmetric devices with comparable performance to other paired high rate electrode chemistries such as the Ni-Fe ultrabattery.[24, 44-51]

Finally, to demonstrate the versatility of this process, we show the capability to anodize random scrap metal items such as screws, pipes, and metal shavings and then implement them as electrodes for the scrap metal batteries (**Figure 6.5)**. In particular **Figure 6.5b-c** show the paired battery performance of these anodized pipes, screws and metal shavings in true scrap metal battery architectures. In addition to demonstrating the versatility of this process, the ability to anodize screws, pipes and other functional materials suggests the possibility of developing multifunctional batteries using this approach. Outside of simply converting scrap metals into batteries, the ability to produce energy storing screws that could be mounted into an ion conducting (but electrically insulating) backplane, or metal pipes with integrated energy storage in the inactive materials represents systems that our work emphasizes as being feasible. As the different surface to volume ratios of these different objects will result in different amounts of surface oxide for identical anodization conditions, optimizing parameters such as time, voltage, temperature and electrolyte concentration can account for this difference.[22, 52] On this note many types of scrap consist of large items that are not immediately useable in this type of battery architecture. However, one of the key steps in the scrap recycling process is the shredding of these larger items prior to melting, purification and casting. For these larger items it would be feasible to develop them into batteries after this shredding process eliminating the energy expensive, melting and purification steps in the traditional scrap recycling process. (See Table S6)

Finally, whereas we report here the specific instance of processing brass and steel into a scrap metal battery system that builds upon copper oxide and iron oxide active materials, we emphasize that this

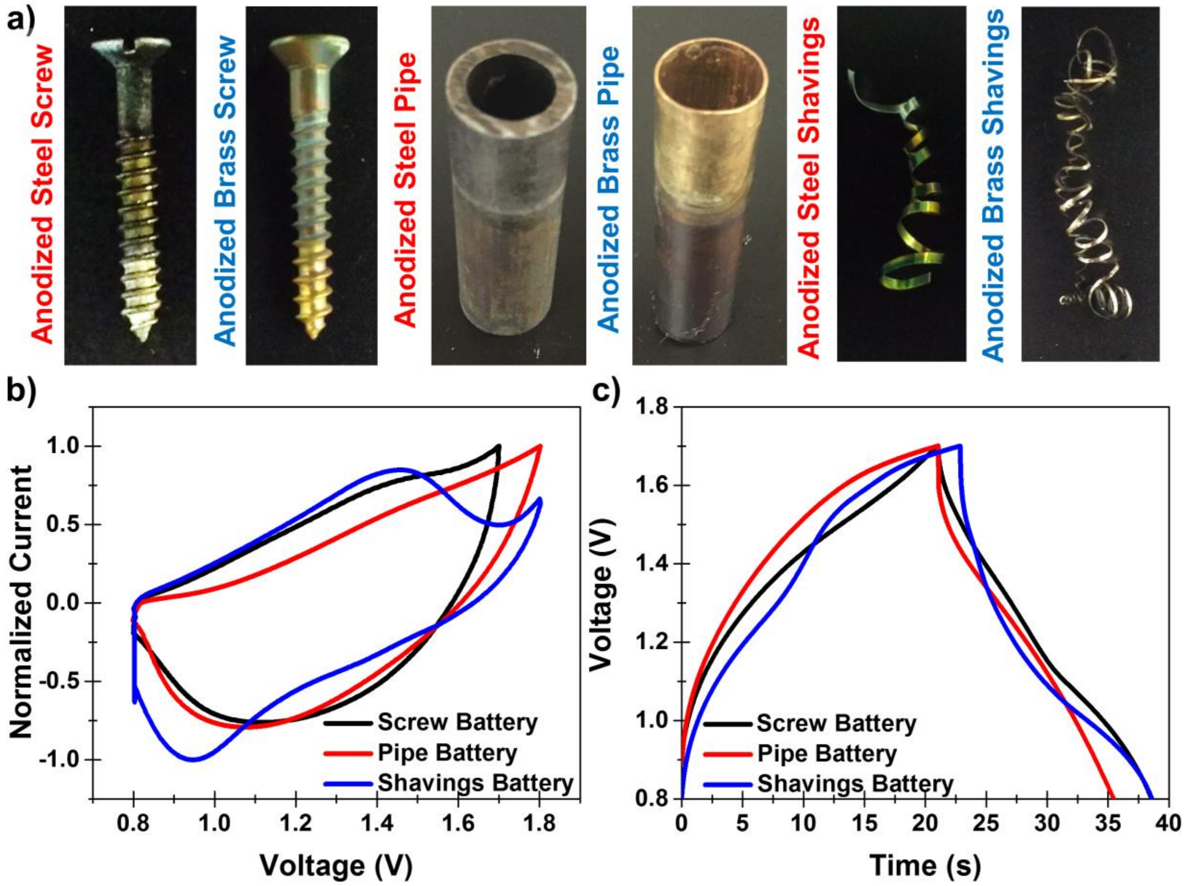

Figure 6.5 (a) Optical image of the anodized steel and brass screws, pipes and shavings. (b) Cyclic voltammograms of the scrap metal batteries made from anodized steel and brass screws, pipes and shavings. (c) Galvanostatic charge discharge curves of the scrap metal batteries made from anodized steel and brass screws, pipes and shavings.

approach is not limited to this reaction pair. Chemical processes to leverage zinc[53-55] electrochemistry using brass alloys,[56, 57] chromium and nickel oxide reactions in stainless steel,[7, 21, 22, 24, 58] and metal hydride and Aluminum air electrochemistry using Aluminum[59, 60] should all be distinct possibilities. This provides a broadly generalizable platform to repurpose otherwise discarded materials into functional energy storage electrodes in a manner that can be performed in a local environment. Whereas consumer-driven development of stationary storage systems is likely to be a controversial idea based on the status quo of large-scale battery manufacturing, our work gives promise to a future vision where researchers can provide an instruction manual to a consumer, as opposed to a product, to generate local energy storage solutions. This not only bypasses the significant technological barriers to commercializing low-cost stationary storage, but also gives promise to a sustainable method of repurposing abundant, low-value manufactured alloys common in a household setting into functional energy storage materials.

6.4 Conclusion

In summary, we demonstrate the first ever entirely scrap metal rechargeable battery as well as the first instance of pairing steel and brass materials into a battery system. Low-voltage anodization processes are developed that isolate nanostructured redox-active copper oxide and iron oxide materials from these multicomponent alloys, which we show to be well-suited for energy storage applications. The individual electrodes boast superb specific capacitance values of up to 800 F/g and 265 F/g for the steel and brass respectively and when paired into a full cell yield energy storage capability of up to 20 Wh/kg, power densities of up to 20 kW/kg, and cycling stability over 5000 cycles. As anodization is a simple process generalizable to 3-D objects, we further demonstrate the ability to use this technique to form highly accessible redox storage on the surface of commonplace steel or brass objects such as screws and shavings. This work lays the foundation to envision a sustainable route to low-cost and repurposed stationary energy storage materials. Further, inspired by the first documented reports of batteries where the materials were locally recovered, processed, and fabricated into small-scale battery systems, we present a vision that builds on the simplicity of anodization and the commonplace of brass and steels in a household setting that can enable the “scaling-down” of battery assembly in a manner that parallels the relationship of 3-D printing to large-scale centralized manufacturing processes.

6.A Appendix

6.A.1 EDS compositional analysis:

Elemental mapping and analysis of the iron oxide nanorods using EDS

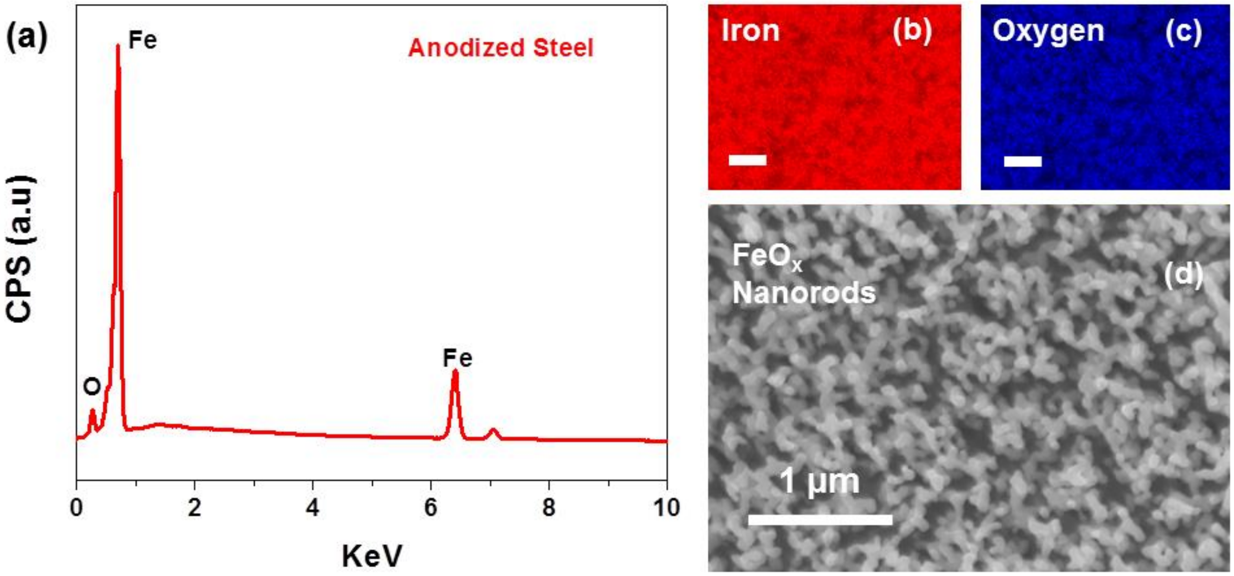

Figure 6.A1 (a) Energy Dispersive Spectroscopy (EDS) spectra of the treated steel surface consisting of the FeO$_x$ nanorods. (b) EDS map of the iron oxide nanorods showing the elemental signature of iron. (c) EDS map of the iron oxide nanorods showing the elemental signature of oxygen. (d) Electron image of the iron oxide nanorods.

Presence of surface oxides of iron forming the iron oxide nanorods are observed in the elemental analysis. This indicates that the surface treatments render the bare steel surface oxidized.

Elemental mapping and analysis of the copper oxide nanothorns using EDS

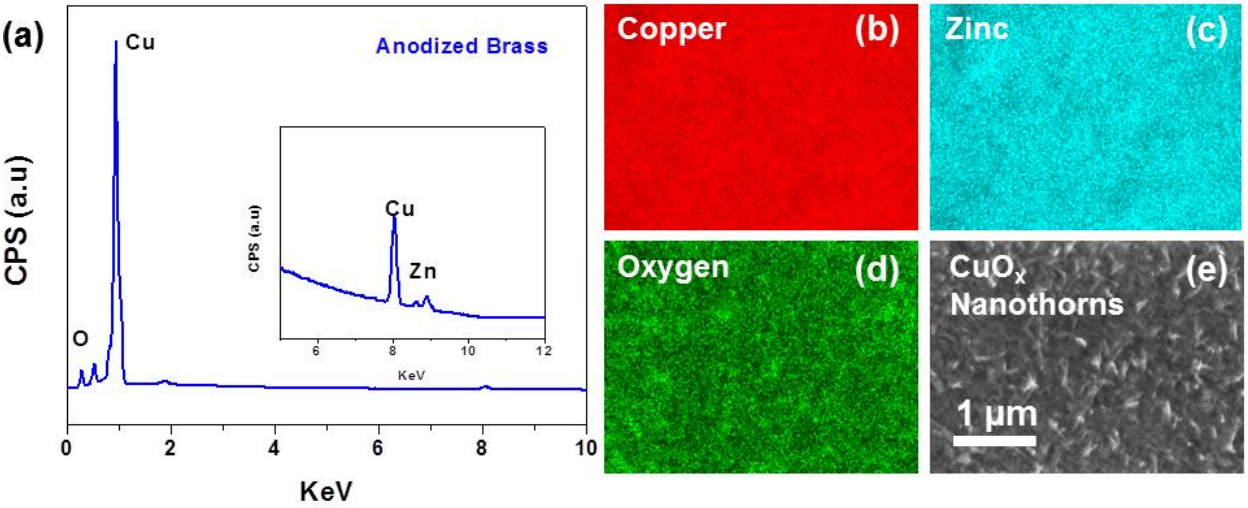

Figure 6.A2 (a) Energy Dispersive Spectroscopy (EDS) spectra of the treated brass surface consisting of the CuO_x nanothorns, inset – EDS spectra between 5 and 12 KeV showing elemental signature of copper and zinc (b) EDS map of the copper oxide nanothorns showing the elemental signature of copper. (c) EDS map of the copper oxide nanothorns showing the elemental signature of zinc. (d) EDS map of the copper oxide nanothorns showing the elemental signature of oxygen. (e) Electron image of the copper oxide nanothorns.

EDS elemental analysis indicates the presence of copper, zinc and oxygen for the anodized brass surface indicating the presence of oxides of copper and zinc.

6.A.2 Classification of Batteries, Supercapacitors and Pseudocapacitors

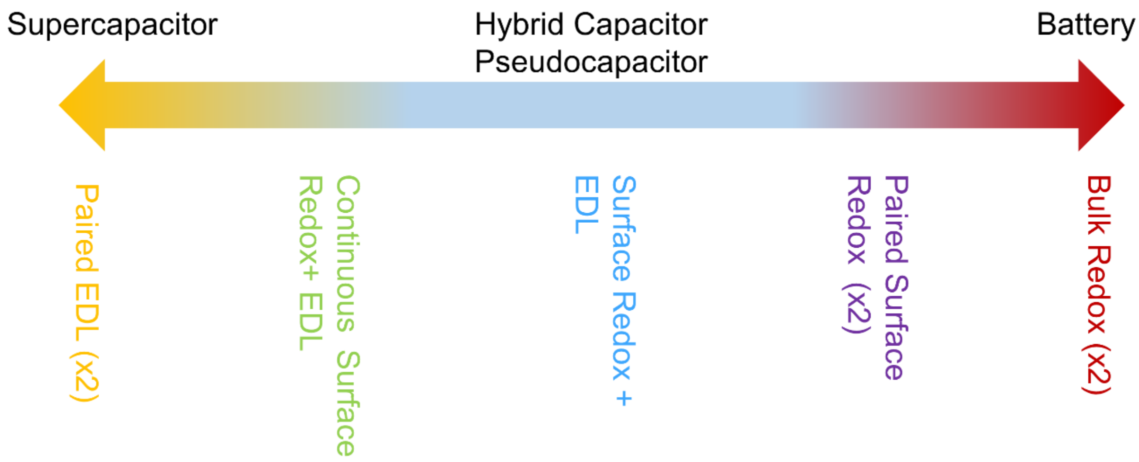

Figure 6.A3 Schematic representation of the general classification of supercapacitors, batteries and hybrid devices

Electric double layer (EDL)	High Power	Low Energy	Electrostatic	CNT[61], AC, Graphene[62]
Continuous Surface Redox	High Power	Moderate Energy	Faradaic	MnO$_2$,[63] RuO$_2$.[64]
Surface Redox	High Power	Moderate Energy	Faradaic	NiOH,[65] Fe$_2$O$_3$,[66] Cu(OH)$_2$, Co$_2$O$_3$,[67] Nanoparticles
Bulk Redox	Low	High Energy	Faradaic	Zn[68], Pb[69], Ni[70], LiCoO$_2$,[3] Graphite,[71]

Table 6.A4 Classification of the similarities and difference between different electrode types for energy storage

There has been considerable debate as to what exactly is the distinction between the different types of energy storage devices. Conventionally these have been split into three different categories Electric Double Layer Capacitors (EDLC), Pseudocapacitors, and Batteries. Where the terms Supercapacitor and ultracapacitor have often been used to describe both EDLC and pseudocapacitors. The most comprehensive and possibly insightful description of these types of devices was given by Conway.[72] He clearly described the distinction between each of the different types of energy storage electrodes. According to Conway there are essentially four different types of electrodes (see above Table S4). The first of these is electric double layer capacitors, where the energy is stored electrostatically by forming an ionic double layer on the surface of an electrode and except for a few exceptions consist almost entirely of carbon nanomaterials. The second is that of electrodes that exhibit a series of faradaic surface redox reactions such that in almost all respects their behavior mimics that of an EDLC with box-like CV curves and triangular charge discharge curves. The most common examples of these are MnO_2 and RuO_2. The third type of electrode is similar to the surface redox reactions exhibited by the second, except whereas this second type of electrode exhibits a series of continuous chemical reactions causing the performance to mimic that of a traditional EDLC, this third type exhibit a much narrower range of faradaic reactions, often coming from a single chemical reaction. He distinguishes this third type of electrode from traditional faradaic battery electrodes in that the chemical reactions for the most part happen on the surface of the material and do not cause a permanent phase change in the bulk of the material. Finally the fourth type he describes is that of battery electrodes which rely on bulk chemical reactions that cause a complete phase change of the electrode material.

Although the classifications between the different types of electrodes is very clear, when pairing the devices together the definitions become more vague and less well defined. In particular for the electrodes that are traditionally classified as pseudocapacitor electrodes, just as for any redox reaction these electrodes cannot be paired with themselves and form a fully functioning energy storage device. The vast majority of full cell applications of these ‘pseudocapacitor’ electrodes have involved the pairing of them with traditional EDLC and for these hybrid devices classifying them as supercapacitors, hybrid supercapacitors, asymmetric supercapacitors or any variation of such which is extremely appropriate. Recently however there has been a new class of full cell devices that pair what sometimes are traditionally considered ‘pseudocapacitor’ electrodes in order to maximize the voltage separation and capacities in the same manner as that used for designing traditional batteries. For these devices in almost all respects the full cells behave like that of a battery, with distinct faradaic energy storage peaks in the CV curves and long plateaus in the charge and discharge curves. The one distinction between these materials and that of traditional batteries is that the energy storage is primarily on the surface leading to excellent energy performance in the high power regime which is normally dominated by supercapacitors and hybrid supercapacitor architectures. Authors of works describing these paired systems have commonly referred to them as ‘high rate batteries’, ‘ultrafast batteries’, and ‘ultrabatteries’. This is in accordance with the recently published works by Simon, Gogotsi and Dunn[39, 62] that recommended that although these devices may exhibit high power it is still most appropriate to refer to these devices as batteries.[40]

Our electrodes clearly fall into this final type of full cell device, where we have the pairing of two electrodes that exhibit surface based redox reactions. In accordance with the guidelines outlined by Simon, Gogotsi, and Dunn where the device is characterized by the electrochemical behavior in both charge-discharge and CV measurements we refer to our devices as batteries. Because of the high rate performance of the devices, and due to the fact that each electrode could be individually paired with an EDLC to form a hybrid asymmetric supercapacitors we also feel strongly that the characterization of the performance of the individual electrodes should be characterized in terms of capacitance as well.”

6.A.3 Electrochemical Impedance Spectroscopy of the Scrap Metal Battery (Full Cell)

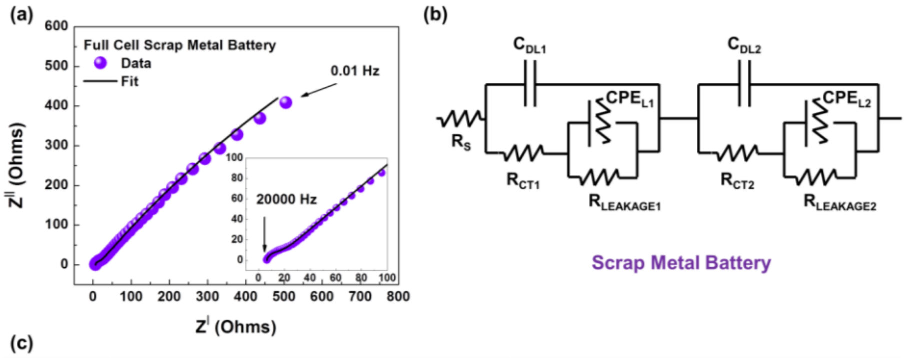

(c)

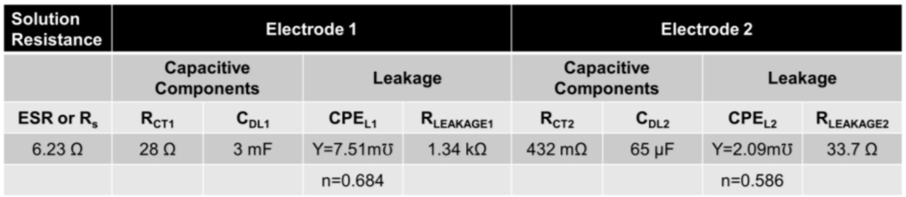

Solution Resistance	Electrode 1				Electrode 2			
	Capacitive Components		Leakage		Capacitive Components		Leakage	
ESR or R_s	R_{CT1}	C_{DL1}	CPE_{L1}	$R_{LEAKAGE1}$	R_{CT2}	C_{DL2}	CPE_{L2}	$R_{LEAKAGE2}$
6.23 Ω	28 Ω	3 mF	Y=7.51m℧	1.34 kΩ	432 mΩ	65 μF	Y=2.09m℧	33.7 Ω
			n=0.684				n=0.586	

Figure 6.A5 (a) Electrochemical impedance spectroscopy (Nyquist plot) of the scrap metal battery – full cell, (b) Equivalent circuit of the response of the scrap metal battery and (c) Fitting parameters for the full cell comprising of two electrodes (anodized steel and brass) of the scrap metal battery.

EIS measurements were performed in a full cell configuration to infer the equivalent series resistance (ESR) and charge transfer resistances (R_{CT}) of the scrap metal battery. **Figure 6.A5a** gives the Nyquist plot comprising of the real (x-axis) and imaginary components of impedance (y-axis) of the response of the scrap metal battery. The obtained response was fitted to a model typically applied for redox electrodes (**Figure 6.A5b**).[73] Considering the fact that in our case, the system consists of a steel anode and brass cathode, the redox electrodes can be modeled identically and in a full cell configuration separated by the solution resistance $R_{S.}$ From the Nyquist plots, ESR values were estimated from the intercept of the curve with x-axis corresponding to a value of 6.23 Ω. For the scrap metal battery, the response of both electrodes was modeled using C_{DL}, R_{CT}, CPE_L and R_L which are all in series with the R_S or ESR and the fitting parameters are shown in **Figure 6.A5c**. The high frequency regime gives the ESR of the system arising from electronic resistances. The charge transfer resistances and C_{DL} lie in the high to mid frequency region where the double layer component arises from the nanostructured nature of these electrodes. In the low frequency region, both the electrodes (anodized steel and brass) were modeled to have leakage capacitance and resistance associated with them represented by CPE_L and R_L respectively. The association of the resistive element R_L with CPE_L suggests a deviation from ideal behavior at low frequencies. As the electrodes used in this case are scrap metals which have a considerable amount of impurities, the effective energy storage capabilities are not that expected from ideal cases where ultrapure materials are used. Further purification steps prior to anodization treatment and optimizing the process parameters can further improve the performance of this scrap metal battery.

6.A.3 Recycling steps and their feasibility for battery processing

Recycling Process	**Potential for Battery Processing**
Collection	
Separation	Small items – direct anodization into a battery architecture
Shearing	
Shredding	Large items - could be anodized into a battery architecture after this step
Melting	
Purification	(could possibly skip this step for battery architectures)
Casting	All items - Could be cast into optimal architecture for battery performance

Table 6.A6 A table showing the steps in the recycling process on the left, and the potential for the development of scrap metal into batteries after various steps in the process.

6.A.4 Commercially available common chemically for scrap metal battery fabrication

Chemicals Used	Availability	Concentration	Cost
Hydrochloric Acid **HCl (diluted from 37%)**	Muriatic acid (Cleaning acid)	~31.5%	$6 /liter (Walmart)
Potassium Hydroxide **KOH (1-2M)**	Commercially available in the form of flakes for liquid soap making	Caustic	$3 /lb (Amazon)
Ammonium Fluoride **NH_4F (0.05M)**	For preventing fermentation, antiseptic agent	Reagent grade (available for moth proofing applications too as well as brewing malts)	$33 /400g (eBay)
Ethylene Glycol	Antifreeze agent	Commercial grades for using in automobiles	$9 /Gal (Walmart)

Table 6.A7. Commercially available common chemicals that can be potentially used to develop the scrap metal battery system

Acknowledgements

The authors would like to thank Matt McCarthy and PSC metals for useful insights into scrap metal refining procedures and on-site tours of PSC metals – a local scrap metal processing facility. We would also like to acknowledge Rizia Bardhan for use of Raman facilities. This work was supported in part by NASA EPSCoR grant NNX13AB26A and by the Vanderbilt University Discovery Grant program.

References

1. Armand, M.; Tarascon, J.-M. *Nature* **2008,** 451, (7179), 652-657.
2. Goodenough, J. B.; Park, K.-S. *J. Am. Chem. Soc.* **2013,** 135, (4), 1167-1176.
3. Tarascon, J.-M.; Armand, M. *Nature* **2001,** 414, (6861), 359-367.
4. Scrosati, B. *J. Solid State Electrochem.* **2011,** 15, (7), 1623-1630.
5. Pancaldi, G. *Hist. Stud. Phys. Biol. Sci.* **1990,** 21, (1), 123-160.
6. Chakkaravarthy, C.; Periasamy, P.; Jegannathan, S.; Vasu, K. *J. Power Sources* **1991,** 35, (1), 21-35.
7. Guo, W. X.; Xue, X. Y.; Wang, S. H.; Lin, C. J.; Wang, Z. L. *Nano Lett.* **2012,** 12, (5), 2520-2523.
8. Shukla, A.; Ravikumar, M.; Balasubramanian, T. *J. Power Sources* **1994,** 51, (1-2), 29-36.
9. Dunn, B.; Kamath, H.; Tarascon, J.-M. *Science* **2011,** 334, (6058), 928-935.
10. Chen, H.; Cong, T. N.; Yang, W.; Tan, C.; Li, Y.; Ding, Y. *Prog. Nat. Sci.* **2009,** 19, (3), 291-312.
11. Leung, P.; Li, X.; De León, C. P.; Berlouis, L.; Low, C. J.; Walsh, F. C. *RSC Adv.* **2012,** 2, (27), 10125-10156.
12. Kim, H.; Boysen, D. A.; Newhouse, J. M.; Spatocco, B. L.; Chung, B.; Burke, P. J.; Bradwell, D. J.; Jiang, K.; Tomaszowska, A. A.; Wang, K. *Chem. Rev.* **2012,** 113, (3), 2075-2099.
13. Campbell, T.; Williams, C.; Ivanova, O.; Garrett, B. *Technologies, Potential, and Implications of Additive Manufacturing, Atlantic Council, Washington, DC* **2011**.

14. Ambrosi, A.; Pumera, M. *Chem. Soc. Rev.* **2016,** 45, (10), 2740-2755.

15. Petrick, I. J.; Simpson, T. W. *Res. Technol. Manage.* **2013,** 56, (6), 12-16.

16. Mineral Commodities Summary 2015. Interior, U. D. o. t., Ed. US Geological Survey: Reston, Virginia, **2015**.

17. Goonan, T. G., *Copper Recycling in the United States in 2004*. US Department of the Interior, US Geological Survey: **2010**.

18. Ayres, R. U. *Resour. Conserv. Recycl.* **1997,** 21, (3), 145-173.

19. Damuth, R. J. *Iron and Steel Scrap: Accumulation and Availability as of December 31, 2009* US Institute of Scrap Recycling Industries **2010**.

20. Wu, X.; Bai, H.; Zhang, J.; Chen, F. e.; Shi, G. *J. Phys. Chem. B* **2005,** 109, (48), 22836-22842.

21. Macak, J. M.; Tsuchiya, H.; Schmuki, P. *Angew. Chem. Int. Ed.* **2005,** 44, (14), 2100-2102.

22. Hang, R.; Liu, Y.; Zhao, L.; Gao, A.; Bai, L.; Huang, X.; Zhang, X.; Tang, B.; Chu, P. K. *Sci. Rep.* **2014,** 4, 7547.

23. Kim, J.-H.; Zhu, K.; Yan, Y.; Perkins, C. L.; Frank, A. J. *Nano Lett.* **2010,** 10, (10), 4099-4104.

24. Sarkar, D.; Shukla, A. K.; Sarma, D. D. *ACS Energy Lett.* **2016,** 1, 82-88.

25. Jiang, W.; Liang, F.; Wang, J.; Su, L.; Wu, Y.; Wang, L. *RSC Adv.* **2014,** 4, (30), 15394-15399.

26. Lei, D.; Lee, D.-C.; Magasinski, A.; Zhao, E.; Steingart, D.; Yushin, G. *ACS Appl. Mater. Interfaces* **2016,** 8, (3), 2088-2096.

27. Lu, W.; Sun, Y.; Dai, H.; Ni, P.; Jiang, S.; Wang, Y.; Li, Z.; Li, Z. *RSC Adv.* **2016,** 6, (20), 16474-16480.

28. Shinde, S.; Dubal, D.; Ghodake, G.; Kim, D.; Fulari, V. *J. Electroanal. Chem.* **2014,** 732, 80-85.

29. Golev, A.; Corder, G. *J. Cleaner Prod.* **2016,** 112, 4296-4303.

30. Sagu, J. S.; Wijayantha, K. U.; Bohm, M.; Bohm, S.; Kumar Rout, T. *ACS Appl. Mater. Interfaces* **2016,** 8, (9), 6277-6285.

31. Qin, C.; Zhang, Y.; Wang, Z.; Xiong, H.; Yu, H.; Zhao, W. *J. Mater. Sci. Mater. Electron.* **2016,** 27, (9), 9206–9215.

32. Song, K.; Lee, Y.; Jo, M. R.; Nam, K. M.; Kang, Y.-M. *Nanotechnology* **2012,** 23, (50), 505401.

33. Sirivisoot, S.; Harrison, B. S. *Int. J. Nanomed.* **2015,** 10, 4447.

34. Akgul, F. A.; Akgul, G.; Yildirim, N.; Unalan, H. E.; Turan, R. *Mater. Chem. Phys.* **2014,** 147, (3), 987-995.

35. Wang, S.; Huang, Q.; Wen, X.; Li, X.-y.; Yang, S. *Phys. Chem. Chem. Phys.* **2002,** 4, (14), 3425-3429.

36. Fuentes, S.; Zárate, R.; Munoz, P.; DÍaz-Droguett, D. E. *J. Chil. Chem. Soc.* **2010,** 55, (1), 147-149.

37. Lin, Y.-G.; Hsu, Y.-K.; Chen, S.-Y.; Chen, L.-C.; Chen, K.-H. *A* **2011,** 21, (2), 324-326.

38. Doyle, R. L.; Godwin, I. J.; Brandon, M. P.; Lyons, M. E. *Phys. Chem. Chem. Phys.* **2013,** 15, (33), 13737-13783.

39. Simon, P.; Gogotsi, Y.; Dunn, B. *Science* **2014,** 343, (6176), 1210-1211.

40. Brousse, T.; Bélanger, D.; Long, J. W. *J. Electrochem. Soc.* **2015,** 162, (5), A5185-A5189.

41. Nyström, G.; Marais, A.; Karabulut, E.; Wågberg, L.; Cui, Y.; Hamedi, M. M. *Nat. Commun.* **2015,** 6, 7259.

42. Halpert, G. *J. Power Sources* **1984,** 12, (3-4), 177-192.

43. Padbury, R.; Zhang, X. *J. Power Sources* **2011,** 196, (10), 4436-4444.

44. Lu, X.; Yu, M.; Zhai, T.; Wang, G.; Xie, S.; Liu, T.; Liang, C.; Tong, Y.; Li, Y. *Nano Lett.* **2013,** 13, (6), 2628-2633.

45. Brousse, T.; Bélanger, D. *Electrochem. Solid State Lett.* **2003,** 6, (11), A244-A248.

46. Lin, Y.-P.; Wu, N.-L. *J. Power Sources* **2011,** 196, (2), 851-854.

47. Shanmugavani, A.; Selvan, R. K. *RSC Adv.* **2014,** 4, (51), 27022-27029.

48. Wang, R.; Yan, X.; Lang, J.; Zheng, Z.; Zhang, P. *J. Mater. Chem. A* **2014,** 2, (32), 12724-12732.

49. Cottineau, T.; Toupin, M.; Delahaye, T.; Brousse, T.; Belanger, D. *Appl. Phys. A* **2006,** 82, (4), 599-606.

50. Lu, X.; Wang, G.; Zhai, T.; Yu, M.; Xie, S.; Ling, Y.; Liang, C.; Tong, Y.; Li, Y. *Nano Lett.* **2012,** 12, (10), 5376-5381.

51. Jin, W.-H.; Cao, G.-T.; Sun, J.-Y. *J. Power Sources* **2008,** 175, (1), 686-691.

52. Gao, Z.-D.; Han, Y.; Wang, Y.; Xu, J.; Song, Y.-Y. *Sci. Rep.* **2013,** 3, 3323.

53. Gupta, T.; Kim, A.; Phadke, S.; Biswas, S.; Luong, T.; Hertzberg, B. J.; Chamoun, M.; Evans-Lutterodt, K.; Steingart, D. A. *J. Power Sources* **2016,** 305, 22-29.

54. Chamoun, M.; Hertzberg, B. J.; Gupta, T.; Davies, D.; Bhadra, S.; Van Tassell, B.; Erdonmez, C.; Steingart, D. A. *NPG Asia Mater.* **2015,** 7, (4), e178.

55. Zamarayeva, A. M.; Gaikwad, A. M.; Deckman, I.; Wang, M.; Khau, B.; Steingart, D. A.; Arias, A. C. *Adv. Electron. Mater.* **2016,** 2, (5), 1500296.

56. R Mainar, A.; Leonet, O.; Bengoechea, M.; Boyano, I.; Meatza, I.; Kvasha, A.; Guerfi, A.; Alberto Blázquez, J. *Int. J. Energy Res.* **2016**, 1032–1049.

57. Park, J.; Park, M.; Nam, G.; Lee, J. s.; Cho, J. *Adv. Mater.* **2015,** 27, (8), 1396-1401.

58. Zeng, Y.; Zhou, X.; An, L.; Wei, L.; Zhao, T. *J. Power Sources* **2016,** 324, 738-744.

59. Zidan, R. A.; Takara, S.; Hee, A. G.; Jensen, C. M. *J. Alloys Compd.* **1999,** 285, (1), 119-122.

60. Li, Q.; Bjerrum, N. J. *J. Power Sources* **2002,** 110, (1), 1-10.

61. Futaba, D. N.; Hata, K.; Yamada, T.; Hiraoka, T.; Hayamizu, Y.; Kakudate, Y.; Tanaike, O.; Hatori, H.; Yumura, M.; Iijima, S. *Nat. Mater.* **2006,** 5, (12), 987-994.

62. Simon, P.; Gogotsi, Y. *Nat. Mater.* **2008,** 7, (11), 845-854.

63. Yu, G.; Hu, L.; Liu, N.; Wang, H.; Vosgueritchian, M.; Yang, Y.; Cui, Y.; Bao, Z. *Nano Lett.* **2011,** 11, (10), 4438-4442.

64. Park, B.-O.; Lokhande, C.; Park, H.-S.; Jung, K.-D.; Joo, O.-S. *J. Power Sources* **2004,** 134, (1), 148-152.

65. Feng, L.; Zhu, Y.; Ding, H.; Ni, C. *J. Power Sources* **2014,** 267, 430-444.

66. Wang, H.; Liang, Y.; Gong, M.; Li, Y.; Chang, W.; Mefford, T.; Zhou, J.; Wang, J.; Regier, T.; Wei, F. *Nat. Commun.* **2012,** 3, 917.

67. Rakhi, R.; Chen, W.; Cha, D.; Alshareef, H. N. *Nano Lett.* **2012,** 12, (5), 2559-2567.

68. Higashi, S.; Lee, S. W.; Lee, J. S.; Takechi, K.; Cui, Y. *Nat. Commun.* **2016,** 7, 11801.

69. Palacin, M. R. *Chem. Soc. Rev.* **2009,** 38, (9), 2565-2575.

70. Majeau-Bettez, G.; Hawkins, T. R.; Strømman, A. H. *Environ. Sci. Technol.* **2011,** 45, (10), 4548-4554.

71. Marom, R.; Amalraj, S. F.; Leifer, N.; Jacob, D.; Aurbach, D. *J. Mater. Chem.* **2011,** 21, (27), 9938-9954.

72. Conway, B. E., *Electrochemical supercapacitors: scientific fundamentals and technological applications*. Springer Science & Business Media: 2013.

73. Barzegar, F.; Bello, A.; Momodu, D.; Dangbegnon, J.; Taghizadeh, F.; Madito, M.; Masikhwa, T.; Manyala, N. *RSC Adv.* **2015,** 5, (47), 37462-37468.

CHAPTER 7

STRETCHING ION CONDUCTING POLYMER ELECTROLYTES: *IN-SITU* CORRELATION OF MECHANICAL, IONIC TRANSPORT, AND OPTICAL PROPERTIES[1]

Andrew S. Westover,[1,2] *Farhan Nur Shabab,*[1] *John Wenpu Tian,*[1] *Shivaprem Bernath,*[1] *Landon Oakes,*[1,2] *William R. Erwin,*[3] *Rachel Carter,*[1] *Rizia Bardhan,*[2,3] *and Cary L. Pint*[1,2]

[1]Department of Mechanical Engineering, Vanderbilt University, Nashville, TN 37235.

[2]Interdisciplinary Materials Science Program, Vanderbilt University, Nashville, TN 37235

[3]Department of Chemical and Biomolecular Engineering, Vanderbilt University, Nashville, TN 37235

Abstract: In this work we perform mechanical stretching tests while monitoring optical and ionic transport properties of ion-intercalated semi-crystalline polyethylene-oxide (PEO) electrolytes *in-situ*. Utilizing ionic liquid ($EMIBF_4$) – PEO electrolytes, we demonstrate a correlation between the degree of crystallinity, which depends on the ion concentration, and the Young's modulus, ultimate tensile strength, and yield stress. Upon stretching solid-state PEO electrolytes, we observe an anisotropic increase in ionic conductivity that we correlate to the optical polarized Raman spectroscopic and microscopic signatures of polymer domain alignment - especially notable in the plastic regime. *In-situ* Raman spectroscopic studies indicate mechanically-induced ionic transport effects originate from chemical and structural rearrangement of polymer chains, and are independent of the ion species utilized. To emphasize this, we demonstrate the ideas of this study to be similarly transferrable to $LiPF_6$ and LiI/I_2 intercalated PEO solid-state electrolytes which exhibit similar mechanical-ionic transport response as ionic liquids. This study lays the groundwork for studying the mechanochemistry of solid-state electrolytes, with relevance toward specific electrolyte configurations employed in supercapacitors, lithium ion batteries, and dye sensitized solar cells.

This work was originally published in **J. Electrochem. Soc., 161, E112-E117, Apr. 2014** and is reproduced with permission. © *Journal of the Electrochemical Society (2014)* DOI: 10.1149/2.035406jes

7.1 Introduction

A key challenge for future energy storage and conversion systems is the development of fully integrated, mechanical load-bearing device architectures. Such devices require both a solid-state electrolyte and active material coupled to the electrolyte with mechanical integrity under normal operating conditions.[2-5] For this reason, polymer electrolytes have received considerable attention due to the analog between a fully solid-state storage system and a conventional reinforced composite material, where the polymer plays the role of enabling mechanical rigidity and also allowing ions to shuttle between electrodes. Solid-state polymer electrolytes also increase device safety and lower environmental impact since they are air-stable and involve no toxic, volatile species. These solid state electrolytes are central to the development of next-generation energy storage and conversion devices, and in particular supercapacitors,[6-15] metal-ion and metal-air batteries,[2, 16-22] and dye-sensitized solar cells.[20, 23-27] Each of these device platforms requires an electrolyte permitting ion transport between electrodes, and general understanding of processes in these materials impacts devices capable of fast charge-discharge operation, energy storage capability *on par* with fossil fuels, and low-cost solar energy conversion devices, respectively. In each of these cases using solid state electrolytes is imperative to ensure a modicum of thermal stability, simplicity in packaging, and most importantly to provide a strong mechanical interface between the active materials.

Many materials have been suggested for solid state electrolytes. The majority of these materials involve ion-intercalated polymers, such as polyethylene oxide (PEO), polyacrylonitrile (PAN), or polyvinylalcohol (PVA) intercalated with ionic liquids (IL) or other salts.[28-32] Among these, PEO is a good candidate for solid state electrolytes due to its relative thermal and electrochemical stability and mechanical strength. The advantage of using ILs is that they exhibit a high ionic conductivity (.001-100 mS/cm),[27-35] are considered "green" due to their virtually zero vapor pressure in air, and exhibit electrochemical stability windows often greater than 4 V. [34, 36] Using these polymer-IL electrolytes, it is possible to create a stable solid-state electrolyte that simultaneously maintains a high ionic conductivity and a structurally sound interface between the electrodes and the electrolyte.

There have been several studies that have successfully developed, and reported on the ionic, thermal, and optical properties of these solid state polymer/IL electrolytes.[28-32, 37, 38] However, there has been little characterization of the mechanical-chemical effects in such materials despite their basic function as mechanical interfaces between the active materials that store charge in a device. Previous studies have demonstrated that the addition of IL into PEO results in a decrease in the polymer crystallinity,[28, 39] which can be expected to impact the polymer mechanical properties, even though this has not yet been fully explored. Although it has been shown that an applied stress can result in irreversible changes that increase ionic conductivity in PEO/LiI,[40, 41] the origins of such changes during loading have not been studied. It is therefore imperative for practical use of polymer electrolytes in solid-state integrated energy storage systems to understand the role of mechanical forces on both the structural and ionic conducting character of the polymer.

In this spirit, we report here a study focused on the mechanical properties of solid-state polyethylene oxide (PEO) polymers intercalated with varying ions, and ion concentrations. We couple simultaneous mechanical, ionic conductivity, and optical Raman spectroscopic testing to develop a mechanistic understanding of the correlation between mechanical stresses, ionic conductivity, and the microscopic and macroscopic structure of the polymer electrolyte. We observe tunable mechanical and ionic conductivity properties that can be engineered to a specific device specification, and a clear correlation between structural, chemical, and ion transport properties when a stress is applied to the material. This effort provides a mechanistic foundation to the development of practical, fully solid-state polymer-based energy devices.

7.2 Experimental Methods

The polymer electrolytes were synthesized using a solution casting method.[28-31] PEO (M.W. = 1,000,000 Fisher Scientific) was dissolved in propylene carbonate (Sigma Aldrich), and placed on a hot plate at 50˚C and stirred until viscous. At this point the ionic liquid, either EMIBF$_4$ (98%, Sigma) or EMIHSO$_4$ (98%, Sigma) was added and mixed followed by casting of the solution onto a glass petri dish.

The solution was then placed under vacuum at 50˚ C until the polymer solidified. The PEO/$LiPF_6$ and PEO/LiI/I_2 polymers were synthesized using the same method as for $EMIBF_4$ based polymers except the IL was replaced by $LiPF_6$ and LiI/I_2/Tetrabutylpyrridine (TBP) respectively. Following the fabrication of the polymers, ionic conductivity measurements were obtained by performing electrochemical impedance spectroscopy (EIS) tests on approximately 1cm x 6cm x 1mm thin films with stainless steel electrodes attached at either end using a Metrohm Autolab Multichannel analyzer with frequencies ranging from 1 MHz to 10 mHz around 0 bias with a signal amplitude of 10 mV. X-ray diffraction measurements were taken using a Scintag X-1 Powder X-Ray Diffractometer with Cu k-alpha radiation (1.5418 Å). Crystallite size was determined using Scherrer's equation[42] on the crystalline PEO peak at 19.5º assuming a Scherrer's constant of .94. Degree of crystallinity was determined by dividing the integrated area under the crystalline peaks by the total integrated area under both the crystalline peaks and the amorphous peak ranging from 15º to 30º.[43, 44]

Tensile testing measurements were performed by using a homebuilt apparatus enabling the application of a controlled force along the long-axis of PEO polymer strips. In order to achieve accurate mechanical and ionic conductivity measurements, the polymer sample was cut into thin rectangular strips approximately 1cm in width, and 6cm in length connected at both ends using conductive clamps that also served as EIS electrodes. To apply tensile force, a controllable load was applied to one conductive clamp while the other remained anchored. EIS measurements were taken *in-situ* during the application of tensile force to characterize the electrochemical-mechanical response. For perpendicular conductivity measurements silver paint was applied along both edges of the polymer to obtain conductivity measurements across the entire polymer. Raman spectroscopy measurements were taken using a Renishaw inVia MicroRaman system with 785nm laser excitation. *In-situ* Raman studies were performed by assembling the apparatus utilized for PEO-ionic liquid tensile tests inside of the Raman spectrometer. In order to ensure that the Raman measurements were comparable, the intensities were normalized to the CH_2 stretching mode for the PEO chains at 1479 cm^{-1} peak in the initial spectra, and to the BF stretching peak at 778 cm^{-1} in the in-situ and polarized Raman measurements.

7.3 Results and Discussion

Prior to combined mechanical, ionic transport, and optical testing of the PEO-ionic liquid materials, we first assessed the properties of PEO intercalated with different concentrations of $EMIBF_4$ ionic liquid electrolyte. **Figure 7.1** shows characterization of the polymers with different ionic liquid concentrations. Ionic conductivity measurements of PEO/$EMIBF_4$ polymer electrolytes emphasize an increase in ionic conductivity linearly with $EMIBF_4$ concentration, with conductivities ranging from .1 to 1.6 mS/cm. These conductivities are consistent with that observed for other IL polymer conjugates,[28-32] including the observed values of .5-.6 mS/cm for ~30% IL PEO/$EMIBF_4$ polymers observed by Lewandowski *et al.*[31] Raman spectra were collected both for pure and mixed PEO/$EMIBF_4$ (**Figures 7.1b**). The PEO and $EMIBF_4$ Raman spectra are consistent with those found in literature for these materials, and PEO/$EMIBF_4$ Raman

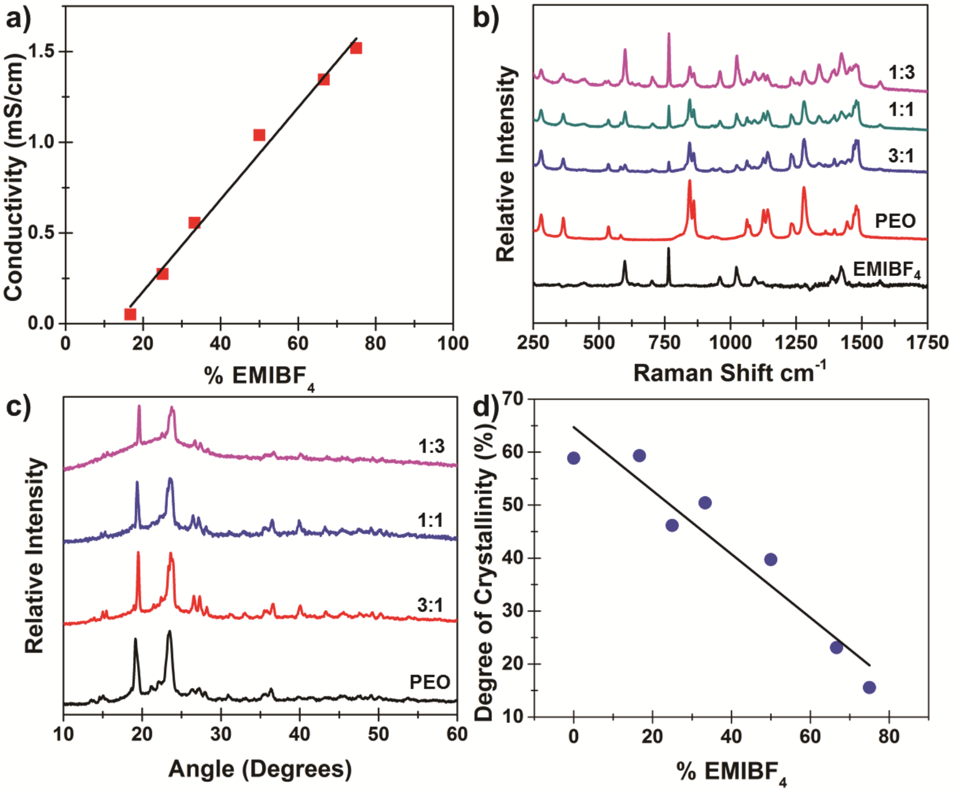

Figure 7.1 (a) Conductivity vs. ionic liquid concentration in PEO/$EMIBF_4$ films. (b) Raman spectra of pure $EMIBF_4$, pure PEO film, and PEO/$EMIBF_4$ 3:1, 1:1, and 1:3 films. (c) XRD data for polymers for 100% PEO, and PEO/$EMIBF_4$ 3:1, 1:1, and 1:3 films. (d) Degree of crystallinity determined form XRD spectra in (c).

spectra clearly show a combination of both the PEO and EMIBF$_4$ spectra.[45-49] It is significant to note that no new Raman peaks are observed, and there are no significant changes in Raman peak location as the percentage of IL is increased.. We also observe that as the IL % is increased, the normalized intensity of the EMIBF$_4$ Raman peaks steadily increases. This can be attributed to the change in the relative amount of EMIBF$_4$ and PEO in each film. A complete listing of all Raman peaks can be found in the appendix.

PEO generally forms a semi crystalline complex of single phase crystalline spherulites interconnected by amorphous regions.[50] XRD of PEO films (**Figure 7.1c**) show that there are two sharp peaks at 19.5º and 24º due to the crystalline portion of the polymer, and a broad peak ranging from 15º to 30º due to the amorphous portion of the polymer film. The degree of crystallinity of these peaks, which is obtained through a ratio of the crystalline to non-crystalline peak areas, decrease as more IL is added (**Figure 7.1d**). This decrease in crystallinity is correlated to the increase in conductivity with IL concentration observed in **Figure 7.1a**. [28, 39, 51] We also calculated the crystallite size (appendix) finding that it ranged from 10-40 nm.

To understand the correlation between solid-state PEO/EMIBF$_4$ ionic transport properties and tensile strength, we performed tensile measurements with an incremental application of stress (**Figure 7.2a**) while monitoring the ionic conductivity *in-situ*. In these measurements, a clear elastic region exists under the application of small stresses, whereas a plastic region emerges as the applied load, (*i.e.* strain) increases, exhibiting behavior consistent with pure PEO materials.[52, 53] These curves enabled the analysis of ultimate tensile stress and yield stress (**Figure 7.2b**), which both fell into the range of .2-4.5 MPa. The Young's modulus was also measured with a range of 2-50 MPa, roughly 10 times greater than the ultimate tensile stress. With increasing IL concentration the yield stress, ultimate tensile stress, Young's modulus, and percent elongation all decreased in a roughly exponential fashion. This decrease in the mechanical properties is also exponentially correlated with the decrease in the crystallinity of the polymers (**Figure**

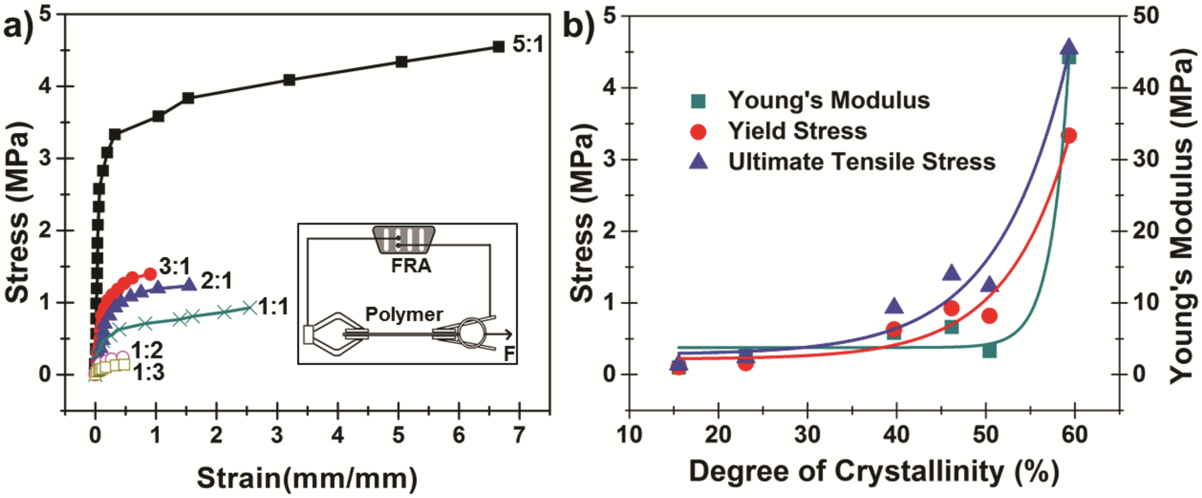

Figure 7.2 (a) Stress-strain plots of polymers of different compositions, with PEO/EMIBF4 ratio labeled. Inset shows basic schematic of tensile testing setup. (b) Yield stress (left axis), ultimate tensile stress (left axis), and Young's Modulus (right axis) as a function of degree of crystallinity, with their corresponding exponential fits.

7.2b). Comparing these results to ionic conductivities measured on polymers without loading (**Figure 7.1a**) emphasizes that whereas the ionic conductivity increases linearly with IL concentration, the mechanical properties degrade exponentially. This may indicate that for devices that require mechanical integrity, but not the capability for high power (*e.g.* metal-ion batteries), a lower IL concentration may be ideal. However, for high power applications (*e.g.* supercapacitors) and moderate mechanical properties, a 50% or greater concentration of IL may be a better choice.

Before further discussing results from *in-situ* conductivity measurements obtained during mechanical testing, we analyzed the physical mechanisms associated with elongation and breaking in PEO/EMIBF$_4$ films with different IL concentrations. As shown in **Figure 7.3a-d**, two different elongation behaviors are observed. Films containing less than 50% IL exhibited a tendency to neck, with the necking extending along the entire length of the polymer just prior to breaking, similar to pure PEO materials. Polymers containing greater than 50% IL initially started to neck in a manner similar to the lower concentration samples, but rapidly developed large voids that led to premature material failure. The difference between these two mechanisms is illustrated in **Figure 7.3a-d**, where **Figure 7.3a** and **7.3b** correspond to the 1:1 polymer, and **Figure 7.3c** and **7.3d** correspond to the 2:1 polymer. In these pictures, both polymers are shown at the yield stress and just before failure respectively. This emphasizes that the low degree of crystallinity in the high $EMIBF_4$ concentration polymer electrolytes promotes the nucleation of voids prior to failure that lead to premature mechanical failure and poor mechanical integrity under stress. This underlines the importance of engineering the performance of ion conducting polymers without compromising the mechanical integrity of these materials.

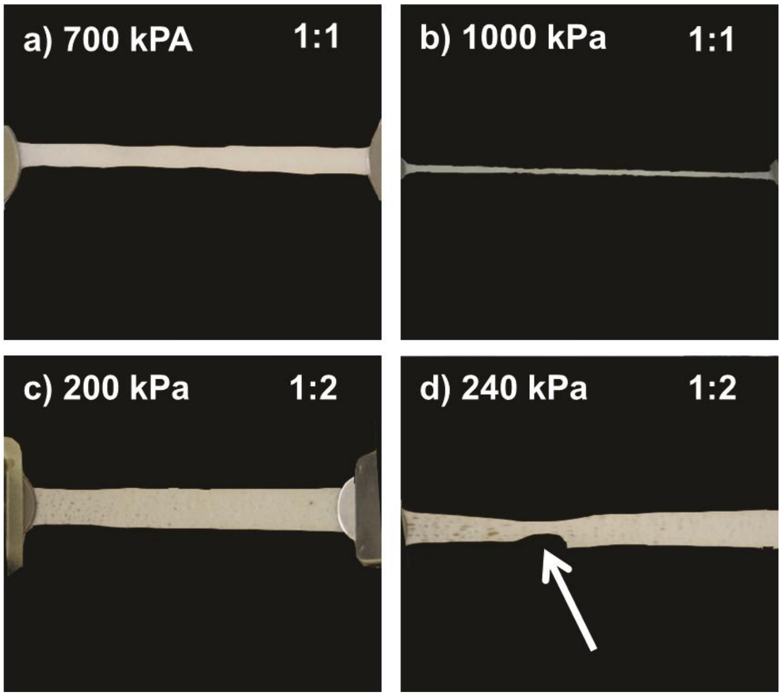

Figure 7.3 PEO/$EMIBF_4$ polymers in tension. (a) PEO/$EMIBF_4$ 1:1 at yield stress. (b) PEO/$EMIBF_4$ 1:1 just before failure. (c) PEO/$EMIF_4$ 1:2, at yield stress. (d) PEO/$EMIBF_4$ 1:2 just before failure. Arrow points to failure location.

In this spirit, *in-situ* analysis of ionic conductivity was recorded during tensile measurements to ascertain the role of an applied stress on the conductivity (**Figure 7.4**). Each of the PEO/$EMIBF_4$ polymers is observed to exhibit an initial linear increase in conductivity followed by a transition to an exponential increase upon continued applied stress. Comparing **Figure 7.4** to corresponding tensile test results presented in **Figure 7.2**, the transition between the linear and exponential regions are observed to correspond approximately to the yield stress of the polymers. Additionally, just prior to failure, a few of the samples exhibit a sharp decrease in conductivity. This is ascribed to partial failure at a point where the polymer still remains in-tact, but some of the regions exhibit local failure that breaks ionic conduction pathways and lowers the conductivity. A similar increase in conductivity before and after stretching of a PEO/LiI polymer was observed by Chung et al,[40] emphasizing enhanced ionic conductivity after elongation. *In-situ* perpendicular conductivity tests on a 1:1 polymer demonstrate the emergence of anisotropy in the

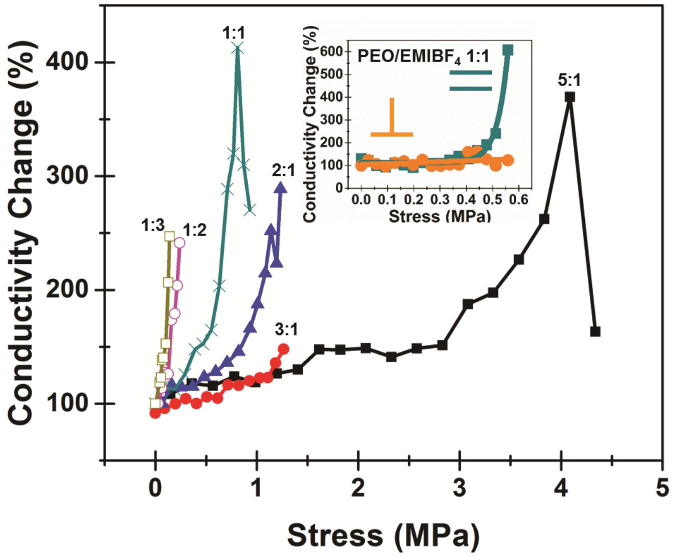

Figure 7.4 Change in ionic conductivity with applied stress for PEO/EMIBF$_4$ films of varying concentrations. The inset shows a change in conductivity for a PEO/EMIBF$_4$ 1:1 film for the ionic conductivity both parallel (cyan) and perpendicular (orange) to the tensile

conductivity (inset in **Figure 7.4**). Whereas the conductivity along the tensile axis increases exponentially, the conductivity perpendicular to the tensile axis shows little to no change in the conductivity.

In order to explore the reversibility of the conductivity change, we also performed a measurement where we cycled a small tensile force within the elastic regime, finding that within this elastic regime the increase in ionic conductivity is reversible (appendix). We also performed a one-time static measurement on a polymer that had been stretched well into the plastic regime before releasing the force, finding a permanent increase in the ionic conductivity of 350%. These two measurements combine to show that within the elastic regime ionic conductivity increases are reversible, but in the plastic regime corresponding increases in conductivity are permanent.

Visual analysis of the PEO/EMIBF$_4$ 1:1 polymer under an optical microscope (**Figure 7.5a**) before and after stretching clearly shows a mechanically induced alignment of domains within the polymer. Prior to stretching, the polymer exists in semi-crystalline state with randomly oriented domains and no visible signature of domain alignment. Following stretching, aligned polymer domains are observed along the axis in which a tensile stress is applied. (Further images are contained in the appendix) This suggests that stretching the polymer causes the chains to unwind and form ordered aligned domains that extend along the length of the polymer. XRD measurements of the polymer before and after stretching (**Figure 7.5b**) show a dramatic decrease in the crystallite size from ~29 to 9 nm, and a moderate increase in

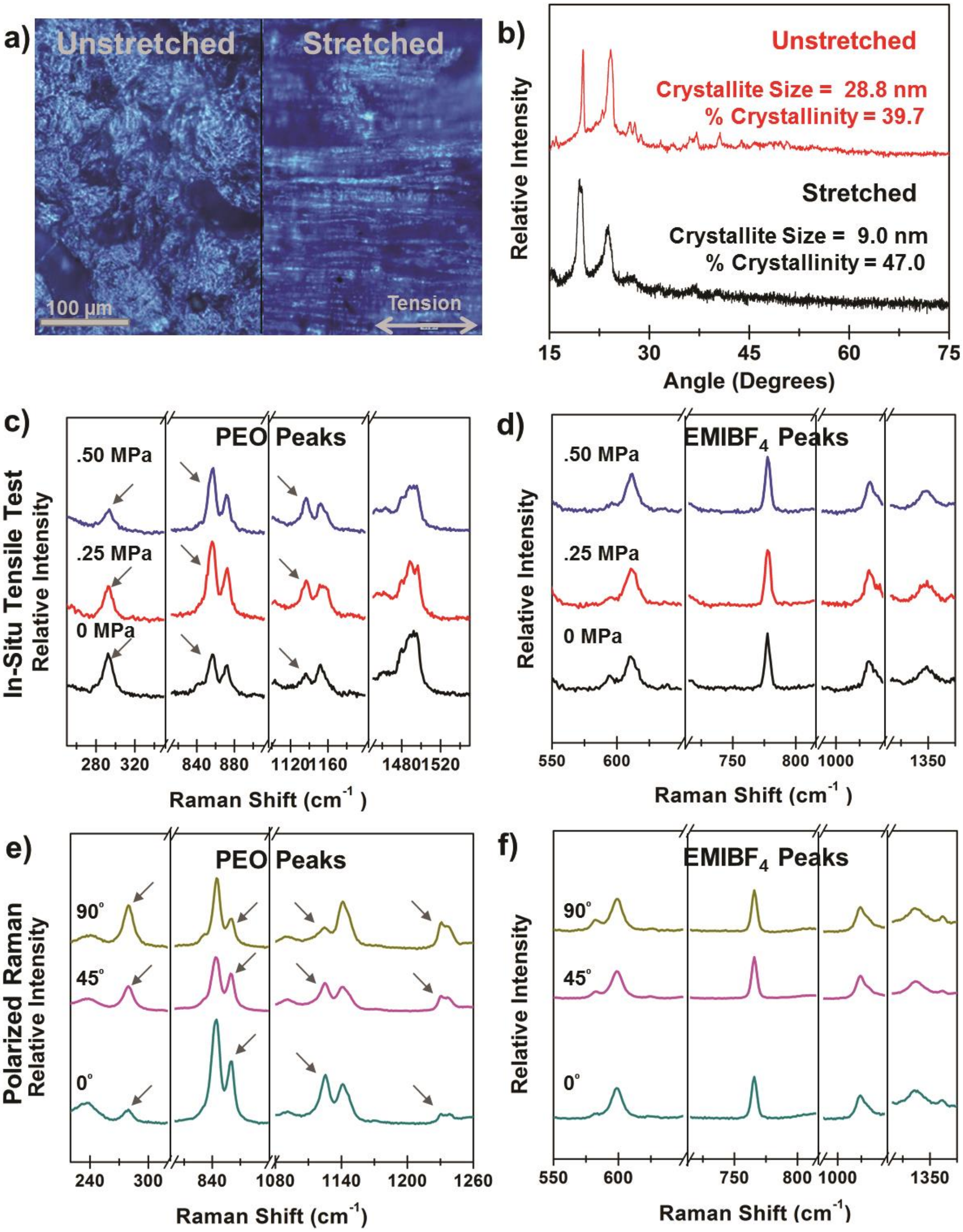

Figure 7.5 (a) Optical microscope images at 20x magnification of the unstretched (left) and stretched (right) with arrow to indicate direction of applied stress. (b) XRD data for a PEO/EMIBF$_4$ 1:1 polymer with the corresponding crystallite size and degree of crystallinity noted. (c-f) Raman spectra of 1:1 PEO/EMIBF$_4$ film, (c-d) under tension (*in-situ*), at 0, .25 MPa, and .50 MPa, with main PEO (c) and EMIBF$_4$ (d) peaks shown and (e-f) after stretching using polarized Raman showing (e) PEO and (f) EMIBF$_4$ primary stretch modes.. 0° represents polarization along the tension axis, and 90° represents polarization perpendicular to tension axis.

the degree of crystallinity of about 8%. This increase in crystallinity, and decrease in crystallite size support the notion that the tensile forces causes the polymers to unwind and form long aligned domains. In addition we do not see any apparent phase separation before or after stretching in the optical microscope as is often observed in polymer blends.[54]

In order to further investigate this change in microstructure we performed both *in-situ* Raman spectroscopy on PEO-EMIBF$_4$ films under a tensile force (**Figure 7.5c-d**), and polarized Raman spectroscopy on a stretched (**Figure 7.5e-f**) and unstretched film (appendix). Under the application of tensile stress, we observed several PEO peaks to exhibit changes in measured peak intensity, with no observed corresponding changes in the EMIBF$_4$ peak intensities. Most notably we observed decreases in the peak intensity at 279 cm^{-1} and at 1479 cm^{-1}, corresponding to COC bending and CH$_2$ bending respectively, and an increase in peak intensity at 844 cm^{-1} and 1126 cm^{-1} corresponding to CH$_2$ rocking and COC stretching respectively (all peaks correlated to PEO features). In addition we observed no change in the major EMIBF$_4$ peaks located at 611 cm^{-1}, 778 cm^{-1}, 1025 cm^{-1}, and 1348 cm^{-1}.

Polarized Raman spectroscopy on the stretched and unstretched 1:1 PEO/EMIBF$_4$ polymer showed similar results to that of the *in-situ* Raman spectroscopy. Polarized Raman microscopy was performed by polarizing the incident laser excitation and rotating the stretched polymer from 0^o to 90^o (see **Figure 7.5e-f**) with 0^o representing light polarized along the axis of stretching, and 90^o representing light polarized perpendicular to the polymer chain alignment. While we observed that the major EMIBF$_4$ peaks again show no preferential direction after stretching, we observed that the PEO peaks at 279 cm^{-1}, and 1235 cm^{-1} corresponding to COC bending and CH$_2$ twisting were more intense perpendicular to the tensile axis, and that the PEO peaks at 860 cm^{-1} and 1126 cm^{-1}, corresponding to COC stretching, and CC stretching respectively, were more intense along the tensile axis clearly showing that an anisotropy in the structure of the polymer chains has been induced by the application of tensile force. This is in direct contrast to the PEO peaks in the unstretched case that show no preferential direction (appendix).

These chemical changes within the polymer films as a force is applied emphasize that the mechanically induced anisotropy that is visually apparent occurs not just on the macroscopic scale observed in optical microscopy images, but occurs on a microscopic and even a molecular level as well, further suggesting that the mechanism responsible for the increase in ionic conductivity is related to structural anisotropy within the PEO films that are induced as a force is applied, and is independent of the ion species. It is well understood that as a force is applied to a polymer such as PEO, the large tangled polymer domains tend to unwind and stretch uniaxially in the direction of force resulting in plastic deformation prior to failure, as observed in **Figure 7.2**. Since the polymer structure provides the medium for ion transport in this material, the alignment of the polymers, generates a more direct path for ion transport, resulting in a corresponding increase to the ionic conductivity measured *in-situ* along the aligned direction. This notion is supported in the literature[55] suggesting that regions between aligned polymer chains (domain walls) act to inhibit the ionic conduction through the polymer material. Furthermore, previous studies showed that the use of a 6 T magnetic field can induce polymer alignment that yields enhanced ionic conductivity,[56] whereas other studies have also emphasized the role the polymer structure can play in influencing or controlling ionic conductivity.[57-63]

So far, the focus of our studies has been centered on a single IL ($EMIBF_4$) intercalated into a PEO matrix. However, results from Raman spectroscopic studies emphasize the changes to ionic conductivity

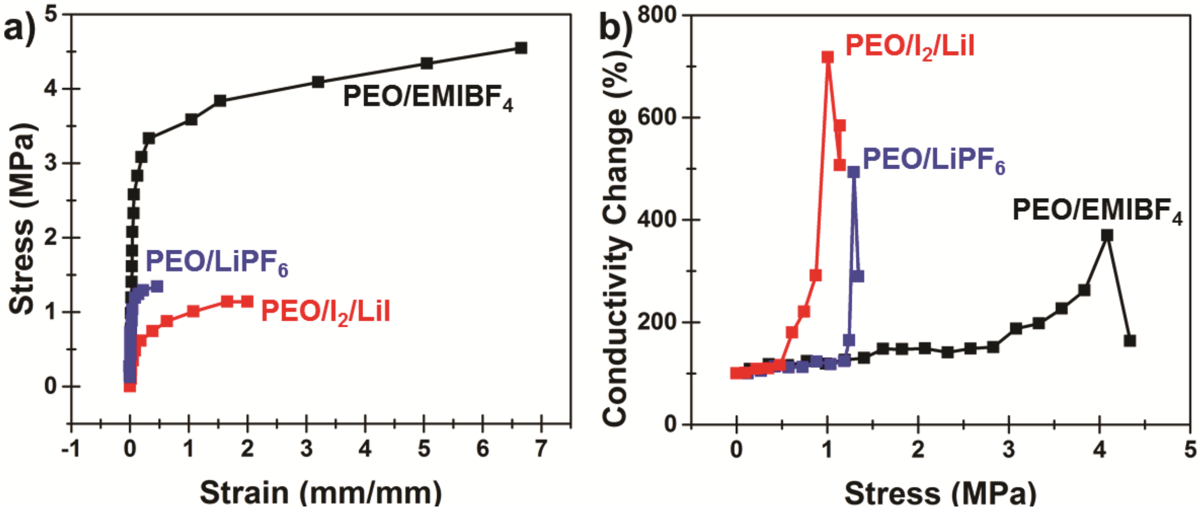

Figure 7.6 (a) Comparison of stress strain behavior for PEO/$EMIBF_4$ 5:1 and PEO/$LiPF_6$ 5:1, and PEO/LiI/I_2 5:1 films. (b) Comparison in conductivity behavior under an applied stress for the same PEO/$EMIBF_4$ 5:1 and PEO/$LiPF_6$ 5:1, and PEO/LiI/I_2 5:1 films.

under an applied stress are independent of the ion species in the PEO structure. To further analyze this result, we also performed simultaneous mechanical and EIS measurements of PEO-$LiPF_6$, and PEO-LiI-I_2 polymer films, which are suitable electrolytes for lithium ion batteries and dye sensitized solar cells respectively. **Figure 7.6** shows a comparison of the tensile loading behavior of PEO/$EMIBF_4$ 5:1 discussed previously in comparison to PEO/$LiPF_6$ 5:1 and PEO/LiI/I_2 with a total ratio of 5 PEO to 1 LiI, $I_{2,}$ and TBP. All three films exhibit similar mechanical properties with individual tensile strengths attributed to differences in the ion species chemical and physical make up. The ionic conductivity of PEO/$LiPF_6$, and PEO/LiI/I_2 (**Figure 7.6b**) both show the same trend as PEO/$EMIBF_4$ in that as tensile stress is applied, the conductivity increases linearly in the elastic region, and exponentially in the plastic region. This validates the results of in-situ Raman spectroscopic measurements which emphasize that changes to ionic conductivity of the polymer-IL electrolytes can be explained fully by the corresponding change in the microstructure of the PEO polymer chains and are invariant with a changing ion species.

This study therefore provides a general framework for understanding the correlation of mechanical properties and ionic transport characteristics in solid-state polymers that is critical for the development and optimization of fully solid-state structures that can be integrated or load-bearing, and currently remains unexplored. Our work is directly applicable to solid-state energy devices, as such devices involve two active electrodes requiring ion transport through a solid-state polymer. Our experimental setup is therefore a model system for this configuration, and our measurement of the effects of tensile force isolates this component in any applied mechanical stress as being the most relevant for ion transport between the two electrodes (appendix **Figure 7.A10**). This is due to the notion that tensile properties of polymers are not geometry dependent, and our measurement technique eliminates tensile behavior associated with electrode/electrolyte interfaces. As a result, our measurements elucidate a route to both (*i*) assess and understand the changes in ion-conducting polymers operating in devices under exposure to mechanical stresses, and (*ii*) enable engineering platforms manipulating the electrolyte mechanochemistry to specifications outside of static ion conducting polymer performance. As PEO-based electrolytes exhibit significant commercial promise, our work demonstrates that one can overcome limiting features for these electrolytes, such as high electrolyte resistance at low ion concentrations and poor mechanical properties at high ion concentrations, by mechanically modulating the polymer chain configuration. As the application of PEO-based electrolytes for high power energy storage systems, such as high power batteries or supercapacitors, involves resistive power loss proportional to the electrolyte resistance, routes to utilize low-cost, scalable platforms and improve energy efficiency of these devices are critical to overcome challenges currently limiting solid-state energy device technology. Our study provides mechanistic insight into the origin of these effects, and highlights a correlation between mechanical, ionic transport, and optical properties that lays the framework for energy applications with improved performance.

7.4 Conclusion

We demonstrate here the fabrication of solid-state ion conducting polymers, specifically PEO/EMIBF_4, PEO/LiPF_6, and PEO/LiI/I_2 and study these materials using complementary techniques of mechanical testing, ionic conductivity measurements, and Raman spectroscopy *in-situ* to correlate mechanical properties, ionic transport properties, and the chemical architecture of the polymer in real time. Our results demonstrate an exponential relationship between the degree of crystallinity of the ion conducting polymer and the mechanical properties such as tensile strength and Young's modulus. Upon an applied tensile stress, we observe a linear reversible increase in ionic conductivity in the elastic regime, and a permanent exponential increase in conductivity in the plastic regime. In-situ Raman studies elucidate the polarization of PEO backbone chains upon stretching that enable more efficient pathways for ion transport in the polymer matrix, but emphasize this effect to be invariant with the ion species utilized. These ionic conducting polymer materials have great promise for a range of solid-state structurally-integrated energy storage and conversion devices, and our work provides insight into the fundamental mechanochemistry that can be engineered to overcome current limiting characteristics of these electrolytes for a broad range of energy device applications.

7.A Appendix

7.A.1 Image of fully formed polymer film

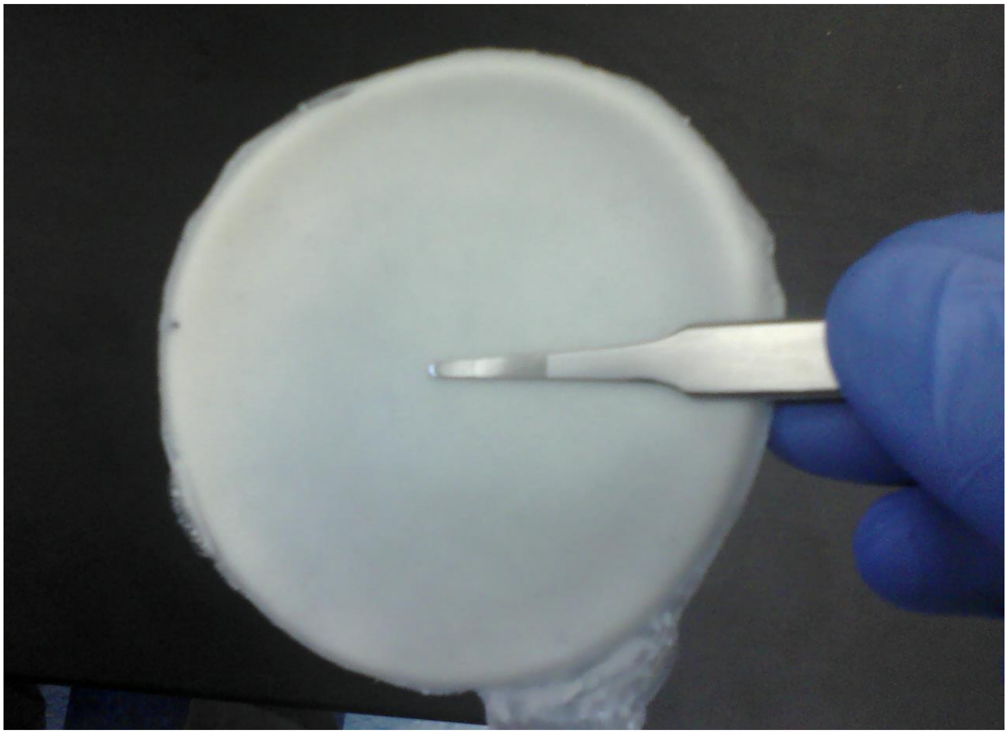

Figure 7.A1 Picture of finished PEO/EMIBF$_4$ film.

7.A.2 Variations in ionic conductivity due to external environmental conditions

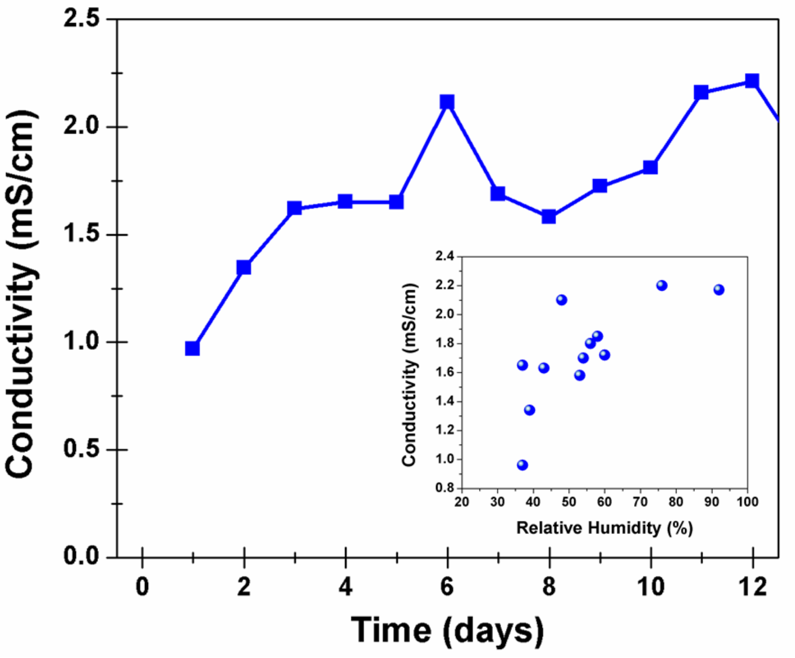

Figure 7.A2 Graph of ionic conductivity of PEO/EMIBF$_4$ 1:1 film over time, with an inset corresponding relative humidity in these measurements to ionic conductivity.

Figure 7.A2 Shows a graph of the ionic conductivity over a period of 12 days. We found that the ionic conductivity changed up to ~230% due to environmental conditions, primarily humidity. Even small changes in the environmental conditions had a noticeable effect on the ionic conductivity.

7.A.3 Complete listing of Raman peak positions, and band identifications

Raman Shift (cm^{-1})			**Band Assignments**	**Reference**
PEO	EMIBF$_4$	PEO/EMIBF$_4$		
234	246	238	COC bend., COC sym. twist., CH_3 bend.	43-45
281	-	279	OCC bend., COC bend., CC twist.	42,45
364	-	364	COC bend., OCC sym. bend.,	42,45
-	443	446	CCH bend., CH_3 bend.	43-44
536	-	536	COC bend., asym. OCC bend.	42,45
583	-	583	OCC asym. bend., COC bend., COC asym. str.	42,45
-	599	600	ring ip sym. bend.	43-44
-	701	702	ring ip bend., CH_3 bend., CH_2 bend.	43-44
-	765	766	BF str.	38-39
846	-	846	CH_2 asym. rock.	42,45
861	-	860	CH_2 sym. rock., COC sym. str.	42,45
934	-	934	CH_2 sym. rock., COC asym. str.	42,45
-	960	959	CC str.	43-44
-	1023	1024	ring sym. str., CH_3 str., CH_2 str.	43-44
1063	-	1064	COC asym. str., CH_2 sym. rock.	42,45
1073	-	1073	COC sym. str., CH_2 sym. rock.,	40-42
-	1092	1091	CC str., ring ip sym. str.	43-44
1127	1123	1126	CC str., COC asym. str., ring HCCH sym. bend., ring sym. str.	43-45
1142	-	1141	CC str., COC sym. wag.	42,45
1232	-	1231	CH_2 sym. twist., CH_2 asym. twist.	42,45
1280	-	1281	CH_2 asym. twist., CH_2 sym. twist., ring ip asym. str., CC bend.	42,45
-	-	1338	ring sym. str., CH_2 bend. (EMI peak)	43-44

1362	-	1362	CH_2 wag., CC str.,	42,45
-	1385	1387	ring ip asym. str., CH_2 bend.	43-44
1397	-	1396	CH_2 sym. wag., CC str., ring ip asym. Str., CH_2 bend.	42,45
-	1421	1422	ring ip asym. str., CH_2 bend.	43-44
1444	-	1443	CH_2 asym. bend., CH_2 sym. bend.	42,45
-	1451	1453	ring ip asym. str.	43-44
1471	-	1470	CH_2 sym. bend., CH_2 asym. bend.	42,45
1479	-	1479	CH_2 asym. bend., CH_2 sym. bend.	42,45
1485	-	1486	CH_2 sym. bend.	42,45
-	1570	1569	ring ip sym. str., CH_3 str., CH_2 str.	43-44

Table 7.A1. Raman band positions of PEO, $EMIBF_4$, and PEO/$EMIBF_4$ from Raman spectra in **Figure 7.1**. In the table the following abbreviations are used: bend.- bending, twist. - twisting, str.- stretching, rock. - rocking, wag. - wagging, sym. - symmetric, asym. - asymmetric, ip - in plane. Ring refers to the central ring in the EMI^+ molecule made up of three carbon, and two nitrogen atoms**.**

7.A.4 XRD Analysis: Crystallite Size

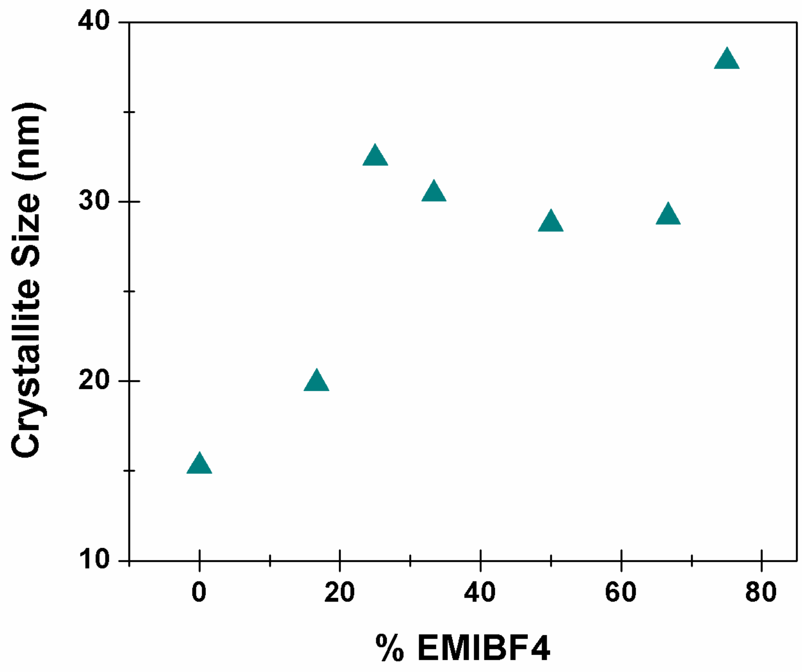

Figure 7.A3 Crystallite size as a function of EMIBF$_4$ loading, derived using Scherrer's equation on the XRD peak at 19.5°.

7.A.5 Mechanical Properties vs. Ionic Liquid Concentration

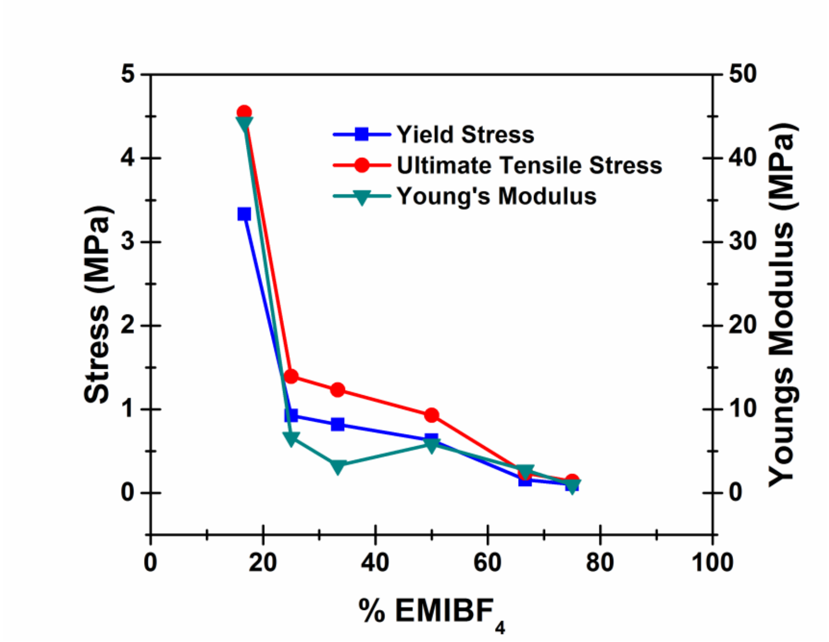

Figure 7.A4 Yield stress, ultimate tensile stress, and Young’s modulus vs. ionic liquid concentration.

7.A.6 Ionic conductivity during in-situ tensile test

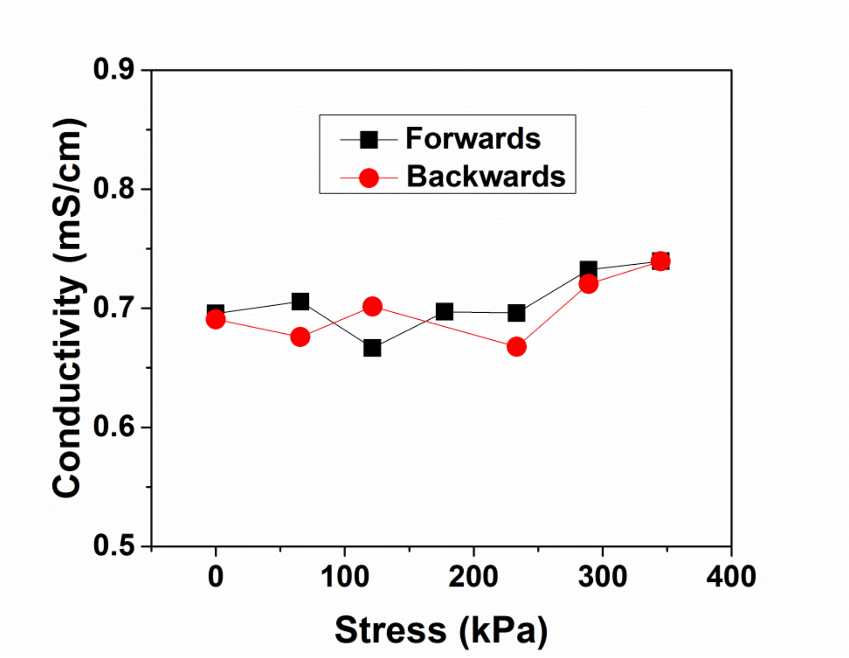

Figure 7.A5 In-situ conductivity during a cyclic tensile test, with black indicating the loading of tensile force, and red indicating the unloading of tensile force.

In addition to the cyclic tensile test within the elastic regime we also did a one-time measurement of the conductivity after stretching well into the plastic regime and then releasing the load. This plastic deformation resulted in a permanent increase in the conductivity of ~350%. These two measurements combine to show that within the elastic regime the conductivity change is reversible, but in the plastic regime permanent changes to the polymer structure cause permanent changes in the conductivity.

7.A.7 Optical microscope images of PEO:EMIBF$_4$ films

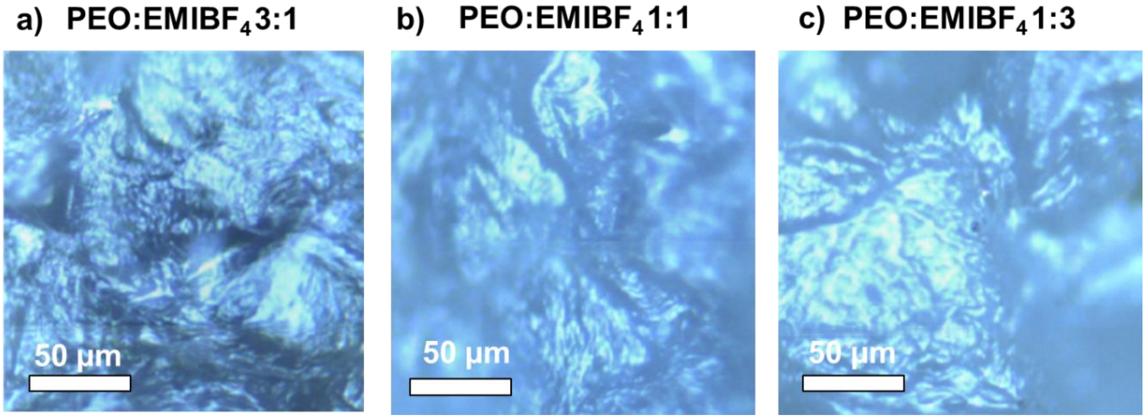

Figure 7.A6 Optical microscope images of PEO:EMIBF$_4$ films with rations 3:1 (a), 1:1 (b), and 1:3 (c).

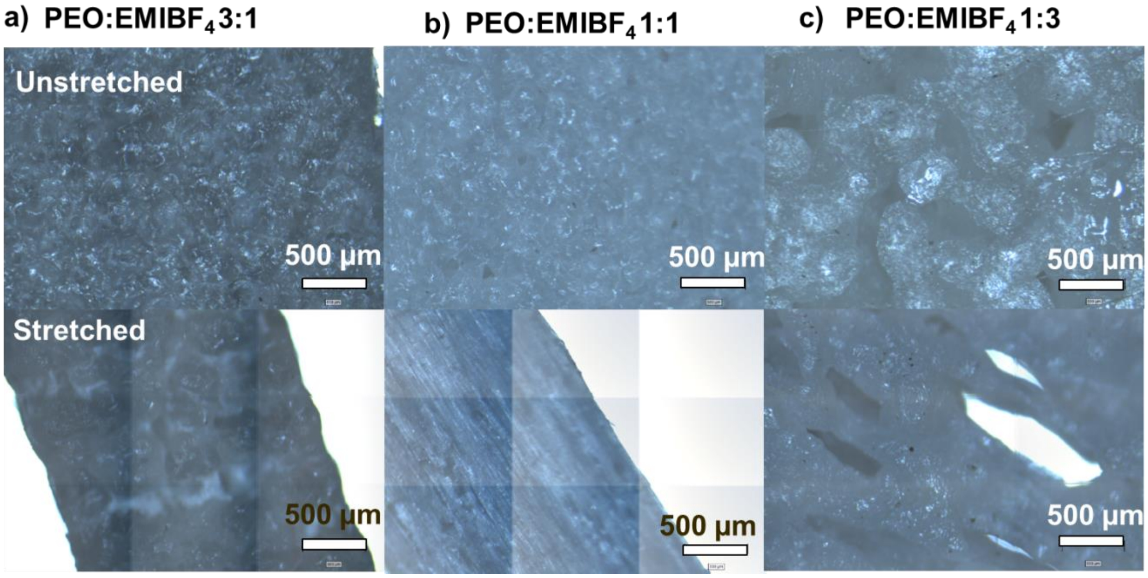

Figure 7.A7 Optical microscope images of PEO:EMIBF$_4$ films before stretching (upper) and after stretching (lower) for films with rations 3:1 (a), 1:1 (b), and 1:3 (c).

7.A.8 Polarized Raman of unstretched PEO/EMIBF$_4$ films

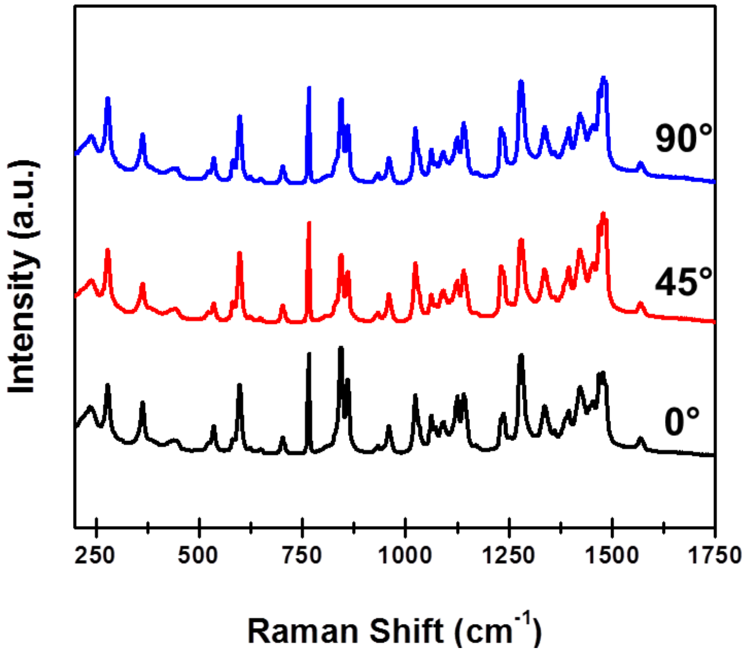

Figure 7.A8 Polarized Raman spectra of unstretched PEO/EMIBF$_4$ 1:1 film. Corollary to **Figure 7.5c**.

The polarized Raman spectra of the unstretched PEO/EMIBF$_4$ 1:1 film shows little to no change as the polarization of the incident light is changed, suggesting that there are no structural differences along the axes of the film. This is in stark contrast to **Figure 7.5c** that shows several peaks that change in intensity as the polarization is changed, confirming that the results in **Figure 7.5c** are due to the stretching of the polymer film, and are not inherent to the material.

7.A.9 Comparison of PEO/EMIHSO$_4$ and PEO/EMIBF$_4$

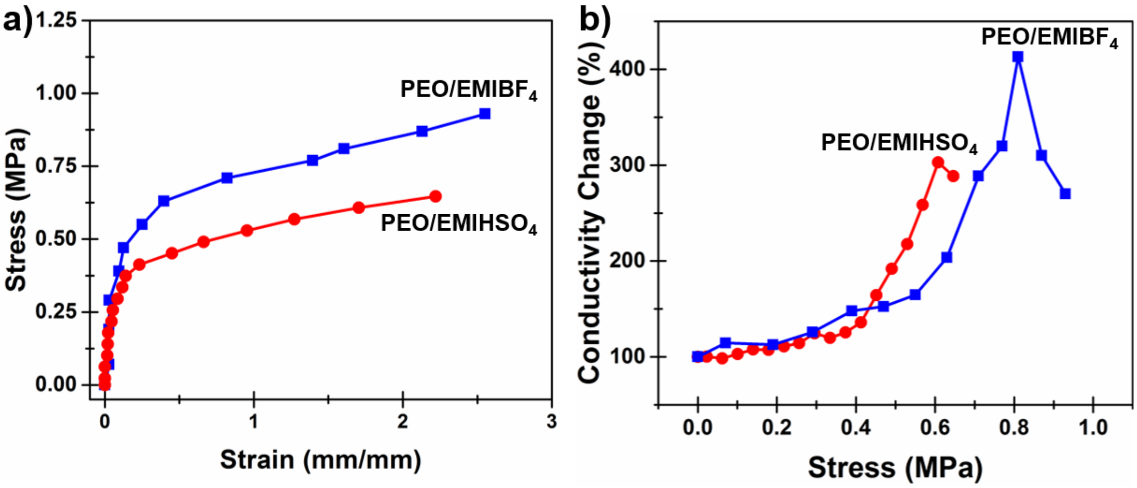

Figure 7.A9 Comparison of PEO/EMIBF$_4$ and PEO/EMIHSO$_4$ polymers mechanical (a) and ionic properties (b) as a tensile stress is applied.

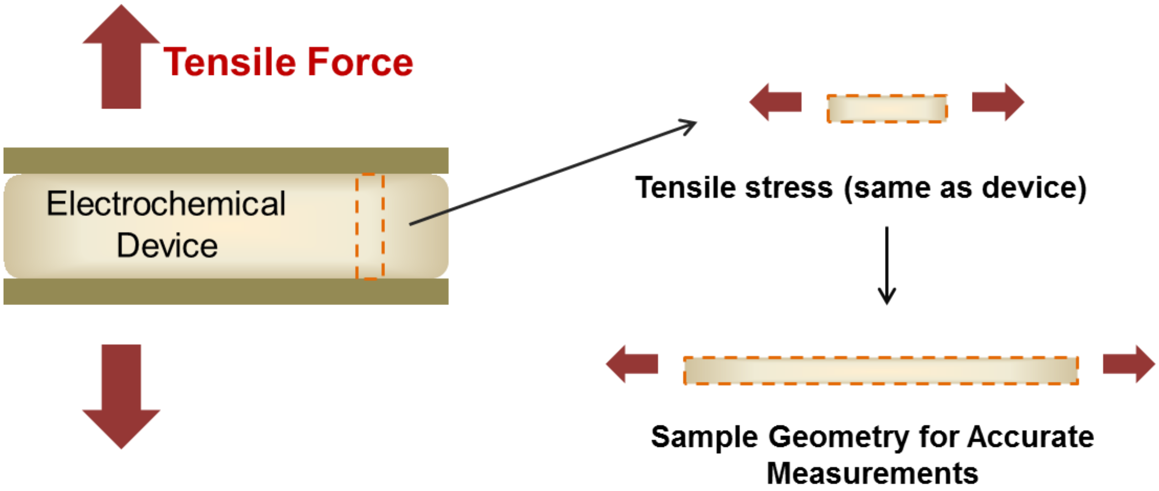

Figure 7.A10 Illustration emphasizing the relation of tensile tests conducted in this study to the device-level geometry of an electrochemical energy storage device. In this configuration, the sample geometry is based on narrow strips of polymer, which overcomes the challenge of mechanical property measurement on a polymer in the device configuration without influence of interfaces/contacts.

Acknowledgements

The authors thank R. Caprara and A. Fauzi for early assistance with PEO material fabrication. This work was supported in part (A.W.) by NSF TNSCORE grant EPS-1004083, Vanderbilt University start-up funds, and the ORAU Powe Award.

References

1. Westover, A. S.; Shabab, F. N.; Tian, J. W.; Bernath, S.; Oakes, L.; Erwin, W. R.; Carter, R.; Bardhan, R.; Pint, C. L. *J Electrochem Soc* **2014,** 161, (6), E112-E117.

2. Song, J. Y.; Wang, Y. Y.; Wan, C. C. *J. Power Sources* **1999,** 77, (2), 183-197.

3. Chen, H. W.; Chiu, C. Y.; Wu, H. D.; Shen, I. W.; Chang, F. C. *Polymer* **2002,** 43, (18), 5011-5016.

4. Yuan, J.; Antonietti, M. *Polymer* **2011,** 52, (7), 1469-1482.

5. Zhao, S. L.; Fu, Z. W.; Qin, Q. Z. *Thin Solid Films* **2002,** 415, (1-2), 108-113.

6. Cao, L.; Xu, F.; Liang, Y. Y.; Li, H. L. *Adv. Mater.* **2004,** 16, (20), 1853.

7. Fan, Z. J.; Yan, J.; Wei, T.; Zhi, L. J.; Ning, G. Q.; Li, T. Y.; Wei, F. *Adv. Funct. Mater.* **2011,** 21, (12), 2366-2375.

8. Gao, H. C.; Xiao, F.; Ching, C. B.; Duan, H. W. *ACS Appl. Mater. Intefaces* **2012,** 4, (12), 7019-7025.

9. Gomez-Romero, P.; Chojak, M.; Cuentas-Gallegos, K.; Asensio, J. A.; Kulesza, P. J.; Casan-Pastor, N.; Lira-Cantu, M. *Electrochem. Commun.* **2003,** 5, (2), 149-153.

10. Hashmi, S. A.; Latham, R. J.; Linford, R. G.; Schlindwein, W. S. *Polym. Int.* **1998,** 47, (1), 28-33.

11. Lee, J. A.; Shin, M. K.; Kim, S. H.; Cho, H. U.; Spinks, G. M.; Wallace, G. G.; Lima, M. D.; Lepro, X.; Kozlov, M. E.; Baughman, R. H.; Kim, S. J. *Nat. Commun.* **2013**.

12. Meng, C. Z.; Liu, C. H.; Chen, L. Z.; Hu, C. H.; Fan, S. S. *Nano Lett.* **2010,** 10, (10), 4025-4031.

13. Meng, F. H.; Ding, Y. *Adv. Mater.* **2011,** 23, (35), 4098.

14. Qian, H.; Kucernak, A. R.; Greenhalgh, E. S.; Bismark, A.; Shaffer, M. S. P. *ACS Appl. Mater. Intefaces* **2013,** 5, 6113-6122.

15. Xu, Y. F.; Wang, Y.; Liang, J. J.; Huang, Y.; Ma, Y. F.; Wan, X. J.; Chen, Y. S. *Nano Res.* **2009,** 2, (4), 343-348.

16. Armand, M.; Tarascon, J. M. *Nature* **2008,** 451, (7179), 652-657.

17. Croce, F.; Appetecchi, G. B.; Persi, L.; Scrosati, B. *Nature* **1998,** 394, (6692), 456-458.

18. Hiralal, P.; Imaizumi, S.; Unalan, H. E.; Matsumoto, H.; Minagawa, M.; Rouvala, M.; Tanioka, A.; Amaratunga, G. A. J. *ACS Nano* **2010,** 4, (5), 2730-2734.

19. MacFarlane, D. R.; Huang, J. H.; Forsyth, M. *Nature* **1999,** 402, (6763), 792-794.

20. Nejati, S.; Lau, K. K. S. *Nano Lett.* **2011,** 11, (2), 419-423.

21. Tigelaar, D. M.; Meador, M. A. B.; Bennett, W. R. *Macromolecules* **2007,** 40, (12), 4159-4164.

22. Tigelaar, D. M.; Meador, M. A. B.; Kinder, J. D.; Bennett, W. R. *Macromolecules* **2006,** 39, (1), 120-127.

23. Akhtar, M. S.; Kwon, S.; Stadler, F. J.; Yang, O. B. *Nanoscale* **2013,** 5, (12), 5403-5411.

24. Freitas, F. S.; de Freitas, J. N.; Ito, B. I.; De Paoli, M. A.; Nogueira, A. F. *ACS Appl. Mater. Intefaces* **2009,** 1, (12), 2870-2877.

25. Li, B.; Wang, L. D.; Kang, B. N.; Wang, P.; Qiu, Y. *Sol. Energy Mater. Sol. Cells* **2006,** 90, (5), 549-573.

26. Shi, C. Z.; Qiu, L. H.; Chen, X. J.; Zhang, H. G.; Wang, L.; Yan, F. *ACS Appl. Mater. Intefaces* **2013,** 5, (4), 1453-1459.

27. Wang, P.; Zakeeruddin, S. M.; Moser, J. E.; Nazeeruddin, M. K.; Sekiguchi, T.; Gratzel, M. *Nat. Mater.* **2003,** 2, (6), 402-407.

28. Ketabi, S.; Le, Z. Y.; Lian, K. *Electrochem Solid St* **2012,** 15, (2), A19-A22.

29. Ketabi, S.; Lian, K. *Solid State Ionics* **2012,** 227, 86-90.

30. Lewandowski, A.; Swiderska, A. *Solid State Ionics* **2003,** 161, (3-4), 243-249.

31. Lewandowski, A.; Swiderska, A. *Solid State Ionics* **2004,** 169, (1-4), 21-24.

32. Zhou, D. Z.; Spinks, G. M.; Wallace, G. G.; Tiyapiboonchaiya, C.; MacFarlane, D. R.; Forsyth, M.; Sun, J. Z. *Electrochim. Acta* **2003,** 48, (14-16), 2355-2359.

33. Armand, M.; Endres, F.; MacFarlane, D. R.; Ohno, H.; Scrosati, B. *Nat. Mater.* **2009,** 8, (8), 621-629.

34. Ogihara, W.; Kosukegawa, H.; Ohno, H. *Chem. Commun.* **2006**, (34), 3637-3639.

35. Zech, O.; Stoppa, A.; Buchner, R.; Kunz, W. *J. Chem. Eng. Data* **2010,** 55, (5), 1774-1778.

36. Lu, W.; Qu, L. T.; Henry, K.; Dai, L. M. *J. Power Sources* **2009,** 189, (2), 1270-1277.

37. Montazami, R.; Liu, S.; Liu, Y.; Wang, D.; Zhang, Q. M.; Heflin, J. R. *J. Appl. Phys.* **2011,** 109, (10).

38. Wu, Q.; Xu, Y.; Yao, Z.; Liu, A.; Shi, G. *ACS Nano* **2010,** 4, (4), 1963-1970.

39. Kim, S.; Park, S. J. *Electrochim. Acta* **2009,** 54, (14), 3775-3780.

40. Chung, S. H.; Wang, Y.; Greenbaum, S. G.; Golodnitsky, D.; Peled, E. *Electrochem Solid St* **1999,** 2, (11), 553-555.

41. Golodnitsky, D.; Livshits, E.; Ulus, A.; Barkay, Z.; Lapides, I.; Peled, E.; Chung, S. H.; Greenbaum, S. *J Phys Chem A* **2001,** 105, (44), 10098-10106.

42. Zhu, L.; Huang, P.; Chen, W. Y.; Ge, Q.; Quirk, R. P.; Cheng, S. Z. D.; Thomas, E. L.; Lotz, B.; Hsiao, B. S.; Yeh, F. J.; Liu, L. Z. *Macromolecules* **2002,** 35, (9), 3553-3562.

43. Wieczorek, W.; Such, K.; Wycislik, H.; Plocharski, J. *Solid State Ionics* **1989,** 36, (3-4), 255-257.

44. Black, D. B.; Lovering, E. G. *The Journal of pharmacy and pharmacology* **1977,** 29, (11), 684-7.

45. Alia, J. M.; Edwards, H. G. M. *J. Solut. Chem.* **2000,** 29, (9), 781-797.

46. Papke, B. L.; Ratner, M. A.; Shriver, D. F. *J. Electrochem. Soc.* **1982,** 129, (7), 1434-1438.

47. Talaty, E. R.; Raja, S.; Storhaug, V. J.; Dolle, A.; Carper, W. R. *J. Phys. Chem. B* **2004,** 108, (35), 13177-13184.

48. Umebayashi, Y.; Fujimori, T.; Sukizaki, T.; Asada, M.; Fujii, K.; Kanzaki, R.; Ishiguro, S. *J Phys Chem A* **2005,** 109, (40), 8976-8982.

49. Yoshihara, T.; Tadokoro, H.; Murahashi, S. *J. Chem. Phys.* **1964,** 41, 2902-2911.

50. Appetecchi, G. B.; Henderson, W.; Villano, P.; Berrettoni, M.; Passerini, S. *J Electrochem Soc* **2001,** 148, (10), A1171-A1178.

51. Jiang, Y. X.; Xu, J. M.; Zhuang, Q. C.; Jin, L. Y.; Sun, S. G. *J. Solid State Electrochem.* **2008,** 12, (4), 353-361.

52. Fan, L. Z.; Maier, J. *Electrochem. Commun.* **2006,** 8, (11), 1753-1756.

53. Wu, H. Y.; Li, X. X.; Wang, Y. H.; Wu, J.; Huang, T.; Wang, Y. *Mat Sci Eng a-Struct* **2011,** 528, (27), 8013-8020.

54. Kohn, P.; Rong, Z. X.; Scherer, K. H.; Sepe, A.; Sommer, M.; Muller-Buschbaum, P.; Friend, R. H.; Steiner, U.; Huttner, S. *Macromolecules* **2013,** 46, (10), 4002-4013.

55. Stoeva, Z.; Martin-Litas, I.; Staunton, E.; Andreev, Y. G.; Bruce, P. G. *J. Am. Chem. Soc.* **2003,** 125, (15), 4619-4626.

56. Majewski, P. W.; Gopinadhan, M.; Jang, W. S.; Lutkenhaus, J. L.; Osuji, C. O. *J. Am. Chem. Soc.* **2010,** 132, (49), 17516-17522.

57. Gadjourova, Z.; Andreev, Y. G.; Tunstall, D. P.; Bruce, P. G. *Nature* **2001,** 412, (6846), 520-523.

58. Gopinadhan, M.; Majewski, P. W.; Osuji, C. O. *Macromolecules* **2010,** 43, (7), 3286-3293.

59. Gwee, L.; Choi, J.; Winey, K. I.; Elabd, Y. A. *Polymer* **2010,** 51, 5516-5524.

60. Hickenboth, C. R.; Moore, J. S.; White, S. R.; Sottos, N. R.; Baudry, J.; Wilson, S. R. *Nature* **2007,** 446, (7134), 423-427.

61. Wright, P. V.; Zheng, Y.; Bhatt, D.; Richardson, T.; Ungar, G. *Polym. Int.* **1998,** 47, (1), 34-42.

62. Zhou, X. Y.; Yin, Y. J.; Wang, Z. D.; Zhou, J. J.; Huang, H.; Mansour, A. N.; Zaykoski, J. A.; Fedderly, J. J.; Balizer, E. *Solid State Ionics* **2011,** 196, (1), 18-24.

63. Chen, H.; Choi, J. H.; Salas-de La Cruz, D.; Winey, K. I.; Elabd, Y. A. *Macromolecules* **2009,** 42, (13), 4809-4816.

CHAPTER 8

A MULTIFUNCTIONAL LOAD-BEARING SOLID-STATE SUPERCAPACITOR[1]

*Andrew S. Westover[1,2], John Tian[1], Shiva Bernath[1], Landon Oakes[1,2], Rob Edwards[1], Farhan Nur Shabab[1], Shahana Chatterjee[1], Amrutur Anilkumar[1], and Cary L. Pint[1,2]**

[1]Department of Mechanical Engineering, Vanderbilt University, Nashville TN 37235

[2]Interdisciplinary Materials Science Program, Vanderbilt University, Nashville, TN 37235

Abstract: A load-bearing, multifunctional material with the simultaneous capability to store energy and withstand static and dynamic mechanical stresses is demonstrated. This is produced using ion-conducting polymers infiltrated into nanoporous silicon that is etched directly into bulk conductive silicon. This device platform maintains energy densities near 10 Wh/Kg with Coulombic efficiency of 98% under exposure to over 300 kPa tensile stresses, and 80 g vibratory accelerations, among excellent performance in other shear, compression, and impact tests. This demonstrates performance feasibility as a structurally integrated energy storage material broadly applicable across renewable energy systems, transportation systems, and mobile electronics, among others.

This work was originally published in **Nano Letters, 14 (6), 3197–3202, May 2014** and is reproduced with permission. © *Nano Letters (2014)*. DOI: 10.1021/nl500531r

8.1 Introduction

Advances in modern technology are often accompanied by the need for energy systems that are more compact, integrated, and functional for power delivery. Whereas conventional energy technology involves externally situated energy storage or power systems, performance requirements in future technological platforms mandate more efficient use of system components for energy integration. One route to achieve this is to integrate energy storage into multifunctional templates dually serving as the structural materials used in system assembly. Such multifunctional materials could transform energy utilization in diverse systems ranging from building components for a distributed energy grid system to structural materials utilized in transportation systems.[2-4]

Practical development of a multifunctional energy storage platform must simultaneously enable structural integrity and energy storage capability. This requires synergy in the performance life between the structural material and the energy device. Supercapacitors can be engineered to achieve stability over a million cycles, currently making them better-suited for structural applications in comparison to other storage technologies.[5] Furthermore, a multifunctional energy storage device must exhibit the capability to store and maintain energy as a structural material amidst exposure to static and dynamic loads, a requirement not imposed on devices externally situated from the load-bearing components. Despite significant innovation in solid-state materials for energy storage,[6-15] architectures involving particulate-based electrodes such as nanostructured carbons,[6, 8, 16-23] lack mechanical rigidity necessary for load-bearing integration. Here we demonstrate a route to develop multifunctional energy materials utilizing porous silicon (P-Si),[24, 25] nanoporous layers that remain both electrically and mechanically tethered to bulk conductive silicon. Utilizing ionic liquid-polymer composites,[15] we observe excellent simultaneous load-bearing and charge storage performance of these materials under static and dynamic loads to demonstrate feasibility for structural applications spanning across diverse technological systems. Whereas the specific use of silicon enables direct application of this platform in areas such as electronics and solar devices, this work more generally demonstrates a route toward integrated multifunctional energy systems with porous material interfaces critical for innovation in modern technology and energy sustainability.

8.2 Results and Discussion

Solid-state load bearing supercapacitors were fabricated utilizing electrochemically etched P-Si layers ~ 4 µm in thickness (75% porosity) and vacuum infiltrated with polyethylene oxide (PEO) 1-ethyl-3-methyl imidizolium tetrafluoroborate ($EMIBF_4$) composites (**Figures 8.A1-A3**). P-Si was chosen due to its native structure where the active material is mechanically and electrically connected to the collector, which is not straightforward with many carbon-based materials. Whereas the minimum polymer electrolyte for device operation is based on the electrolyte needed to fill the porous region, we measured a ~ 0.4 mm thick polymer electrolyte layer spanning the two electrodes in our devices, on average, which could be decreased by optimizing processing techniques. Surface passivation of the P-Si was achieved by ultra-thin, graphene-like carbon coatings performed directly on the P-Si by chemical vapor deposition.[26] This yielded devices capable of sustaining structural integrity under application of mechanical loads while operating as a supercapacitor (**Figure 8.1a-b**). Central to this load-bearing supercapacitor is the design scheme of an

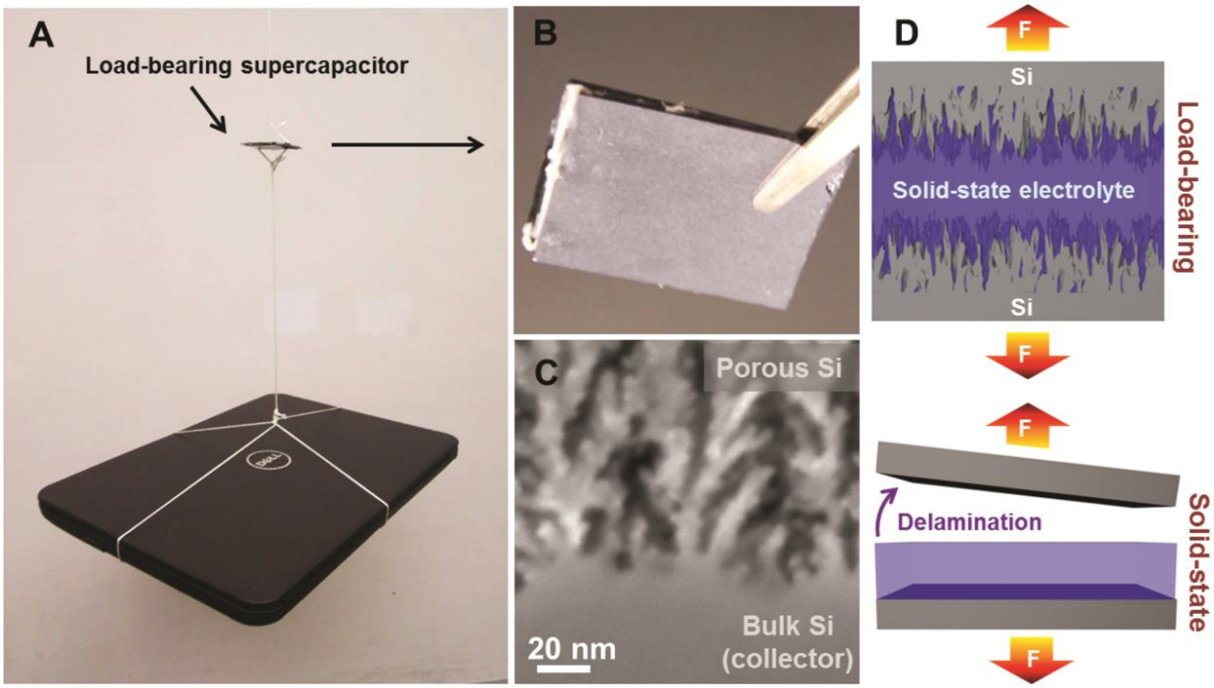

Figure 8.1 (a) Photograph of a load-bearing supercapacitor suspending a laptop (b) Close-up photograph of a silicon-based load-bearing supercapacitor (c) High magnification SEM image of the mechanical-electrical interface in porous silicon that enables a load-bearing device, and (d) Schematic illustrating the difference between the load-bearing supercapacitor developed in this study versus a solid-state supercapacitor.

interconnected active material for energy storage that is mechanically tethered to a conductive electrical collector material to which it is integrated (**Figure 8.1c**). This is a distinguishing feature between a "solid-state" device and a "load-bearing" device (**Figure 8.1d**). The coupling of a non-load-bearing solid-state storage material to a collector interface in a layered composite leads to poor interfacial adhesion and delamination under mechanical stress. This is representative of flexible or plastic supercapacitor materials where structural integration with a current collector is not straightforward, leading to additional integration steps to develop structural composites that are likely to inhibit or degrade the function of the charge storage device. However, a three-dimensional P-Si material both mechanically reinforces the electrode-polymer interface and provides electrical and mechanical addressability to a conductive silicon substrate which serves as a charge collector. This yields structural integrity and supercapacitor performance simultaneously for an integrated system – a concept not achievable with current solid-state energy storage devices.

To assess the electrochemical performance of these load-bearing devices, electrochemical testing was performed under no external mechanical stresses (**Figure 8.2**). We tested devices with different mass ratios of PEO:EMIBF$_4$ ranging from 1:3, 1:1, and 3:1, respectively. We generally observed the best results for the 1:1 and 1:3 combinations. Galvanostatic charge-discharge cycling of solid-state devices at 1.5 A/g with 1:1 and 1:3 PEO:EMIBF$_4$ ratios (**Figure 8.2a-b**) indicates stable, triangular charge-discharge curves representative of good device performance, especially for 1:3 mass ratios. Coulombic efficiencies are measured near ~ 98% for these devices, emphasizing excellent reversibility and the lack of non-Faradaic reactions. These ideal discharge characteristics hold true for discharge currents ranging from 1-4 A/g in both devices (**Figure 8.2c-d**). Cyclic voltammetry (CV) curves at 50 mV/s scan rates (**Figure 8.2e**) indicate stable, non-Faradaic double-layer energy storage until voltages above 3.6 V for the 1:1 device, and until voltages of ~ 3 V for the 1:3 device, the first case being comparable to state-of-the-art graphene-based ultracapacitors [17, 21] and near the potential window of EMIBF$_4$. CV scans were carried out over a wider voltage window compared to Galvanostatic measurements to assess the electrochemical window for non-Faradaic storage in the context of a supercapacitor. This testing, and specifically the rate-dependent

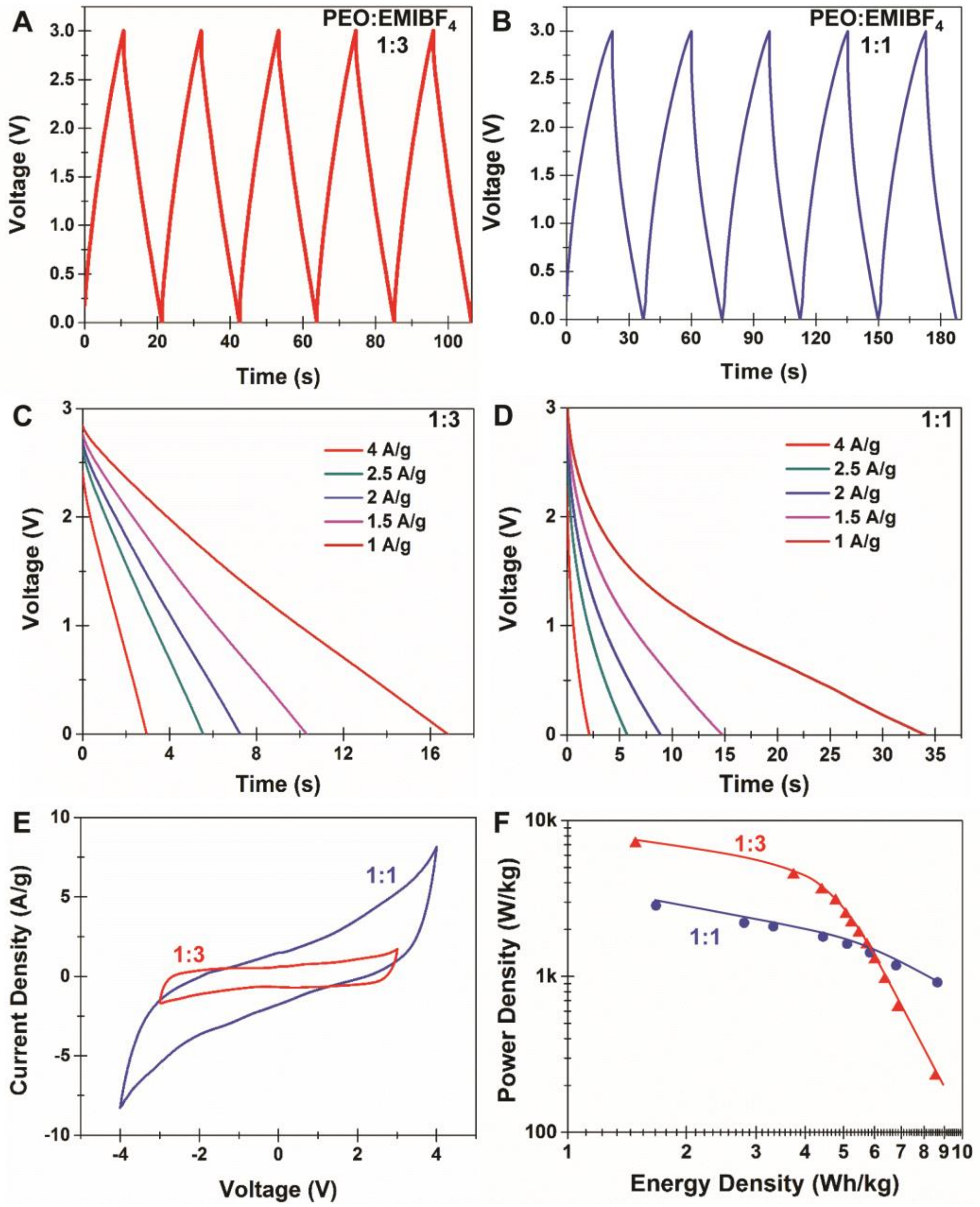

Figure 8.2 (a-b) Five consecutive Galvanostatic charge-discharge curves for load-bearing devices with different PEO:EMIBF$_4$ mass ratios of (a) PEO:EMIBF$_4$ 1:3 and (b) PEO:EMIBF$_4$ 1:1. (c-d) Discharge curves at different discharge currents ranging from 1-4 A/g for (c) PEO:EMIBF$_4$ 1:3 and (d) PEO:EMIBF$_4$ 1:1. (e) Cyclic voltammetry measurements taken at scan rates of 50 mV/sec for both 1:3 and 1:1 ratios of PEO:EMIBF$_4$, and (f) Ragone plot illustrating the energy-power performance characteristics of the load-bearing supercapacitor devices with 1:3 and 1:1 PEO:EMIBF$_4$ mass ratios.

Galvanostatic measurements enables us to assess the energy-power performance of both devices by numerically integrating the discharge curve profiles (**Figure 8.2f**). From this analysis, we observe energy densities between ~ 2-10 Wh/kg for both devices, and power densities from 1-3 kW/kg for the 1:1 device, and up to 8 kW/kg for the 1:3 device. Notably, energy densities are calculated up to 20 Wh/kg using the standard ½CV^2 technique used for supercapacitors (**Figure 8.A8**). This performance is improved compared to commercially-available supercapacitors packaged with liquid electrolytes,[26] and our devices exhibit mechanical integrity without need for external packaging.

As a multifunctional structural material must exhibit stable operation under mechanical stresses, we applied tensile, shear, and compressive loads on these devices while simultaneously analyzing specific capacitance and energy density based on Galvanostatic cycling. Simple test systems were designed for each individual measurement (**Figure 8.A9**). For the shear measurements, a small compressive force (5 kPa) was applied to eliminate torque on the test sample and assess pure shear response on the devices. In both the shear and tensile measurements, control experiments were performed with equivalent "solid-state" devices, or devices prepared using PEO-ionic liquid electrolytes and bulk Si wafer collectors. This "solid-state" device architecture represents a supercapacitor where the active material is dispersed in the PEO-ionic liquid electrolyte, but the energy storage material is laminated on a flat conductive substrate. For primary studies, we utilized PEO:$EMIBF_4$ ratios of 1:1 (**Figure 8.3a-d**), but we compare these results to varying PEO:$EMIBF_4$ ratios including 3:1, 1:1, and 1:3 (**Figures 8.3e-f**).

As numerous cycles are required to assess the effects of mechanical stresses on the device performance, cyclic studies were used to determine the stability of the capacitance with cycling (**Figure 8.3a**). We observe little change in capacitance over 1000 cycles at 2 A/g (3% over 700 cycles, as shown), which enables us to establish the effects of the mechanical stresses on device performance independent of device degradation. Under tensile loading, we observe our load-bearing supercapacitors maintain nearly 100% of the initial energy and capacitance until > 60 kPa applied stress (**Figure 8.3b**). Below 60 kPa, we observe no mechanically induced degradation effects under cyclic tensile measurements (**Figures 8.A13-14**). Near 80 kPa, a transition occurs between the stable device performance and irreversible mechanically-induced device degradation that we attribute to transient effects in delamination. Post-mortem analysis of devices after failure leads us to attribute the decline in capacitance after 80 kPa to gradual pore fracturing and less electrically connected active material (**Figure 8.A16**). Tensile failure at the P-Si/Si interface is also supported by tensile measurements of PEO-IL electrolytes, suggesting tensile strength of several MPa for the 1:1 polymer (**Figure 8.A12**). However, for the solid-state supercapacitor control device, the measured tensile stress at which delamination occurred was below 1 kPa (0.7 kPa). Conservatively assuming a 1 kPa tensile strength for the solid-state device, the load-bearing device interface led to over

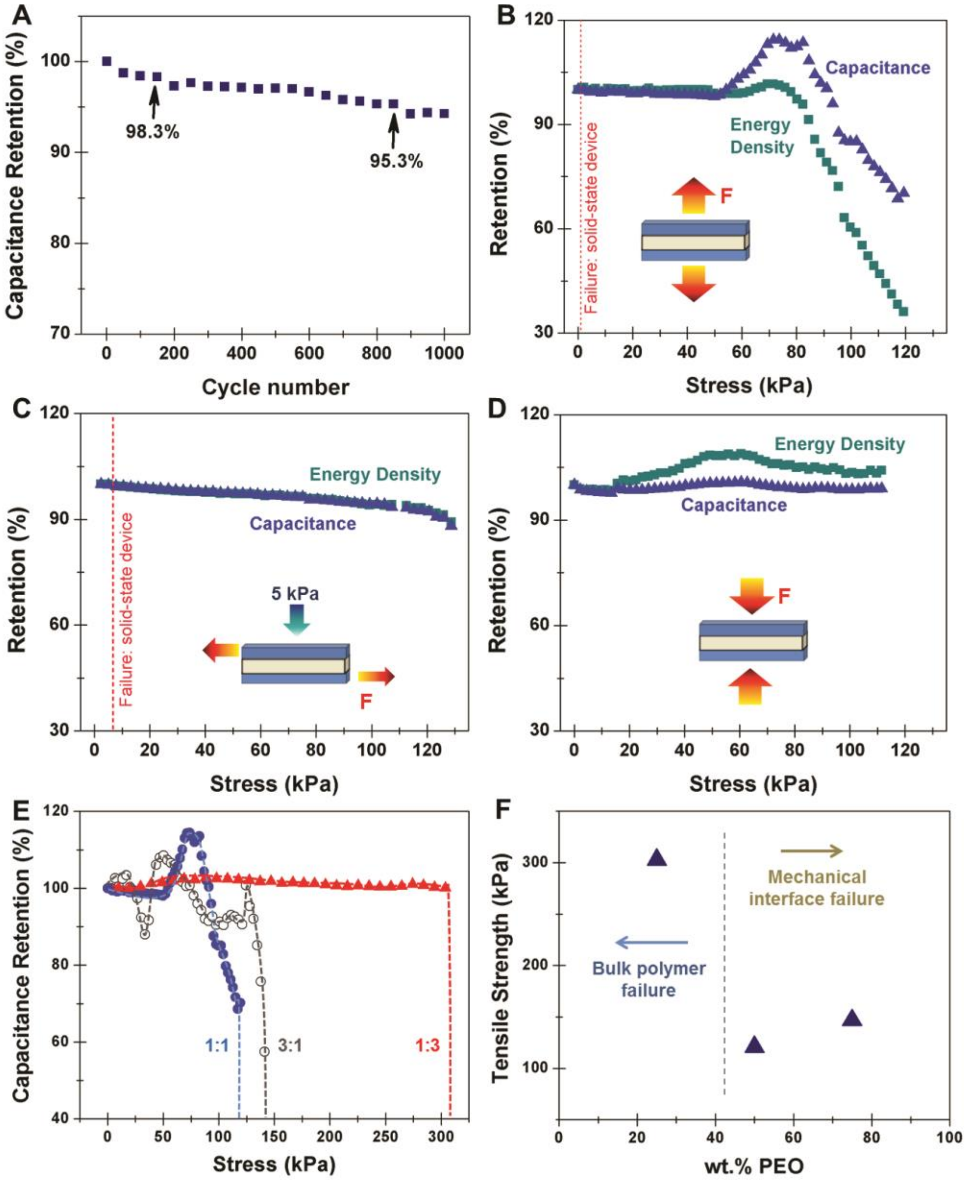

Figure 8.3 (a) Retention of specific capacitance over the course of 1000 cycles applied at a rate of 1.5 A/g. Over 700 cycles, the device exhibits a ~ 3% loss in capacitance. (b-d) Simultaneous electrochemical-mechanical measurements of the retention of both capacitance and energy density for load-bearing supercapacitors under exposure to (b) tensile stress, (c) shear stress, and (d) compressive stress. (e) Retention of specific capacitance as a function of tensile stress for three PEO:EMIBF$_4$ mass ratios of 3:1, 1:1, and 1:3, with lines included to guide the eye. (f) Ultimate tensile strength as a function of PEO:EMIBF$_4$ mass ratio.

120X improvement in tensile strength, and reversible mechanical behavior at stresses 60X greater than the solid-state control device, emphasizing the importance of a load-bearing device.

In the shear testing of these devices (**Figure 8.3c**), we observed stable energy density and capacitance up to shear stresses of ~ 120 kPa before failure rapidly occurred. Post-mortem SEM analysis indicates failure under shear stress at the polymer-P-Si interface. Equivalent solid-state control devices yielded shear strength of 7 kPa, which is ~ 18X lower than that measured with the P-Si material. Finally, we also performed experiments where a uniform compressive force was applied to the load-bearing device (**Figure 8.3d**). In this case we observe stable capacitance and a slightly enhanced energy density that we attribute to a lower series resistance and thus better voltage retention.

In order to assess how these mechanical properties are affected by make-up of the polymer electrolyte, we carried out tensile tests for devices composed of 3:1, 1:1, and 1:3 PEO:EMIBF$_4$ polymer ratios, respectively (**Figure 3e**). Even though the mechanical properties of pure 1:3 polymers are significantly poorer than the 1:1 or 3:1 polymers (**Figure 8.A12**), we observe the 1:3 mass ratio to yield the best tensile strength and an invariant specific capacitance until a rapid failure point above 300 kPa. This is distinguished from the 1:1 and 3:1 electrolytes, which exhibit much improved bulk tensile properties (**Figure 8.A12**), but over 3X lower device-scale tensile strength. Based upon the scaling of the ESR with PEO:EMIBF$_4$ mass ratio (**Figure 8.A7**), and the tensile properties measured for bulk polymers (**Figure 8.A12a**), we expect that the 1:3 polymer exhibits the best performance due to the uniform and complete penetration of the polymer electrolyte into the porous reinforcing interface, hence leading to a correlation between the device tensile behavior and the bulk tensile properties of the polymer (**Figure 8.3f**). In the case of the 1:1 and 3:1 electrolytes, the device tensile properties remain well below the bulk polymer electrolyte tensile properties, and the variation in the capacitance prior to failure indicates partial breaking or premature plasticity due to inhomogeneous pore filling of the reinforcing interface.

As tensile, shear, and compressive forces are collectively the components that make up static forces exhibited in a structural material, these load-bearing devices emphasize the capability to retain energy storage behavior while under significant mechanical loads. For example, for a solid-state device to reversibly operate under up to 300 kPa of tensile stress (or ~ 44 psi), a 4-inch square panel of load bearing energy storage material can withstand over 700 pounds of tensile stress without compromising the charge storage capability of the device. Therefore, such tensile and shear strengths of these devices promote their feasibility for a broad range of structural applications without the need for external packaging.

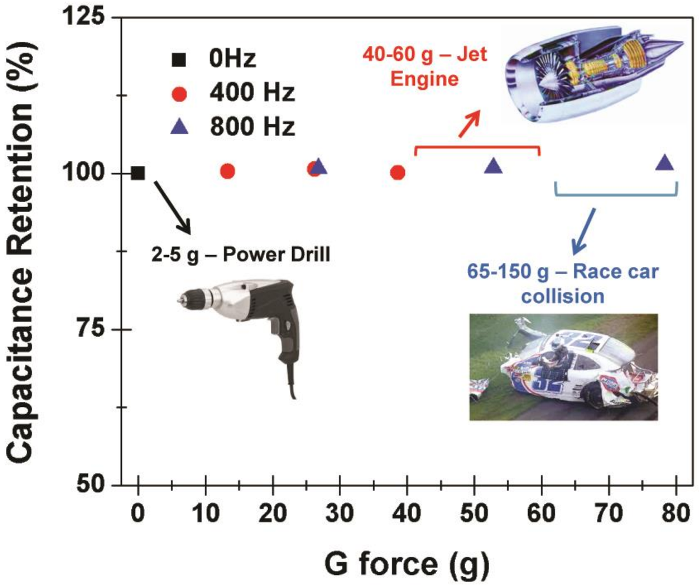

Figure 8.4 Specific capacitance of the load-bearing energy storage devices measured under vibratory loads, indicated by the G-force of the vibrations. Inset into the figure are illustrations of different systems and the G-forces associated with them to emphasize physical meaning to our results.

Finally, in addition to static mechanical stresses, for integration into many systems such as personal vehicles or aerospace systems, multifunctional energy materials must also exhibit stability amidst dynamic vibrational loads or impact events. In this context, we performed experiments where load-bearing supercapacitors were encased in test cells and subjected to dynamic vibratory accelerations ranging in frequency from 400-800 Hz and with amplitudes up to 80 μm (up to 80 g, **Figure 8.4**, experimental setup **Figure 8.A11**).[27] The devices exhibited no noticeable capacitance modulation in real-time testing under g-forces up to 80 g, which was the limit of our system with the weight of the test cell assembly. As illustrated in **Figure 8.4**, this testing regime is within the operation range exhibited in nearly any practical technological system. At G-forces less than 5 g, systems such as home appliances (power drills), roller coasters, and personal vehicles operate. At G-forces between 10 – 60 g, heavy machinery such as fighter jets and jet engine assemblies operate. Finally, G-forces higher than 60 g are encountered in events such as collisions in high-speed vehicles (*e.g.* race cars) and other unique systems. In addition to vibration tests, we also performed experiments where impact was exerted on a fully charged device prior to discharge. Our results suggest that impact energy up to 230 J/cm^2 on a fully charged device incurred no noticeable loss of charge storage behavior in these devices (**Figure 8.A17**). The ability for these load-bearing devices to maintain full functionality as a supercapacitor amidst both vibrational loads representing the most extreme operational environments and impact events in a fully charged state emphasizes their feasibility for integration into diverse technological systems.

8.3 Conclusion

Whereas the utilization of silicon-based materials reflects a route that has direct application in areas such as solid-state, integrated energy conversion and storage systems with silicon-based photovoltaics or electronics, we envision this general route for load-bearing energy storage systems transferrable to a diverse scope of materials, especially micro- and mesoporous materials produced in other technologically relevant metals or materials.[28] This opens a general path for relevant materials besides silicon to be developed with mechanically and electrically addressable interfaces to form load-bearing laminates. In a society where the generation, storage, and transmission of energy is the basis of both technological advancement and energy sustainability, the ability to store energy in structural materials making up the basic infrastructure of any system is a direct pathway toward a more efficient method for energy storage in next-generation technology

8.A Appendix

8.A.1 Porous Silicon Materials Fabrication and Characterization

Porous Silicon Electrochemical Etching.

In order to perform electrochemical etching to fabricate porous Si, highly boron doped silicon wafers were placed in a 3:8 v/v HF (50% H_2O by volume) and ethanol solution with a spiral Pt counterelectrode. (**Figure 8.A1**) The wafers were etched for 180 seconds at a current density of 45 mA/cm^2 resulting in a thin porous layer with 75 % porosity, and 4μm (determined from SEM images). The resulting porous Si films were then stored in a N_2 environment until carbonization to prevent interaction with ambient conditions.

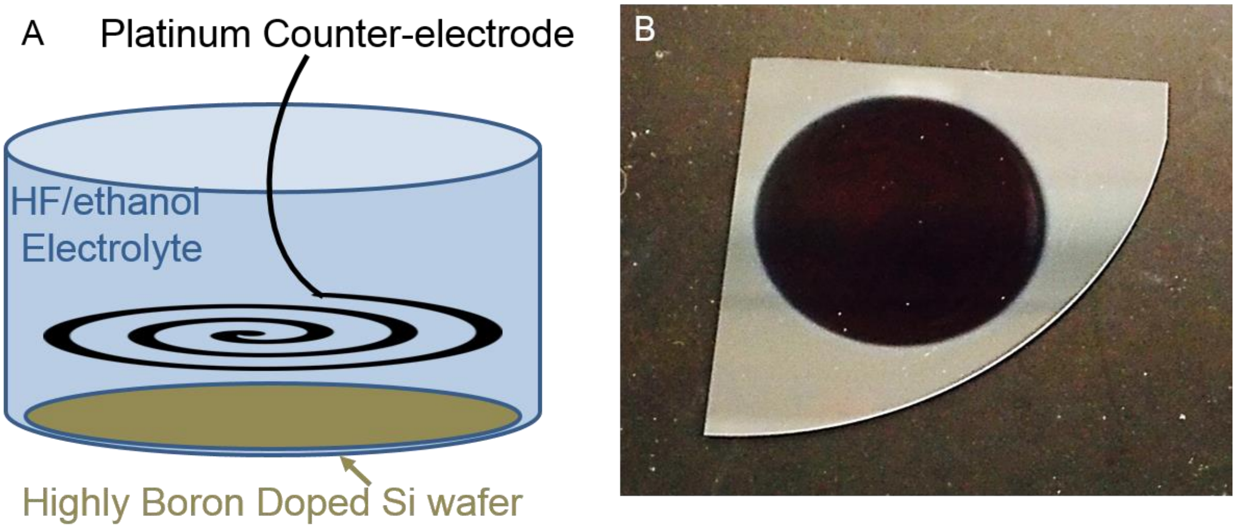

Figure 8.A1 (a) Schematic diagram of system used to etch the porous Si, consisting of a spiral platinum counter-electrode, highly boron doped silicon wafers, and a HF/Ethanol electrolyte. (b) A picture of a silicon wafer after the etching process. The dark region in the center of the wafer is the porous region.

Atomically thin carbon surface passivation of porous silicon.

A carbon coating was applied to the porous Si wafers using chemical vapor deposition (CVD) in a 3-zone Lindberg Blue furnace with a 4’’ quartz tube. The porous Si was mounted on a silicon wafer and then placed in the center of the tube. The furnace was then ramped up to 650 ˚C under a constant gas flow of 1 SLM of Argon and 200 SCCM of H_2. At 650 ˚C 10 SCCMs of C_2H_2 were added to the gas mixture. The temperature was then ramped up to 750 ˚C held for 10 minutes, and finally ramped up to 850 ˚C and held for another 10 minutes. As soon as the 10 minutes at 850 ˚C was completed the C_2H_2 was turned off and the sample was cooled under the Argon, H_2 mixture. This resulted in a few layer conformal coating of graphene like carbon as seen in SEM and TEM

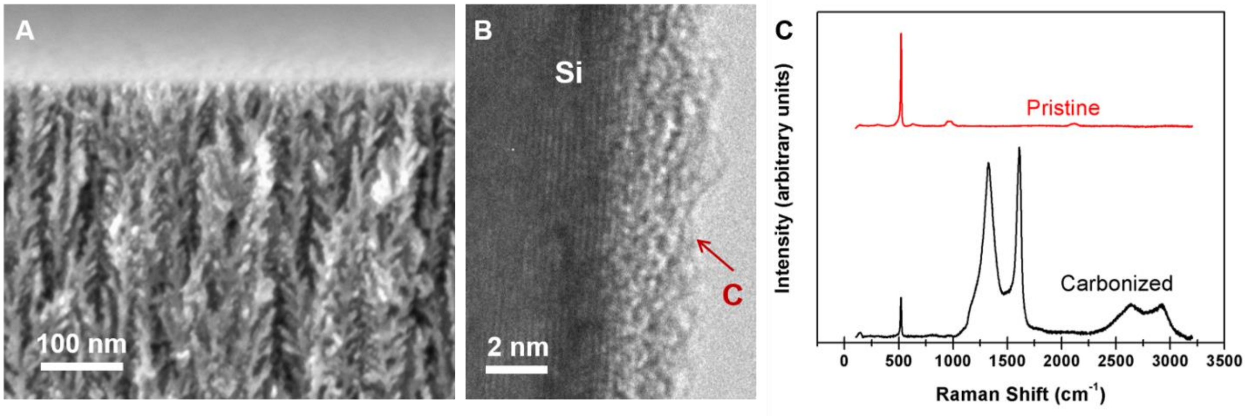

Figure 8.A2 (a) SEM image of carbonized porous Si. (b) TEM image of porous Si region (left), with a few layers of graphene (right). (c) Raman analysis of pristine (red) and carbonized porous Si (black).

images in **Figure 8.A2a-b**. The presence of the graphene like carbon was further confirmed by Raman, showing the characteristic D and G peaks corresponding to a few-layer, disordered graphene material in addition to the silicon peak at 520 cm^{-1} (**Figure 8.A2c**), as opposed to the pristine porous Si wafer which only showed the strong Si Raman peak.

8.A.2 Ion-conducting polymer fabrication and infiltration into porous silicon

Processing of ionic liquid intercalated pfolyethylene oxide.

The solid state polymer electrolyte was synthesized using the solution casting method. Polyethylene oxide (PEO) was dissolved in propylene carbonate (PC) and placed on a hot-plate until the PEO was fully dissolved, as evidenced by the solution turning translucent and viscous (**Figure 8.A3a**). 1-ethyl 3- methyl imidizolium tetrafluoroborate ($EMIBF_4$) was then mixed into the PEO/PC solution (80 wt. % PC, 10 wt. % PEO, 10 wt. % $EMIBF_4$) adding a slightly yellowish hue to the solution. The solution was then poured onto the carbonized porous Si electrodes before finally sandwiching the two electrodes together (**Figure 8.A3b**). The electrodes were then placed in a vacuum oven (MTI)

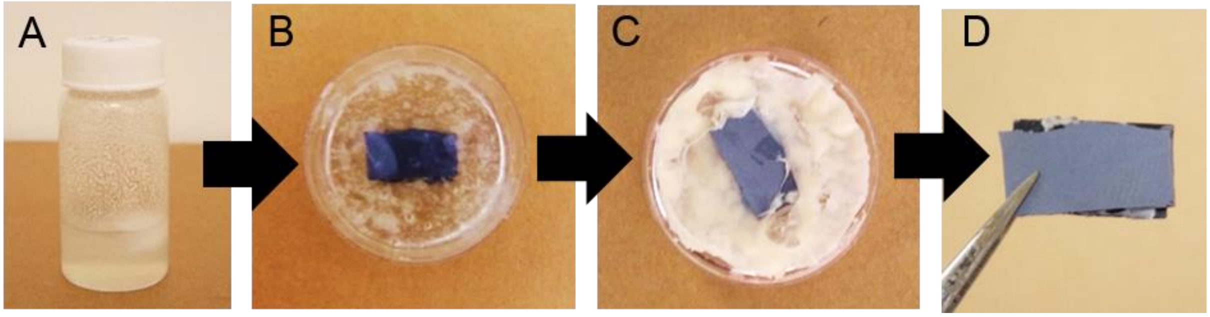

Figure 8.A3 Images showing the major steps in the process of making the load bearing solid state porous Si supercapacitors. (a) solution of PC with PEO dissolved into it. (b) Two carbonized porous Si electrodes with the PC/PEO/$EMIBF_4$ solution in between. (c) The supercapacitor after being placed in a vacuum oven for several days at 50 ˚C, the polymer forming a strong opaque solid state electrolyte. (d) Finished load bearing solid state supercapacitor.

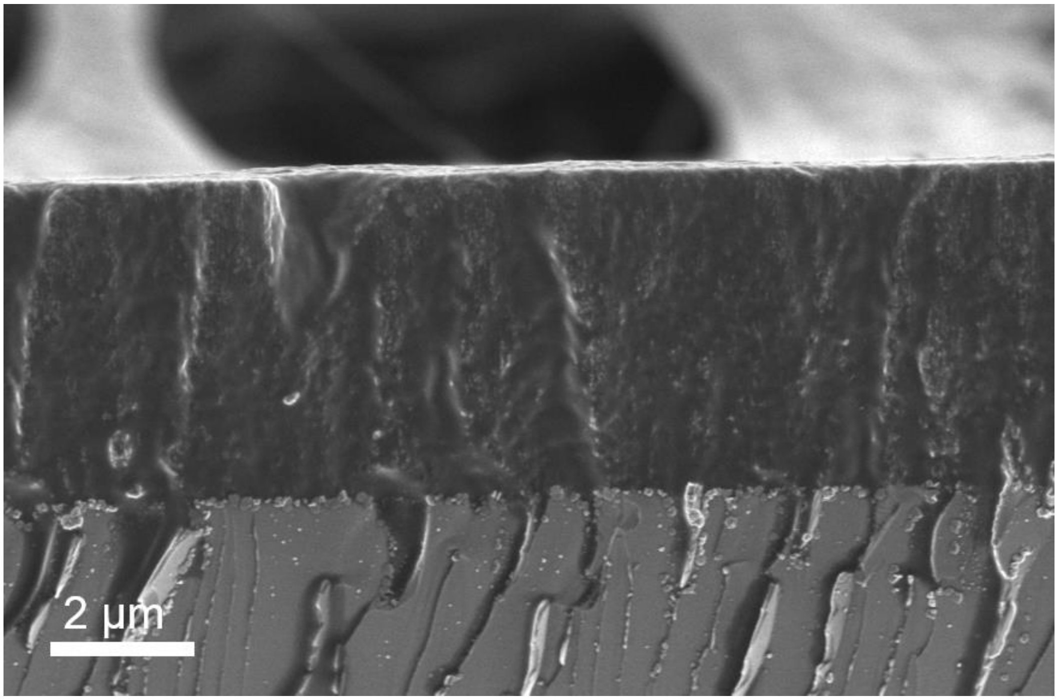

Figure 8.A4. Cross sectional SEM of a fully completed supercapacitor. Clearly showing polymer infiltration into the pores. (Compare with **Figure 8.A2a**)

to both drive vacuum infiltration of the polymer electrolyte into the pores, and to evaporate the PC to form a strong robust polymer. The vacuum oven was heated to 50° C and the electrodes were left in the vacuum oven for 4-10 days, until the PC was completely evaporated and the polymer had turned opaque white (**Figure 8.A3c**). The excess polymer was then removed to yield the final solid state device (**Figure 8.A3d**).

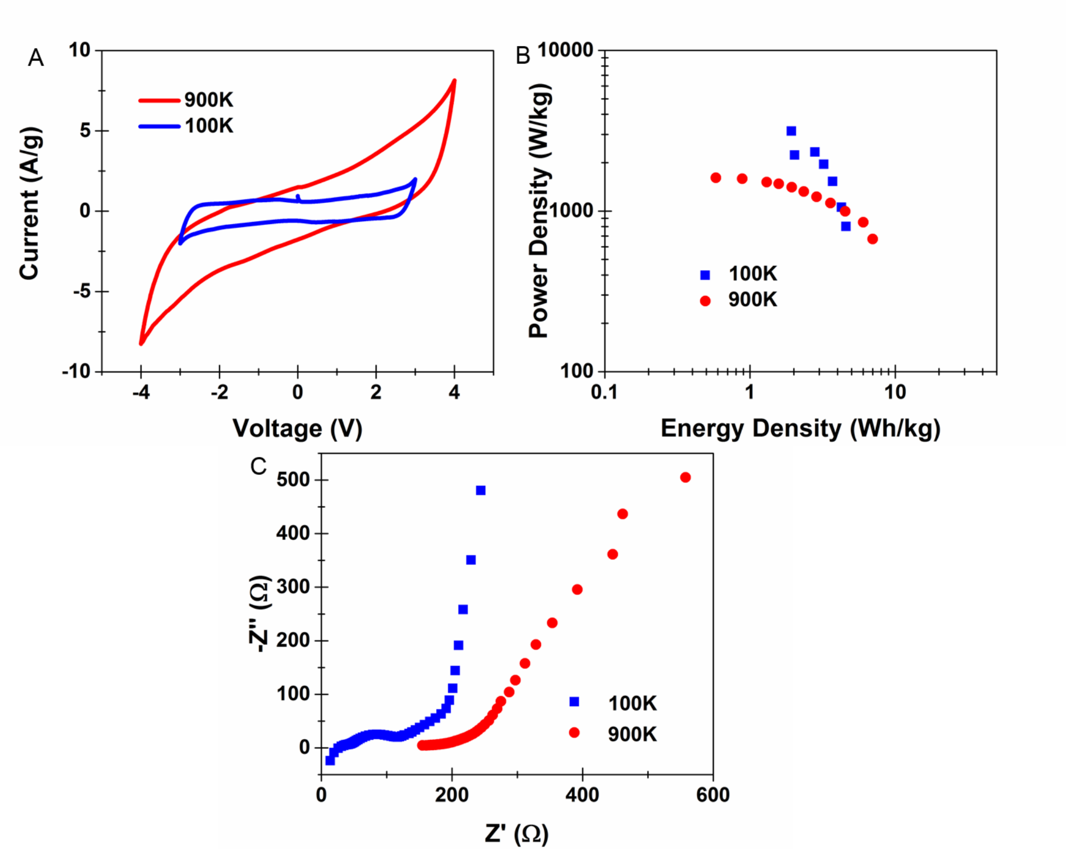

Figure 8.A5 Electrochemical comparison of 100,000 M.W. PEO and 900,000 M. W. PEO based devices. (a) Cyclic voltammetry curves at 100 mV/s scan rate. (b) Ragone plots. (c) Frequency response analysis.

Electrochemical characterization of polymer-infiltrated supercapacitors.

Electrochemical device testing, including cyclic voltammetry, charge discharge and frequency response analysis were performed using a Metrohm Autolab multichannel analyzer. Galvanostatic charge discharge cycles used current ranges from .1 mA - 5mA, cyclic voltammetry measurements were performed with scan rates of 25 – 100 mV/s, and frequency response analysis was performed from 1 MHz to 10 mHz around 0 bias with a signal amplitude of 10 mV. The active mass for the specific device analysis was measured by calculating the mass of the porous region using porosity, area, and thickness measurements. The mass of graphene deposited was found to be negligible in comparison with the active Si mass, and thus the active mass was assumed to be that of the of porous Si.

8.A.3 Considerations for Electrochemical Testing

Influence of polymer molecular weight on electrochemical analysis.

900,000 M.W. PEO was used for the solid state electrolyte due to its high mechanical strength, however we also made several devices with the lower mechanical strength 100,000 MW PEO and found that the 100,000 M.W. had a lower maximum energy density (**Figure 8.A5a**), but also had smaller resistive losses (**Figure 8.A5b-c**) due to better pore infiltration as one might expect from a smaller molecular weight polymer.

Charge/discharge curves for PEO:EMIBF4 3:1

Figure 8.A6 shows charge discharge curves for the PEO:EMIBF$_4$ 3:1 polymer electrolyte infiltrated devices. The Galvanostatic characteristics of these devices becomes less ideal as the PEO concentration increases, as noted from the nonlinear charge and discharge profiles.

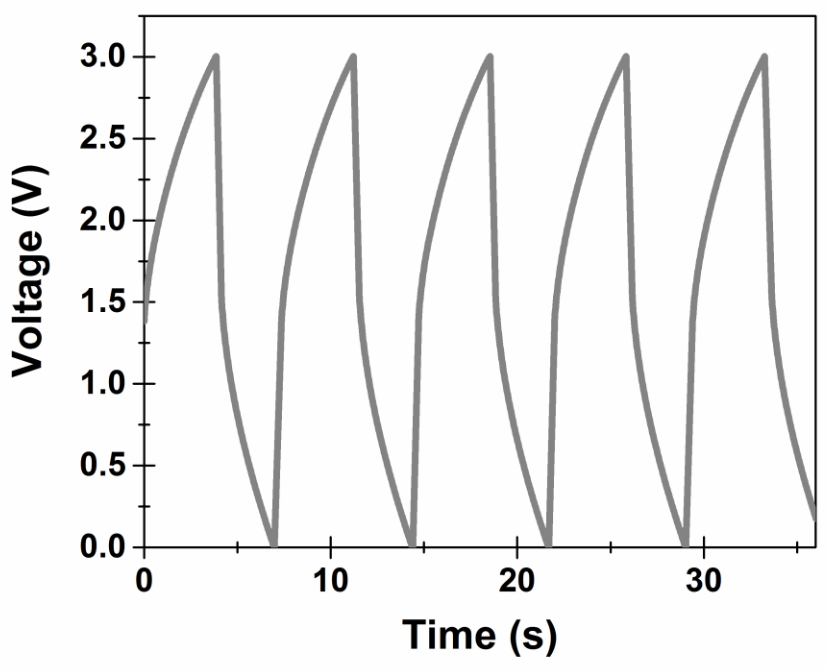

Figure 8.A6 Charge discharge curves for PEO:EMIBF$_4$ 3:1 infiltrated load-bearing device.

Effect of PEO:EMIBF$_4$ concentration of equivalent series resistance (ESR)

Equivalent series resistance (ESR) was calculated using the charge discharge curves in **Figure 8.2a** and **b** and **Figure 8.A6**. As the amount of EMIBF$_4$ increases the ESR of the devices decreases as shown in **Figure 8.A7**. We attribute this effect mostly to the inhomogeneous penetration of the polymer electrolyte into the nanoporous interface, which seems to be ideal at high EMIBF$_4$ concentrations.

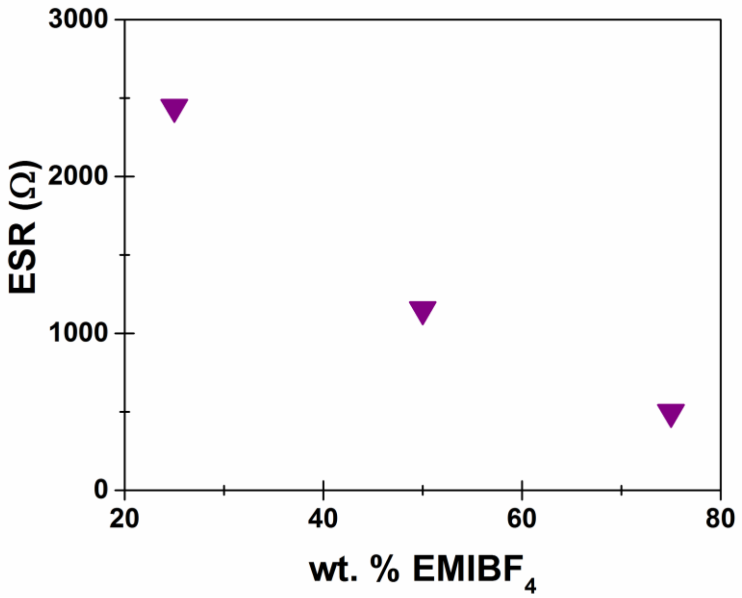

Figure 8.A7 Equivalent series resistance (ESR) of PEO:EMIBF$_4$ 3:1, 1:1, and 1:3 devices.

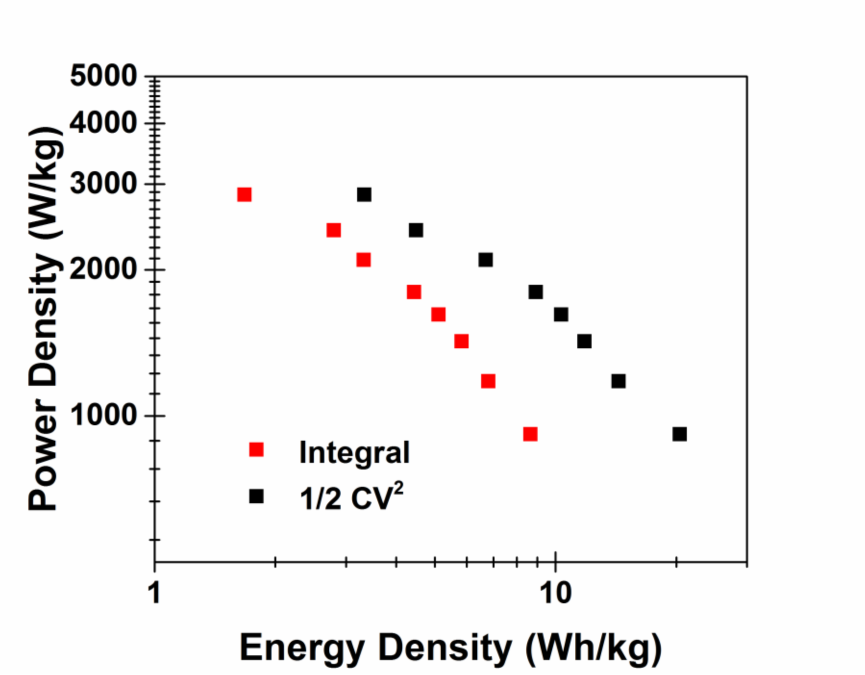

Figure 8.A8 Ragone plots comparing the ½ CV^2 method, and Integral method of determining the energy density.

Considerations for measurements of energy density.

The standard way to calculate energy density for capacitors is to use the formula E = ½ CV^2. This formula is derived from the integral $E = \int_0^t IVdt$ assuming *V(t)* to be a constant function with time. This is only accurate in cases for a supercapacitor exhibiting a perfectly linearly decreasing slope in the charge or discharge curves. Despite the broad use of ½CV^2 to calculate energy densities for supercapacitors, any non-linear discharge characteristics can lead to significant alterations from the true energy stored in the device. **Figure 8.A8** shows a comparison between the two different methods for calculating energy density, showing that the conventional method using E = ½ CV^2 exaggerates the energy density by about a factor of two in comparison to numerically integrating the discharge curve. Therefore, our approach provides the exact energy stored in the device, and it is important to emphasize this is a value 2X lower than the value obtained utilizing the approach employed in nearly every study in the literature.

8.A.4 Experimental setups for mechanical measurements and additional details

Experimental setup for tensile, strain, and compressive tests.

For tensile testing of the load bearing supercapacitors, steel brackets were super-glued to each electrode. Holes were drilled into the brackets for nylon rope to be threaded to allow for the application of a tensile load. (**Figure 8.A9a**). For shear testing, steel plates were super-glued to either electrode and shear forces were applied along the plates. In order to carry out shear testing as accurately as possible, it was necessary to remove any potential tensile forces, thus a secondary plate was glued to the lower of the two to ensure the shear forces were applied in the same plane. In addition, a small 5 kPa compressive force was applied to the sample to counteract the torque applied from gravity (**Figure 8.A9b**). For compression testing, a large steel sheet was super-glued to the upper electrode so that a large weight could be applied directly to the supercapacitor. (**Figure 8.A9c**).

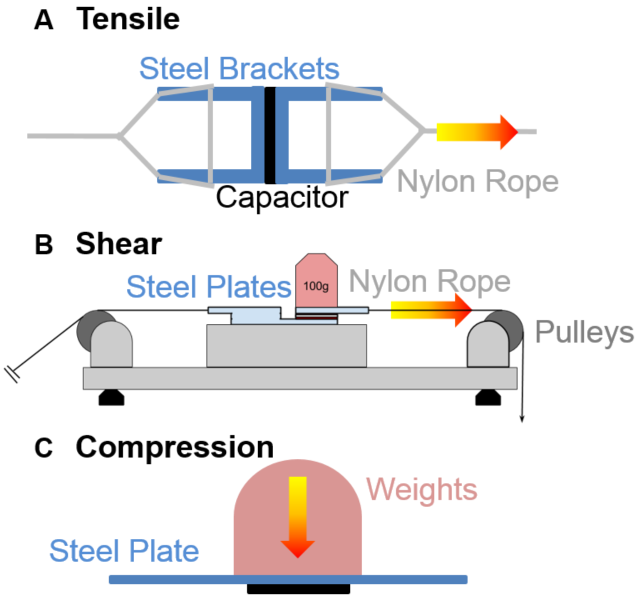

Figure 8.A9 Experimental setups of the (a) tensile tests, (b) Shear plus small compression, and (c) compression tests.

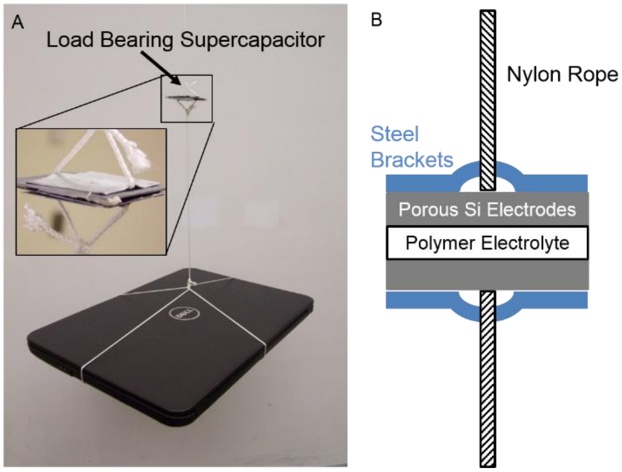

Figure 8.A10. (a). Picture from **Figure 8.1a** with a close up image of the supercapacitor. (b) A schematic of the close up image in (a) showing experimental setup including the steel brackets, nylon rope, Si electrodes and polymer electrolyte.

Experimental setup for vibration testing.

In order to perform vibration testing, the supercapacitor was secured in a laser-cut plexiglass test cell specifically designed for the supercapacitor dimensions (**Figure 8.A11a**). The holder was then attached to the drumhead through a screw to ensure the test cell and supercapacitor experienced the same magnitude of vibration as the drumhead. A Polytec vibrometer (OFV 2200) was used to induce the vibration in the drumhead ranging from 100 Hz to 800 Hz, with amplitudes ranging from 5 µm – 80 µm, and the amplitude of vibration was determined using a Polytec laser interferometer (OFV 511) in combination with a Tektronix Digital Oscilloscope.

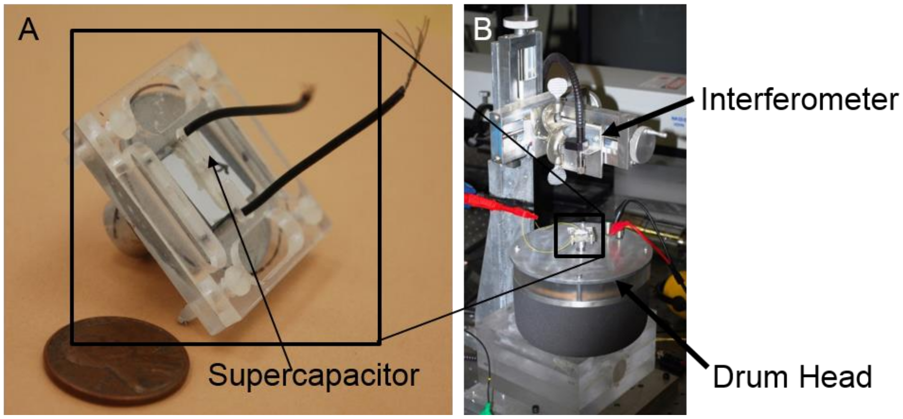

Figure 8.A11 Pictures of experimental setup of vibration tests. (a) close up of the test cell used to secure the supercapacitor to the drum head. (b) Entire vibration setup up, with the test cell secured on the drumhead, and the interferometer used to measure the vibration amplitude.

Control studies of PEO-ionic liquid electrolyte mechanical testing.

Tensile testing of the PEO-ionic liquid polymers were carried out using a home-built test cell. In order to test these materials, the polymers were formed into thin films using the technique discussed above. Following this, they were cut into rectangles and contacted with mechanical pads that simultaneously served as electrodes for EIS measurements. Weight was then added to the tensile stretching rig, and the ionic conductivity was measured simultaneously. Tensile measurements of the PEO-ionic liquid polymer with ratios of 3:1, 1:1, and 1:3, is shown in **Figure 8.A12a**, with the corresponding ionic conductivity for the 1:1 polymer in **Figures 8.A12b**.

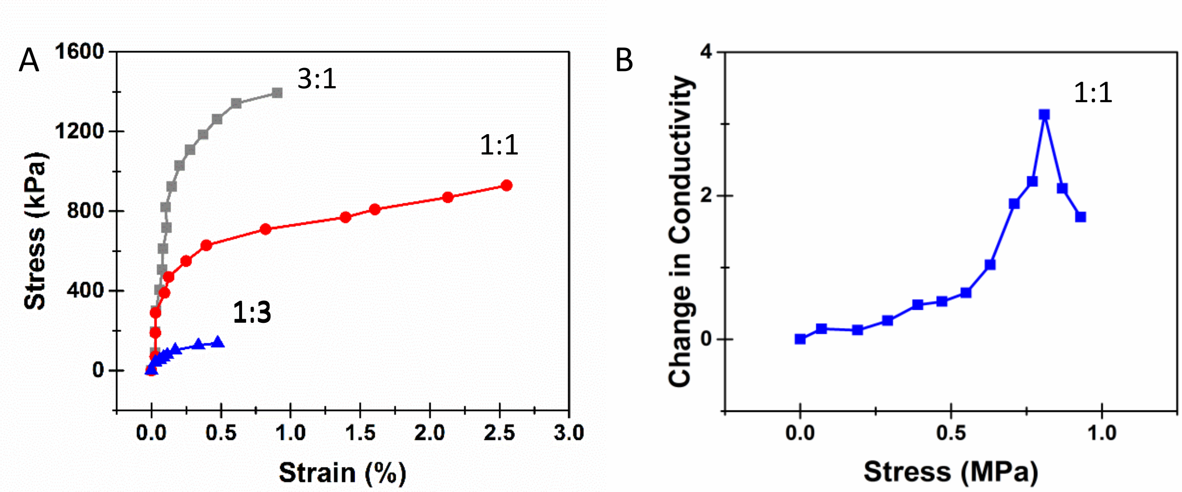

Figure 8.A12 (a) Tensile tests of PEO/EMIBF$_4$ polymers of with ratios of 1:3, 1:1, and 3:1. (b) Measurement of ionic conductivity of the PEO/EMIBF$_4$ solid state electrolyte as a tensile load is applied.

Assessment of electrochemical performance during tensile stress.

Figure 8.A13 shows the discharge curves corresponding to the tensile test in **Figure 8.3a**. Up until 50 kPa the discharge curves show the exact same behavior (**Figure 8.A13b**), emphasizing that loads up to 50 kPa have no effect on the electrochemical performance. From 50 kPa to 80 kPa the capacitance steadily

increases. In the discharge curves this is observed as an increase in the discharge time, and a slight change in the overall shape of the curve (**Figure 8.A13c**). From 80 kPa to 120 kPa there is a steady decrease in the capacitance until failure, which is clearly observed in the discharge curves showing a steady decrease in discharge time, and a steady increase in ESR voltage drops (**Figure 8.A13d**).

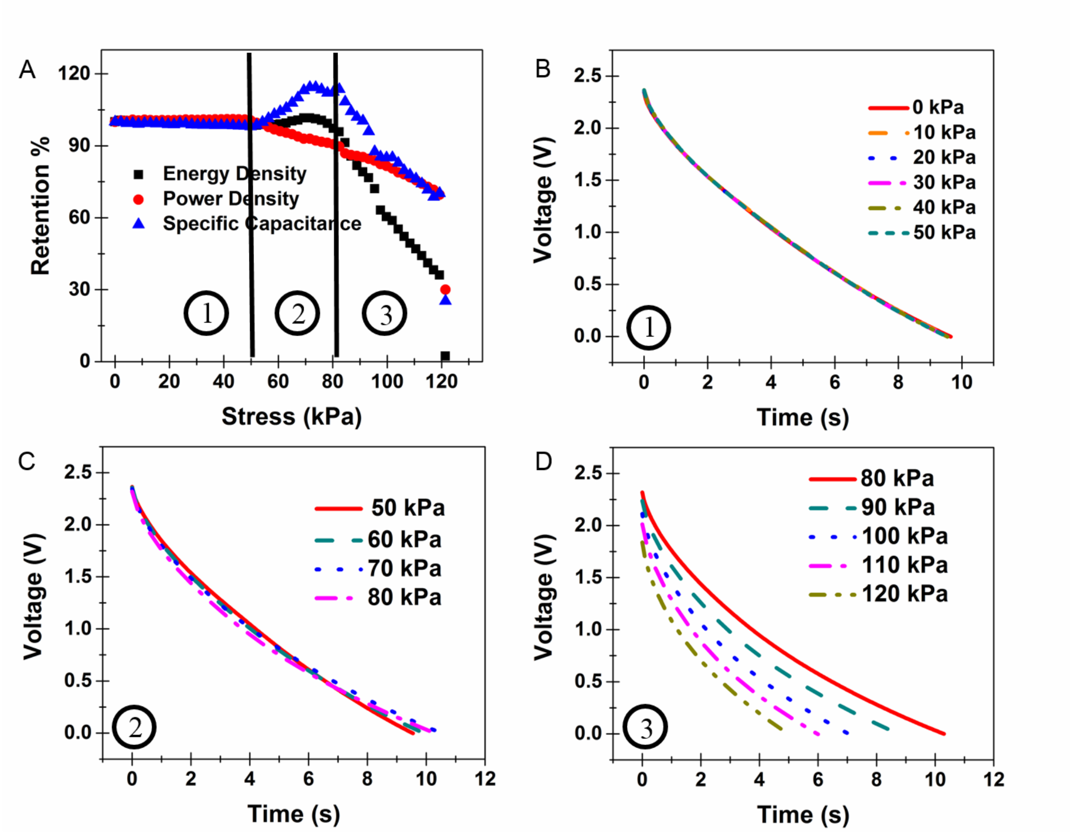

Figure 8.A13. (a) Capacitance, energy density, and power density, as a function of applied tensile load. (b) Discharge curves for loads ranging from 0-50 kPa for tensile test in (a). (c) Discharge curves for loads ranging from 50 -80 kPa for tensile test in (a). (d) Discharge curves for loads ranging from 80 kPa to 120 kPa for tensile test in (a).

Cyclic tensile testing to determine reversible and irreversible storage regimes.

Figure 8.A14 shows the characteristic cyclic tensile testing behavior of our devices. For tensile tests with maximum stresses below a threshold stress, denoted by γ, the devices show no degradation in the electrochemical device performance. For tensile tests with magnitudes greater than γ the devices showed

steady degradation for all tensile loads greater than γ. Although the exact magnitude of this threshold stress γ varied based on the individual devices, all the devices showed a clear demarcation between these reversible (α) and irreversible (β) regimes that were consistently measured. For our devices that we discuss in **Figure 8.3**, this point is near 60 kPa, whereas other devices where we obtained poor penetration of the polymer into the P-Si pore structure, this value could be as low as 10 kPa.

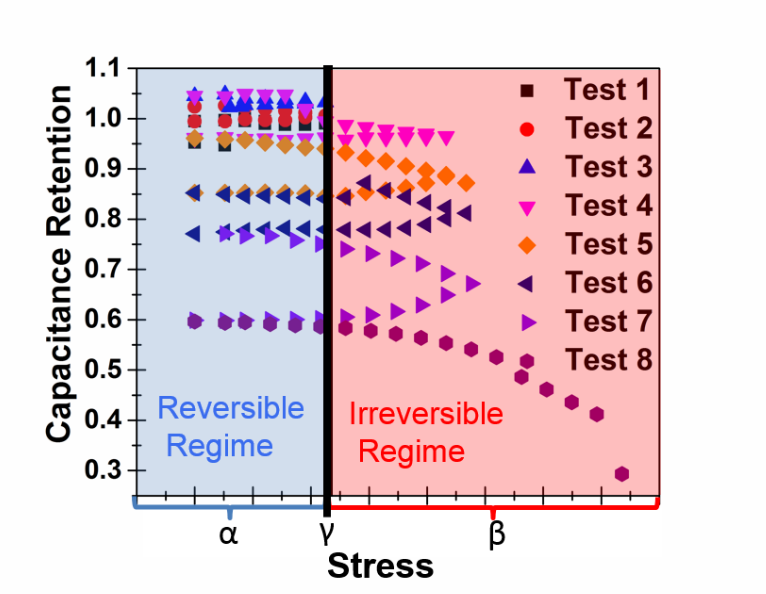

Figure 8.A14 Characteristic cyclic tensile behavior of our devices, with the reversible regime marked by α, and the irreversible regime marked by β, and the threshold stress between the two regimes marked as γ.

Shear test without compression.

In addition to the shear plus small compression measurements (**Figure 8.3c**) we also performed pure shear measurements (**Figure 8.A15**). We found that the general behavior of the shear measurements to be the same, with the small compressive load causing an increase of almost double in the ultimate shear strength. This suggests that the function of the small compressive force was to eliminate unwanted torque in the shear testing setup that was causing premature failure.

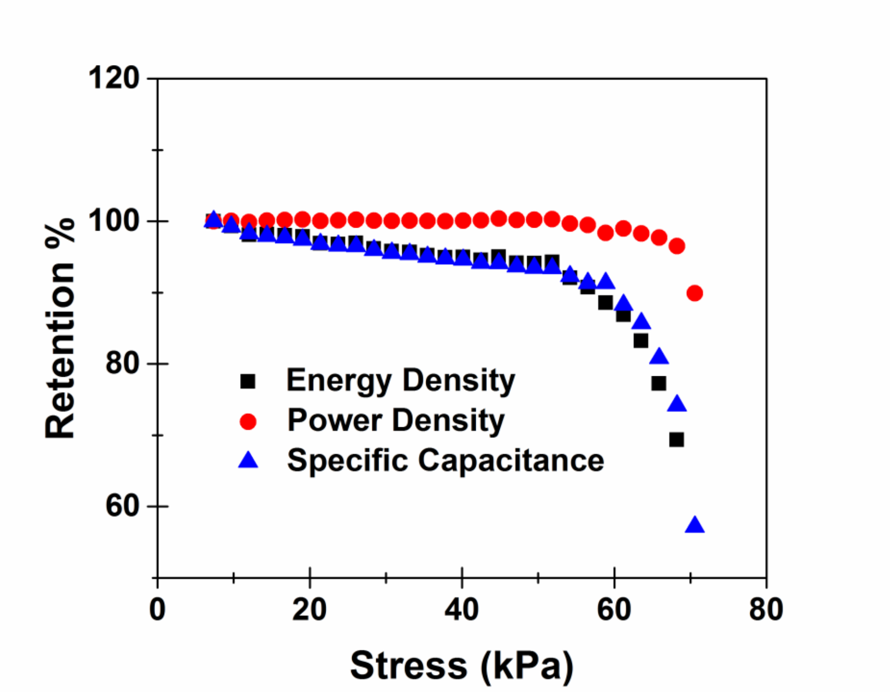

Figure 8.A15 Retention percent of energy density, power density, and specific capacitance as a load is applied in a shear measurement.

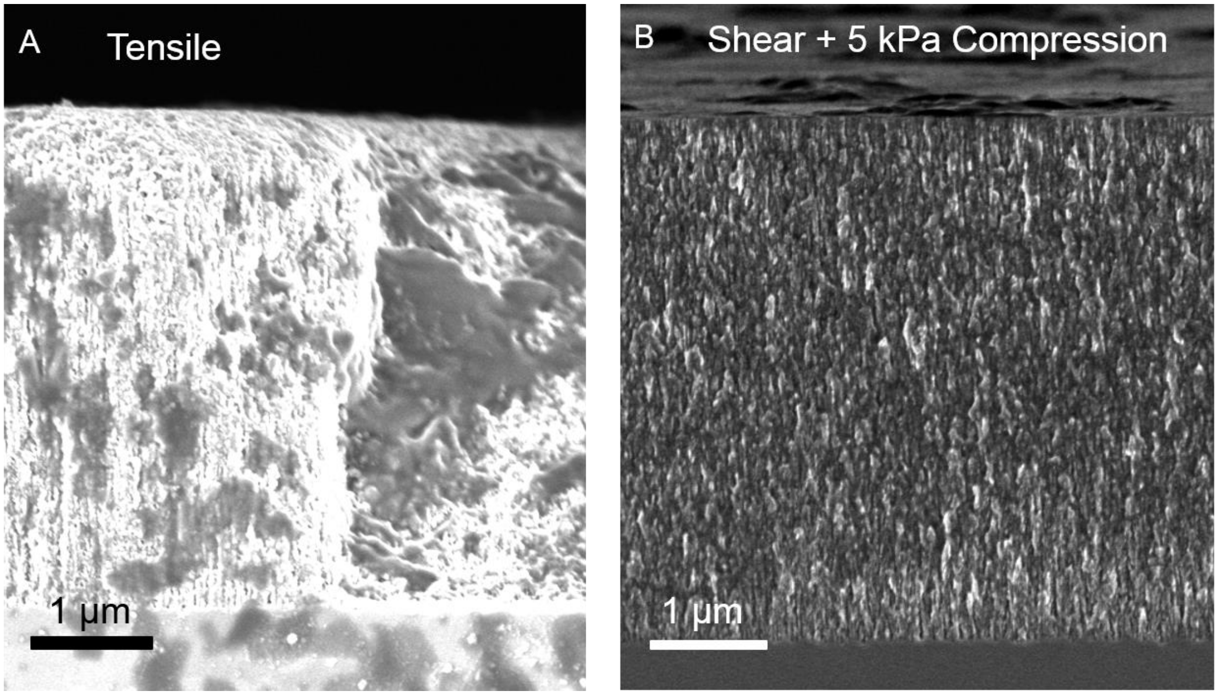

Figure 8.A16. Post mortem SEM images for devices loaded to failure for (a) Tensile, and (b) Shear plus small compression.

SEM analysis of devices tested to failure.

Figure 8.A13 shows SEM images of both the tensile (**Figure 8.A16a**) and the shear plus small compression (**Figure 8.A16b**) tests from **Figure 8.3**. For the tensile test we see that the failure in the device occurred due to fracturing of the porous silicon structure. For the shear test we do not see any of this fracturing, and thus the failure can be assumed to have occurred at the porous Si-polymer interface.

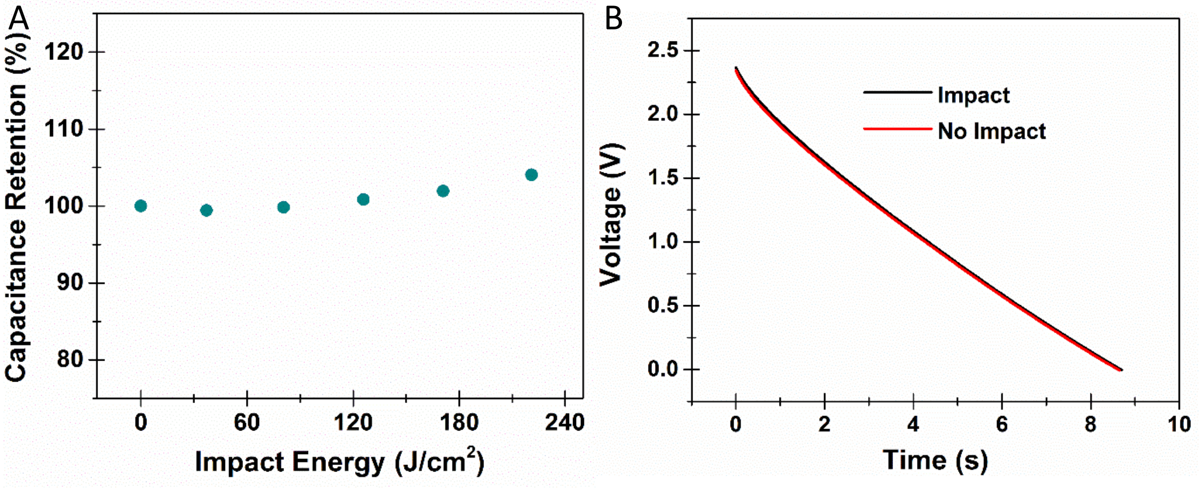

Figure 8.A17 (a) Capacitance retention as a function of impact energy. (b) comparison of an impacted and un-impacted discharge curves.

Impact/Drop testing.

Impact testing was performed by dropping a 54g cylindrical Teflon weight through a PVC pipe onto a PEO:EMIBF$_4$ 1:1 device. This is accurate under the premise that the impact energy is absorbed by the load-bearing device, which is satisfied given that the hardness of the weight will be less than that of the polymer electrolyte, causing the energy to be absorbed primarily in the load-bearing energy storage device upon impact. In this device configuration, the impact energy was varied by adjusting the height from which the weight was dropped. Two sets of studies were conducted in these experiments – the first of which where the device was impacted in an uncharged state, prior to charge-discharge measurements. In this case, we observed no change in the charge storage properties until impact energies that caused the silicon electrodes to shatter. The more relevant case for a device application involves impact where the energy storage device is impacted while in a “charged” state. In order to test this, we Galvanostatically charged load-bearing devices and performed a drop test at a point between reaching a charged state and Galvanostatically discharging the device. We then measured the capacitance retention of these devices as a function of the drop or impact energy (**Figure 8.A17a**) with impact energy up to 230 J/cm^2. Overall, such impact energies incurred only slight (positive) changes to the total charge storage, as is also evidenced by the discharge curves showing the comparison between devices discharged with no impact, and devices impacted in a charged state and then discharged (**Figure 8.A17b**).

Acknowledgements

We thank Adam Cohn, Rachel Carter, William Erwin, and Rizia Bardhan for useful discussions, and Sharon Weiss for facilities in part to conduct P-Si etching. Materials development aspects of this work are supported by National Science Foundation (NSF) grant CMMI 1334269 and by an ORAU Powe Award. Support for A.W. and TEM imaging was enabled by NSF grant EPS 1004083. Support for J.W.T. was from a VUSRP summer fellowship. SEM and CVD materials fabrication aspects of this research were conducted in part at the Center for Nanophase Materials Sciences at Oak Ridge National Laboratory

References

1. Westover, A. S.; Tian, J. W.; Bernath, S.; Oakes, L.; Edwards, R.; Shabab, F. N.; Chatterjee, S.; Anilkumar, A. V.; Pint, C. L. *Nano Lett.* **2014,** 14, 3197-3202.

2. Carrasco, J. M.; Franquelo, L. G.; Bialasiewicz, J. T.; Galvan, E.; Guisado, R. C. P.; Prats, A. M.; Leon, J. I.; Moreno-Alfonso, N. *IEEE T. Ind. Electron.* **2006,** 53, (4), 1002-1016.

3. Alanne, K.; Saari, A. *Renew. Sust. Energ. Rev.* **2006,** 10, (6), 539-558.

4. Driesen, J.; Katiraei, F. *IEEE Power Energy M.* **2008,** 6, (3), 30-39.

5. Simon, P.; Gogotsi, Y. *Nat. Mater.* **2008,** 7, (11), 845-854.

6. Gao, H. C.; Xiao, F.; Ching, C. B.; Duan, H. W. *Acs Appl Mater Inter* **2012,** 4, (12), 7019-7025.

7. Huang, C.; Grant, P. S. *Sci. Rep.* **2013,** 3, 2393.

8. Kang, Y. J.; Chung, H.; Han, C. H.; Kim, W. *Nanotechnol.* **2012,** 23, (28), 065401.

9. Li, F. J.; Kitaura, H.; Zhou, H. S. *Energy Environ. Sci.* **2013,** 6, (8), 2302-2311.

10. Notten, P. H. L.; Roozeboom, F.; Niessen, R. A. H.; Baggetto, L. *Adv. Mater.* **2007,** 19, (24), 4564-4567.

11. Pint, C. L.; Nicholas, N. W.; Xu, S.; Sun, Z. Z.; Tour, J. M.; Schmidt, H. K.; Gordon, R. G.; Hauge, R. H. *Carbon* **2011,** 49, (14), 4890-4897.

12. Quartarone, E.; Mustarelli, P. *Chem. Soc. Rev.* **2011,** 40, (5), 2525-2540.

13. Xu, Y.; Lin, Z.; Huang, X.; Liu, Y.; Huang, Y.; Duan, X. *ACS Nano* **2013,** 7, (5), 4042-4049.

14. Banerjee, P.; Perez, I.; Henn-Lecordier, L.; Lee, S. B.; Rubloff, G. W. *Nat. Nanotechnol.* **2009,** 4, (5), 292-296.

15. Yuan, J. Y.; Mecerreyes, D.; Antonietti, M. *Prog. Polym. Sci.* **2013,** 38, (7), 1009-1036.

16. Izadi-Najafabadi, A.; Yasuda, S.; Kobashi, K.; Yamada, T.; Futaba, D. N.; Hatori, H.; Yumura, M.; Iijima, S.; Hata, K. *Adv. Mater.* **2010,** 22, (35), E235-+.

17. Liu, C. G.; Yu, Z. N.; Neff, D.; Zhamu, A.; Jang, B. Z. *Nano Lett.* **2010,** 10, (12), 4863-4868.

18. Stoller, M. D.; Park, S. J.; Zhu, Y. W.; An, J. H.; Ruoff, R. S. *Nano Lett.* **2008,** 8, (10), 3498-3502.

19. Wang, Y.; Shi, Z. Q.; Huang, Y.; Ma, Y. F.; Wang, C. Y.; Chen, M. M.; Chen, Y. S. *J. Phys. Chem. C* **2009,** 113, (30), 13103-13107.

20. Zhu, Y.; Li, L.; Zhang, C. G.; Casillas, G.; Sun, Z. Z.; Yan, Z.; Ruan, G. D.; Peng, Z. W.; Raji, A. R. O.; Kittrell, C.; Hauge, R. H.; Tour, J. M. *Nat. Commun.* **2012,** 3, 1225.

21. Zhu, Y. W.; Murali, S.; Stoller, M. D.; Ganesh, K. J.; Cai, W. W.; Ferreira, P. J.; Pirkle, A.; Wallace, R. M.; Cychosz, K. A.; Thommes, M.; Su, D.; Stach, E. A.; Ruoff, R. S. *Science* **2011,** 332, (6037), 1537-1541.

22. Chmiola, J.; Yushin, G.; Gogotsi, Y.; Portet, C.; Simon, P.; Taberna, P. L. *Science* **2006,** 313, (5794), 1760-1763.

23. Merlet, C.; Rotenberg, B.; Madden, P. A.; Taberna, P. L.; Simon, P.; Gogotsi, Y.; Salanne, M. *Nat. Mater.* **2012,** 11, (4), 306-310.

24. Granitzer, P.; Rumpf, K. *Materials* **2010,** 3, (2), 943-998.

25. Parkhutik, V. *Solid State Electron.* **1999,** 43, (6), 1121-1141.

26. Oakes, L.; Westover, A.; Mares, J.; Chatterjee, S.; Erwin, W.; Bardhan, R.; Weiss, S. M.; Pint, C. L. *Sci. Rep.* **2013,** 3, 3020.

27. Anilkumar, A. V.; Grugel, R. N.; Bhowmick, J.; Wang, T. G. *J. Cryst. Growth* **2005,** 276, (1-2), 194-203.

28. Schuth, F.; Schmidt, W. *Adv. Mater.* **2002,** 14, (9), 629-638.

CHAPTER 9

MULTIFUNCTIONAL HIGH STRENGTH AND HIGH ENERGY EPOXY COMPOSITE STRUCTURAL SUPERCAPACITORS WITH WET-DRY OPERATIONAL STABILITY[1]

Andrew S. Westover[1,2], Bradly Baer[1,2], Babatunde H. Bello[1], Haotian Sun[1], Landon Oakes[1,2], Leon Bellan[1,2], Cary L. Pint[1,2]

[1]Department of Mechanical Engineering, Vanderbilt University, Nashville TN 37235

[2]Interdisciplinary Materials Science Program, Vanderbilt University, Nashville, TN 37235

Abstract: We demonstrate the fabrication of multifunctional structural supercapacitors that maintain energy storage capability under both mechanical stresses and water immersion. This is based on the infiltration of bisphenol A ionic liquid epoxy resin electrolytes infiltrated into nanoporous silicon interface that play the dual role of charge storage and mechanical reinforcement of the energy storage composite material. These structural composites maintain full energy storage capability (5-8 Wh/kg) under tensile stresses over 1 MPa, with nearly 100% energy retention after 4000 cycles. We observe this mechanical and charge storage performance to be preserved through extreme water immersion conditions in contrast to polymer-based solid-state electrolytes that spontaneously lose mechanical integrity under water immersion conditions. As structural energy storage is required to simultaneously maintain mechanical integrity, store charge, and operate in unpackaged environments exposed to humidity and wet-dry conditions, we demonstrate the first device architecture capable of all these conditions while demonstrating energy capability near current packaged commercial supercapacitor devices.

This work was originally published in the **J. Mater. Chem. A, 3 (40), 20097-20102, Sep. 2015** and is reproduced with permission. © *Journal of Materials Chemistry A (2015)* DOI: 10.1039/C5TA05922D

9.1 Introduction

Advances in energy storage materials have been the foundation for broad innovation in emerging technologies such as portable electronics, electric vehicles, and grid-scale energy systems in recent years. Systematic technological advancements in these areas require development of energy storage systems with higher energy density,[2-6] higher power density,[7-10] and with lower costs,[11-13] building on a conventional platform where energy storage devices are situated externally from the systems they power. In recent years, an emerging field of research has focused on multifunctional energy storage systems where energy storage can be built into energy conversion systems as well as wearable, flexible, or structural systems.[14-22] In the specific case of structural energy storage systems, these systems must exhibit the basic requirement of simultaneously maintaining structural integrity and sustaining the ability to store and release energy. Unlike conventional energy storage analogues, structural energy storage materials have the potential to greatly reduce the weight of energy-using systems by multipurposing existent materials with energy storage, or to maintain the same weight and significantly enhance the total on-board energy storage capability of a system. This represents two key trajectories that are critical to advancing next-generation technological systems.

Due to the simplicity of the charge storage mechanism, reports on structural capacitive storage systems have emerged in recent years.[23-30] Early efforts have demonstrated carbon fiber based epoxy composite electrodes that exhibit excellent mechanical properties with the capability to store charge (5-26MPa of Shear strength, and Young's modulus of up to 30GPa).[17, 23-26, 28] However, the use of carbon fibers is a bottleneck to achieve practical charge storage capability, as these materials exhibit surface area that is near 10,000X lower than state-of-the-art nanomaterials for supercapacitors. Furthermore, combining high surface area materials with these templates leads to weakly coupled electrical-mechanical interfaces that challenge the load-bearing energy storage capability of the material. In previous studies on multifunctional energy storage, electrochemical and mechanical properties are tested and reported separately, and in some cases the mechanical properties of the full device are not assessed due to the use of liquid electrolytes.[26] As charge storage in an electrochemical supercapacitor occurs at the electrode-electrolyte interface, which is the interface under stress in a structural energy storage device, multifunctional energy storage capability must be determined by the synergistic assessment of energy storage performance *under* mechanical stress.

Among the many important features for a structural supercapacitor, the choice of electrolyte is critical in dictating mechanical, ionic, and diffusion properties into the charge storage material. Polymer electrolytes, such as polyethylene oxide (PEO), poly(ethylene glycol) diglycidylether (PEGDGE), polyvinyl alcohol (PVA), and polyvinylidene fluoride (PVdF) ionic liquid (IL) composites have been lauded as candidates for solid state electrolytes for energy storage systems, such as batteries and supercapacitors.[23, 24, 31-38] However, most polymers exhibit extreme environmentally-induced fluctuations in ionic transport and mechanical properties, challenging their use for structural systems. Unlike packaged devices, structural energy storage systems must exhibit invariant energy storage performance when subjected to environmental conditions, such as rain or humidity. Polymers such as PEO and PVA spontaneously lose structural integrity in such conditions,[39-41] making them unsuitable for practical use in this application. To the best of our knowledge, no studies have been conducted on the ability for unpackaged energy storage devices to maintain operational integrity underwater or in wet/humid conditions, even though this is one of the most critical factors for an energy storage material dually implemented as a structural material.

In this communication, we demonstrate the first report of a multifunctional energy storage device that simultaneously exhibits high Young's modulus mechanical performance, energy storage capability commensurate with commercial supercapacitors, and operation in and through cycles of extreme water immersion environments. This is enabled through the fabrication of ionically conductive epoxy/(IL)/silicon composites using nanoporous Si electrodes directly etched into bulk silicon current collectors, which are infiltrated with a biphasic bisphenol A/F based epoxy resin-IL electrolyte (hereafter referred to as epoxy-IL electrolyte). This design enables high surface-area mechanically robust interfaces, with a water-stable mechanically robust electrolyte that is capable of infiltrating and curing into these high aspect-ratio nanoporous interfaces.

The work builds upon the use of nanoporous silicon, as our previous efforts have shown the capability to etch high surface-area nanoporous silicon into bulk silicon platforms and passivate the silicon nanomaterials with ultra-thin carbon coatings that reverse the effect of surface traps and enable electrochemical stability of the silicon surface and that allow for good interfacial contact with electrolytes .[42, 43] Whereas the nanoporous silicon architecture is of direct interest for structural electronics and solar applications[14], similar nanoporous interfaces can be engineered in many technological materials, such as carbons or metals, leaving the implications of this work to be broadly applicable to many different technologies. In this case, it is of interest due to the strong covalently adhered nanoporous silicon/silicon current collector interface which makes it an excellent case study for a structural supercapacitor.

9.2 Experimental Methods

In order to develop a water resistant electrolyte, hydrophobic and commercially obtained bisphenol A/F based Super Sap CCR epoxy resin (Entropy Resins) was mixed with 1-butyl 3-methyl imidizolium tetrafluoroborate ($BMIBF_4$) and lithium tetrafluoroborate ($LiBF_4$) and then cured at 40-45°C overnight. Compared to other IL, $BMIBF_4$ was observed to yield the best isotropic mixtures with the resin, and $LiBF_4$ was mixed into the solution to enable curing at higher IL loadings as demonstrated previously by Shirshova et al.[44, 45] The Super Sap CCR epoxy resin was chosen as the structural portion of the electrolyte because of its high viscosity in the uncured state, and it’s relatively long working time of 3 hours when used with the corresponding CCS slow hardener (Polyoxypropylenediamine – Entropy Resins) that is important to achieve full infiltration of the nanoporous charge storage interface. To fabricate the structural supercapacitors, nanoporous Si electrodes were first synthesized via an electrochemical hydrofluoric acid (HF) etch and passivated via a carbonization procedure, after which the epoxy-IL electrolyte was infiltrated into individual nanoporous electrodes, and then sandwiched into a device and allowed to cure (**Figure 9.1a**). Full infiltration of the porous structure, whereas evident from electrochemical measurements, was

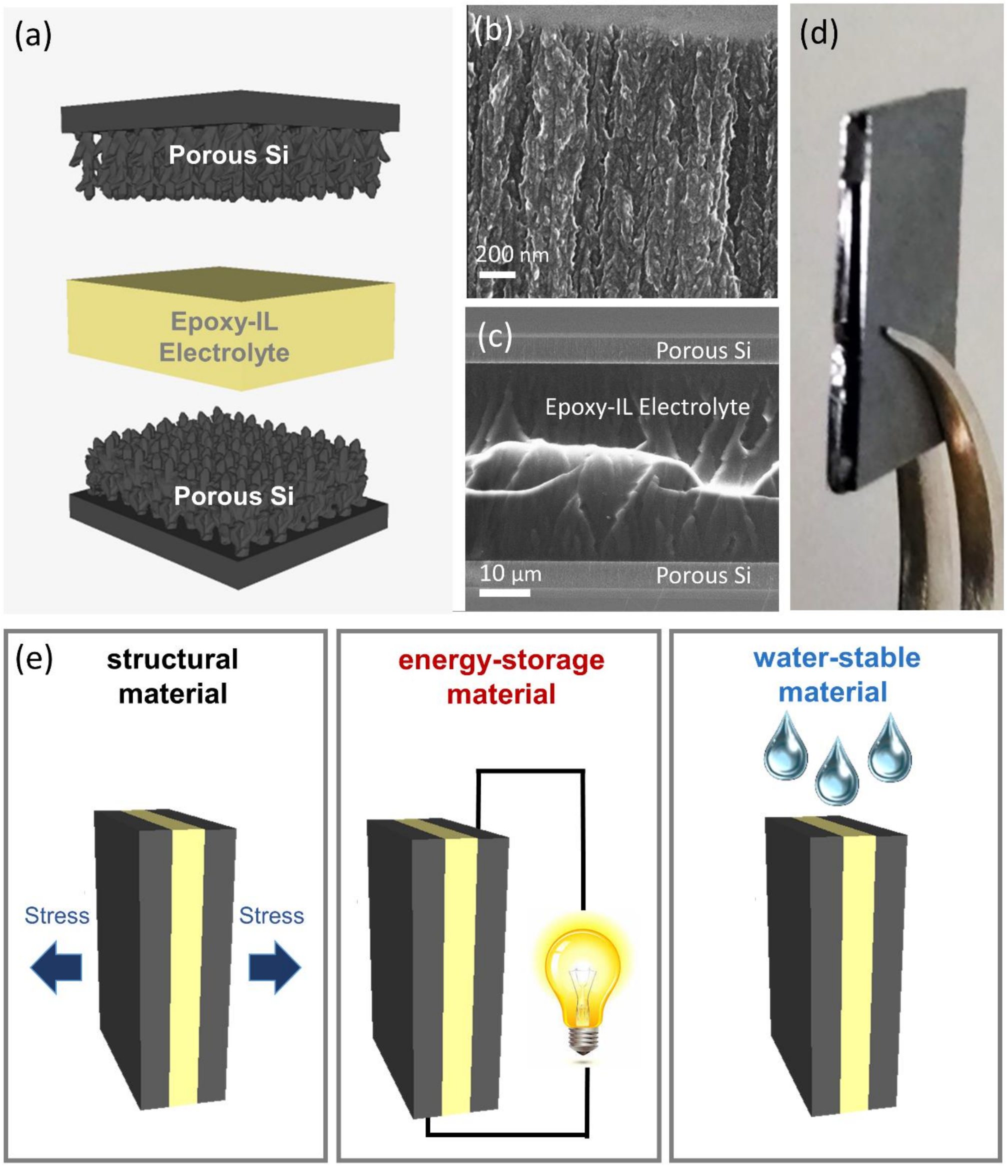

Figure 9.1 (a) Schematic of the epoxy/IL/nanoporous Si composite material. (b) SEM image of epoxy-IL infiltrated nanoporous Si. (c) SEM image of full epoxy/IL/nanoporous Si device. (d) Picture of a full device. (e) Schematic illustrating the multifunctional nature of the epoxy/IL/nanoporous Si composite material.

confirmed using scanning electron microscopy (SEM) (**Figure 9.1b-c**, **Figure 9.A1**). Full cross sectional SEM imaging of the device (**Figure 9.1c**) demonstrates an epoxy-IL film approximately 40 µm in thickness bridging the reinforced silicon interface on either side, with a photograph of a typical device in Figure 1d. This process resulted in a composite epoxy/IL/porous Si composite material capable of functioning as a water resistant structural composite and energy storage material (**Figure 9.1e**).

9.3 Results and Discussion

Two preliminary steps critical to this effort are (*i*) the development of the epoxy-IL electrolyte, and (*ii*) infiltration of the electrolyte into the nanoporous material to yield a structural supercapacitor. In this manner, tensile stress and ionic conductivity measurements were performed on epoxy-IL electrolytes with compositions ranging from 70% resin and 30% IL to 40% resin and 60% IL. Epoxy-IL electrolytes with greater than 70% resin did not provide measureable ionic conductivities, and ratios with less than 40% resin did not cure properly. We observe the mechanical strength and Young's modulus to decrease exponentially

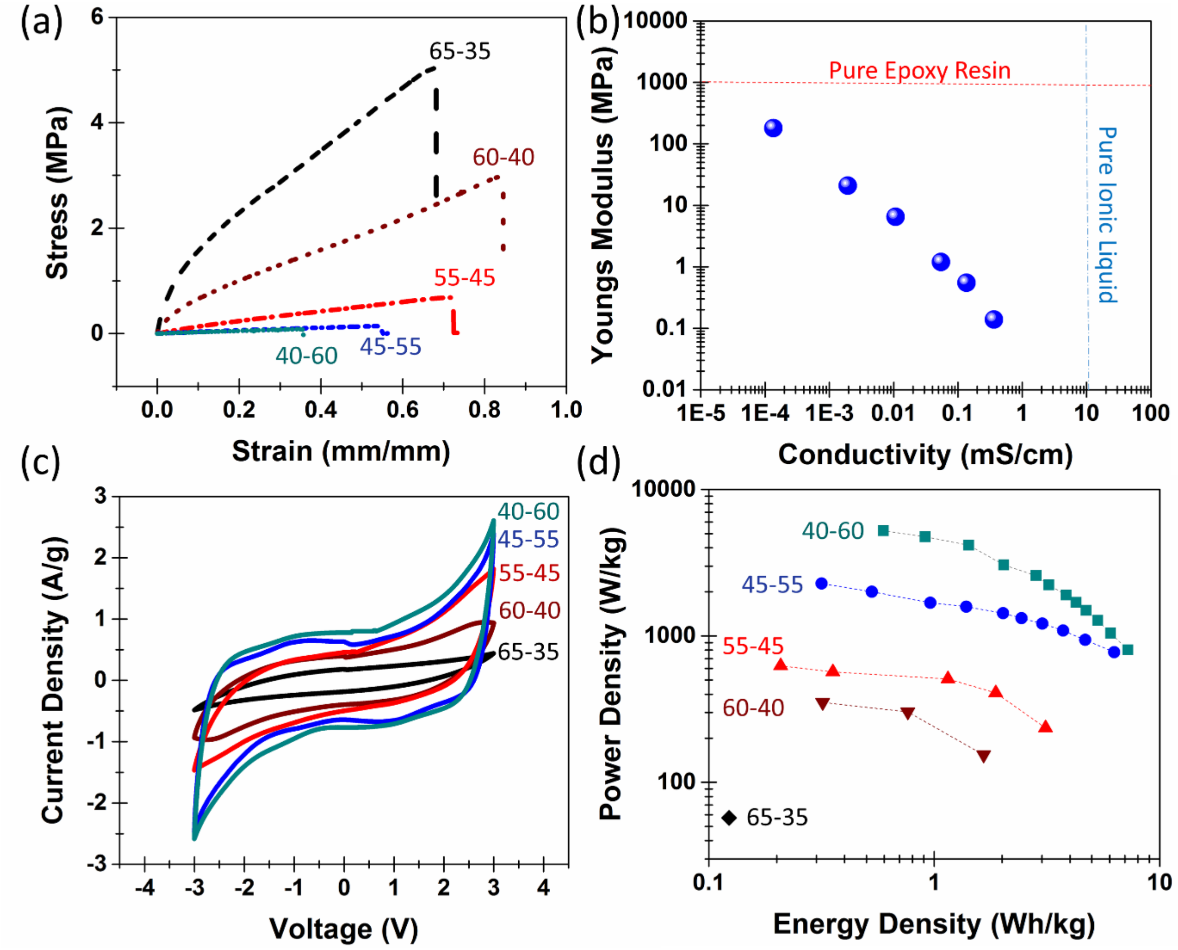

Figure 9.2 (a) Stress-strain curves for epoxy-IL electrolytes with epoxy-IL ratios ranging from 65%-35%, 40-60. (b) Graph showing the tradeoff between ionic conductivity and Young's modulus for epoxy-IL electrolytes with epoxy-IL ratios ranging from 70-30 to 40-60. (c) Cyclic voltametry curves of epoxy/IL/nanoporous Si composite with the same epoxy-IL ratios as in curve (a). (d) Ragone curves showing the effect of varying epoxy-IL ratios on epoxy/IL/nanoporous Si composite device energy and power performance for same electrolyte ratios as in (a).

as the IL concentration increases (**Figure 9.2a, 9.A2**) whereas the ionic conductivity increased exponentially (**Figure 9.A3**). This indicates a balance in IL loading and structural integrity that is highlighted in **Figure 9.2b.** Here, the dotted line across the top represents the Young's modulus of a pure Super Sap CCR epoxy resin, and the dashed line along the right represents the ionic conductivity of a pure IL. The ideal structural electrolyte would occur at the intersection of the two lines having the same strength as a pure resin, but maintaining the ionic conductivity of a pure IL. In our experimental system we observe IL loadings greater than 50% all indicate sufficient ionic conductivity (over .1 mS/cm) to provide competitive energy storage characteristics while at the same time maintaining enough structural integrity (tensile strength over 100kPa) to function as a structural material.

Next, we studied the effect of differing epoxy-IL ratios on the full device performance. **Figure 9.2c** shows cyclic voltammetry (CV) curves of full composite devices with varying epoxy-IL ratios. These CV curves indicate a stable voltage window near 3V for all epoxy-IL ratios and a linear increase of capacitance with IL loading (**Figure 9.A4a-b**), which is further confirmed with galvanostatic charge-discharge measurements (**Figure 9.A5**), galvanostatic measurements also indicate a linear and exponential increase of energy and power density, respectively, with IL loading (**Figure 9.2d**) attributed to the effect of series resistance on ion concentration (**Figure 9.A4d**). As a result, structural supercapacitors could only be practically developed with 40% or greater IL concentration. This was evidenced by the fact that we could only get a single data point for the Ragone curve in **Figure 9.2d** for the ratio of 65-35, and none for higher epoxy loadings due to instantaneous discharge due to resistance. This leads to devices, with optimal electrolyte configurations, which yield energy density of 5-8 Wh/kg and power density near 4 kW/kg. This is on par with activated carbon materials utilized in commercial supercapacitors and at minimum two orders of magnitude better than structural capacitor storage capability exhibited with carbon fiber electrodes.[19-21, 24] Notably, cycling tests demonstrate the ability to retain almost 100% of the energy density over the course of 4000 cycles (**Figure 9.A6**).

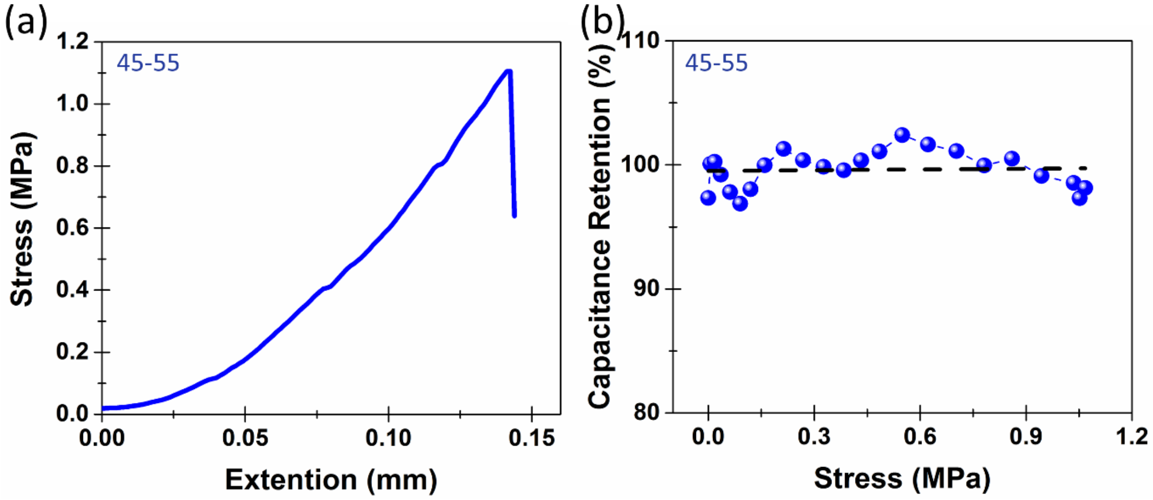

Figure 9.3 (a) Stress strain curve of epoxy/IL/nanoporous Si composite. (b) In-situ mechano-electrochemical data showing the effect of stress on specific capacitance of epoxy/IL/nanoporous Si composite devices.

Whereas this represents the operation of the individual components of the device, in order for this to be considered a multifunctional structural energy storage device it must demonstrate mechanical integrity and high quality energy storage *simultaneously*. This distinguishes our work from other reports, which only consider the separate mechanical and electrochemical performance of structural or multifunctional energy storage systems. To carry this out, we assess *in-situ* mechano-electrochemical performance of the devices using standard tensile tests at slow rates in order to perform *in-situ* electrochemical measurements**. Figure 9.3a** shows the *in-situ* stress strain curve for a nanoporous epoxy/IL/silicon composite with an epoxy-IL ratio of 45-55 by weight. The full device exhibited standard elastic behavior until failure occurred in the electrode's mechanical connections (at the grip/silicon interface) at about 1.1 MPa. At this tensile stress, structural device failure had not yet occurred, emphasizing this result as a lower limit of tensile strength for the structural storage device, which still represents a 3-4X improvement over PEO based devices.[31] The greater tensile strength measured for the device versus the long molded bulk epoxy-IL electrolyte sample also represents the difference in geometry on defect mediated bulk failure of the epoxy-IL electrolyte. Following from this result, **Figure 9.3b** indicates that the overall capacitance remains stable, with exception of minor (<3- 4%) fluctuations, over the course of the tensile measurement. This emphasizes the signature of a structural energy storage material, with excellent charge storage capability even when subject to mechanical stresses.

Whereas the basic requirement for a structural energy storage material is the ability to simultaneously maintain mechanical integrity and store and release energy, most structural materials integrated into technological systems are subject to environmental conditions, unless otherwise packaged. In this manner, the prospect of packaging for a composite material that would be integrated into a building or on an electric vehicle or an aircraft would present significant challenges. Therefore, the native function of structural energy storage would need to be maintained in an environment subject to humidity and precipitation. This poses a significant challenge for many conventional polymeric systems when used as ionic conducting polymer electrolytes which are highly unstable in aqueous environments, such as PEO which spontaneously dissolve in water (**Figure 9.A7**). To assess the water stability of our structural energy storage devices, we simulated an extreme condition where the devices or epoxy-IL electrolytes are soaked underwater for 2 hours prior to testing. **Figure 9.4a** shows two tensile tests of 45-55 bulk epoxy-IL electrolytes that were prepared at the same time. One of them was tested after being soaked in water for 2 hours while the other one was tested in its pristine condition (no water exposure) (A picture of the wet and dry electrolytes is found in **Figure 9.A8**). The Young's modulus for the wet sample slightly decreased by 5%, and the ultimate tensile strength was reduced by about 65%. However, we observe this effect to be completely reversible upon drying (**Figure 9.4c, 9.A9**). As the epoxy-IL electrolytes visually indicate a slight effect of physical swelling, we attribute this change to water absorption which is fully reversible after drying occurs. This is in direct contrast to a PEO electrolyte with a similar PEO:EMIBF$_4$ ratio (50:50) where the mechanical integrity was compromised within 1 minute of being immersed in water and complete dissolution occurred within 30 minutes – shorter than the timeframe of water exposure in our epoxy-IL electrolyte tests (**Figure 9.A6**).

In addition to wet-dry testing of epoxy-IL electrolytes, we further performed a similar two hour soak test on a full structural supercapacitor device to ascertain the effect of water immersion on the electrochemical performance. The device was first tested in an as-prepared state, immersed in water and tested in this condition, and then tested again after drying. **Figure 9.4b** shows representative galvanostatic charge discharge measurements taken in these different conditions. While immersed in water the device exhibited a significantly lower equivalent series resistance, and a corresponding significant increase in the specific capacitance (**Figure 9.4c, 9.A10**). It also exhibited a significant decrease in the Coulombic efficiency from 99% to 60% while immersed underwater likely due to a portion of Faradaic localized water

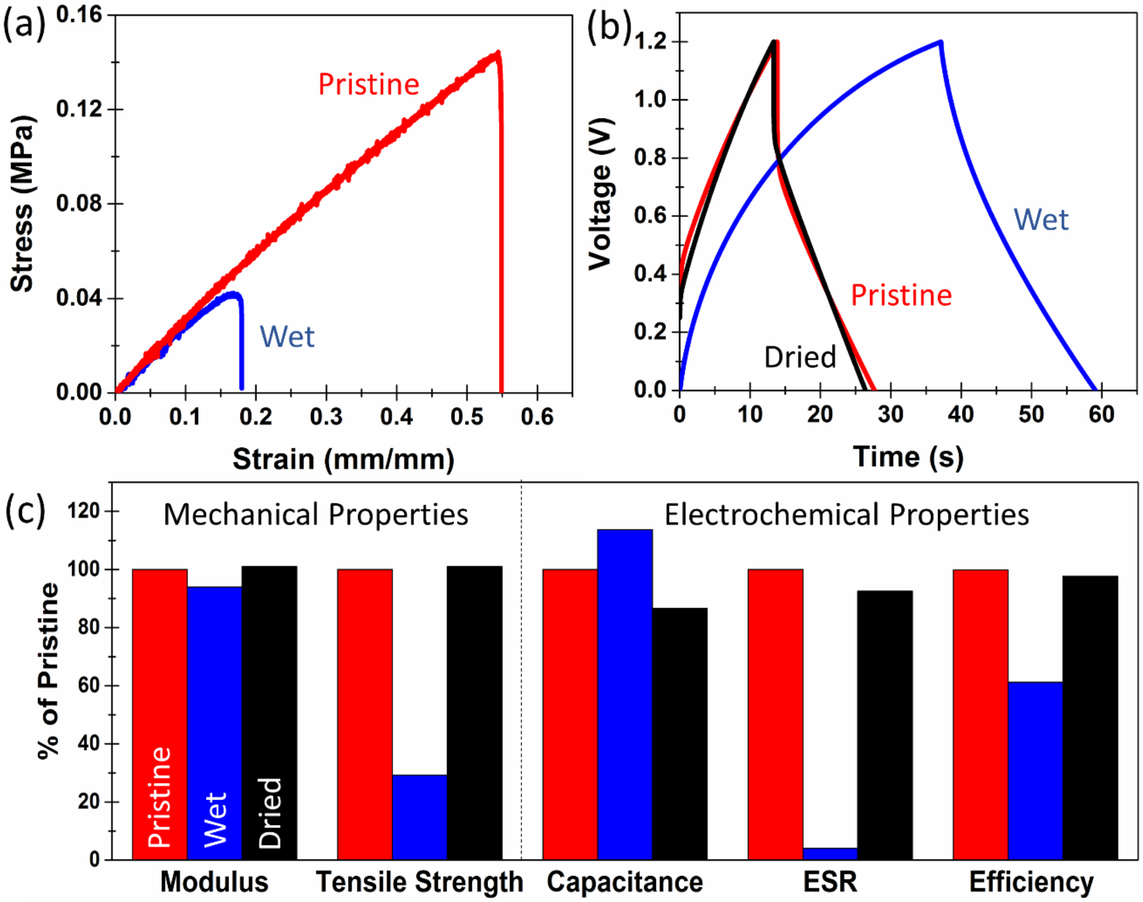

Figure 9.4 (a) Stress-strain curves of an epoxy-IL electrolyte in its prisitne condition and after being soaked in water for 2 hours. (b) galvanostatic charge discharge curves for a pristine device, the same device tested underwater after being soaked in water for 2 hours, and the same device after it was completely dried. (c) Comparison of the wet-dry mechanical properties of the bulk epoxy-IL electrolyte, and the electrochemical properties of the full devices. All measurements are for the epoxy-IL ratio of 45-55.

splitting or electrochemical oxidation. After drying, the device performance recovered very close to its initial pristine condition but with a small decrease in the specific capacitance, which could either represent oxidation effects in either the resin or electrodes. Despite the small decrease in capacitance after an extreme condition of water exposure, the device performance is maintained for both charge storage and mechanical integrity during and after immersion. Therefore, under exposure to less extreme environments such as high humidity or periods of rain that are more likely in working environments, the inherent function of the multifunctional structural energy storage material would remain in-tact.

9.4 Conclusion

Overall, we demonstrate the first structural supercapacitor capable of simultaneously storing and releasing energy under tensile stresses of greater than 1 MPa and under extreme conditions of water immersion. This is enabled through the development of a bisphenol A/F epoxy-IL electrolyte exhibiting passive behavior in humid or aqueous environments, but with curing characteristics enabling epoxy-IL infiltration into a high surface nanoporous reinforcing interface. We measure energy densities of up to 5-8 Wh/kg with nearly 100% energy retention over 4000 cycles and at tensile stresses over 1 MPa. We further observe any temporary adverse effect of extreme water exposure on these devices to be reversible, motivating their use for long-term energy carriers without the need for additional packaging to achieve stable operation in outdoor environments. This work lays the foundation for an emerging class of energy storage materials that can both catalyze technological progress and foster new applications requiring built-in energy delivery capability.

9.A Appendix

9.A.1 Detailed Experimental Procedures

Synthesis of carbonized porous Si electrodes:

Nanoporous silicon was synthesized from silicon wafers (.01-.02 Ω cm^{-1}) using an electrochemical etch with an electrolyte of 3:7 v/v HF (50% H_2O by volume) and ethanol at 45mA/cm^2 for 180s in an AMMT etching system. This yields a porous layer mechanically tethered to bulk silicon that exhibits approximately 75% porosity and is 4.5μm in thickness. A passivating carbon coating was then applied to the porous Si using chemical vapor deposition using a ramp procedure where a mixture of acetylene, hydrogen and argon were flowed over the sample in a ratio of 1:20:100, with two consecutive temperature ramps for 10 minutes each of 650-750 °C and 750-850 °C. Further details on this ramp procedure and the electrochemical stability of passivated nanoporous silicon materials can be found elsewhere, including representative microscopy images and material analysis.[42, 43]

Synthesis of epoxy-IL electrolyte and full devices*:*

Epoxy-IL electrolytes were developed by first dissolving $LiBF_4$ into $BMIBF_4$ in a ratio of 1:4. Next, Super Sap CCR epoxy resin (Entropy Resins) and its corresponding CCS slow hardener (Entropy Resins) were mixed together in a 2:1 ratio via a 2 stage mixing process in a Thinky ARE 250 Planetary and Centrifugal Mixer with an initial planetary mixing step for 6 minutes at 2000rpm, followed by a centrifugal mix for 2 minutes at 2100rpm to degas the mixture. The SuperSap CCR epoxy is made up of epoxidized pine oils, bisphenol A/F type epoxy resin, benzyl alcohol, and proprietary reactive epoxy diluents, and the CCS slow hardener is polyoxypropylenediamine. The epoxy mixture was then combined with $LiBF_4$/$BMIBF_4$ with varying epoxy-IL ratios ranging from 70% epoxy and 30% IL to 40% epoxy and 60% IL. The final uncured epoxy-IL electrolyte was then poured into the desired shape and placed in an oven at 40-45 °C and allowed to cure overnight. Full devices were synthesized by pouring the same uncured epoxy-IL electrolyte mixture over the passivated nanoporous silicon electrodes and placing them in a vacuum oven under vacuum at 50°C for approximately 20 minutes to remove the excess air from the porous Si electrodes before placing in the oven for the overnight cure.

Mechanical testing of bulk epoxy-IL electrolyte:

Mechanical testing of the bulk epoxy-IL electrolyte was performed using an Instron 5944 single column load frame at a rate of 2 mm/s with a 2kN load cell.

Electrochemical testing of bulk epoxy-IL electrolyte and devices:

Ionic conductivity was determined by placing steel disks on the either side of a bulk epoxy-IL electrolyte (~1cm by 1cm) and performing electrochemical impedance spectroscopy (EIS) from 1 MHz to .1 Hz with a sinusoidal wave pattern of amplitude 10 mV around 0V. EIS, cyclic voltammetry, and galvanostatic charge discharge measurements were performed using a portable Autolab potentiostat/galvanostat. Energy density was calculated from galvanostatic discharge curves by numerical integration according to the following equation $E = \int_0^t IVdt$ where I represents the current, and V the voltage and t is the total discharge time. This notably yields the exact energy density; this number is lower than the energy density obtained using the more conventional approximate $E = 1/2CV^2$ relation which assumes a perfectly linear discharge current.[29, 42, 43] Specific Capacitance was calculated from both the CV and galvanostatic charge discharge curves. In order to calculate the specific capacitance from the CV curves (Csp), the area under the positive and negative sides of the CV curve was averaged and then divided by the scan rate (R), the weight (m), and the total voltage range (ΔV) according to the following equation:

$$C_{sp} = \frac{1}{m\Delta VR}\int_{V_b}^{V_a} I(V)dV$$

Specific capacitance was calculated from galvanostatic discharge curves by fitting a line to the discharge curve to find a slope which is equivalent to the change in Voltage over time or $\Delta V/\Delta t$. The current was then divided by this slope and by the device mass. Or equivalently

$$C_{sp} = \frac{I\ \Delta t}{m\ \Delta V}$$

In-situ mechano-electrochemical tests:

In order to perform simultaneous mechanical and electrochemical measurements, we first built custom-designed grips with a flat top surface that clipped into the Instron testing system. The top of these grips, and the outer surfaces of the supercapacitor electrodes were both roughened using 100 grit sandpaper and a diamond scribe respectively, after which a pure low viscosity MAS epoxy resin (MAS Epoxies), with the corresponding MAS slow hardener (MAS Epoxies), was applied and cured as an adhesive layer between the grips and the devices. The outer edges of the device electrodes were then used as electrical contacts allowing for simultaneous tensile and electrochemical measurements. In order to ensure that the measured tensile load was essentially the same for any single electrochemical measurement the tensile stress was applied at the relatively slow rate of .0008 mm /s.

Wet-dry testing:

Wet-dry testing of the bulk epoxy-IL electrolyte tensile samples was performed by synthesizing two identical tensile specimens with the same batch of epoxy-IL electrolyte. One of the specimens was then immersed in water for two hours, and then quickly tested after removal from the water, while the other was tested in its pristine condition. The electrochemical wet-dry testing of the devices was performed using galvanostatic charge discharge tests under 1.2V on the same device first in the pristine condition, then while immersed in water after soaking for 2 hours, and finally after drying for over 3 days.

9.A.1 ***Supporting Figures***

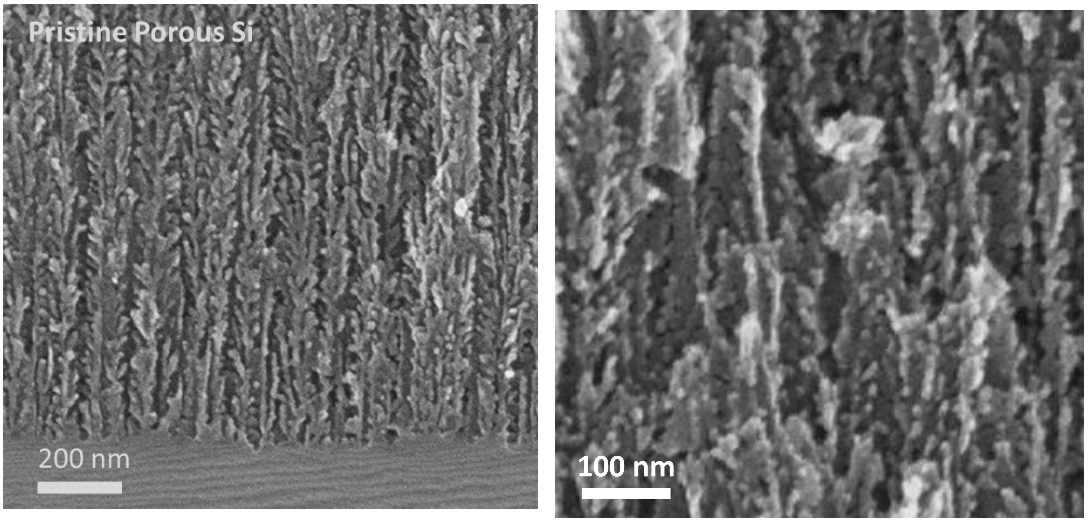

Figure 9.A1 SEM images of pristine porous Si showing the detailed pore structure

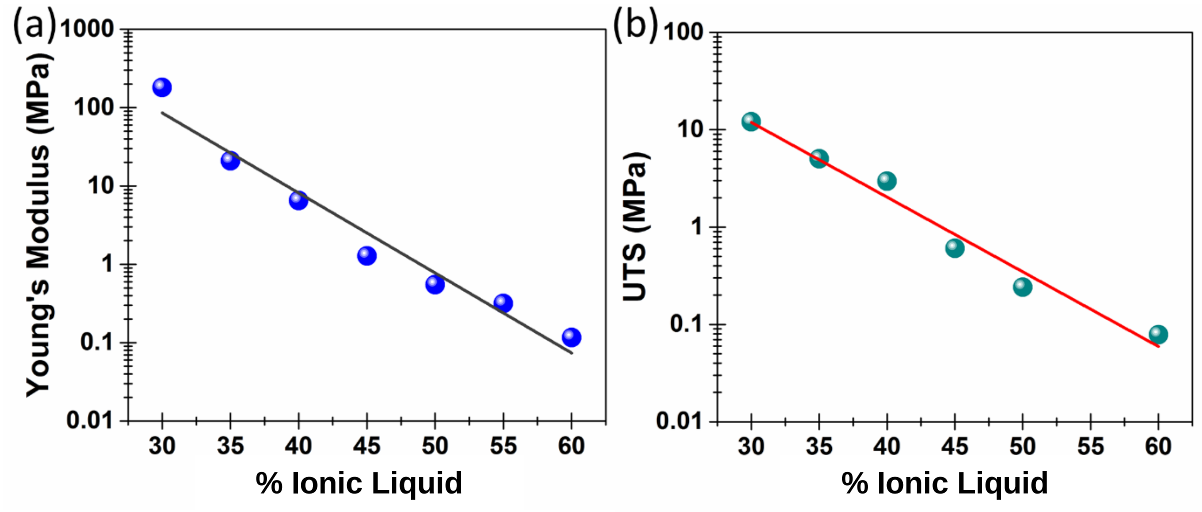

Figure 9.A2 (a) Young's Modulus as a function of IL loading. (b) Ultimate tensile stress (UTS) as a function of IL loading.

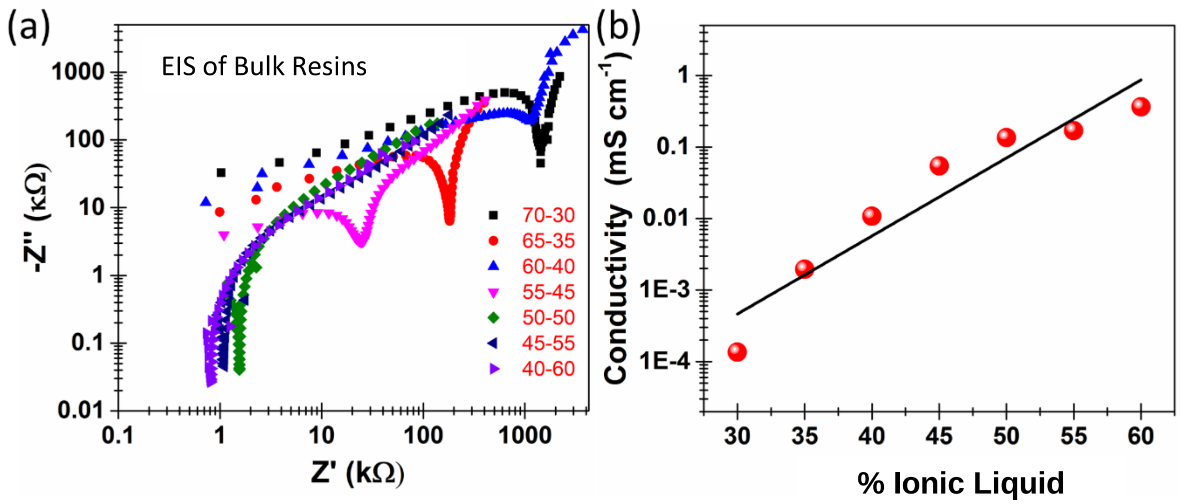

Figure 9.A3 (a) Electron Impedance Spectroscopy (EIS) curves of bulk epoxy-IL electrolytes placed on a log scale to enable comparisons. (b) Ionic conductivity as a function of IL loading as measured from EIS curves.

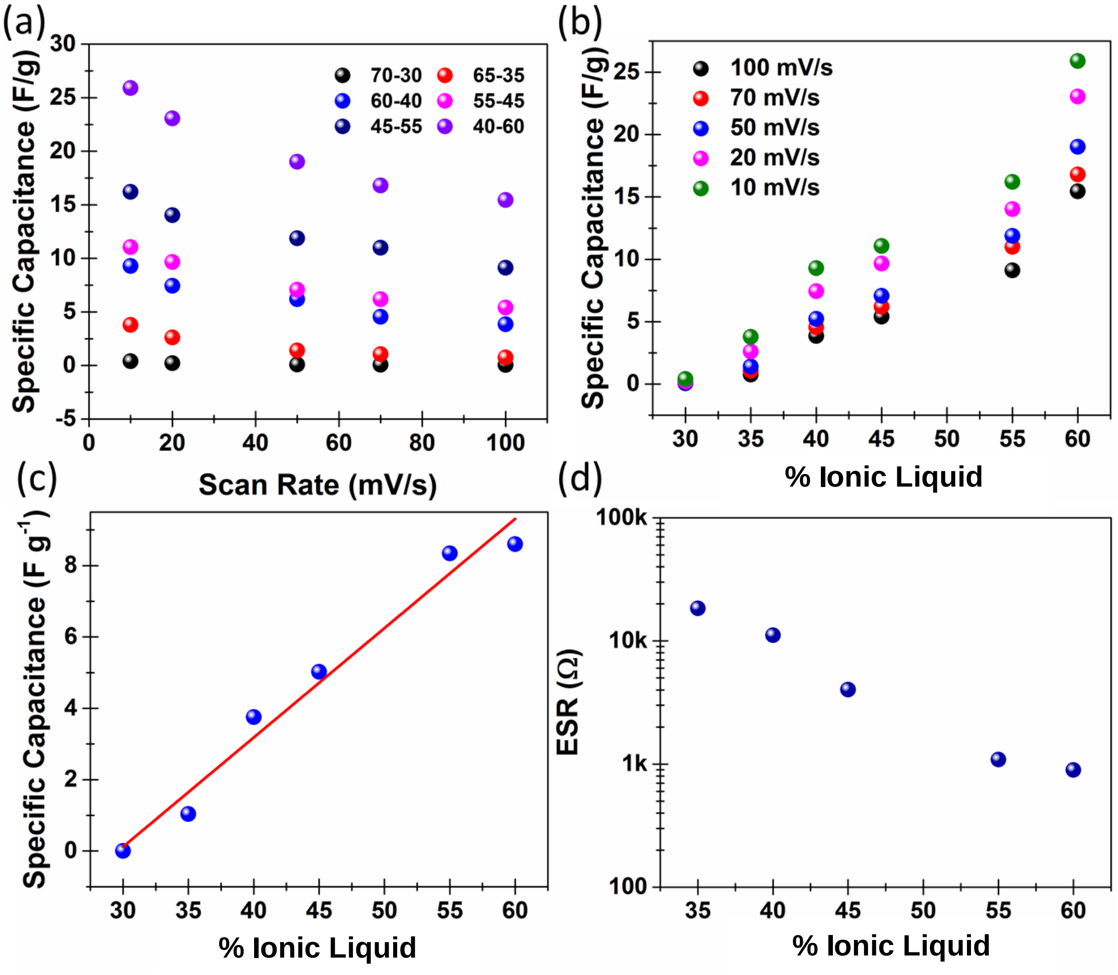

Figure 9.A4 (a) Specific capacitance as a function of scan rate as measured by cyclic voltammetry (CV) for various epoxy-IL ratios. (b) Specific Capacitance as a function of IL loading measured from CV curves. (c) Specific Capacitance as a function of IL loading as measured from galvanostatic discharge curves. (d) Equivalent series resistance (ESR) as a function of IL loading from galvanostatic discharge curves.

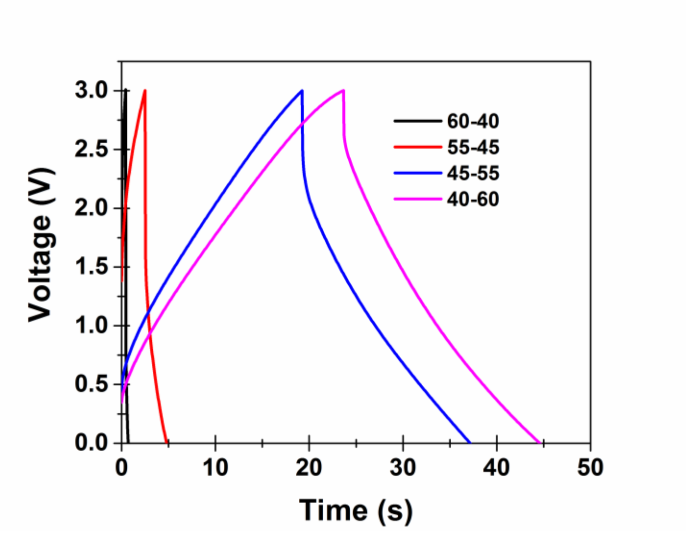

Figure 9.A5 Comparison of Galvanostatic charge discharge curves of the devices with various Epoxy Resin-IL ratios at 1 A/g.

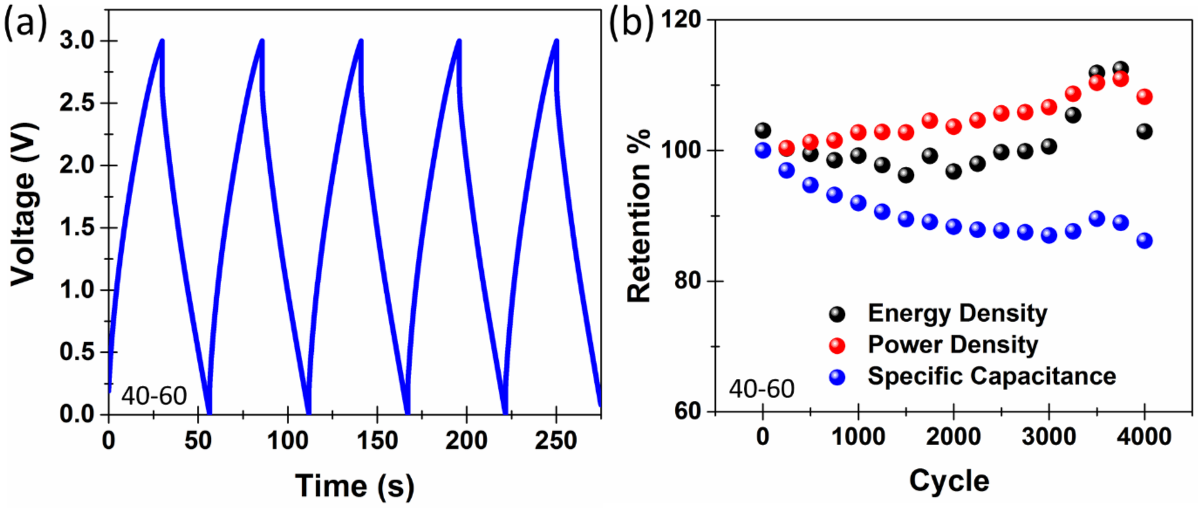

Figure 9.A6 (a) Consecutive charge discharge curves for a device with epoxy-IL electrolyte ratio of 40-60. (b) Cycling performance over 4000 cycles.

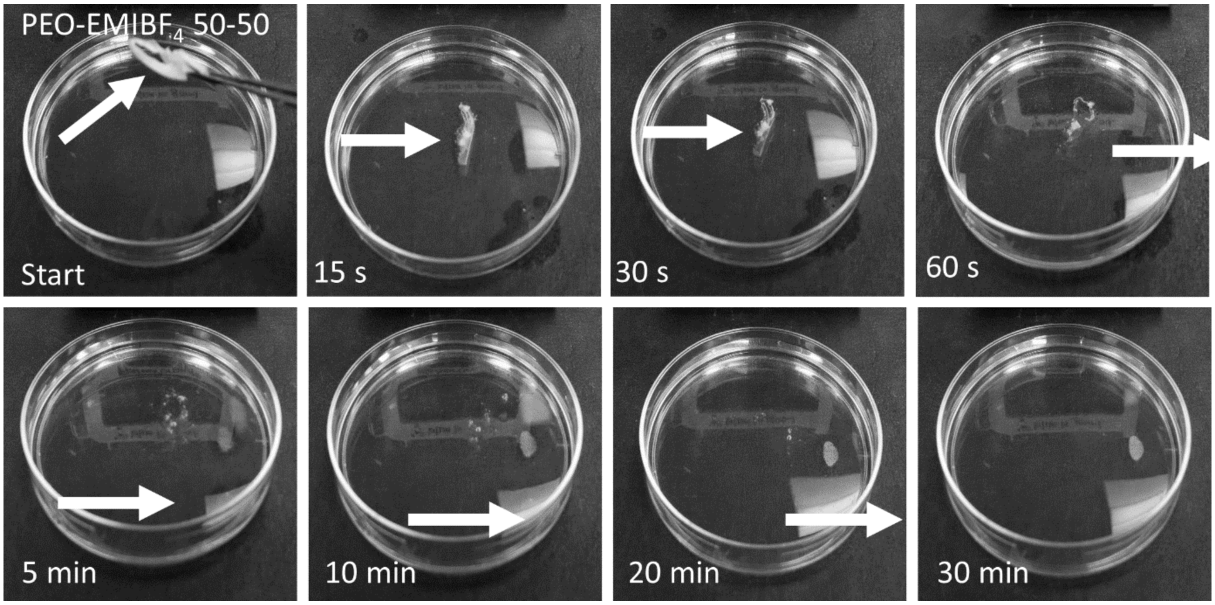

Figure 9.A7 A series of photographs showing the dissolution of a polyethylene oxide (PEO) / 1-ethyl 3-methyl imidizolium tetra fluoroborate (EMIBF$_4$) polymer electrolyte in water.

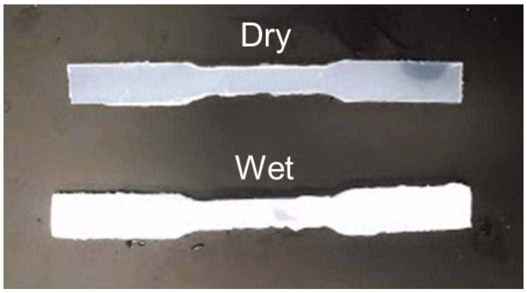

Figure 9.A8 Picture of the epoxy-IL composite electrolyte in the initial (dry) state and after being immersed in water for 2 hours (wet).

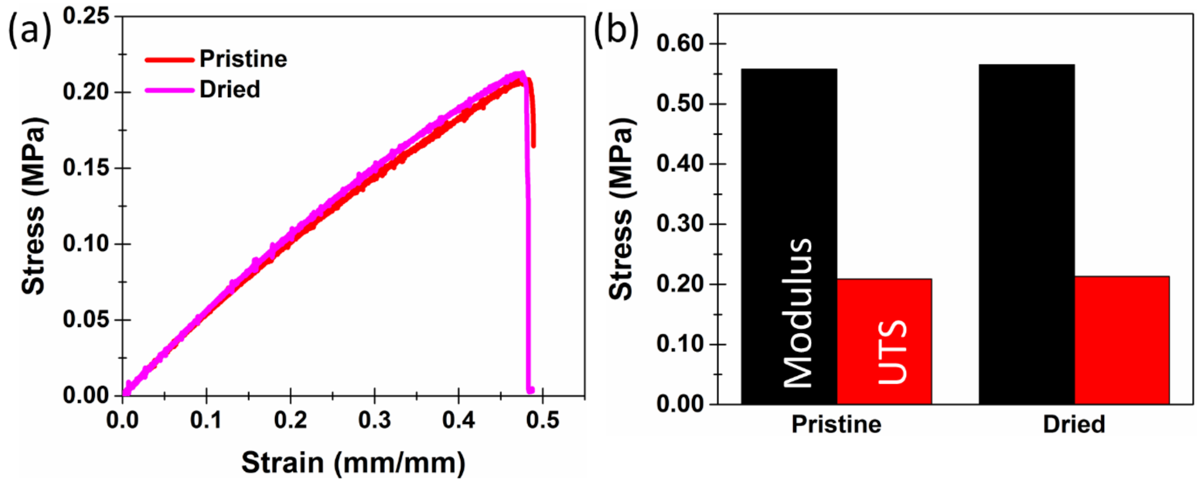

Figure 9.A9 (a) Stress/strain measurement for bulk epoxy resin electrolytes with epoxy-IL ratio of 45-55 in the pristine condition and after both a 2 hour soak in water and subsequent drying. (b) Young's modulus and the ultimate tensile strength (UTS) for the pristine and dried samples as measured from **Figure 9.A6a**.

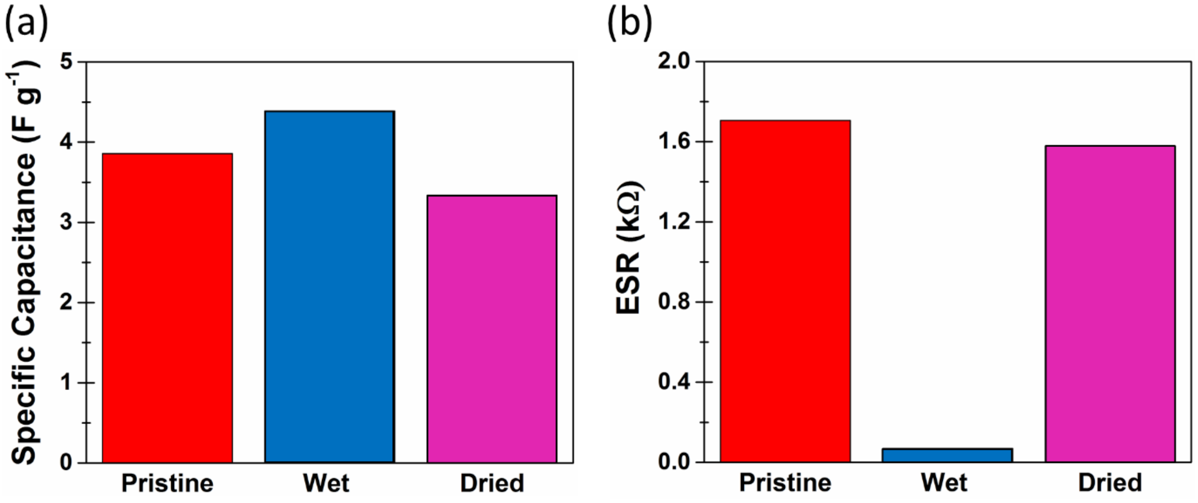

Figure 9.A10 (a) Actual numerical values for the specific capacitance for the galvanostatic charge discharge curves in **Figure 9.3d**, and reported in **Figure 9.3e**. (b) Actual numerical values of the equivalent series resistance (ESR) for the galvanostatic charge discharge curves in **Figure 9.3d**, and reported in **Figure 9.3e**.

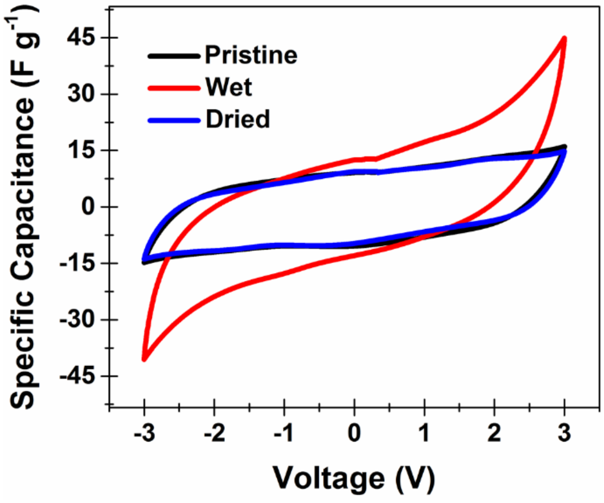

Figure 9.A11 Cyclic Voltammetry curves of a full device in its pristine condition, tested while underwater after a 2 hour soak, and after the device had been completely dried.

Acknowledgements

We thank K. Share, A. Cohn, and R. Carter for useful discussions related to this work. This work was supported in part by NSF grant CMMI 1334269, and an ORAU Ralph E. Powe award.

References

1. Westover, A. S.; Baer, B.; Bello, B. H.; Sun, H.; Oakes, L.; Bellan, L. M.; Pint, C. L. *Journal of Materials Chemistry A* **2015,** 3, (40), 20097-20102.

2. Lee, J. S.; Tai Kim, S.; Cao, R.; Choi, N. S.; Liu, M.; Lee, K. T.; Cho, J. *Advanced Energy Materials* **2011,** 1, (1), 34-50.

3. Rahman, M. A.; Wang, X.; Wen, C. *Journal of Applied Electrochemistry* **2014,** 44, (1), 5-22.

4. Aricò, A. S.; Bruce, P.; Scrosati, B.; Tarascon, J.-M.; Van Schalkwijk, W. *Nature materials* **2005,** 4, (5), 366-377.

5. Evers, S.; Nazar, L. F. *Accounts of chemical research* **2012,** 46, (5), 1135-1143.

6. Gao, X.-P.; Yang, H.-X. *Energ Environ Sci* **2010,** 3, (2), 174-189.

7. Dunn, B.; Kamath, H.; Tarascon, J.-M. *Science* **2011,** 334, (6058), 928-935.

8. Kang, B.; Ceder, G. *Nature* **2009,** 458, (7235), 190-193.

9. Simon, P.; Gogotsi, Y. *Nat. Mater.* **2008,** 7, (11), 845-854.

10. Westover, A. S.; Freudiger, D.; Gani, Z. S.; Share, K.; Oakes, L.; Carter, R. E.; Pint, C. L. *Nanoscale* **2015,** 7, (1), 98-103.

11. Kim, S. W.; Seo, D. H.; Ma, X.; Ceder, G.; Kang, K. *Advanced Energy Materials* **2012,** 2, (7), 710-721.

12. Weber, A. Z.; Mench, M. M.; Meyers, J. P.; Ross, P. N.; Gostick, J. T.; Liu, Q. *Journal of Applied Electrochemistry* **2011,** 41, (10), 1137-1164.

13. Slater, M. D.; Kim, D.; Lee, E.; Johnson, C. S. *Advanced Functional Materials* **2013,** 23, (8), 947-958.

14. Westover, A. S.; Share, K.; Carter, R.; Cohn, A. P.; Oakes, L.; Pint, C. L. *Applied Physics Letters* **2014,** 104, (21), 213905.

15. Chen, T.; Yang, Z.; Peng, H. *ChemPhysChem* **2013,** 14, (9), 1777-1782.

16. Guo, W.; Xue, X.; Wang, S.; Lin, C.; Wang, Z. L. *Nano Lett.* **2012,** 12, (5), 2520-2523.

17. Snyder, J. F.; Wong, E. L.; Hubbard, C. W. *J Electrochem Soc* **2009,** 156, (3), A215-A224.

18. O'Brien, D.; Baechle, D.; Wetzel, E. *Journal of Composite Materials* **2011,** 45, (26), 2797-2809.

19. Pereira, T.; Guo, Z.; Nieh, S.; Arias, J.; Hahn, H. T. *Journal of composite materials* **2009,** 43, (5), 549-560.

20. Huang, Y.; Hu, H.; Huang, Y.; Zhu, M.; Meng, W.; Liu, C.; Pei, Z.; Hao, C.; Wang, Z.; Zhi, C. *ACS nano* **2015**.

21. Huang, Y.; Huang, Y.; Meng, W.; Zhu, M.; Xue, H.; Lee, C.-S.; Zhi, C. *ACS applied materials & interfaces* **2015,** 7, (4), 2569-2574.

22. Huang, Y.; Huang, Y.; Zhu, M.; Meng, W.; Pei, Z.; Liu, C.; Hu, H.; Zhi, C. *ACS nano* **2015,** 9, (6), 6242-6251.

23. Shirshova, N.; Qian, H.; Shaffer, M. S.; Steinke, J. H.; Greenhalgh, E. S.; Curtis, P. T.; Kucernak, A.; Bismarck, A. *Composites Part A: Applied Science and Manufacturing* **2013,** 46, 96-107.

24. Qian, H.; Kucernak, A. R.; Greenhalgh, E. S.; Bismarck, A.; Shaffer, M. S. *ACS applied materials & interfaces* **2013,** 5, (13), 6113-6122.

25. Qian, H.; Diao, H.; Shirshova, N.; Greenhalgh, E. S.; Steinke, J. G.; Shaffer, M. S.; Bismarck, A. *Journal of colloid and interface science* **2013,** 395, 241-248.

26. Javaid, A.; Ho, K.; Bismarck, A.; Shaffer, M.; Steinke, J.; Greenhalgh, E. *Journal of Composite Materials* **2014,** 48, (12), 1409-1416.

27. Lin, Y.; Sodano, H. A. *Journal of Applied Physics* **2009,** 106, (11), 114108.

28. Shirshova, N.; Qian, H.; Houllé, M.; Steinke, J. H.; Kucernak, A. R.; Fontana, Q. P.; Greenhalgh, E. S.; Bismarck, A.; Shaffer, M. S. *Faraday discussions* **2014,** 172, 81-103.

29. Westover, A. S.; Tian, J. W.; Bernath, S.; Oakes, L.; Edwards, R.; Shabab, F. N.; Chatterjee, S.; Anilkumar, A. V.; Pint, C. L. *Nano Lett.* **2014,** 14, (6), 3197-3202.

30. Benson, J.; Kovalenko, I.; Boukhalfa, S.; Lashmore, D.; Sanghadasa, M.; Yushin, G. *Advanced Materials* **2013,** 25, (45), 6625-6632.

31. Agrawal, R.; Pandey, G. *Journal of Physics D: Applied Physics* **2008,** 41, (22), 223001.

32. Hallinan Jr, D. T.; Balsara, N. P. *Annual Review of Materials Research* **2013,** 43, 503-525.

33. Mecerreyes, D. *Progress in Polymer Science* **2011,** 36, (12), 1629-1648.

34. Wu, Z. S.; Winter, A.; Chen, L.; Sun, Y.; Turchanin, A.; Feng, X.; Müllen, K. *Advanced Materials* **2012,** 24, (37), 5130-5135.

35. Westover, A. S.; Shabab, F. N.; Tian, J. W.; Bernath, S.; Oakes, L.; Erwin, W. R.; Carter, R.; Bardhan, R.; Pint, C. L. *J Electrochem Soc* **2014,** 161, (6), E112-E117.

36. Tang, C.; Hackenberg, K.; Fu, Q.; Ajayan, P. M.; Ardebili, H. *Nano letters* **2012,** 12, (3), 1152-1156.

37. Stephan, A. M. *European Polymer Journal* **2006,** 42, (1), 21-42.

38. Srivastava, N.; Tiwari, T. *e-Polymers* **2009,** 9, (1), 1738-1754.

39. Devanand, K.; Selser, J. *Nature* **1990,** 343, (6260), 739-741.

40. Maggi, L.; Segale, L.; Torre, M.; Machiste, E. O.; Conte, U. *Biomaterials* **2002,** 23, (4), 1113-1119.

41. Van Wagner, E. M.; Sagle, A. C.; Sharma, M. M.; La, Y.-H.; Freeman, B. D. *Journal of Membrane Science* **2011,** 367, (1), 273-287.

42. Chatterjee, S.; Carter, R.; Oakes, L.; Erwin, W. R.; Bardhan, R.; Pint, C. L. *J. Phys. Chem. C* **2014,** 118, (20), 10893-10902.

43. Oakes, L.; Westover, A.; Mares, J. W.; Chatterjee, S.; Erwin, W. R.; Bardhan, R.; Weiss, S. M.; Pint, C. L. *Sci. Rep.* **2013,** 3, 3020.

44. Shirshova, N.; Bismarck, A.; Carreyette, S.; Fontana, Q. P.; Greenhalgh, E. S.; Jacobsson, P.; Johansson, P.; Marczewski, M. J.; Kalinka, G.; Kucernak, A. R. *Journal of Materials Chemistry A* **2013,** 1, (48), 15300-15309.

45. Shirshova, N.; Bismarck, A.; Greenhalgh, E. S.; Johansson, P.; Kalinka, G.; Marczewski, M. J.; Shaffer, M. S.; Wienrich, M. *The Journal of Physical Chemistry C* **2014,** 118, (49), 28377–28387.

CHAPTER 10

TOWARD STRONG CARBON NANOTUBE MECHANICAL INTERFACES WITH SOLID SURFACES: A CHALLENGE INTERSECTING GROWTH SCIENCE AND APPLICATIONS

*Andrew S. Westover[1,2], Eti Teblum[3], Farhan N. Shabob[1], Gilbert D. Nessim[3], and Cary L. Pint[1,2]**

[1]Department of Mechanical Engineering, Vanderbilt University, Nashville TN 37235, USA

[2]Interdisciplinary Materials Science Program, Vanderbilt University, Nashville, TN 37235, USA

[3]Department of Chemistry, Bar Ilan Institute for Nanotechnology and Advanced Materials (BINA), Bar Ilan University, 52900 Ramat Gan, Israel

Abstract: Central to many applications possible for carbon nanotubes (CNTs) is the necessity to form a mechanically robust heterogeneous interface that can harness the mechanical and electrical properties of CNTs. Here we report a study of CNT arrays grown on stainless steel substrates, infiltrated with ion-conducting polymers, and subjected to *in-situ* mechanical-electrochemical testing to identify the signature of failure. Mechanical failure occurs near 15 kPa through delamination at the steel-CNT interface, emphasizing a weak interface that presents a key challenge for many CNT-based applications. As mechanical properties of CNT interfaces are largely unexplored, we highlight this as an important area of research where the synergy of CNT growth science and mechanical testing can lead to a new paradigm of multifunctional devices.

10.1 Introduction

Carbon nanotube (CNT) mechanical properties are have often been reported on both the single-CNT level and in bulk homogenous composite materials containing CNTs as one component. The mechanical properties of individual CNTs are extraordinary, touting tensile strength up to 10X that of steel, but with a lower mass density than metals.[1] However, a challenge that remains open to the research community is how to address these extraordinary mechanical properties in bulk CNT systems. Front and center to this challenge is the ability to control mechanical properties of CNT materials to solid surfaces – a research area that has not been widely explored.[2] Whereas studies have qualitatively indicated the presence of robust mechanical interfaces,[3-5] no progress has been made to translate these principles to bulk CNT-based applications.

CNTs present an ideal system for multifunctional applications, such as structural energy storage, composite electrodes for energy conversion, and structural thermal interfaces. To harness the full potential of CNT mechanical properties in these applications, electrode design requires excellent mechanical and electrical connectivity between a growth substrate and the active CNT material. Whereas research on CNT growth science, particularly in organized CNT arrays, has widely emerged in the past several years, measuring the mechanical properties of interfaces has not yet been coupled with these efforts. However, for as-grown CNT materials, the mechanisms underlying CNT growth processes overlap with the resulting mechanical connection between CNTs and substrates. In this brief letter, we demonstrate a straight-forward *in-situ* electrochemical-mechanical testing technique to address mechanical properties of as-grown CNT materials. Our efforts highlight the weak mechanical tensile properties of CNT arrays grown on steel substrates, and provide an open area of exciting research intersecting growth science and next-generation CNT-based applications to improve mechanical properties at these interfaces.

10.2 Experimental Methods

10.2.1 CNT growth experimental details

Type 316 grade stainless steel coins (0.5mmthick, 15.5mm diameter) were purchased from Tzamal D- Chem laboratories Ltd. and were used as substrates for CNT growth. We performed the CNT synthesis in a three zone atmospheric-pressure tube furnace (Carbolite model HZS-E), using a single fused-silica tube with an internal diameter of 22 mm.[6-8]. For the growth, we introduced the following mixture of of gases: 100 sccm of Ar, 400 sccm of H_2, 250 sccm of Ar/O_2 (99/1) and 200 sccm of C_2H_4. The first two zones of the furnace preheated the precursor gases at 770 °C, decomposing the hydrocarbon gases and forming water vapor from O_2 and H_2.[9]

The vertically aligned CNTs (VA-CNTs) were characterized using field-emission scanning electron microscopy (FESEM; FEI, Helios600) operating at 5 keV and high-resolution transmission electron microscopy (HRTEM) using a JEOL-2100 operating at 200 keV. HRTEM samples were prepared by dispersing a section of the CNT carpet in 2-propanol with gentle sonication for an hour and then placing 1 drop of the solution on a 300 mesh Cu holey carbon grid (from SPI).

The morphology, structure, and substrate coverage of VA-CNTs on stainless steel substrate were characterized using FESEM. VACNTs uniformly covered the stainless steel substrate. The height of the VA-CNT carpet varied from 25 μm up to 40 μm. The average diameter of the as-grown VA-CNTs is 10 nm with 4–5 walls and exhibited a high degree of crystallinity.

10.2.2 Synthesis of structural supercapacitors

CNT/Steel structural supercapacitors were made by first dissolving Polyethylene oxide (PEO, Sigma Aldrich 900,000 MW) in propylene carbonate (PC) and placing on a hot-plate until the PEO was fully dissolved, as evidenced by the solution turning translucent and viscous; then mixing in 1-ethyl 3-methyl imidizolium tetrafluoroborate (EMIBF4) into the PEO/PC solution (80 wt. % PC, 5 wt. % PEO, 15 wt. % $EMIBF_4$) adding a slightly yellowish hue to the solution; and finally pouring the solution onto the CNT/Steel electrodes, sandwiching the two electrodes together and then placing the full device in a vacuum oven (MTI) heated to 50°C to both vacuum infiltrate the CNT film and remove the excess PC.[10, 11]

10.2.3 In-situ mechano-electrochemical measurements

For tensile testing of the structural supercapacitors, steel brackets were super-glued to each electrode. Holes were drilled into the brackets for nylon rope to be threaded through them to allow for the application of a tensile load. Wires were then attached to each of the steel brackets and silver paint was used to electrically connect both the CNT/steel electrodes and the steel tensile testing brackets to allow for simultaneous measurement of the electrochemical and mechanical properties of the structural supercapacitors.[11] Electrochemical measurements were taken with an Autolab multichannel analyzer. Before mechanical testing began a range of electrochemical tests were performed including cyclic voltammetry and galvanostatic charge discharge measurements (**Figure 10.2**). Capacitance was calculated from the slope of the galvanostatic discharge curves according to the following equation.

$$C = \frac{I\Delta t}{\Delta V}$$

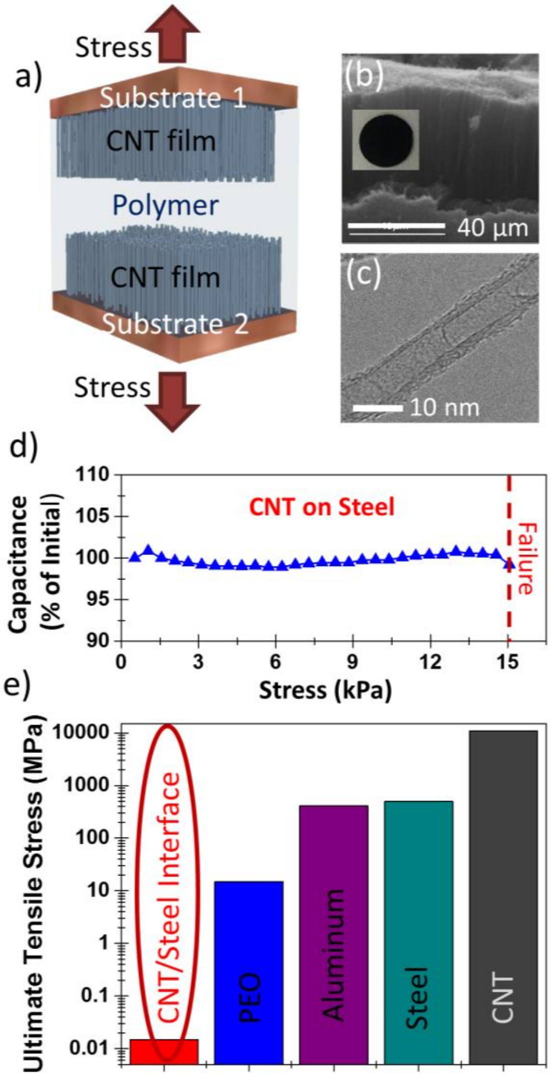

Figure 10.1 (a) Schematic of the in-situ mechanical-electrochemical device testing configuration based on CNT/steel materials infiltrated with PEO-based conducting polymers. (b) SEM image of the CNT/Steel electrodes. (c) Representative TEM image of an individual CNT. (d) Capacitance used as a real-time measure of failure as a function of the applied stress. (e) A comparison of the failure of our CNT/steel interfaces as compared to typical structural materials and CNT by themselves.

For the in-situ mechano-electrochemical measurements the devices were charged up to 2V with a charging current of 2A/g.

10.3 Results and Discussion

The CVD growth resulted in uniform layers of crystalline multi-walled CNT arrays with total height of ~ 30-40 µm based on field-emission scanning electron microscope (FESEM) analysis (**Figure 10.1b**). Individual CNTs in this array were measured to exhibit 4-5 walls and an outer diameter near 10 nm based on high resolution transmission electron microscope (HRTEM) analysis (**Figure 10.1c**). In order to characterize the structural CNT-steel interface, CNT/steel electrodes were infiltrated with a polymer electrolyte consisting of polyethylene oxide (PEO) and 1-ethyl 3-methylimidizolium tetrafluoroborate ($EMIBF_4$) with a ratio of 1 PEO:3 $EMIBF_4$ and sandwiched together in a symmetric configuration. (**Figure 10.1a**) This configuration, which is equivalent to a structural supercapacitor, can establish the real-time signature of mechanical failure in the case when the interface tensile properties are weaker than the bulk polymer properties. This can be identified using galvanostatic charge-discharge testing of the device that is continuously assessed with an increasing or varying applied mechanical stress. Further information on

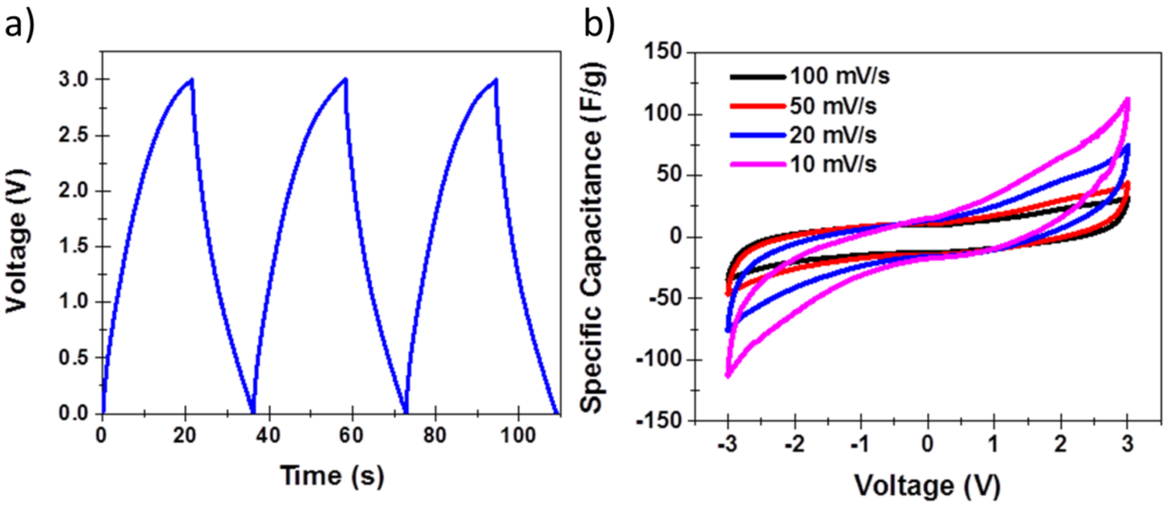

Figure 10.2 (a) Three consecutive galvanostatic charge discharge curves at 1.25A/g. (b) Cyclic voltammetry curves at various scan rates.

this technique is included in the supplementary data, and as an isolated supercapacitor, this system exhibited a specific capacitance of ~ 5 F/g calculated from the electrochemical measurements in **Figure 10.2**.

Under an increasing applied mechanical stress, the device showed little to no degradation in the electrochemical performance until it suddenly failed at 15 kPa of tensile stress (**Figure 10.1d**). Notably, this was one of multiple devices tested in a similar manner that indicated 5 – 15 kPa tensile strength. The tensile stress is therefore a key limiting factor to the incorporation of this material in applications requiring structural integrity. This indicates a tensile strength that is 1000 times less than that of the pure PEO polymer, and over 100,000 times weaker than typical structural metals such as steel and aluminum. This is of particular note as the tensile strength of the individual CNTs is significantly greater than steel (see **Figure 10.1e**).[1]

To assess the mechanism for failure, inspection of the electrodes after failure (**Figure 10.3**) indicated that the CNTs from electrode 1 had delaminated from the electrode surface as evidenced by the black CNT patches on the white polymer still visible on electrode 2. This elucidates that the failure in the devices occurred at the CNT/substrate interface as expected based on the low 15 kPa tensile strength. Notably, comparison of CNT-steel interfaces with porous silicon/silicon interfaces using the same PEO based electrolyte indicates 20X improved tensile properties, with bulk failure near 300 kPa due to the failure of the polymer, and not of the reinforced interface.[11, 12] This highlights a key challenge to the community of CNT researchers since silicon is a brittle, weaker material, even though the interface between porous silicon and silicon is a continuous covalently bonded architecture. As a result, despite the extraordinary mechanical properties of the individual CNTs, the mechanical properties of bulk materials based on these CNTs are limited by the interface between the CNTs and a solid surface, which are notably very weak. This leads to brittle, structurally-weak materials such as porous silicon, to significantly outperform the bulk mechanical properties of CNT materials grown on solid substrates.

10.4 Conclusion

Going forward, one of the challenges that have impeded the correlation of CNT mechanical interfaces to CNT growth processes has been the lack of robust testing techniques to address failure in these systems. The approach that we demonstrate here provides a straight-forward route to address these properties in a laboratory environment without a highly sophisticated toolset. Due to an interface between the substrate and CNTs that is mediated by a catalyst surface, we anticipate that there exists an unexplored dimension of research that correlates CNT growth processes to the mechanical properties of the interface or post-growth treatment such as atomic layer engineering.[13] In this letter we emphasize the importance of this characteristic in CNT-based materials as a means to enable a next-generation of CNT-based devices in energy storage, energy conversion, thermal transport, and structural composites, among others.

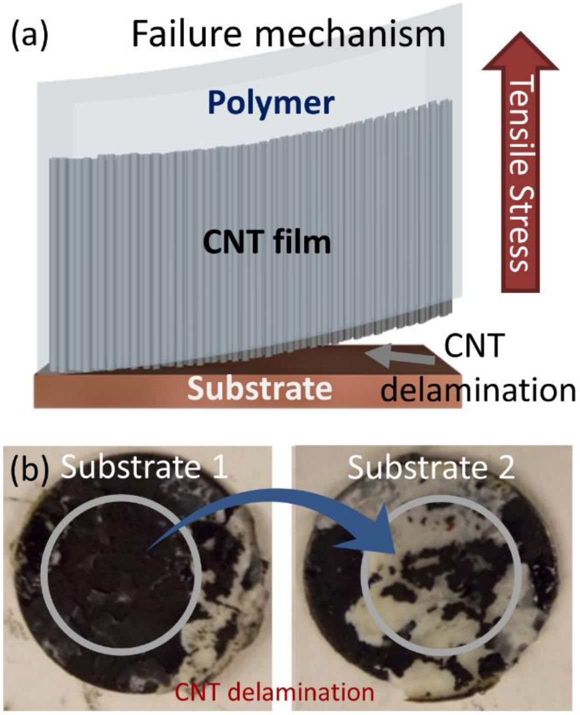

Figure 10.3 (a) Schematic highlights CNT delamination as the mechanism of failure. (b) Pictures the two electrodes for a failed CNT/Steel load bearing supercapacitors. Clearly showing CNT delamination from electrode 1 to electrode 2.

Acknowledgements

This work was funded by the US-Israel Binational Science Foundation (BSF) start-up grant #2014041. The authors declare no competing financial interest.

References

1. De Volder, M. F. L.; Tawfick, S. H.; Baughman, R. H.; Hart, A. J. *Science* **2013,** 339, (6119), 535-539.

2. Lahiri, I.; Lahiri, D.; Jin, S.; Agarwal, A.; Choi, W. *ACS nano* **2011,** 5, (2), 780-787.

3. Talapatra, S.; Kar, S.; Pal, S.; Vajtai, R.; Ci, L.; Victor, P.; Shaijumon, M.; Kaur, S.; Nalamasu, O.; Ajayan, P. *Nature nanotechnology* **2006,** 1, (2), 112-116.

4. Zhu, Y.; Li, L.; Zhang, C. G.; Casillas, G.; Sun, Z. Z.; Yan, Z.; Ruan, G. D.; Peng, Z. W.; Raji, A. R. O.; Kittrell, C.; Hauge, R. H.; Tour, J. M. *Nature Communications* **2012,** 3, 1225.

5. Pint, C. L.; Alvarez, N. T.; Hauge, R. H. *Nano Research* **2009,** 2, (7), 526-534.

6. Nessim, G. D.; Seita, M.; O'Brien, K. P.; Hart, A. J.; Bonaparte, R. K.; Mitchell, R. R.; Thompson, C. V. *Nano Letters* **2009,** 9, (10), 3398-3405.

7. Nessim, G. D.; Hart, A. J.; Kim, J. S.; Acquaviva, D.; Oh, J.; Morgan, C. D.; Seita, M.; Leib, J. S.; Thompson, C. V. *Nano Letters* **2008,** 8, (11), 3587-3593.

8. Teblum, E.; Gofer, Y.; Pint, C. L.; Nessim, G. D. *Journal of Physical Chemistry C* **2012,** 116, (46), 24522-24528.

9. Nessim, G. D.; Al-Obeidi, A.; Grisaru, H.; Polsen, E. S.; Oliver, C. R.; Zimrin, T.; Hart, A. J.; Aurbach, D.; Thompson, C. V. *Carbon* **2012,** 50, (11), 4002-4009.

10. Westover, A. S.; Shabab, F. N.; Tian, J. W.; Bernath, S.; Oakes, L.; Erwin, W. R.; Carter, R.; Bardhan, R.; Pint, C. L. *J Electrochem Soc* **2014,** 161, (6), E112-E117.

11. Westover, A. S.; Tian, J. W.; Bernath, S.; Oakes, L.; Edwards, R.; Shabab, F. N.; Chatterjee, S.; Anilkumar, A. V.; Pint, C. L. *Nano letters* **2014,** 14, (6), 3197-3202.

12. Westover, A. S.; Baer, B.; Bello, B. H.; Sun, H.; Oakes, L.; Bellan, L. M.; Pint, C. L. *Journal of Materials Chemistry A* **2015,** 3, (40), 20097-20102.

13. Abadi, P.; Maschmann, M. R.; Baur, J. W.; Graham, S.; Cola, B. A. *Nanotechnology* **2013,** 24, (47), 475707.

CHAPTER 11

LOAD DEPENDENT FRICTIONAL RESPONSE OF VERTICALLY ALIGNED SINGLE-WALLED CARBON NANOTUBE FILMS[1]

Andrew S. Westover,[1,2], Junho Choi[3], Kehang Cui[3], Takumi Ishikawa[3], Taiki Inoue[3], Rong Xiang[3], Shohei Chiashi[3], Takahisa Kato[3], Shigeo Maruyama[3,4,], and Cary L. Pint[1,2]

[1]Interdisciplinary Materials Science and Engineering Program, Vanderbilt University, Nashville, TN 37212, USA

[2]Mechanical Engineering Department, Vanderbilt University, Nashville, TN 37212, USA

[3]Department of Mechanical Engineering, The University of Tokyo, Tokyo 113-8656, JAPAN

[4]Energy NanoEngineering Lab., National Institute of Advanced Industrial Science and Technology, Tsukuba 305-8564, JAPAN

Abstract: Here we use microscratch testing to demonstrate how a single-walled carbon nanotube (SWCNT) forest material can exhibit variable adhesion properties with solid surfaces ranging from negligible adhesion at low loading due to the normal alignment of SWCNTs to maximum adhesion at high loading that exploits the extraordinary sidewall adhesion of SWCNTs. This observation, which exhibits no analog in conventional bulk materials, is correlated to loading-induced structural modification of the low-density SWCNT-substrate interface morphology. This observation opens new pathways to use structural modification of low density materials to engineer and control a wide range of adhesion properties with solid surfaces.

This work was originally published in the **Scripta Materialia 125, 63-67, Aug. 2016** and is reproduced with permission. © *Scripta Materialia (2016)* DOI: 10.1016/j.scriptamat.2016.07.032

11.1 Introduction

Nanostructured material interfaces with solid surfaces represent a platform for technologies ranging from batteries, flexible electronics, and solar cells, to transparent conductive thin films.[2-4] Despite the widespread application of these systems, the interfacial mechanics associated with such nanostructured material interfaces remains poorly understood.[5-7] Building from a vast body of literature on the mechanical properties of interfaces of inorganic and organic films, characteristics such as the microstructure, crystal structure, grain size, material homogeneity, and defects[8] in inorganic films and crystallinity, polymer chain length, chain orientation, and plasticizer content[9-11] in organic films can describe the film-dependent mechanical properties. In contrast, nanomaterial interfaces exhibit mechanical properties entirely distinct from these previous studies that arise from characteristics such as nanomaterial density, nanomaterial morphology, and individual chemical/physical properties of the nanomaterials.[12-14] Whereas mechanical behavior of individual nanostructures is a dynamic area of research due to observations of superlubrication and other phenomena at the nanoscale, studies extending fundamental ideas observed at single-particle scales to complex film assemblies are only starting to recently emerge.[15-19]

Of particular interest to such applications are carbon nanotubes, which are readily grown or processed into complex networks that can exhibit unique frictional characteristics, such as strong shear-on binding response up to 100 N/cm^2 and easy normal lift off.[20-22] These unique carbon nanotube networks have been shown to exhibit frictional properties 10X improved from a natural gecko foot, and further enable contact transfer of complex stacks of organized carbon nanotubes to arbitrary substrates.[23, 24] Other recent advances have focused on *in-situ* TEM and SEM compression and tensile testing of nanomaterial pillars and films,[13, 25, 26] and nanoindentation of CNT films to understand and engineer the hardness and compressive behavior.[14, 27] Whereas early studies have indicated the ability to apply scratch testing approaches to complex CNT-based networks,[28, 29] studies intersecting the exciting applications of the CNT-based frictional characteristics, such as forming functional adhesives, and more conventional techniques for testing mechanical properties of inorganic and organic film interfaces remain mostly unexplored.

Here we adapt a microscratch technique traditionally used to determine the adhesion of thin films to substrates[30, 31] to study the load-dependent frictional response of vertically aligned single-walled carbon nanotube (SWCNT) thin films grown by alcohol-assisted catalytic chemical vapor deposition (ACCVD).[32-34] Our experiments indicate a load-dependent frictional response where coupling of mechanical energy into the SWCNT material modifies the interfacial morphology of the SWCNTs and leads to increased adhesion properties until reaching a load threshold where maximum frictional response is obtained. Our work highlights how external loading can be used to actuate frictional properties in low density networks of SWCNTs in a manner generalizable to other low density materials composed of nanostructured building blocks.

11.2 Experimental Methods

SWCNT films were synthesized using ACCVD as detailed in the appendix. Microscratch tests in this study were performed using a RHESCA CSR-02 microscratch testing system with a 100 µm diameter diamond tipped stylus. The testing apparatus (**Figure 11.1**) consists of a traditional audio cartridge typically used for record players, where a magnetic stylus is connected to a magnetic sensing coil. The scratch tests involve two motions in a single x-y plane: (1) an oscillatory motion in the x-direction described by $X = X_0\ Cos(\omega t)$ (**Figure 11.1a**), and (2) a linear lateral motion normal to the oscillatory motion (y-direction). To induce a constantly increasing force on the SWCNT film, the film was maintained at a slight angle of 1° relative to the lateral motion in the y direction (**Figure 11.1b**). With this angle and tip the microscratch measurement has a loading rate of 17.64 µN/µm in the y-direction of motion while oscillatory motion in the x-direction enables the measurement of friction. In this system, the frictional force between the stylus and the film causes the stylus to lag behind the cartridge motion, generating a voltage response. This voltage response is proportional to the frictional response of the thin film, and is conventionally represented in units of V or in arbitrary units due to known calibration challenges.[35] Following fast Fourier transform (FFT) noise correction, the measured response is proportional to the friction force measured by the stylus. In a

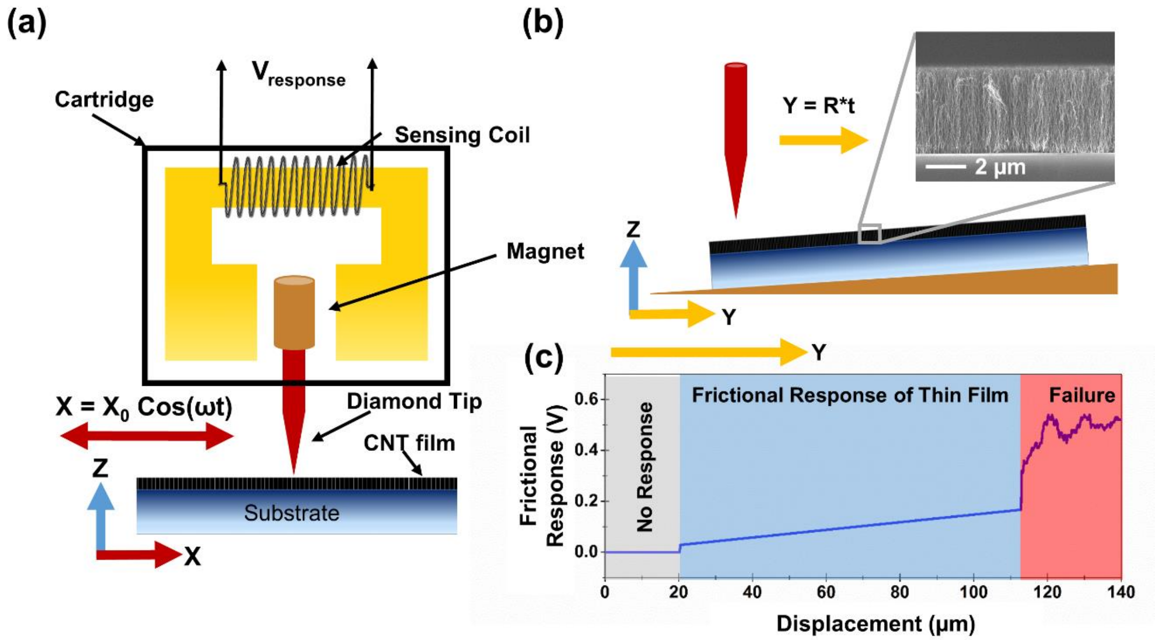

Figure 11.1 Microscratch testing approach used for this study with the experimental apparatus and oscillatory motion depicted in (a) and the lateral motion depicted in (b) with an inset SEM image of the alcohol catalytic CVD grown SWCNT film tested. (c) A typical response using this technique with a conventional thin film coating.

traditional microscratch measurement on a conventional thin film, initially the stylus is maintained at a z-distance above the thin film and there is an initial period with no measured response. Once the stylus engages the thin film through movement in the y-axis direction, mechanical energy is coupled into the film with the normal component of the applied load proportional to the displacement, and a linearly increasing frictional response is observed until the thin film detaches from the substrate at a critical load which corresponds to a rapid jump in the frictional response followed by large fluctuations (see **Figure 11.1c**).[30] A comparison of the raw signal and the FFT signal for the data in the main text is presented in **Figure 11.A1**. Notably, the microscratch data in **Figure 11.1c** is representative of a measurement using this technique from a conventional coating, and only included for a generalized comparison between a conventional scratch test and our microscratch data on a SWCNT film.

11.3 Results and Discussion

Figure 11.2 shows three microscratch experiments on a SWCNT film showing the measured frictional response of the SWCNT film as a function of displacement (bottom) and applied load (top). By

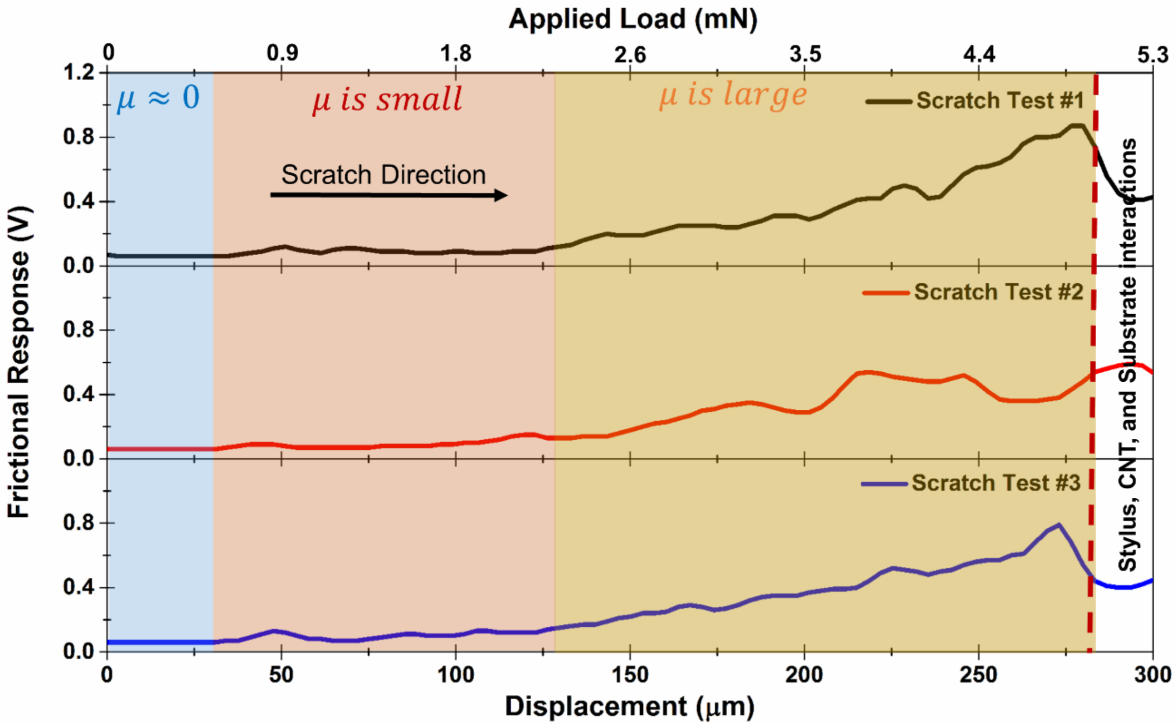

Figure 11.2 (a) Shows three microscratch measurements of the frictional response as a function of displacement(bottom) and applied load(top) on the same vertically aligned SWCNT sample with the different frictional regimes noted.

comparing the measured frictional response with the traces of the scratches (**Figure 11.A2**), three general regimes are identified. The first regime is highlighted in blue in **Figure 11.2**, and corresponds to a range of displacements where the stylus had engaged the SWCNT film and removed it from the surface without any measureable frictional response (from 0 to 0.6 mN). We attribute this regime to the weak normal binding of SWCNTs oriented perpendicular to a solid substrate in a low density SWCNT material. With increasing lateral displacement in the y-direction, a second regime highlighted in red is encountered where both the stylus is engaged with the SWCNT film and a small frictional response is recorded (from 0.6 to 2.3 mN). The onset of this regime (~ 0.6 mN) represents the point where external loading starts to disrupt the normal orientation of SWCNTs at the SWCNT-substrate interface, and increased adhesion is measured. Finally, a third regime is highlighted in gold where a greater slope is observed in the frictional response indicating a significantly enhanced coefficient of friction (from 2.3 mN to 5.7 mN). At the very end of this regime, a maximum value of the frictional response is achieved at a point attributed to a condition where increasing mechanical energy leads to no further increase in the frictional response. With exception of minor variance between measurements, it is notable that this same pattern was measured in all three of the microscratch experiments shown in **Figure 11.2**. Beyond the point of maximum frictional response from the CNT film, a stick-slip response is measured that is attributed to the convoluted frictional response between the stylus, the SWCNT film, and the underlying substrate.

Closer examination of the SEM trace from the scratches (**Figure 11.3** and **Figure 11.A2**) indicates full removal of the SWCNT film in the first regime, with only partial removal of the SWCNT film in the subsequent regimes. Removal of the film indicates that the adhesion of the SWCNT film to the stylus is greater than to the substrate. As more of the CNT film remain after the microscratch tests when a greater

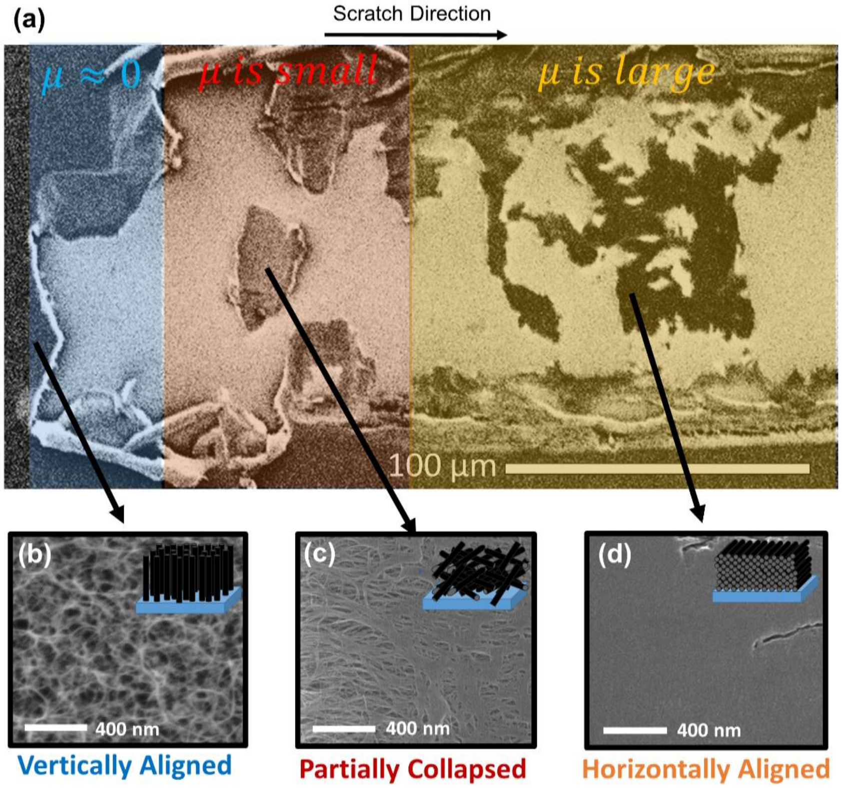

Figure 11.3 (a) SEM image of the trace of one of the microscratch measurements depicted in **Figure 11.2** (scratch test #3). (b-d) correspond to SEM images of the morphology of the CNT film as load is applied starting in the initial low-density aligned forest (b) changing to a partially collapsed SWCNT morphology (c) and finally reaching a high density horizontally aligned morphology (d). Notably in the SEM image there are regions with CNT and without CNT. Whether or not a CNT film remains after scratching is determined by whether or not the adhesion to the substrate or the adhesion to the stylus is greater. As more CNT remain with larger applied forces this implies the adhesion to the substrate is increasing significantly.

force is applied to the substrate, we can deduce that the SWCNT film has increased adhesion to the substrate when greater forces are applied to the substrate. In order to better understand the measured frictional response, SEM imaging was performed of the SWCNT films remaining following the scratch tests, and reveals a distinct change in the morphology of the film as a load is applied. Initially the SWCNT film is in a low-density vertically aligned architecture (**Figure 11.3b**), which becomes partially collapsed into a randomly aligned network (**Figure 11.3c**) in the second regime. Finally in the third regime, the packing of the SWCNTs on the surface is too dense to resolve individual SWCNT bundles in the SEM images (**Figure 11.3d**). Building from previous studies,[23] this is correlated to the formation of a highly dense and semi-aligned SWCNT material due to the applied load.

These results indicate that the applied load from the stylus is coupled into mechanical energy that modifies the morphological properties of the SWCNT material, and the SWCNT-substrate interface. This is attributed to the observed load-dependent frictional response. Previous studies have highlighted the strong sidewall adhesion of SWCNT materials with surfaces that enable exceptional adhesion capability for CNT-based gecko tapes.[20-22] However, our work not only emphasizes the importance of sidewall adhesion, but the application of controlled loading to maximize the density of SWCNT-substrate interfacial contact sites. At the very end of the third regime in **Figure 11.2**, the maximum loading is achieved at a point where further coupling of mechanical energy into the SWCNT material leads to no further modification of the frictional properties, and hence no further morphological change of SWCNT at the solid surface.

To better understand this we calculated the areal packing fraction, or the percentage of a surface cross section occupied by SWCNTs (details in the appendix) as a function of lateral displacement and applied load (**Figure 11.4a** –black) and compared this to a traditional thin film (**Figure 11.4a** – red) where the entire surface is exposed to the stylus resulting in an areal packing fraction of approximately 100%. As the load is increased on the SWCNT film, the confined space between the stylus and the substrate causes the SWCNT to be compressed thus exposing more of the individual SWCNT side walls to interact with the

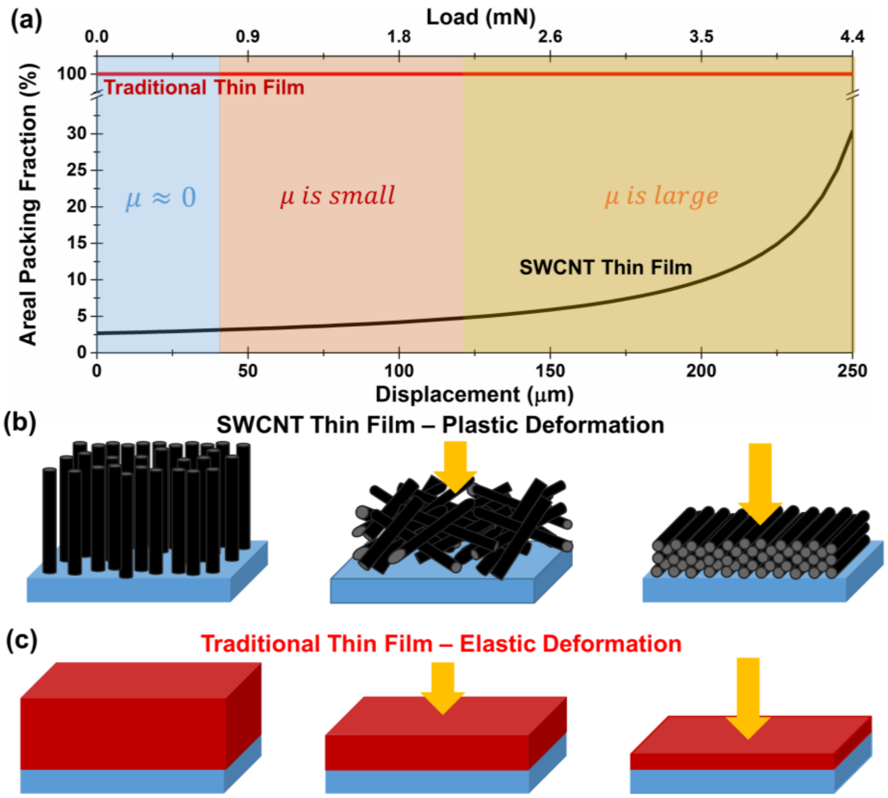

Figure 11.4 (a) Calculations of estimated areal packing fraction of the SWCNT as a function of discplacement (bottom) and applied load (top) and compared to a traditional thin film. This curve is consistent with the shape of the frictional response in **Figure 11.2**, supporting interfacial morphology change as a mechanism of the frictional response. (b) Depicts the change in morphology of the SWCNT film with an increasing load and is contrasted with the elastic response of a traditional thin film (c).

stylus. The correlation between the curve presented in **Figure 11.4** and the experimental data in **Figure 11.2&11.3** indicates that the increasing coefficient of friction observed as the load increases on the SWCNT film is likely explained by the restructuring of the SWCNT film with an applied load as illustrated in **Figure 11.4b**. Notably this response differs significantly from a traditional thin film. Whereas a traditional thin film typically consists of a bulk material without void space, increasing loads cause elastic compression of the film (**Figure 11.4c**). This typically results in a frictional response similar to the simulated response in **Figure 11.1c**, and does not typically exhibit a significant change in the coefficient of friction until the critical load is reached and the thin film detaches from the substrate.

A key outcome of this analysis is the observation that the maximum frictional response of a carbon nanotube adhesive is a function of the maximum areal packing fraction that can be achieved by coupling of mechanical energy into the material. This opens routes to understand not only interface properties of CNT materials, but also the response of CNT assemblies with different characteristics such as alignment, density, diameter, and surface treatment that will directly impact the frictional characteristics of the surfaces. This type of morphology-dependent frictional response is unique to a low-density nanostructured network and is significantly distinguished from that obtained in conventional bulk coatings or films of organic or inorganic materials.

11.4 Conclusion

In summary, our study reports the use of microscratch analysis to elucidate the load-dependent frictional response of aligned SWCNT materials. Unlike traditional coatings, we observe that morphological changes at the SWCNT-substrate interface lead to an increasing frictional response as a load is applied due to the coupling of mechanical energy into the SWCNT material that leads to restructuring at the SWCNT-substrate interface. This occurs until a maximum frictional response is achieved, at which point no further mechanical energy can be coupled into the SWCNT array and the frictional response levels off. This work opens new exciting avenues for research in areas such as (1) the study of how network properties of SWCNTs or CNTs can modulate the maximum frictional response, since the total mechanical energy coupled into the material will be a function of the initial morphology, and (2) the study of how surface engineering, such as with atomic layer deposition, can simultaneously impact the elastic properties and interfacial frictional properties of similar low-density materials. The technique and results reported in this work opens a pathway for the advanced study and design of next-generation nanoscale adhesives as well as actuators that can widely modulate the frictional characteristics of surfaces using external stimuli.

11.A Appendix

11.A.1 CNT film preparation

Vertically aligned CNT films were grown using the standard alcohol catalytic chemical vapor deposition technique.[36-38] Initially Si/SiO_2 substrates were dip coated in Co acetate and Mo acetate solutions consecutively. The dip coated film was then heated up in air to 450°C to reduce the acetates and oxidize the Co/Mo nanoparticles. The dip coated Si/SiO_2 substrate was then placed in a quartz tube surrounded by an electric furnace and heated up to 800°C under a flow of 300 sccm of Ar containing 3% H_2 at 40 kPa. The sample was then held at 800°C with the same gas flow for 10 minutes to reduce the catalyst. After 10 minutes the Ar/H_2 flow was stopped, and Ethanol (dehydrated, 99.5% Wako Chemical) was flowed through the furnace at 450 SCCM at 1.3 kPa for ~5 minutes.

11.A.2 Microscratch testing

Microscratch tests were performed using a RHESCA CSR-02 microscratch testing system with a 100 µm diameter diamond tipped stylus for the majority of the tests, and using a 10 µm diameter diamond tipped stylus in one instance. For the majority of the microscratch testing, tests were performed with a loading speed of 5 µm/s with a gain of 500, an angle between the sample and the stylus plane of 1°, a loading rate of 17.64 mN/mm, and an excitation of 80 µm. The lone exception was the test in **Figure 11.A3** which used testing conditions of a 10 µm diameter diamond tip, a loading speed of 12.5 µm/s, a gain of 750, an angle between the sample and the stylus plane of 1°, a loading rate of 13.7 mN/mm, and an excitation of 80 µm. In addition to generating the data for the raw signal the signal was processed to remove the noise generated by the oscillatory motion of the stylus using a fast Fourier transform (FFT) a common technique. A comparison of the raw signal and the FFT signal for the data in the main text is presented in **Figure 11.A1**.

11.A.3 Calculation of the SWCNT areal packing fraction

The SWNCT areal packing fraction was calculated in two ways giving nearly identical results. First the volumetric density of SWCNT film was calculated using the measured areal density (8500 CNT/µm^2)[36] for films with these growth conditions[1] and the confined height of the CNT film between the substrate and the stylus, which was calculated to change as $z = h_{CNT} - y\, Tan(\theta)$, where z is the CNT film height, h_{CNT} is the initial height of the CNT film of 4.3µm, y is the lateral displacement, and θ is the angle between the stylus and the film (~1° in this case.) The volumetric packing fraction was then calculated by calculating the volume of each SWCNT assuming they were perfect cylinders and using the measured average CNT diameter of 2nm[1] according to the following equation where V_{CNT} is the volume of each CNT, r_{CNT} is the radius of each CNT (1nm) and h_{CNT} is the height of each CNT (4.3 µm).

$$V_{CNT} \;=\; \pi {r_{CNT}}^2 h_{CNT}$$

Knowing the approximate volume of each individual CNT we can then multiply this by the CNT density to get the volumetric packing fraction. If we then assume that the packing fraction is uniform across the material we can assume that the areal packing fraction is equal to the volumetric packing fraction.

Alternately the areal packing fraction was calculated by assuming that as the z distance between the stylus and the substrate was confined by this caused each of the CNT films to be bent over at a given angle. We then took a horizontal slice of this tipped over cylinder assuming that this was approximately equal to the amount of the CNT sidewall exposed to the stylus as shown in **Figure 11.A3**. By multiplying the area of these horizontal slices by the CNT density, we can calculate the approximate CNT areal packing fraction. As can be seen in **Figure 11.A4** this gave a nearly identical value.

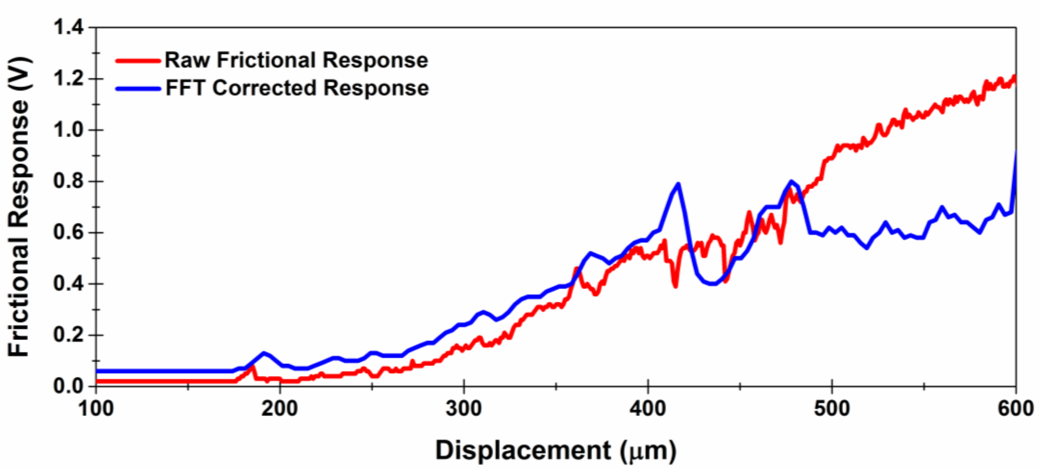

Figure 11.A1. Comparison of the raw response and the FFT corrected response for the data in the main text.

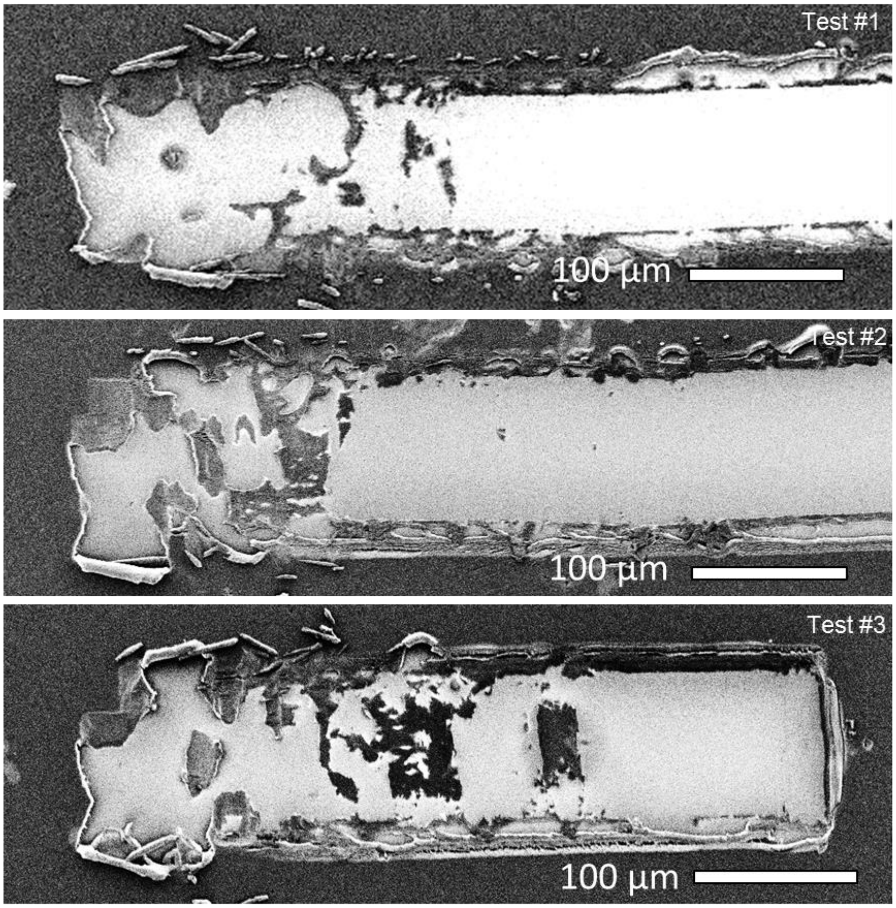

Figure 11.A2 SEM images of the scratch traces for the microscratch tests in **Figure 11.2**.

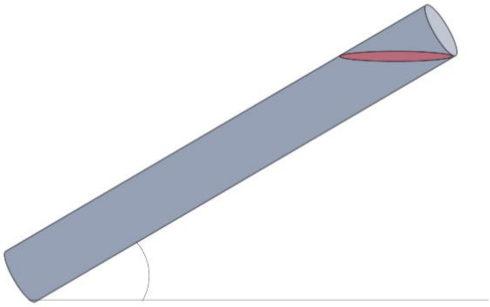

Figure 11.A3 Scheme illustrating the 2nd method used to calculate the areal packing fraction of the CNT film.

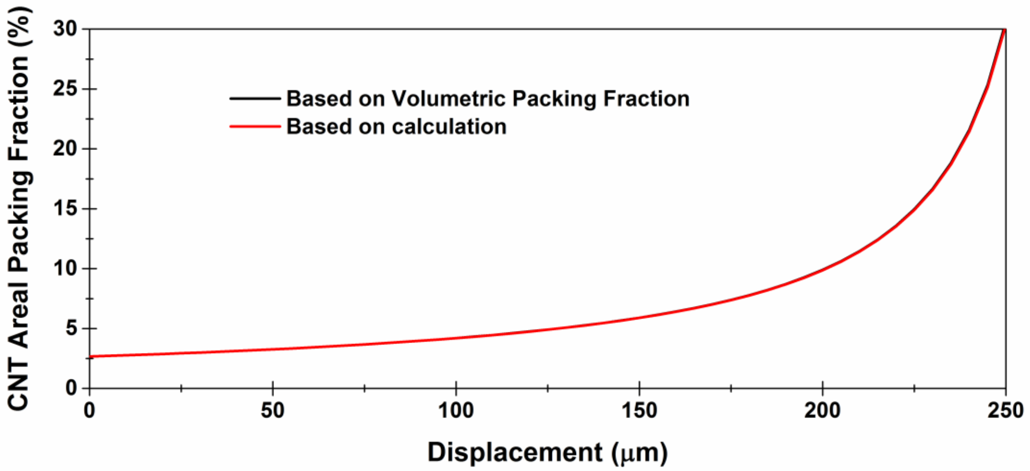

Figure 11.A4 Comparison of two different methods for calculating the CNT areal packing fraction showing they give nearly identical results.

Acknowledgements

The authors thank Anna Douglas, Keith Share, and Landon Oakes for insightful discussions. This project was supported by the National Science Foundation East Asia and Pacific Summer Institute 2015 award number 1515541, and the Japan Society for the Promotion of Science's summer program 2015. A part of this work was financially supported by Grants-in-Aid for Scientific Research (15H02219, 15H05760) and IRENA Project by JST-EC DG RTD, Strategic International Collaborative Research Program, SICORP.

References

1. Westover, A. S.; Baer, B.; Bello, B. H.; Sun, H.; Oakes, L.; Bellan, L. M.; Pint, C. L. *Journal of Materials Chemistry A* **2015,** 3, (40), 20097-20102.

2. Gorkina, A. L.; Tsapenko, A. P.; Gilshteyn, E. P.; Koltsova, T. S.; Larionova, T. V.; Talyzin, A.; Anisimov, A. S.; Anoshkin, I. V.; Kauppinen, E. I.; Tolochko, O. V. *Carbon* **2016,** 100, 501-507.

3. Carter, R.; Oakes, L.; Cohn, A. P.; Holzgrafe, J.; Zarick, H. F.; Chatterjee, S.; Bardhan, R.; Pint, C. L. *J. Phys. Chem. C* **2014,** 118, (35), 20137-20151.

4. Cui, K.; Anisimov, A. S.; Chiba, T.; Fujii, S.; Kataura, H.; Nasibulin, A. G.; Chiashi, S.; Kauppinen, E. I.; Maruyama, S. *J. Mater. Chem. A* **2014,** 2, (29), 11311-11318.

5. Xu, J.; Fisher, T. S. *Int. J. Heat Mass Transfer* **2006,** 49, (9), 1658-1666.

6. Su, H.-C.; Chen, C.-H.; Chen, Y.-C.; Yao, D.-J.; Chen, H.; Chang, Y.-C.; Yew, T.-R. *Carbon* **2010,** 48, (3), 805-812.

7. Maeno, Y.; Ishikawa, A.; Nakayama, Y. *Appl. Phys Express* **2010,** 3, (6), 065102.

8. Munz, D.; Fett, T., *Ceramics: mechanical properties, failure behaviour, materials selection*. Springer Science & Business Media: New York, 2013; Vol. 36.

9. Ward, I. M.; Sweeney, J., *Mechanical properties of solid polymers*. John Wiley & Sons: United Kingdom, 2012.

10. Manias, E.; Touny, A.; Wu, L.; Strawhecker, K.; Lu, B.; Chung, T. *Chem. Mater.* **2001,** 13, (10), 3516-3523.

11. Westover, A. S.; Shabab, F. N.; Tian, J. W.; Bernath, S.; Oakes, L.; Erwin, W. R.; Carter, R.; Bardhan, R.; Pint, C. L. *J. Electrochem. Soc.* **2014,** 161, (6), E112-E117.

12. Baji, A.; Mai, Y.-W.; Wong, S.-C.; Abtahi, M.; Chen, P. *Compos. Sci. Technol.* **2010,** 70, (5), 703-718.

13. Hutchens, S. B.; Hall, L. J.; Greer, J. R. *Adv. Funct. Mater.* **2010,** 20, (14), 2338-2346.

14. Maschmann, M. R.; Zhang, Q.; Wheeler, R.; Du, F.; Dai, L.; Baur, J. *ACS Appl. Mater. Interfaces* **2011,** 3, (3), 648-653.

15. Lee, C.; Li, Q.; Kalb, W.; Liu, X.-Z.; Berger, H.; Carpick, R. W.; Hone, J. *Science* **2010,** 328, (5974), 76-80.

16. Spear, J. C.; Ewers, B. W.; Batteas, J. D. *Nano Today* **2015,** 10, (3), 301-314.

17. Egberts, P.; Han, G. H.; Liu, X. Z.; Johnson, A. C.; Carpick, R. W. *ACS Nano* **2014,** 8, (5), 5010-5021.

18. Liu, N.; Lu, Z. D.; Zhao, J.; McDowell, M. T.; Lee, H. W.; Zhao, W. T.; Cui, Y. *Nature Nanotechnology* **2014,** 9, (3), 187-192.

19. Cumings, J.; Zettl, A. *Science* **2000,** 289, (5479), 602-604.

20. Qu, L.; Dai, L.; Stone, M.; Xia, Z.; Wang, Z. L. *Science* **2008,** 322, (5899), 238-242.

21. Sethi, S.; Ge, L.; Ci, L.; Ajayan, P. M.; Dhinojwala, A. *Nano Lett.* **2008,** 8, (3), 822-825.

22. Ge, L.; Sethi, S.; Ci, L.; Ajayan, P. M.; Dhinojwala, A. *Proc. Natl. Acad. Sci.* **2007,** 104, (26), 10792-10795.

23. Pint, C. L.; Xu, Y.-Q.; Pasquali, M.; Hauge, R. H. *ACS Nano* **2008,** 2, (9), 1871-1878.

24. Pint, C. L.; Xu, Y.-Q.; Moghazy, S.; Cherukuri, T.; Alvarez, N. T.; Haroz, E. H.; Mahzooni, S.; Doorn, S. K.; Kono, J.; Pasquali, M. *ACS Nano* **2010,** 4, (2), 1131-1145.

25. Pathak, S.; Lim, E. J.; Pour Shahid Saeed Abadi, P.; Graham, S.; Cola, B. A.; Greer, J. R. *ACS Nano* **2012,** 6, (3), 2189-2197.

26. Zhang, X.; Jiang, K.; Feng, C.; Liu, P.; Zhang, L.; Kong, J.; Zhang, T.; Li, Q.; Fan, S. *Adv. Mater.* **2006,** 18, (12), 1505-1510.

27. Xue, W.; Cui, T. *Nanotechnology* **2007,** 18, (14), 145709.

28. Lahiri, I.; Lahiri, D.; Jin, S.; Agarwal, A.; Choi, W. *ACS nano* **2011,** 5, (2), 780-787.

29. Dickrell, P.; Pal, S.; Bourne, G.; Muratore, C.; Voevodin, A.; Ajayan, P.; Schadler, L.; Sawyer, W. *Tribol. Lett.* **2006,** 24, (1), 85-90.

30. Choi, J.; Kim, J.; Nakao, S.; Ikeyama, M.; Kato, T. *Nucl. Instrum. Methods Phys. Res., Sect. B* **2007,** 257, (1), 718-721.

31. Lu, P.; Gomez, H.; Xiao, X.; Lukitsch, M.; Durham, D.; Sachdeve, A.; Kumar, A.; Chou, K. *Surf. Coat. Technol.* **2013,** 215, 272-279.

32. Xiang, R.; Yang, Z.; Zhang, Q.; Luo, G.; Qian, W.; Wei, F.; Kadowaki, M.; Einarsson, E.; Maruyama, S. *J. Phys. Chem. C* **2008,** 112, (13), 4892-4896.

33. Cui, K.; Chiba, T.; Omiya, S.; Thurakitseree, T.; Zhao, P.; Fujii, S.; Kataura, H.; Einarsson, E.; Chiashi, S.; Maruyama, S. *J. Phys. Chem. Lett.* **2013,** 4, (15), 2571-2576.

34. Maruyama, S.; Kojima, R.; Miyauchi, Y.; Chiashi, S.; Kohno, M. *Chem. Phys. Lett.* **2002,** 360, (3), 229-234.

35. Ogawa, S.; Babai, Y.; Masashi, Y.; Akano, T. N., Two critical events observed on Cu films on glass substrate in the microscratch test. In *Adhesion Aspects of Thin Films, volume 2: Adhesion Aspects of Thin Films*, CRC Press: Boca Raton, Florida, 2005; Vol. 2, p 203.

36. Xiang, R.; Yang, Z.; Zhang, Q.; Luo, G.; Qian, W.; Wei, F.; Kadowaki, M.; Einarsson, E.; Maruyama, S. *J. Phys. Chem. C* **2008,** 112, (13), 4892-4896.

37. Cui, K.; Chiba, T.; Omiya, S.; Thurakitseree, T.; Zhao, P.; Fujii, S.; Kataura, H.; Einarsson, E.; Chiashi, S.; Maruyama, S. *J. Phys. Chem. Lett.* **2013,** 4, (15), 2571-2576.

38. Maruyama, S.; Kojima, R.; Miyauchi, Y.; Chiashi, S.; Kohno, M. *Chem. Phys. Lett.* **2002,** 360, (3), 229-234.

CHAPTER 12

THE EFFECT OF INTERFACIAL CONTACT ON THE ADHESION OF SINGLE WALLED CARBON NANOTUBE FILMS TO FLAT SURFACES

Andrew S. Westover[1,2], Naoki Hayakawa[3], Kehang Cui[3], Xiang Rong[3], Kensuke Tsuchiya[3], Taiki Inoue[3], Shohei Chiashi[3], Esko I. Kauppinen[4], Cary L. Pint[1,2] and Shigeo Maruyama[3]**

[1]Department of Mechanical Engineering, Vanderbilt University, Nashville TN 37235

[2]Interdisciplinary Materials Science Program, Vanderbilt University, Nashville, TN 37235

[3] Department of Mechanical Engineering, University of Tokyo, Tokyo, JAPAN, 113-8654

[4]Aalto University,

Abstract: Here we present our work in adapting a traditional microscratch test to explore the adhesion of single walled carbon nanotube (SWCNT) thin films to solid surfaces. We measure a SWCNT adhesion of up to ~ 5.8×10^{-15} J/CNT for vertically aligned CNT (VACNT) thin films. We further compare the adhesion of several different CNT-substrate interfaces finding that the number of CNT directly in contact with the substrate is the largest determining factor in CNT thin film adhesion. Finally we explored the difference in adhesion behavior between the VACNT films in the previous study and randomly aligned CNT (RACNT) films finding that RACNT films had ~10 times less adhesion than VACNT films due to the low density of CNT-CNT contacts in the RACNT films, the failure point in these films.

12.1 Introduction

Nanomaterials have come to revolutionize the way we think about science and are completely changing the way in which we engineer future technologies.[1-9] Carbon nanotubes in particular have been touted for their high mechanical strength,[10] high electrical conductivity,[11] and high thermal conductivity.[12, 13] These fantastic properties have motivated their development for a wide variety of applications including conductive thin films,[11, 14, 15] energy storage,[16-18] and solar cells.[1, 19, 20] Unfortunately practical implementation of these CNT applications have been extremely limited. One of the reasons for this has been the difficulty in developing mechanically robust interfaces between CNT networks and solid surfaces.[21-29] Whereas recently there has been a surge in studies on the adhesion of individual nanomaterials including CNT,[24, 25, 30-33] there has been almost no studies on the adhesion of nanomaterial thin films. This is extremely significant as in many cases the mechanisms that govern the adhesion of nanomaterial networks to surfaces will be distinctly different than that of the individual nanomaterials they are composed of. Until the mechanisms that dictate the adhesion of these CNT thin films and in a broader sense nanomaterial thin films in general are understood, it will be practically impossible to engineer nanomaterial based devices with strong mechanical adhesion using these thin films.

One of the biggest limitations in this regard has been the lack of standardized testing tools and procedures to measure the adhesion of nanomaterial thin films. Because of this lack most attempts to measure the adhesion of nanomaterial thin films have resorted to ad-hoc tests that try to assess mechanical adhesion using scotch tape[14, 23, 34] or pencil lead hardness techniques,[34, 35] both of which just give the most basic of qualitative knowledge and are often heavily dependent on the methodology of the user.[27] In addition these methods have almost no capability to really explore the mechanisms and factors that dictate CNT thin film adhesion. Atomic force microscopy has recently emerged as an excellent method to measure and understand the adhesion behavior of individual nanomaterials[24, 25, 32] but unfortunately the scale is limited and does not allow for high quality measurement of the adhesion of CNT networks to surfaces. One of the most promising techniques was recently developed by Lahiri et al.,[27, 36, 37] They developed a nanoscratch technique that could be used to measure the adhesion of randomly aligned CNT (RACNT) films on Si and

Cu substrates.[27] Despite the great initial success of Lahiri et al.'s work, their work was limited to a single comparison on extremely large multiwalled CNT of ~70 nm in diameter. In order to truly understand the adhesion behavior of CNT thin films and eventually to engineer this adhesion significant additionally studies are required.

Using a similar methodology to that developed by Lahiri et al., we present here our work in adapting a conventional microscratch testing technique to expand upon the work of Lahiri et al. to explore the adhesion of single walled CNT (SWCNT) films adhered to a variety of different substrates. We observe that the quality of the SWCNT film – substrate interface dictates the overall adhesion behavior of the CNT films for vertically aligned CNT (VACNT) films. We also used this scratch test method to investigate the adhesion of RACNT films made up of SWCNT finding that the adhesion was significantly less than that of the vertically aligned films. SEM investigation of the scratch traces identified that the failure occurred in the CNT-CNT contacts closest to the substrate and that the low density of these CNT-CNT contacts accounted for the difference in the adhesion energy.

12.2 Experimental Methods

12.2.1 Microscratch Testing to Measure Adhesion

Before delving into the specific measurements a brief explanation of the microscratch methodology used to perform the experiments is in order. Microscratch testing has long been the standard testing method for determining the adhesive properties of films.[38-40] Microscratch testing in principle involves scratching a rounded or pointed tip across the surface of a substrate while applying a normal load. Measuring the force required to move the stylus allows one to understand the adhesion behavior of films. When scratch testing was in its infancy Benjamin and Weaver[41, 42] identified that there are 3 main forces that play a role in the measured frictional force during a traditional scratch test: first the force required to deform/scratch the underlying substrate, second the force of adhesion which is required to remove the thin film from the substrate, and finally the plowing force required to plow through the delaminated film. The equation as denoted by Benjamin and Weaver is given in equation (1).

$$F_{friction} = GH_{substrate} + A\tau_{adhesion} + twH_{thin\,film} \tag{1}$$

Where G is a geometric factor corresponding to the contact of the tip with the substrate, $H_{substrate}$ is the hardness of the substrate, A is the scratch area, $\tau_{adhesion}$ is the shear stress due to the thin film adhesion, t is the thickness of the thin film, w is the width of the tip, and $H_{thin\ film}$ is the hardness of the thin film. They note that the first term corresponding to the interaction of the tip with the substrate can be determined experimentally by performing a scratch of the underlying substrate alone. The third term can be estimated using the thin film hardness and the area of the film. If we know these two terms then the adhesion of the thin film can be approximated.

Following this approach and adapting a technique very similar to the nanoscratch technique used by Lahiri et al.[27] (**Figure 12.1b**) we used a micromanipulator probe (**Figure 12.1c**) attached with a force sensor which allowed detailed sensing of the mechanical interaction of the tip with the substrate, in this case a CNT film which can be seen in **Figure 12.1d**. (details on the probe tip and force sensor setup are in the appendix). Scratch tests were performed on the films, by first measuring the interaction of the manipulator probe with the bare uncoated substrate to account for the tip-substrate interactions the first term identified by Benjamin and Weaver (shown in black in **Figure 12.1e**). The force required to plow through the removed CNT film was assumed to be very small due to the almost negligible hardness of the CNT film because to its extremely low density (volumetric fill factor of less than 3%). Indeed Lahiri et al. showed the validity of that assumption in their scratch tests by showing that CNT films with differing heights had essentially the same measured adhesion energy. After accounting for the two extraneous terms we then performed an identical scratch test to the initial test on the bare substrate in a region that contained a CNT film (shown in red in **Figure 12.1e**). Initially, the force profile for the tip was essentially the same as for the unscratched surface. As the manipulator probe entered the CNT coated region (designated as X_i in **Figure 12.1e**) the applied force increased significantly. Looking at the SEM image of the scratch (inset

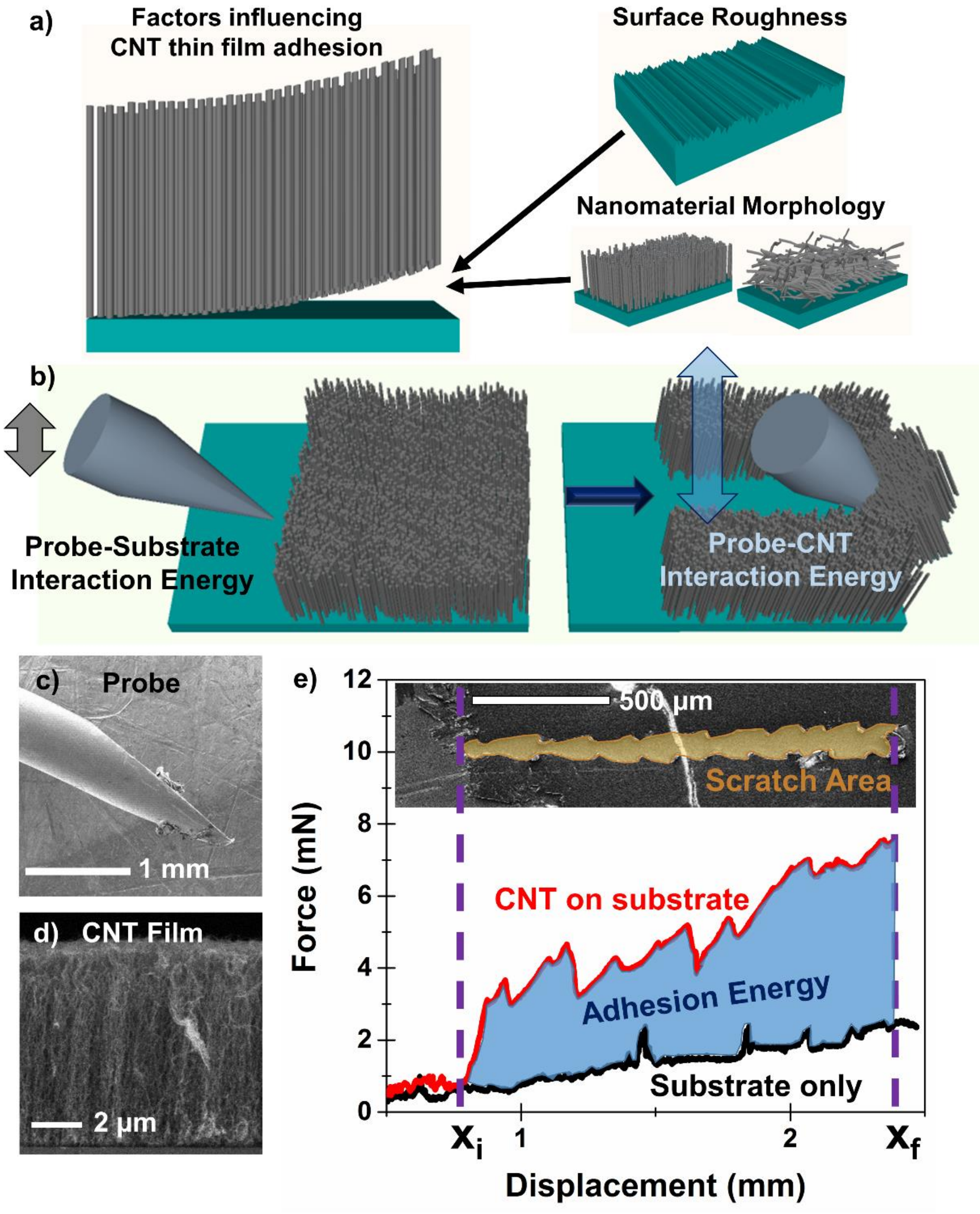

Figure 12.1 (a) Scheme highlighting some factors that influence CNT thin film adhesion. (b) Scheme showing the basic concept of scratch testing used in this paper which allowed the measurement of adhesion energy. (c) An SEM image of the micromanipulator probe tip used to perform the scratch testing. (d) An SEM image of a representative CNT film used for the majority of this study. (e) A scratch test of the film shown in d, which highlights how we calculated adhesion energy from the microscrtach testing.

at the top of **Figure 12.1e**) we can see that this point, X_i, where the force increases dramatically directly correlates to when the tip came in contact with the CNT film. Using these two measurements we can calculate the adhesion energy of the CNT film to the substrate by integrating the area between the two curves according to the following equation (designated in blue in **Figure 12.1e**) where $E_{adhesion}$ represents adhesion energy, X_i and X_f represent the beginning and end of the scratch in the CNT film, and F is the measured force.

$$E_{adhesion} = \int_{X_i}^{X_f} F dx \tag{2}$$

The average adhesion energy per area can then be calculated by dividing the adhesion energy by the total scratch area which can be measured from SEM images or optical microscopy images after testing (highlighted in orange in the inset SEM image in **Figure 12.1d**).

$$E_{area} = \frac{E_{adhesion}}{Area} \tag{3}$$

Finally using the CNT density designated as ρ_{CNT} (~8500 CNT/µm^2)[43] we can estimate the average adhesion energy per CNT.

$$E_{CNT} = \frac{E_{area}}{\rho_{CNT}} \tag{4}$$

Although a good first step in understanding scratch testing, Benjamin and Weavers results have been shown to be an incomplete picture of all that goes on within a scratch test, thus full quantitative values are likely not entirely accurate, but in accordance with other work, it has been shown that such a scratch test is at least semi-quantitative[44-46] and gives a solid foundation by which one can compare the adhesion of different CNT thin film-substrate systems.

12.2.2 CNT film preparation

VACNT films were grown using the standard alcohol catalytic chemical vapor deposition technique (ACCVD). Initially Si/SiO_2 or quartz substrates were dip coated in Co acetate and Mo acetate solutions consecutively. The dip coated film was then heated up in air to 450°C to reduce the acetates and oxidize the Co/Mo nanoparticles. The dip coated Si/SiO_2 substrate was then placed in a quartz tube surrounded by an electric furnace and heated up to 800°C under a flow of 300 sccm of Ar containing 3% H_2 at 40 kPa. The sample was then held at 800°C with the same gas flow for 10 minutes to reduce the catalyst. After 10 minutes the Ar/H_2 flow was stopped, and Ethanol (dehydrated, 99.5% Wako Chemical) was flowed through the furnace at 450 SCCM at 1.3 kPa. For the transferred films, the as grown CNT on Si/SiO_2 was slowly immersed in room temperature water to remove the CNT film from the growth substrate. Once the CNT film was removed we placed the substrate the film was to be transferred to underneath the CNT film and slowly raised the substrate. After catching the CNT film these substrates were allowed to dry overnight in a fume hood at room temperature.

The randomly aligned SWCNT films with high purity and long nanotube bundle lengths were synthesized by an aerosol CVD method. The floating catalyst aerosol CVD was carried out in a scaled-up reaction tube with a diameter of 150 mm. Ferrocene vapor was thermally decomposed in the gas phase in the aerosol CVD reactor at a temperature of 880 °C. The CO gas was supplied at 4 L min^{-1} and decomposed on the iron nanoparticles, which resulted in the growth of the SWCNT. The as-synthesized SWCNT were collected by passing the flow through microporous filters downstream of the reactor. The collected SWCNT films could be transferred to arbitrary substrates using the dry transfer method.

Raman of both samples was carried out using a Renishaw in Via MicroRaman system at 5x magnification with a static scan using 100% laser power for 10s, with a wavelength of 535nm.

12.2.3 Micromanipulator force sensor design and calibration

The force sensor consisted of two parallel plates connected on one end to the micromanipulator probe and to the micromanipulator piezoelectric actuators on the other (**Figure 12.A1**). This parallel plate configuration allows for minute movements in the micromanipulator to be sensed using an eddy current sensor (Shinkawa Electric Co., Ltd.: VS -005L). The magnitude of the force measured by the eddy current sensor is dependent on the size and dimensions of the parallel plate configuration. In order to calibrate the measured force to the voltage measured by the eddy current sensor, a series of weights with known mass up to .1mg of precision were attached to the end of the parallel plate force sensor. The variation in the measured voltage could then be calibrated to the corresponding force. For the specific force sensor used in this study the $F(mN) = 7.25\ V(Volts)$ (see calibration data in **Figure 12.A1**)

12.2.4 Scratch tests

The scratch tests were performed in an SEM (JEOL, JSM-6301F) attached with a 3 axis piezoelectric micromanipulator (Sanyu electron, SMM-7801). The force sensor and probe were attached to the micromanipulator. In order to perform the scratch tests first the micromanipulator and the sample were aligned using the tilt function. We aligned the tip such that there was a very slight angle between the tip and the sample, this allowed us to ensure that we were constantly keeping the micromanipulator tip in contact with the sample during testing and is the cause of the slight slope in the baseline data seen in the scratch tests. After alignment we performed an initial scratch on just the substrate to measure the interaction between the micromanipulator tip and the substrate. We then performed scratch tests on the CNT films starting in a region without CNT and proceeding to scratch into the CNT films. The adhesion energy was then calculated by integrating the difference between the baseline and the measured sample according to equation (2). The adhesion energy per area was then calculated by measuring the scratched region using SEM and optical microscopy images and dividing the adhesion energy by this values as in equation (3). Finally the average energy per CNT was calculated by using the average CNT density for the vertically aligned films (8500 CNT/μm^2) to convert energy per area to energy per CNT (4). For each sample we performed 3-5 scratch tests, so the reported adhesion energies are an average of all scratch tests for each samples.

12.3 Results and Discussion

12.3.1 Effect of Surface to CNT Network Contact Area

In our first set of measurements we explored the effect of the contact area of the CNT films with the surface on the overall adhesion of networks of vertically aligned single walled CNT thin films grown by the alcohol catalytic chemical vapor depositions (ACCVD).[19, 47-50]

Initially we compared the difference between as grown and transferred VACNT films. For this study both CNT films were grown on the same SiO_2 on Silicon substrate using ACCVD. After CNT growth the sample was cleaved in half. One half of the substrate was then dipped in cold water to remove the CNT film from the initial growth substrate and transfer it to an identical Si/SiO_2 substrate. This method was used to ensure that the CNT films used in both the as grown and transferred samples were nearly identical. SEM and Raman results of the as grown and transferred samples show nearly identical CNT films emphasizing that there was little to no change in the CNT films before and after transfer (**Figure 12.A2**). We performed 5 scratches on each sample and representative scratch profiles and corresponding optical microscopy images are shown in **Figure 12.2a-b** for the as grown and transferred CNT films respectively. We found that the as grown sample had an average adhesion energy of ~2 x 10^{-15} J/CNT and the transferred sample had almost triple the amount of average adhesion energy at approximately ~5.8 x 10^{-15} J/CNT (**Figure 12.2c**). Based on these results we can see that for the transferred sample we have a much higher level of adhesion. This can be understood by considering what happens towards the end of CNT growth when the growth is almost saturated. Near the end of the CNT growth the catalyst particles are known to experience Ostwald ripening causing some nanoparticles to all but disappear and others to grow into significantly larger particles.[43, 51-53] Because of this, towards the end of growth the growth termination occurs at slightly different times for different CNT, but because of van der Waals adhesion between the side walls of neighboring CNT they are lifted off of the surface effectively decreasing the number of CNT in contact with the surface (**Figure 12.2d**). This is in contrast to the transferred CNT films where nearly all the CNT come in contact with the surface (**Figure 12.2e**). Indeed SEM analysis (see **Figure 12.S2**) of the interface of the two different films, although likely somewhat clouded by edge effects, strongly suggests that this is the case. SEM images of the as grown sample all show a dark region at the interface of the CNT-substrate suggesting very few CNT at this interface. This is likely an exaggeration of the scarcity of CNT at the interface due to the edge effects that come from sample preparation, but this was in direct contrast to all of the SEM images for the transferred films which showed no dark region and CNT directly in contact with the substrate.

These results were corroborated by our next set of experiments where we transferred similar VACNT films that were again grown on a Si/SiO_2 substrate and then sectioned and transferred to Aluminum, Steel, Quartz and Si/SiO_2 substrates each with different roughness. Three to five scratch tests were then performed on the CNT films on each of these substrates with representative force profiles shown

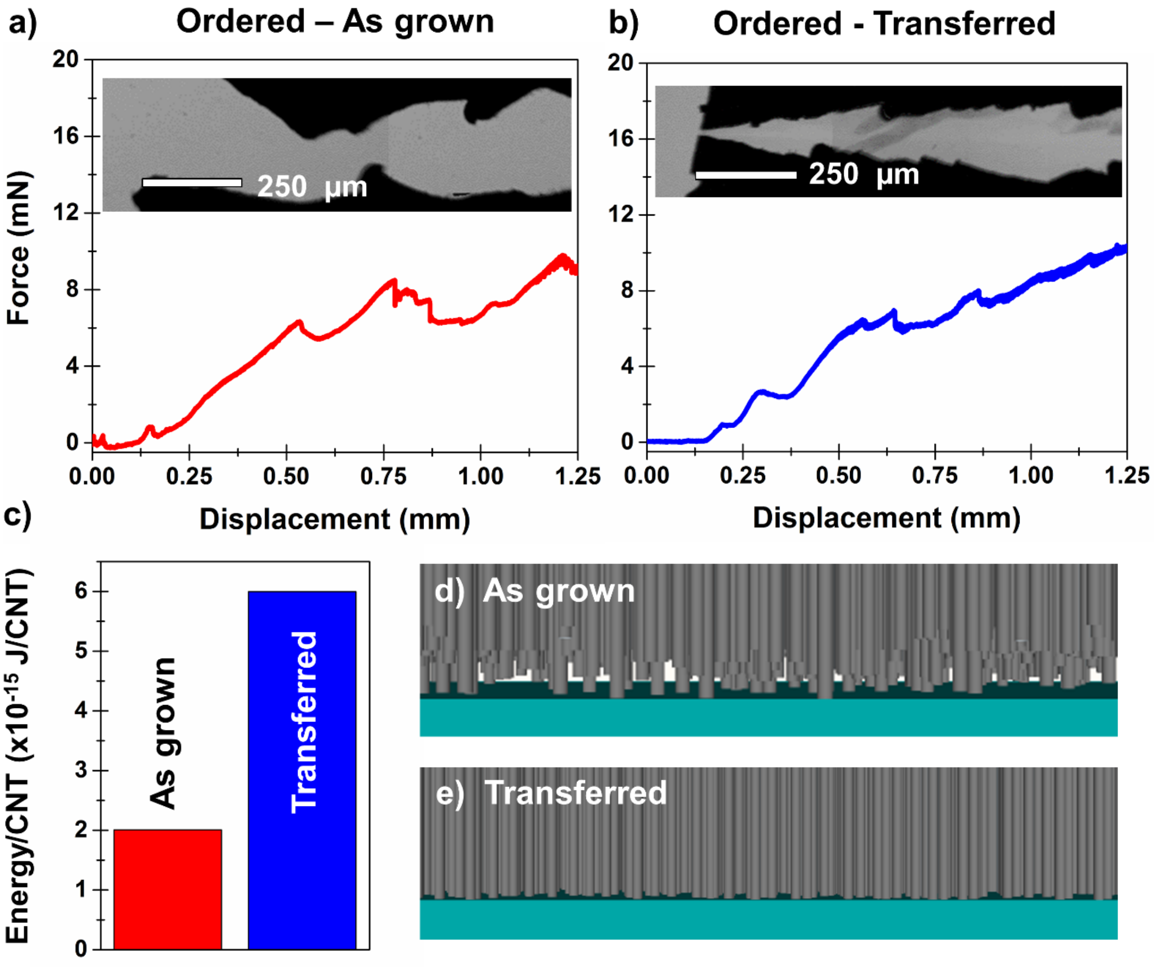

Figure 12.2 (a) Scratch test of an ordered CNT film grown on Si in the as grown state with an inset of the scratch after testing. (b) Scratch test of an ordered CNT film grown on Si and transferred to an identical Si substrate. (c) A comparison of the adhesion energy for ordered CNT films in the as grown state and after being transferred to an identical substrate as calculated from the tests in (a) and (b). (d) A schematic of the interface of the as grown CNT film highlighting the differences in CNT growth termination points. (e) A schematic showing the interface of CNT transferred onto an identical Si

in **Figure 12.3a** and the corresponding optical microscopy images of the scratches in **Figure 12.3b**. The measured adhesion energy/CNT for these films is presented in **Figure 12.3c**. We found that the CNT films transferred to Si/SiO$_2$ and Quartz exhibited the greatest amount of average adhesion with adhesion energies of ~4.4 and ~4.8 x 10^{-15} J/CNT respectively. This was followed by the CNT transferred to Al with about ~2.2 x 10^{-15} J/CNT and finally by Steel with ~ 1.5 x 10^{-15} J/CNT. Although the chemical differences in the substrates likely does contribute to differences in the van der Waals interaction between the films and the surface, we found that the differences in adhesion energy between the various samples was directly

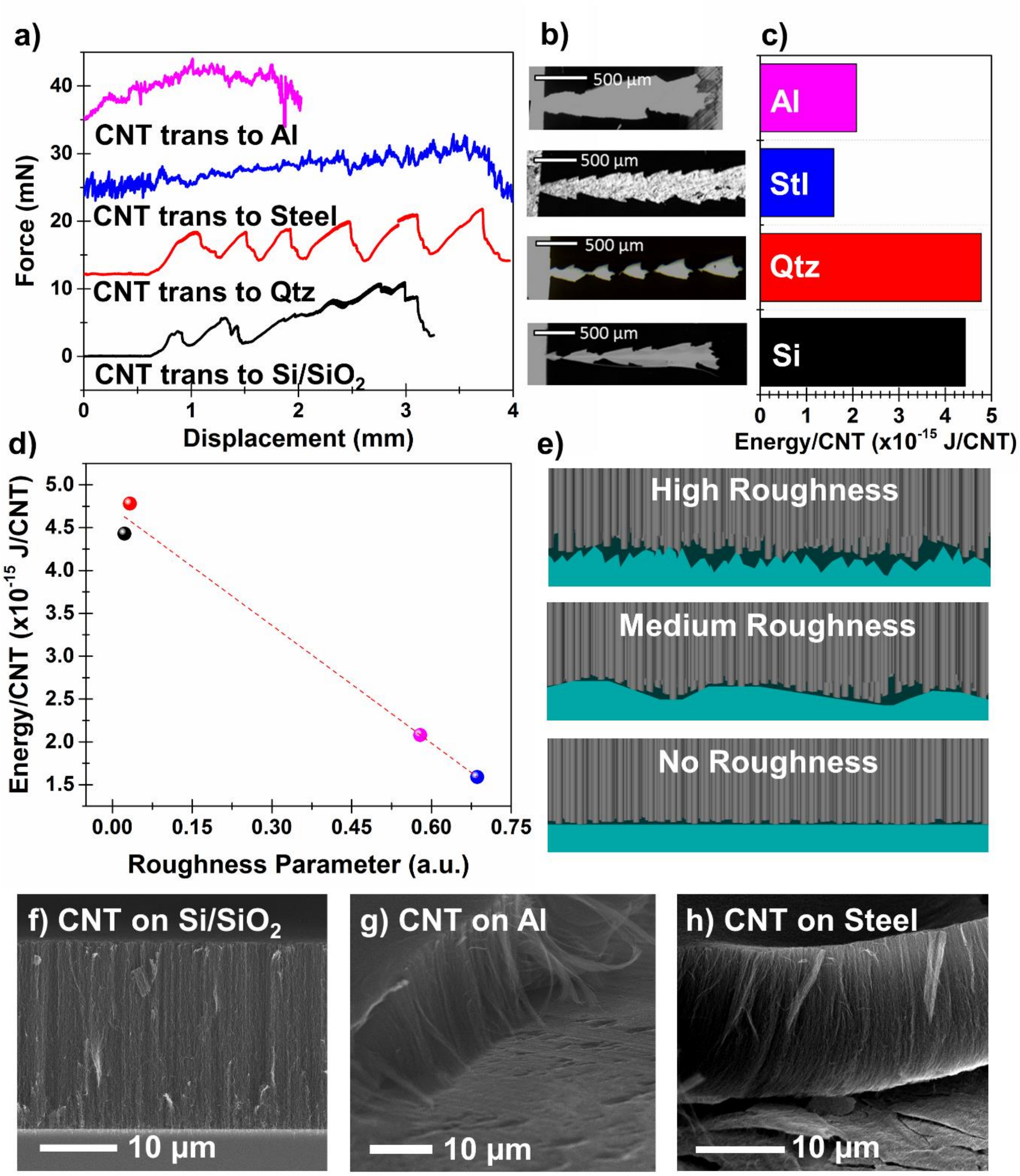

Figure 12.3 (a) Scratch tests of ordered CNT films transferred to aluminum, steel, quartz and Silicon/SiO$_2$. (b) Corresponding SEM images of scratch tests in a. (c) Comparison of adhesion energies for CNT films transferred to aluminum, steel, quartz, and SiO$_2$/Si. (d) A comparison of the roughness of the substrate and the adhesion energy with a line to guide the eye. (e) Schematic of the differences between ordered CNT films with different rough nesses. (f) SEM image of CNT film transferred to Si/SiO$_2$. (g) SEM image of CNT film transferred to Al. (h) SEM image of CNT film transferred to Steel

correlated to the relative roughness of each substrate (**Figure 12.3d**). The difference in roughness between the samples is readily observable even in the scratch profiles in **Figure 12.4a** and in the scratches on the substrates alone in the appendix in **Figure 12.A3**. Although the y value measured is that of the interaction force between the tip and the substrate, this is directly proportional to the roughness of the substrates. As such we calculated the relative amount of roughness by taking the deviation of the force constant from the average force at any given point following the standard procedure for calculating roughness.[54] As force was used instead of the physical change in height, this does not represent the exact roughness but is proportional to the actual roughness of the sample. The magnitude of the average adhesion energy had a direct linear correlation with the roughness, where rougher samples have significantly less adhesion.

In this case the increased roughness on the substrate is on the order such that it creates valleys and holes in which portions of the CNT film are unable to come into direct contact with the surface. This therefore decreases the overall amount of adhesion as the overall van der Waals interaction between the CNT film and the surface is significantly diminished. (**Figure 12.3e**) The increase in roughness and its effect on CNT can be visually observed in the SEM images in **Figure 12.3f-h** for Si/SiO_2, Aluminum and Steel respectively in order of increasing roughness.

Notably in our case the effect of sub-micron scale roughness on the CNT networks is distinctly different than the effect of roughness on individual nanomaterials. In the case of nanomaterials, for sub-micron scale roughness the individual nanomaterials will conform to the contour of the surface and will essentially be unaffected by the roughness of the surface.[23] When the roughness is on the order of the nanomaterial size however the roughness significantly increases the adhesion of the nanomaterials due to the increased nanomaterial surface contact area. It is feasible that the adhesion of the CNT thin film networks could potentially be dramatically increased by optimizing the interplay between these two properties, where sub-micron scale roughness is minimized but nanoscale roughness on the order of the CNT diameter is maximized thus maximizing the amount of surface in contact with each CNT and potentially dramatically increasing the overall adhesion of the CNT films.

12.2.3 The Effect of CNT Network Morphology on CNT Network Adhesion

Whereas the previous study was carried out exclusively on VACNT networks, in this next study we proceeded to compare the adhesion properties of these VACNT networks with the adhesion of randomly oriented and disordered CNT networks. The disordered CNT films were grown using floating catalyst aerosol CVD to form randomly algined CNT (RACNT) bundles with good electrical interconnectivity.[15, 19, 55] These films were then dry transferred to an identical Si/SiO_2 substrate to that used for the VACNT films. We performed scratch tests on the RACNT film with a representative scratch force profile and corresponding SEM image shown in **Figure 12.5c**. This sample had a distinctly different scratch behavior than that of the VACNT film as can partially be seen in the SEM image in **Figure 12.4c**. In the case of the randomly RACNT film the initial scratch started at a point and widened regularly as the scratch progressed similar to tearing a sheet of paper. This was in direct contrast to the VACNT in the previous studies which were pushed back in clumps by the tip. When comparing the measured adhesion energy per unit area to that of the VACNT films (**Figure 12.4b**) we found that the adhesion energy per unit area was significantly smaller for the randomly ordered sample, than for the VACNT sample with ~ 4 and 40 $\mu J/mm^2$ of adhesion energy respectively. This is contrary to expectation as in the RACNT film it is expected that the CNT directly in contact with the surface will have

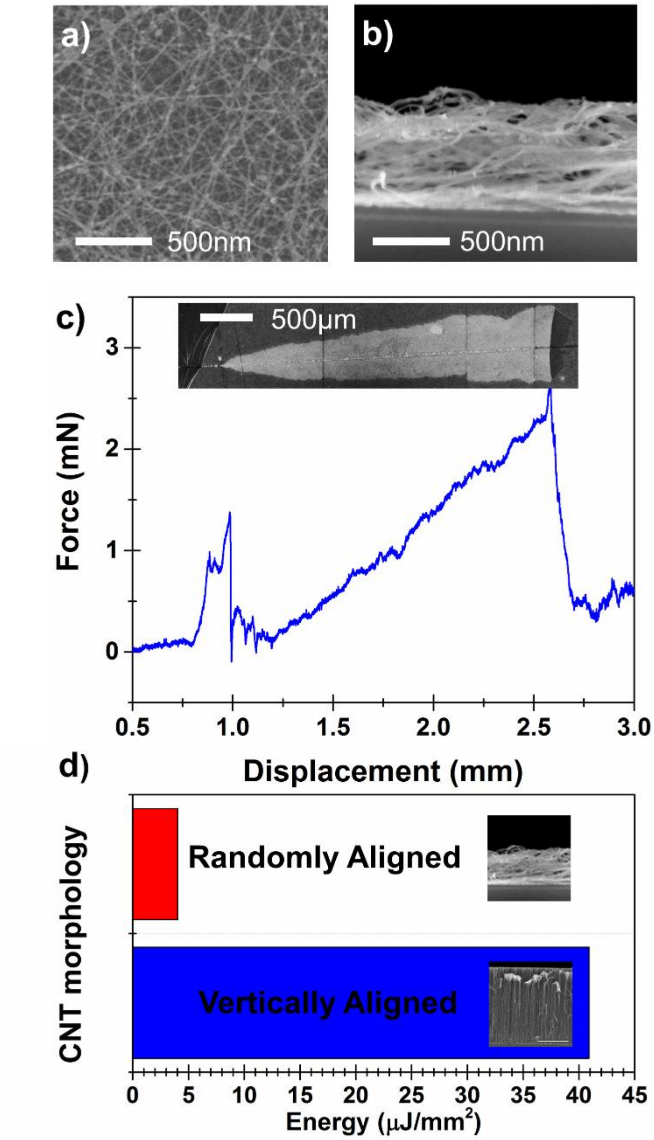

Figure 12.4 (a) Top down SEM image of the disordered CNT film. (b) Cross sectional SEM image of the CNT film. (c) Scratch test of disordered CNT film transferred to Si/SiO_2, with SEM image of scratch inset. (d) Comparison of adhesion energy per area of ordered and disordered CNT films transferred to Si/SiO_2.

significantly higher adhesion do to the large amount of sidewall adhesion between the surface and the CNT.

Indeed a closer analysis of scratch traces (**Figure 12.5**) of the CNT scratches illuminates the origin of this discrepancy. When we look at the scratched region for one of the VACNT films we can clearly see that there are no CNT left behind. This is in direct contrast to the scratched region of the disordered CNT film which clearly leaves a thin layer of CNT that are still adhered to the surface as seen in **Figure 12.5d**. Thus we observe that failure in the RACNT film actually occurred at the CNT-CNT connections closest to the substrate, and the CNT that were directly adhered to the substrate via sidewall interaction had a significantly higher amount of adhesion. The difference in the adhesion energy between the VACNT film and the RACNT film can then be understood by considering the density of CNT-CNT contacts in this randomly oriented film. An analysis of the number of CNT-CNT contacts in the randomly oriented film from SEM images for a given area is presented in the **Figure 12.5e** (SEM images used for the analysis can be found in the appendix **Figure 12.A5**. We found that the RACNT film had ~580 CNT-CNT connections per μm^2 a factor of 15 less

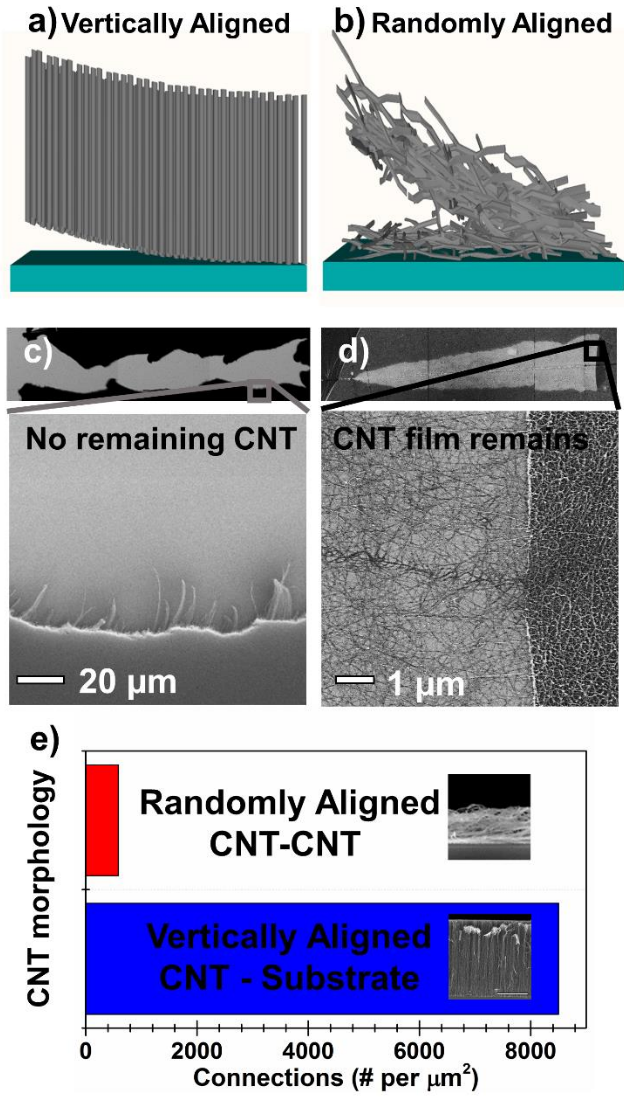

Figure 12.5 (a) Schematic showing the failure method of ordered CNT films. (b) Schematic showing the failure mechanism of disordered CNT films. (c) SEM image of a substrate after scratching an ordered CNT film. (d) SEM image of a substrate after scratching a disordered CNT film. (e) A comparison of the number of CNT-CNT and CNT-substrate connections for the disordered and ordered films respectively.

than the CNT density of the VACNT film (**Figure 12.5e**). Although this is not a perfect comparison, as this number in reality corresponds to CNT bundle - CNT bundle connections and will thus have a different adhesion energy per connection than the adhesion energy per CNT-substrate connection, we can see that the dramatic difference in the density of the connections between the two films is the primary cause for the difference in adhesion energy.

12.4 Conclusion

In summary we have used microscratch testing to both demonstrate the versatility of this technique for identifying and exploring SWCNT adhesion, and to quantitatively identify some of the key factors that determine the adhesion of CNT thin films. In particular our results indicate that the density of CNT directly in contact with the substrate, or the density of CNT-substrate connections directly determines the adhesion strength of VACNT thin films. We expand on these results showing that for a RACNT thin film the determining factor for CNT thin film adhesion is actually the density of CNT-CNT contacts within the film as these are the weakest load bearing elements due to the large sidewall adhesion of the CNT-substrate contacts. These results lay a foundation that emphasizes the potential of further scratch testing to identify mechanisms that determine CNT thin film and other nanomaterial thin film adhesion. These results further highlight that by engineering the number of CNT contacts within a given thin film one can exercise a degree of control in engineering the overall adhesion of these CNT thin films.

12.A Appendix

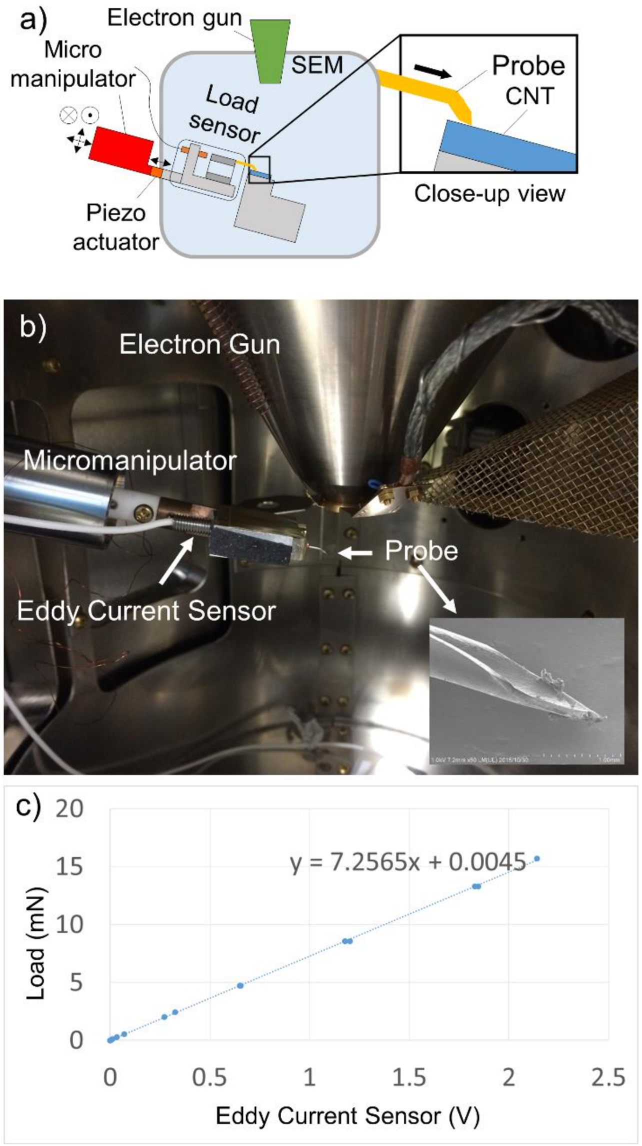

Figure 12.A1 (a) Schematic of the microscratch testing setup. (b) Picture of the microscratch testing setup. (c) Calibration of the force sensor.

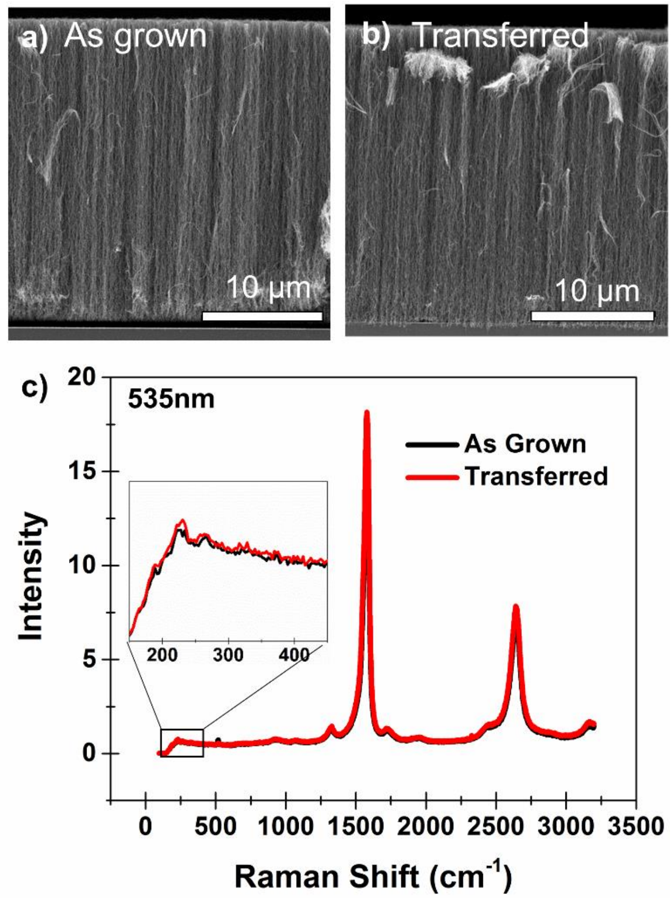

Figure 12.A2 (a) SEM of the as grown vertically aligned CNT. (b) SEM of the transferred vertically aligned CNT. (c) Raman of the as grown and transferred vertically aligned CNT films.

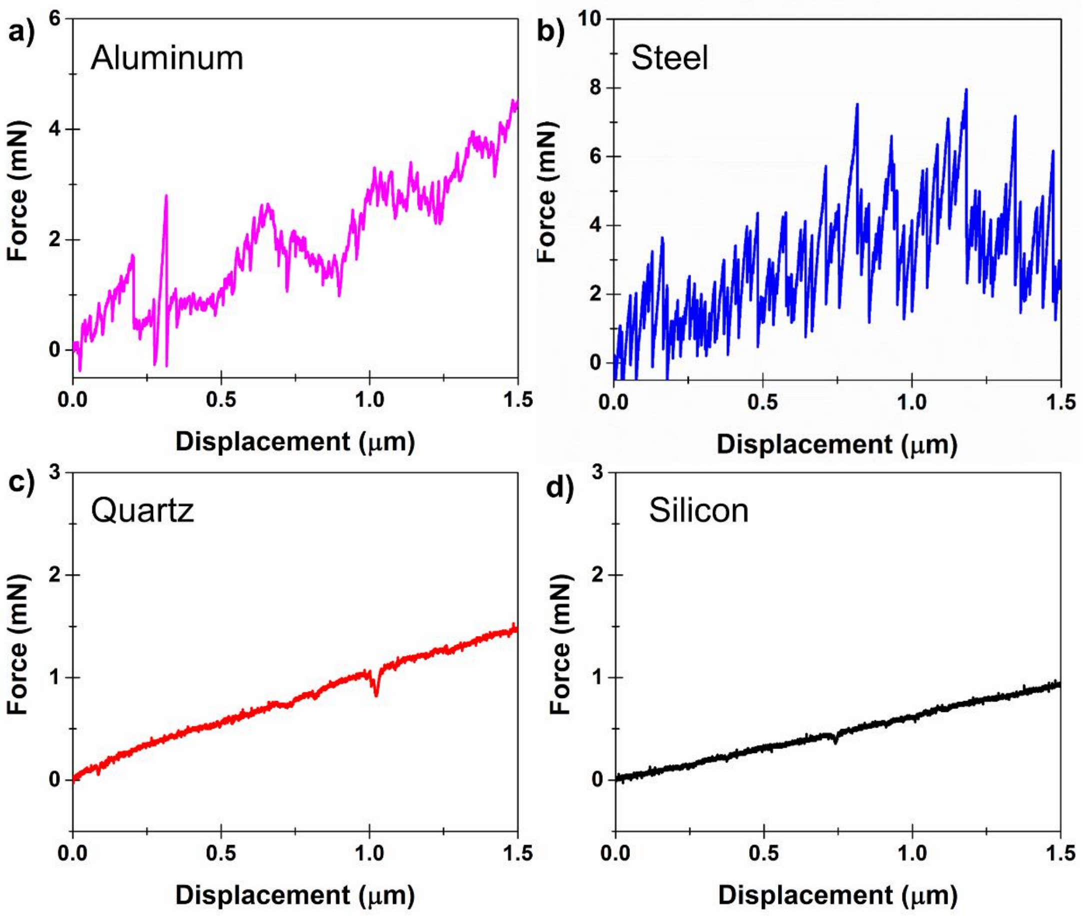

Figure 12.A3 (a) Scratch profile of aluminum substrate. (b) Scratch profile of steel substrate. (c) Scratch profile of the quartz substrate. (d) Scratch profile of the silicon-silicon dioxide substrate.

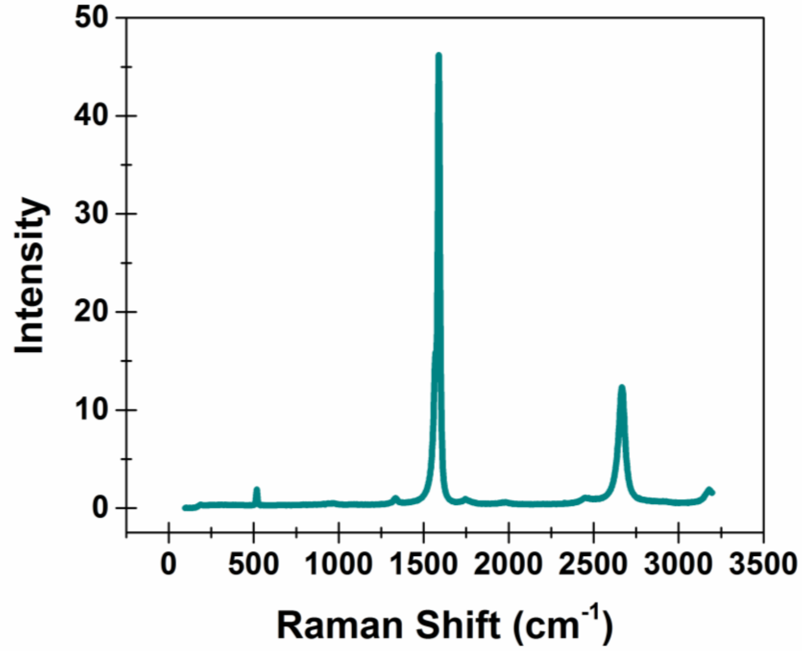

Figure 12.A4. Raman of the randomly aligned disordered CNT film.

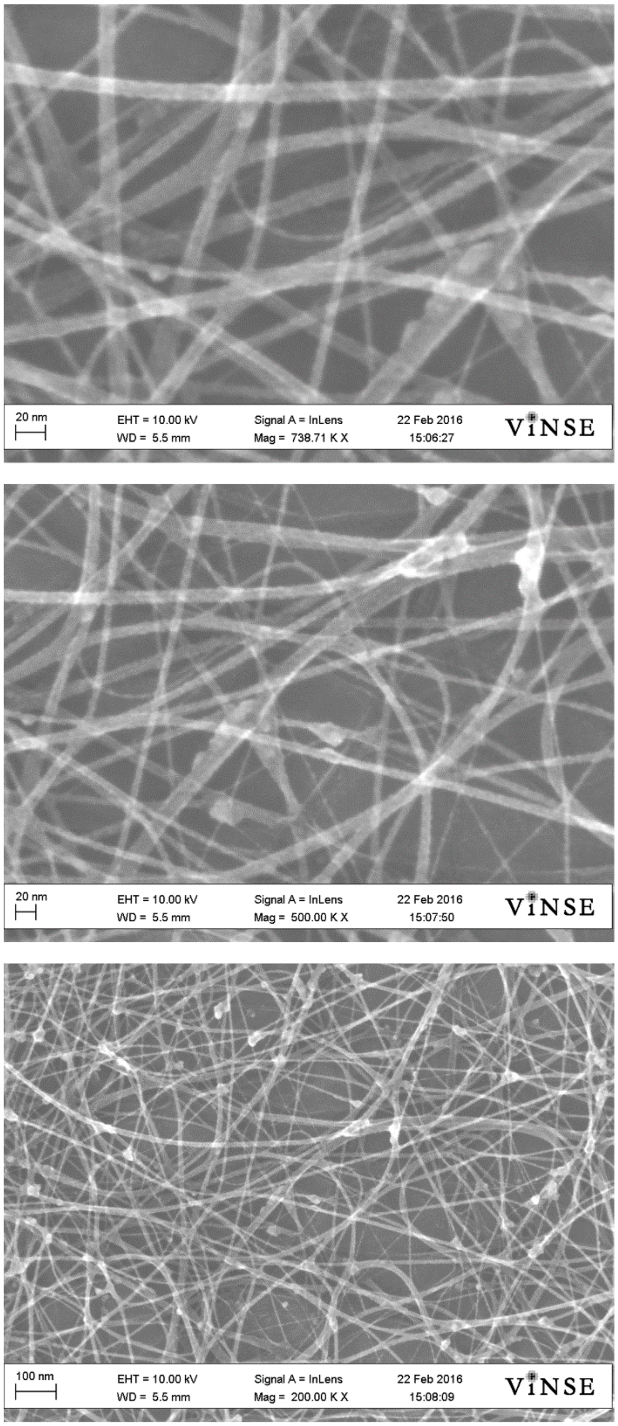

Figure 12.A5. SEM image of the randomly aligned disordered CNT films used to analyze the number of CNT-CNT connections per unit area.

Acknowledgements

Funding for Andrew Westover, and this research was provided jointly by the National Science Foundation East Asia and Pacific Summer Institute 2015 Award number 1515541, and the Japan Society for the Promotion of Science's summer program 2015.

References

1. Brennan, L. J.; Byrne, M. T.; Bari, M.; Gun'ko, Y. K. *Adv. Energy Mater.* **2011,** 1, (4), 472-485.

2. Bruce, P. G.; Scrosati, B.; Tarascon, J. M. *Angew. Chem. Int. Ed.* **2008,** 47, (16), 2930-2946.

3. Espinosa, H. D.; Bernal, R. A.; Minary-Jolandan, M. *Adv. Mater.* **2012,** 24, (34), 4656-4675.

4. Koski, K. J.; Cui, Y. *ACS Nano* **2013,** 7, (5), 3739-3743.

5. Samuelson, L.; Thelander, C.; Björk, M.; Borgström, M.; Deppert, K.; Dick, K.; Hansen, A.; Mårtensson, T.; Panev, N.; Persson, A. *Physica E* **2004,** 25, (2), 313-318.

6. Schmidt, V.; Wittemann, J. V.; Senz, S.; Gösele, U. *Adv. Mater.* **2009,** 21, (25-26), 2681-2702.

7. Wolf, S.; Awschalom, D.; Buhrman, R.; Daughton, J.; Von Molnar, S.; Roukes, M.; Chtchelkanova, A. Y.; Treger, D. *Science* **2001,** 294, (5546), 1488-1495.

8. Zhang, Q.; Huang, J. Q.; Qian, W. Z.; Zhang, Y. Y.; Wei, F. *Small* **2013,** 9, (8), 1237-1265.

9. Douglas, A.; Carter, R.; Oakes, L.; Share, K.; Cohn, A. P.; Pint, C. L. *ACS Nano* **2015**, 9, (11), 11156–11165.

10. Treacy, M. J.; Ebbesen, T.; Gibson, J. *Nature* 381, 678.

11. Wu, Z.; Chen, Z.; Du, X.; Logan, J. M.; Sippel, J.; Nikolou, M.; Kamaras, K.; Reynolds, J. R.; Tanner, D. B.; Hebard, A. F. *Science* **2004,** 305, (5688), 1273-1276.

12. Che, J.; Cagin, T.; Goddard III, W. A. *Nanotechnology* **2000,** 11, (2), 65.

13. Oakes, L.; Cohn, A. P.; Westover, A. S.; Pint, C. L. *Mater. Lett.* **2015,** 159, 261-264.

14. Kim, Y.-K.; Min, D.-H. *Langmuir* **2009,** 25, (19), 11302-11306.

15. Kaskela, A.; Nasibulin, A. G.; Timmermans, M. Y.; Aitchison, B.; Papadimitratos, A.; Tian, Y.; Zhu, Z.; Jiang, H.; Brown, D. P.; Zakhidov, A. *Nano Lett.* **2010,** 10, (11), 4349-4355.

16. Oakes, L.; Hanken, T.; Carter, R.; Yates, W.; Pint, C. L. *ACS Appl. Mater. Interfaces* **2015,** 7, (26), 14201-14210.

17. Cohn, A. P.; Oakes, L.; Carter, R.; Chatterjee, S.; Westover, A. S.; Share, K.; Pint, C. L. *Nanoscale* **2014,** 6, (9), 4669-4675.

18. Carter, R.; Oakes, L.; Cohn, A. P.; Holzgrafe, J.; Zarick, H. F.; Chatterjee, S.; Bardhan, R.; Pint, C. L. *J. Phys. Chem. C* **2014,** 118, (35), 20137-20151.

19. Cui, K.; Chiba, T.; Omiya, S.; Thurakitseree, T.; Zhao, P.; Fujii, S.; Kataura, H.; Einarsson, E.; Chiashi, S.; Maruyama, S. *J. Phys. Chem. Lett.* **2013,** 4, (15), 2571-2576.

20. Jeon, I.; Chiba, T.; Delacou, C.; Guo, Y.; Kaskela, A.; Reynaud, O.; Kauppinen, E. I.; Maruyama, S.; Matsuo, Y. *Nano Lett.* **2015,** 15, (10), 6665-6671.

21. Jiu, J.; Nogi, M.; Sugahara, T.; Tokuno, T.; Araki, T.; Komoda, N.; Suganuma, K.; Uchida, H.; Shinozaki, K. *J. Mater. Chem.* **2012,** 22, (44), 23561-23567.

22. Carrillo, J.-M. Y.; Raphael, E.; Dobrynin, A. V. *Langmuir* **2010,** 26, (15), 12973-12979.

23. Joo, S.; Baldwin, D. F. *Nanotechnology* **2010,** 21, (5), 055204.

24. Li, T.; Ayari, A.; Bellon, L. *J. Appl. Phys.* **2015,** 117, (16), 164309.

25. Roenbeck, M. R.; Furmanchuk, A. o.; An, Z.; Paci, J. T.; Wei, X.; Nguyen, S. T.; Schatz, G. C.; Espinosa, H. D. *Nano Lett.* **2015,** 15, (7), 4504-4516.

26. Liu, C.-H.; Yu, X. *Nanoscale Res. Lett* **2011,** 6, (1), 75.

27. Lahiri, I.; Lahiri, D.; Jin, S.; Agarwal, A.; Choi, W. *ACS nano* **2011,** 5, (2), 780-787.

28. Jin, M.; Feng, X.; Feng, L.; Sun, T.; Zhai, J.; Li, T.; Jiang, L. *Adv. Mater.* **2005,** 17, (16), 1977-1981.

29. Madaria, A. R.; Kumar, A.; Ishikawa, F. N.; Zhou, C. *Nano Res.* **2010,** 3, (8), 564-573.

30. Matthey, D.; Wang, J.; Wendt, S.; Matthiesen, J.; Schaub, R.; Lægsgaard, E.; Hammer, B.; Besenbacher, F. *Science* **2007,** 315, (5819), 1692-1696.

31. Salameh, S.; Schneider, J.; Laube, J.; Alessandrini, A.; Facci, P.; Seo, J. W.; Ciacchi, L. C.; Mädler, L. *Langmuir* **2012,** 28, (31), 11457-11464.

32. Shimoi, N.; Abe, D. *ACS Appl. Mater. Interfaces* **2015,** 7, (25), 13776-13781.

33. Haun, J. B.; Hammer, D. A. *Langmuir* **2008,** 24, (16), 8821-8832.

34. Geng, Z.; He, J. *J. Mater. Chem. A* **2014,** 2, (39), 16601-16607.

35. Geng, Z.; He, J.; Yao, L. *RSC Adv.* **2015,** 5, (108), 89262-89268.

36. Keshri, A. K.; Lahiri, D.; Agarwal, A. *Carbon* **2011,** 49, (13), 4340-4347.

37. Lahiri, D.; Agarwal, A. *Adv. Mater. Processes* **2012**, April, 22-27.

38. Bull, S.; Berasetegui, E. *Tribol. Int.* **2006,** 39, (2), 99-114.

39. Liu, Z.; Sun, J.; Wu, J.-D.; WANG, P.-N.; Shen, W. *Tribol. Trans.* **2004,** 47, (1), 130-137.

40. Dauskardt, R.; Lane, M.; Ma, Q.; Krishna, N. *Eng. Fract. Mech.* **1998,** 61, (1), 141-162.

41. Benjamin, P.; Weaver, C. In *Adhesion of metal films to glass*, Proceedings of the Royal Society of London A: Mathematical, Physical and Engineering Sciences, 1960; The Royal Society: pp 177-183.

42. Benjamin, P.; Weaver, C. In *The adhesion of metals to crystal faces*, Proceedings of the Royal Society of London A: Mathematical, Physical and Engineering Sciences, 1963; The Royal Society: pp 267-273.

43. Xiang, R.; Yang, Z.; Zhang, Q.; Luo, G.; Qian, W.; Wei, F.; Kadowaki, M.; Einarsson, E.; Maruyama, S. *J. Phys. Chem. C* **2008,** 112, (13), 4892-4896.

44. Ting, B.-Y.; Winer, W.; Ramalingam, S. *J. Tribol.* **1985,** 107, (4), 472-477.

45. Ting, B.-Y.; Ramalingam, S.; Winer, W. *J. Tribol.* **1985,** 107, (4), 478-482.

46. Valli, J. *J. Vac. Sci. Technol., A* **1986,** 4, (6), 3007-3014.

47. Murakami, Y.; Chiashi, S.; Miyauchi, Y.; Hu, M.; Ogura, M.; Okubo, T.; Maruyama, S. *Chem. Phys. Lett.* **2004,** 385, (3), 298-303.

48. Xiang, R.; Einarsson, E.; Okabe, H.; Chiashi, S.; Shiomi, J.; Maruyama, S. *Jpn. J. Appl. Phys.* **2010,** 49, (2S), 02BA03.

49. Xiang, R.; Einarsson, E.; Murakami, Y.; Shiomi, J.; Chiashi, S.; Tang, Z.; Maruyama, S. *ACS Nano* **2012,** 6, (8), 7472-7479.

50. Maruyama, S.; Kojima, R.; Miyauchi, Y.; Chiashi, S.; Kohno, M. *Chem. Phys. Lett.* **2002,** 360, (3), 229-234.

51. Amama, P. B.; Pint, C. L.; McJilton, L.; Kim, S. M.; Stach, E. A.; Murray, P. T.; Hauge, R. H.; Maruyama, B. *Nano Lett.* **2008,** 9, (1), 44-49.

52. Sakurai, S.; Nishino, H.; Futaba, D. N.; Yasuda, S.; Yamada, T.; Maigne, A.; Matsuo, Y.; Nakamura, E.; Yumura, M.; Hata, K. *J. Am. Chem. Soc.* **2012,** 134, (4), 2148-2153.

53. Kim, S. M.; Pint, C. L.; Amama, P. B.; Zakharov, D. N.; Hauge, R. H.; Maruyama, B.; Stach, E. A. *J. Phys. Chem. Lett.* **2010,** 1, (6), 918-922.

54. Gadelmawla, E.; Koura, M.; Maksoud, T.; Elewa, I.; Soliman, H. *J. Mater. Process. Technol.* **2002,** 123, (1), 133-145.

55. Nasibulin, A. G.; Kaskela, A.; Mustonen, K.; Anisimov, A. S.; Ruiz, V.; Kivisto, S.; Rackauskas, S.; Timmermans, M. Y.; Pudas, M.; Aitchison, B. *ACS Nano* **2011,** 5, (4), 3214-3221.

CHAPTER 13

CARBON NANOTUBE REINFORCED MULTIFUNCTIONAL ENERGY STORAGE COMPOSITES

Andrew Westover,[1,2] Eti Teblum,[3] Deanna Schauben,[1] Anat Yitzhak ,[3] Nitin Muralidharan,[1,2] Merav Muallem,[3] Gilbert Nessim,[3] Cary L. Pint[1,2]

[1]Department of Mechanical Engineering, Vanderbilt University, Nashville TN 37235, USA
[2]Interdisciplinary Materials Science Program, Vanderbilt University, Nashville, TN 37235, USA
[3]Department of Chemistry, Bar Ilan Institute for Nanotechnology and Advanced Materials (BINA), Bar Ilan University, 52900 Ramat Gan, Israel

Abstract: Structural composites have become a central focus of the manufacturing community for their exceptional weight to strength ratios and versatile engineering design. Meanwhile energy storage has become one of the most important fields of research for electric vehicles and portable electronics. We present here our work in merging these two fields. We did this using carbon nanotubes (CNT) grown directly on stainless steel meshes via chemical vapor depositions (CVD) as electrodes, fiberglass (FG) or Kevlar as separators, and epoxy-ionic liquid (IL) composites as an electrolyte and structural matrix. These structural composites exhibit mechanical strength greater than 85 MPa approaching that of commercial composites and with an energy density of up to 3 mWh/kg for a fully packaged system. Finally we show the in-situ mechano-electro-chemical performance where the capacitance is completely maintained throughout the elastic regime up to the maximum tensile loading >85 MPa.

13.1 Introduction

Fiber based structural composites are one of the most important emerging and researched structural materials in recent years.[1, 2] They are incredibly valuable for their high strength to weight and volume ratios and their versatility both in the ability to mold them into any shape and the ability to tailor their properties by varying the composite components.[3, 4] Meanwhile energy storage including batteries, supercapacitors and hybrid devices have taken center stage in energy research due to their vital importance both in portable electronics, electric vehicles and in enabling renewable energy conversion.[5, 6] Whereas traditional energy storage research focuses on slight alterations in materials chemistry and design to improve performance of traditional battery systems,[7] true progress in the field of energy storage requires out of the box innovative approaches that change the paradigm of traditional energy storage architectures.[8] One such innovative direction of research is the development of multifunctional composite structures that take advantage of the versatility and high strength of fiber based structural composites adapting them to simultaneously function as a structural energy storage material.[9-11]

The field of structural energy storage composites began with the idea of embedding commercial Li ion batteries into the wings of unmanned autonomous vehicles (UAV), the doors of cars, and the walls of marine vessels.[12-14] Whereas this route does show some promise the ultimate strength of these composites will ultimately be limited by the packaged design of batteries. The second and more elegant iteration of energy storage composites has been in the development of composite materials that simultaneously act as both a structural material and as an energy storage material. Initial work in this field has involved the development of structural batteries and supercapacitors. Although there are significant prospects for structural batteries,[10] because of their limited lifetime and complicated chemistry the majority of research in this field has focused on the development of structural supercapacitors which have an estimated lifetime greater than 40 years and have relatively simple design considerations as they primarily rely on electric double layer capacitance (EDLC).[9, 11, 15-19]

The premier work to date in the field of structural supercapacitors has been that of the Greenhalgh group in the Imperial college of London. Adapting a traditional structural composite design they have developed a variety of different structural composites that rely on using carbon fiber for electrode materials or current collectors. Their most advanced work to date has involved the use of carbon fiber as current collectors with high surface area carbon aerogels for electrodes, fiberglass for separators and a poly-ethylene glycol diglycidal ether (PEDGE) – ionic liquid electrolytes.[19] They boast a composite device performance with a capacitance up to 10 mF/g, and energy storage capacity up to 0.1 mWh/kg, a specific power of 3.8 mW/kg with an ultimate tensile strength of 8.71 MPa, and a modulus of 0.9 GPa. Despite this initial success there are still several significant challenges that must be overcome in order to implement structural energy storage. First both the mechanical and electrochemical performance must be improved to a performance on par with commercial composites with mechanical strengths greater than 200 MPa and a Modulus greater than 5 GPa, and an energy storage performance approaching that of a commercial supercapacitor at 0.5-1 Wh/kg for packaged systems. Furthermore almost all reports to date on structural composite supercapacitors have not demonstrated simultaneous mechanical and electrochemical performance which has been demonstrated to be a critical performance metric when designing these systems.[9, 20, 21]

When designing structural composites one of the areas of research that has received significant attention has been the use of carbon nanotube (CNT) based reinforcing materials in the epoxy matrix to increase its conductivity, stiffness, and strength.[5, 22, 23] At the same time, due to their high surface area and conductivity, CNT remain one of the best materials for supercapacitors.[24] As CNT are used both in the development of structural supercapacitors and in the development of advanced structural composites they are naturally one of the ideal candidates for an active energy storage material for structural supercapacitors. The challenges with using CNT in structural supercapacitor applications to date has been the difficulty in integrating a high density CNT material with a fiber based current collector compatible with a structural composite design.[25] On another note, there has been a significant amount of research showing the ability to grow CNT directly onto stainless steel with both mechanical and electrical interconnectivity which is an excellent strategy for many applications including the development of supercapacitors.[26, 27]

Adapting this CNT growth technique we present here our work in developing multifunctional structural supercapacitors that use CNT grown directly on stainless steel fiber mesh as structural electrodes, fiberglass and Kevlar as separators and diglycl based epoxy/ionic liquid as both an electrolyte and a matrix material. These composite materials exhibit an energy storage capability of up to 5 mWh/kg at power densities of up to 1 W/kg, and an ultimate tensile strength greater than 85 MPa with a modulus of more than 5 GPa. Furthermore we show simultaneous in-situ mechano-electro-chemical measurements where the CNT-Steel structural supercapacitors maintain their energy storage performance throughout the elastic regime of the devices and then see steady degradation in the plastic regime highlighting the robustness of these devices as well as the necessity for in-situ mechano-electro-chemical measurements.

13.2 Experimental Methods

13.2.1 *Growth of CNT on stainless steel mesh*

Two types of steel mesh were used in these experiments, a 304 200x200stainless steel mesh (ASTM E2016-06) with a fiber diameter of 53 µm, and a 316 400x400 stainless steel mesh (ASTM E 2016-11) with a fiber diameter of 30.5 µm. CNT growth on these stainless steel meshes was achieved using the same procedure except with small variations in temperature. To grow CNT a three zone furnace was initially heated to the growth temperature. Zones 1 and 2 for preheating the gasses was kept constant at 770ºC and zone 3, the growth zone was varied from 740ºC to 790ºC. The chamber was then purged with 400 SCCM of H_2 and 100 SCCM of Ar for 15 min. At this point the stainless steel mesh was inserted into the center of zone 3, and annealed under 1000 SCCM of Ar/O_2 (99% / 1%) and 100 SCCM of pure Ar for 45 min. The Ar/O_2 was then turned off and the surface was reduced under a flow of 100 SCCM of Ar, and 400 SCCM of H_2 for 40 min. Finally the growth step was initiated with a gas flow of 100 SCCM of Ethylene, 250 SCCM of Ar/O_2 (99%/1%), 400 SCCM of H_2 and 100 SCCM of Ar for 15 min. This growth process was very sensitive to the temperature and we obtained the best growth at a growth temperature of 755ºC for the 304 stainless steel and at 790ºC for the 316 stainless steel.[28, 29]

13.2.2 Layup of structural composites

Structural composite supercapacitors were made using a common layup process. Epoxy-ionic liquid (IL) electrolyte was prepared by first dissolving 6g of lithium tetrafluoroborate ($LiBF_4$) in 24g of 1-butyl 3-methyl imidizolium tetrafluoroborate ($BMIBF_4$).[30] This was followed by mixing supersap CCR epoxy resin with the slow curing hardener in a planetary mixer (Thinky USA). The mixed epoxy and hardener were then combined with the ionic liquid at a ratio of 45%-55% epoxy-IL by weight as was determined to be an optimal balance of electrochemical and mechanical performance in previous studies.[21] While the epoxy-IL was still in an uncured state, the epoxy was poured over the C NT-steel mesh and then put under vacuum to infiltrate the epoxy-IL into the CNT. Following electrolyte infiltration into the CNT-steel mesh, the CNT-Steel mesh was placed against a smooth metal sheet backplate and epoxy-IL was applied to fiberglass (S-Glass, Fiberglasssupply.com) or Kevlar fiber mesh (Fiberglasssupply.com) separators and sandwiched in between the CNT-Steel electrodes. A layer of peel-ply, and an absorbing layer were then used to cover the composites and the entire area was sealed and put under vacuum using traditional composite vacuum bagging. The structural composite was kept under vacuum overnight and then removed from vacuum and placed on a hot plate at 80ºC for 6-10 hours to complete the curing process.

13.2.3 Electrochemical measurements

Electrochemical measurements including cyclic voltammetry (CV) and charge discharge (CD) measurements were performed on an Autolab multichannel analyzer with attached galvanostat/potentiostat modules. CV measurements were performed from -3V to +3V at scan rates ranging from 20 mV/s to 500 mV/s. CD measurements were performed with charging currents ranging from 1.5-8 mA/cm^3. Energy values were calculated by integrating the area under the discharge curves, and average power values were calculated by diving the energy by the discharge time.[9]

13.2.4 Mechanical measurements

In order to perform tensile measurements on the structural supercapacitors the devices were cut in long linear strips about 1cm x 7cm in length and then an additional layup step with pure epoxy resin and fiberglass was used to make tabs to enable gripping of the structural composites. Tensile tests were

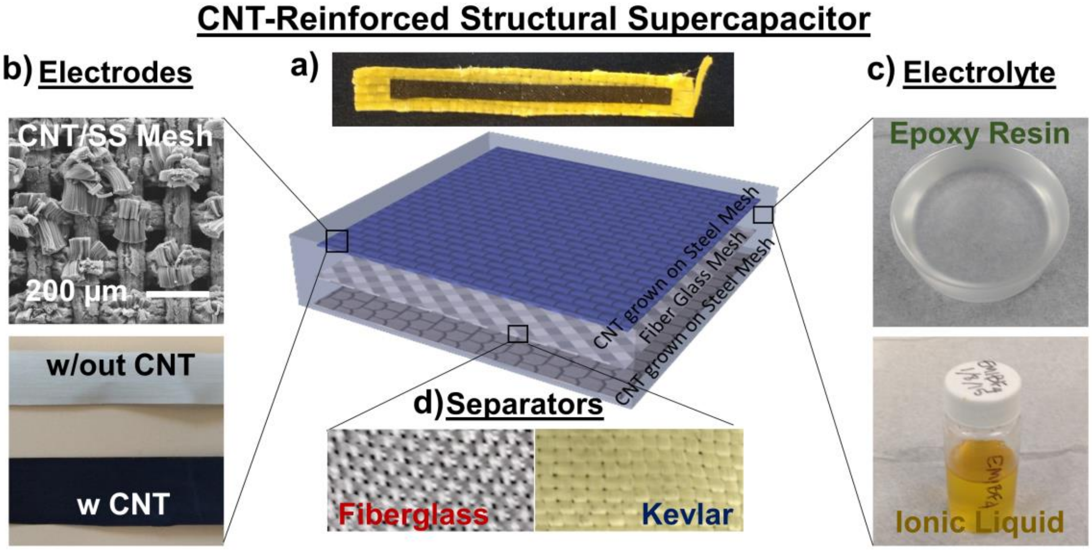

Figure 13.1 (a) Photograph and schematic showing CNT-Steel structural supercapacitor with a kevlar separator. (b) SEM of a CNT-steel mesh showing the CNT on the mesh and a photograph showing a steel mesh with and without CNT. (c) Photographs showing the two components of the epoxy-IL electrolyte. d) Photograph of fiberglass and Kevlar separators

performed with an Instron load cell at a strain rate of 2 mm/min for the mechanical tests by themselves and at a strain rate of 0.5 mm /min for the in-situ mechano-electro-chemical measurements.

In-situ mechano-electro-chemical measurements were performed on the same Instron load cell but with a strain rate of 0.5mm/min and with a portable Autolab potentiostat/galvanostat with alligator clips attached to the respective electrodes. CD measurements were then performed at the same time as the mechanical measurement.[21]

13.3 Results and Discussion

Figure 13.1 illustrates the different parts of the structural composite with a photograph and schematic of the structural supercapacitors depicted in **Figure 13.1a**. For the electrode materials CNT were grown on stainless steel meshes via CVD. In **Figure 13.1b** it can be seen that the CNT completely coated the steel mesh with CNT ranging from 15-60 μm in length. It can also be seen from the photograph in the bottom of **Figure 13.1b** that before the CNT growth changes the color of the mesh from silver to metallic black. **Figure 13.1c** shows photographs of the epoxy and ionic liquid used to make a structural electrolyte and matrix for the composite while **Figure 13.1d** shows photographs of the two different types of separators used in the composites: fiberglass and Kevlar.

Figure 13.2 shows the electrochemical performance of the 400 stainless steel mesh with CNT grown on it with a Kevlar separator and an epoxy-IL electrolyte (45%-55%). CV curves show good capacitance albeit with a high resistance that comes from the solid state nature of the electrolytes and with an electrochemical window of about 2.5V. The capacitance values calculated from the CV curves is shown in **Figure 13.2b** with a maximum capacitance at slow rates of 60 mF/cm^3 (16 mF/g) and a capacitance of 15 mF/cm^3 (3 mF/g) at fast rates of 500 mV/s. This is compared to the best carbon aerogel based devices in literature that have a similar capacitance of about 35 mF/cm^3 (74 mF/g) , but which have a severely limited electrochemical window of about 0.4V. **Figure 13.2c** shows discharge curves for multiple different charging currents ranging from 1.5 mA/cm^3 to 8 mA/cm^3. In **Figure 13.2d** we can see five consecutive charge discharge curves showing the steadiness of the measurements. The CD curves were then used to calculate both the specific and volumetric energy and power densities both for pure liquid based devices and for solid state devices represented in **Figure 13.2a-d**. This is then compared with the liquid and solid state performance of the carbon aerogel/carbon fiber based devices with liquid and solid state electrolytes. We see that our devices have an energy density in the solids state from 3 mWh/kg (10 µWh/cm^3) and a power density of 1 W/kg (70 mW/cm^3). If the solid state electrolyte could be improved we can see that the performance could potentially be improved with an energy density up to 10 mWh/kg (30 µWh/cm^3) and a power density up to 10 W/kg. By contrast the carbon aerogel device in literature[19] has a maximum possible liquid based performance comparable with the solid state of our CNT-Steel mesh based composite structural supercapacitors and a solid state performance an order of magnitude less than our solid state performance in both power and energy for both specific and volumetric performance.

The mechanical performance of the structural composite is presented in **Figure 13.3** where the stress strain curve is shown. We see an initial plateau that corresponds to fibers aligning and pulling taught followed by the linear elastic performance of the composite. From this elastic regime we calculate a

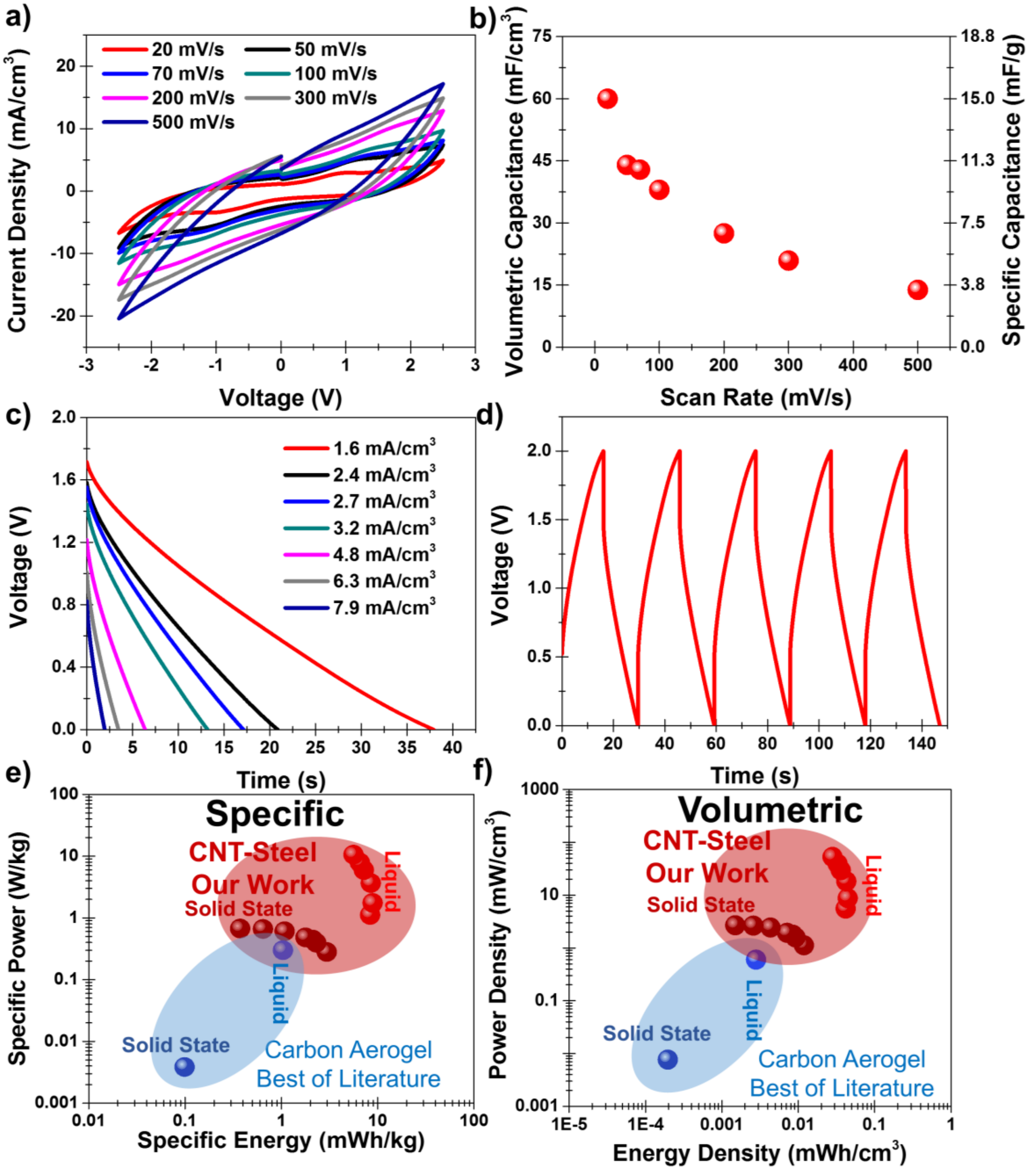

Figure 13.2 (a) CV curves from 20 mV/s to 500 mV/s for a composite structural supercapacitor with a Kevlar separator. (b) Volumetric and specific capacitance calculated from CV curves for the composite supercapacitors. (c) Disharge curves for charging curents ranging from 1.5-8 mA/cm^2 (d) Five consecutive CD measurements for the composite. (e) Ragone plot showing specific energy and power density of CNT-Steel mesh performance with a Kevlar separator and a 100% IL electrolyte and an Epoxy-IL electrolyte compared to the liquid and solid state performance of the best structural supercapacitor composite in literature. (f) Ragone plot for the same but for volumetric performance.

modulus of elasticity of 6.2 GPa. We can also see from the graph that this has an ultimate tensile strength

(UTS) of ~85 MPa (this represents the low end of all devices with other devices exhibiting a strength up to 120 MPa). Notably the limiting factor in these devices were the steel mesh as it can be observed from the images in **Figure 13.3b** that the critical failure occurred in the stainless steel mesh.

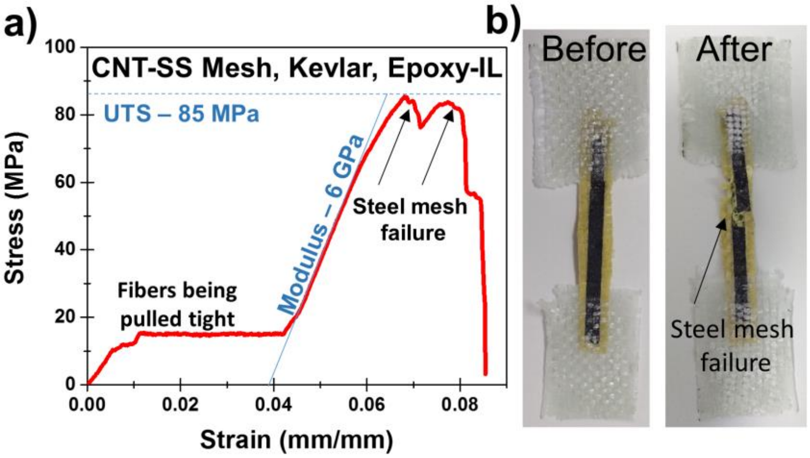

Figure 13.3 (a) Stress strain measurement of a composite structural supercapacitor with the major points, the UTS and the Modulus highlighted. (b) Photograph of the structural supercapcitor before and after mechanical testing, where it can be easily seen that the failure occurs in the steel mesh.

In **Figure 13.4** we can see a comparison of the juxtaposition of the specific energy in comparison to the tensile strength and Young's modulus in **Figure 13.4a** and **Figure 13.4b** respectively of the material and a corresponding comparison to the best of literature, and to the optimal mechanical and energy storage targets. We can see that our work with CNT-Steel electrodes improves upon the best of literature[14] in terms of both mechanical performance and energy performance, with an energy storage performance close to 2 orders of magnitude improved, the tensile strength improved by about 10X and the modulus of the material improved about 5x.These graphs also highlight how far we have come towards reaching the energy storage and mechanical performance targets of developing a composites material that has the energy storage of a packaged commercial supercapacitor of about 0.5-1 Wh/kg and the strength of a commercial structural composite from 200 MPa-1000 MPa.

We have clearly demonstrated how these CNT-Steel based composite structural supercapacitors represent a huge step forward in bringing energy storage composites to a multifunctional performance that is realistic and commercializable. The one last key aspect in verifying the true multifunctionality of our composite material is the performance of in-situ mechano-electro-chemical measurements In **Figure 13.5**

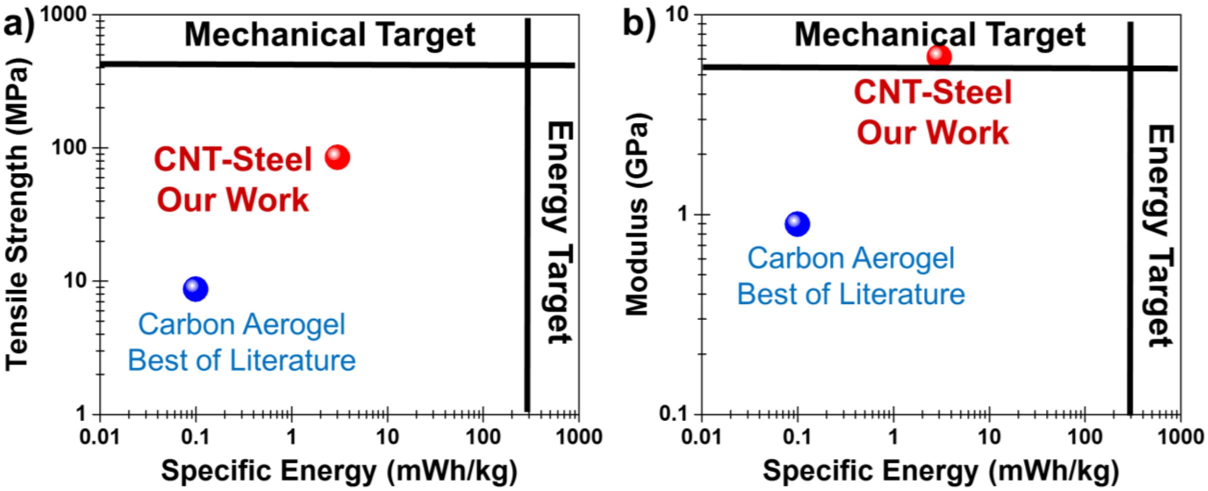

Figure 13.4 (a) Energy-strength plot showing the balance of mechanical strength and energy storage compared to the best of literature and to the mechanical and energy storage targets. (b) Energy-modulus plot also compared to the best of literature and to the mechanical and energy targets.

we present the in-situ performance of the composite material. Within the elastic regime of the material we see steady electrochemical performance without a change in capacitance. As the device enters the plastic regime however we see a steady degradation in capacitance until we the device is no longer able to charge and we see complete electrochemical failure. Notably this occurs after the primary mechanical failure of the device at around 0.085 strain where the steel fibers begin to snap. The initial degradation in the device performance correlates to a significant increase in the equivalent series resistance and corresponding voltage drop and is likely due to the delamination of the steel fibers within the mesh as the tension on the steel causes the fibers to slip and ultimately fail. This measurements demonstrates the robust multifunctional performance highlighting that when stresses are kept within the elastic regime of the device it exhibits exceptional electrochemical stability. Once the plastic regime has been reached in addition to the plastic behavior we see permanent decreases in the performance highlighting that although full mechanical failure has not been reached the electrochemical performance has begun to be compromised. Whereas this measurement highlights the impressive performance of our composite supercapacitors, it also emphasizes the importance of such in-situ measurements for assessing the multifunctional performance of structural energy storage composites.

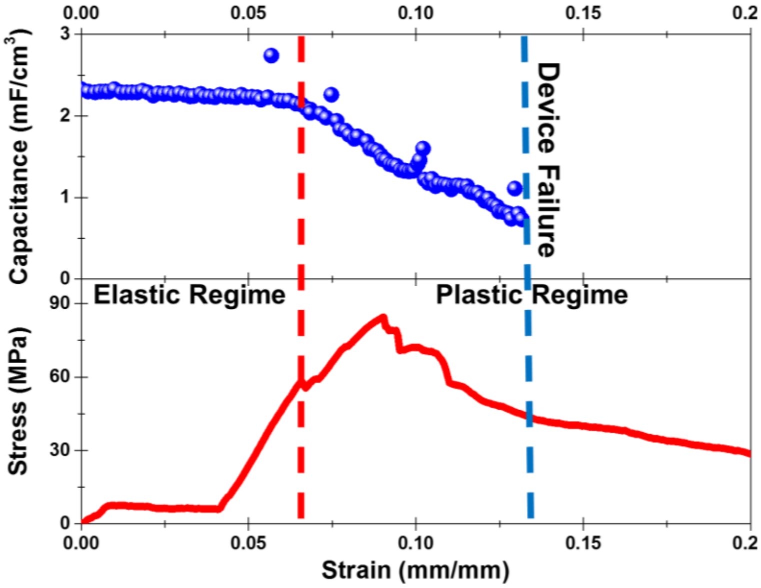

Figure 13.5 An in-situ mechano-electro-chemical test of the performance of a CNT-Steel-Kevlar-Epoxy-IL composite material with the capacitance as a function of strain on the top (blue) and the tensile performance on the bottom (red). The elastic and plastic regimes of the composite are denoted as is the point at which the devices stops functioning as a supercapacitor.

Whereas this work shows one example of a structural supercapacitor with exceptional mechanical and vastly improved energy storage performance, it is clear that in order for such a device to implemented in a commercial design there is still a significant body of research that needs to be performed. Perhaps the single greatest limiting factor in the energy and power performance is the limitations introduced by using a solid state epoxy-IL electrolyte as demonstrated by the Ragone graphs in **Figure 13.2e-f**. For these devices to reach their energy storage potential it is critical that additional research focus on improving the ionic conductivity and stiffness of ion conducting epoxy-IL electrolytes. Despite its current limitations this multifunctional energy storage composite emphasizes the importance of such a multifunctional design and its promise in acting simultaneously as a structural material and as an energy storage device. Furthermore although this research presents one instance of a structural supercapacitor, the versatile nature, and the simple way in which layers can be added, removed and modified to tailor performance suggest that similar designs could be used in the development of structural batteries, and composites with mechanical performance much great than that of the current study.

13.4 Conclusion

In summary our work highlight the feasibility of developing multifunctional structural composite that have both exceptional mechanical performance with a mechanical strength greater than 85 MPa, a modulus greater than 5GPa, and with exceptional composite energy storage performance with a specific energy up to 3 mWh/kg. This represents orders of magnitude improvement in both mechanical and energy performance compared to previous structural supercapacitors. Furthermore we demonstrate in-situ mechano-electro-chemical performance with stable capacitance within the elastic regime of the devices followed by steady degradation to failure within the plastic regime of the devices. Building on this foundation, our work emphasizes a practical route towards the further research and development of structural energy storage composites that can fulfill both structural and energy roles in future technologies.

Acknowledgements

Funding for this work was provided by BSF Grant Number - 2014041 and by a Prof. Rahamimoff Travel Grant 2016. We would also like to acknowledge Dr. Leon Bellan and Dr. Lior Elbaz for partial use of facilities and Keith Share, Adam Cohn, Landon Oakes, Rachel Carter, and Anna Douglass for useful discussions.

References

1. Gibson, R. F., *Principles of composite material mechanics*. CRC press: 2016.

2. Taraghi, I.; Fereidoon, A.; Taheri-Behrooz, F. *Materials & Design* **2014,** 53, 152-158.

3. Salman, S. D.; Leman, Z.; Sultan, M. T.; Ishak, M. R.; Cardona, F. *BioResources* **2015,** 10, (4), 8580-8603.

4. Gay, D., *Composite materials: design and applications*. CRC press: 2014.

5. Chen, H.; Cong, T. N.; Yang, W.; Tan, C.; Li, Y.; Ding, Y. *Progress in Natural Science* **2009,** 19, (3), 291-312.

6. Dunn, B.; Kamath, H.; Tarascon, J.-M. *Science* **2011,** 334, (6058), 928-935.

7. Xu, B.; Qian, D.; Wang, Z.; Meng, Y. S. *Materials Science and Engineering: R: Reports* **2012,** 73, (5), 51-65.

8. Goodenough, J. B.; Park, K.-S. *Journal of the American Chemical Society* **2013,** 135, (4), 1167-1176.

9. Westover, A. S.; Tian, J. W.; Bernath, S.; Oakes, L.; Edwards, R.; Shabab, F. N.; Chatterjee, S.; Anilkumar, A. V.; Pint, C. L. *Nano letters* **2014,** 14, (6), 3197-3202.

10. Liu, P.; Sherman, E.; Jacobsen, A. *J Power Sources* **2009,** 189, (1), 646-650.

11. Shirshova, N.; Qian, H.; Houllé, M.; Steinke, J. H.; Kucernak, A. R.; Fontana, Q. P.; Greenhalgh, E. S.; Bismarck, A.; Shaffer, M. S. *Faraday discussions* **2014,** 172, 81-103.

12. Thomas, J. P.; Keennon, M. T.; DuPasquier, A.; Qidwai, M. A.; Matic, P. In *Multifunctional structure-battery materials for enhanced performance in small unmanned air vehicles*, ASME 2003

International Mechanical Engineering Congress and Exposition, 2003; American Society of Mechanical Engineers: pp 289-292.

13. Qidwai, M. A.; Thomas, J.; Matic, P. In *Structure-battery multifunctional composite design*, SPIE's 9th Annual International Symposium on Smart Structures and Materials, 2002; International Society for Optics and Photonics: pp 180-191.

14. Thomas, J.; Qidwai, S.; Pogue, W.; Pham, G. *Journal of Composite Materials* **2013,** 47, (1), 5-26.

15. Benson, J.; Kovalenko, I.; Boukhalfa, S.; Lashmore, D.; Sanghadasa, M.; Yushin, G. *Advanced Materials* **2013,** 25, (45), 6625-6632.

16. Qian, H.; Diao, H.; Shirshova, N.; Greenhalgh, E. S.; Steinke, J. G.; Shaffer, M. S.; Bismarck, A. *Journal of colloid and interface science* **2013,** 395, 241-248.

17. Javaid, A.; Ho, K.; Bismarck, A.; Shaffer, M.; Steinke, J.; Greenhalgh, E. *Journal of Composite Materials* **2014,** 48, (12), 1409-1416.

18. Shirshova, N.; Qian, H.; Shaffer, M. S.; Steinke, J. H.; Greenhalgh, E. S.; Curtis, P. T.; Kucernak, A.; Bismarck, A. *Composites Part A: Applied Science and Manufacturing* **2013,** 46, 96-107.

19. Qian, H.; Kucernak, A. R.; Greenhalgh, E. S.; Bismarck, A.; Shaffer, M. S. *ACS applied materials & interfaces* **2013,** 5, (13), 6113-6122.

20. Westover, A. S.; Shabab, F. N.; Tian, J. W.; Bernath, S.; Oakes, L.; Erwin, W. R.; Carter, R.; Bardhan, R.; Pint, C. L. *J Electrochem Soc* **2014,** 161, (6), E112-E117.

21. Westover, A. S.; Baer, B.; Bello, B. H.; Sun, H.; Oakes, L.; Bellan, L. M.; Pint, C. L. *Journal of Materials Chemistry A* **2015,** 3, (40), 20097-20102.

22. Gojny, F.; Wichmann, M.; Köpke, U.; Fiedler, B.; Schulte, K. *Composites Science and Technology* **2004,** 64, (15), 2363-2371.

23. Schadler, L.; Giannaris, S.; Ajayan, P. *Applied physics letters* **1998,** 73, (26), 3842-3844.

24. Wang, G.; Zhang, L.; Zhang, J. *Chemical Society Reviews* **2012,** 41, (2), 797-828.

25. Asp, L. E.; Greenhalgh, E. S. *Composites science and technology* **2014,** 101, 41-61.

26. Baddour, C. E.; Fadlallah, F.; Nasuhoglu, D.; Mitra, R.; Vandsburger, L.; Meunier, J.-L. *Carbon* **2009,** 47, (1), 313-318.

27. Masarapu, C.; Wei, B. *Langmuir* **2007,** 23, (17), 9046-9049.

28. Teblum, E.; Noked, M.; Grinblat, J.; Kremen, A.; Muallem, M.; Fleger, Y.; Tischler, Y. R.; Aurbach, D.; Nessim, G. D. *The Journal of Physical Chemistry C* **2014,** 118, (33), 19345-19355.

29. Teblum, E.; Itzhak, A.; Shawat-Avraham, E.; Muallem, M.; Yemini, R.; Nessim, G. D. *Carbon* **2016,** 109, 727-736.

30. Shirshova, N.; Bismarck, A.; Carreyette, S.; Fontana, Q. P.; Greenhalgh, E. S.; Jacobsson, P.; Johansson, P.; Marczewski, M. J.; Kalinka, G.; Kucernak, A. R. *Journal of Materials Chemistry A* **2013,** 1, (48), 15300-15309.

CHAPTER 14

CONCLUSIONS AND OUTLOOK

14.1 Summary

From the Ni-Fe battery of Edison[1] to the Li ion battery of Goodenough,[2] paradigm shifts have defined the energy storage community. Each shift has brought us access to technologies that have fundamentally changed our society including the addition of lead-acid batteries to cars, the addition of Li ion batteries to electronics to start the portable electronics revolution, and more recently the adaptation of Li ion batteries to electric vehicles. This dissertation has presented initial work in three new innovative energy storage solutions which could be the next paradigm shift that completely changes the technology we use in society. The first presents the possibility of directly integrating energy storage and capacitive deionization into silicon solar cells and suggests two options for the possibility of matching the energy production and power profile of the solar cell Chapter 2-5). This idea has the potential to reinvent the way energy storage is coupled with solar energy conversion with simpler manufacturing and higher efficiency in storing the energy generated by the solar cells. The second presents the idea of using recycled scrap metals as batteries using a simple manufacturing design compatible with a do it yourself design (Chapter 6). It motivates two revolutionary concepts, the ability to use recycled waste to make energy storage, and the possibility of batteries being made on a local or even an individual scale. Finally I present initial work in developing multifunctional structural energy storage composites that completely changes the paradigm of energy storage. This includes demonstration of simultaneous mechanical and electrochemical functionality, and a prototype structural supercapacitor which has mechanical strength approaching that of commercial structural composites, and energy densities approaching commercial supercapacitors (Chapter 7-13).

14.2 Outlook of Integrated Solar Power and Energy Storage

Moving forward in the realm of integrated solar and energy storage, I have demonstrated the ability to directly integrate supercapacitors into the back of silicon photovoltaics using porous Si. I have also demonstrated the ability to use carbon coated and PANI coated porous Si as high performance high rate battery electrodes when coated onto porous Si. In order to make this innovation a commercial reality there are several steps that need to be taken. First, in addition to the single electrodes that we integrated with Si photovoltaics, it is crucial that a much wider variety of materials be investigated with the possibility of being coated onto porous Si. One reason for this is the need for paired electrodes that could match with the carbon coated porous Si and the PANI coated porous Si and which are designed to mimic the energy density and power profile of Si solar cells. This must be followed by realizing the direct integration of battery materials onto the back of solar cells. Some very promising candidates include the ability to very simply tailor other Quinone based organic polymer electrodes[3, 4] which are similar to PANI but with slightly different architectures and which could be paired with PANI for a full cell architecture of approximately 0.4-0.5V. Other possibilities include different atomic layer deposition, or wet chemical deposition of coatings on porous Si such as the V_2O_5[5] or TiO_2[6] both of which are compatible with Li based electrochemistry.

14.3 Outlook for Developing Scrap Metal and Do It Yourself Batteries

In the realm of engineering waste or scrap metals to energy storage, our work has demonstrated the initial proof of concept showing that you can indeed take scrap metals and turn them into high performance batteries. Although this initial work shows incredible promise, there are some limitations that make this particular battery system and architecture difficult to implement on a commercial scale. However, whereas our work presented a single possible chemistry for scrap metal batteries this by no means represents a comprehensive list of possibilities. In fact, zinc-air batteries[7] based on brass, and aluminum hydride[8] or aluminum air batteries[9] using recycled aluminum (maybe soda cans) are all extremely interesting possibilities. Furthermore whereas the chemicals used in our initial scrap metal batteries are easily obtainable, they still are somewhat dangerous for the average person to handle, switching to more common and safer chemicals could be a very intriguing possibility such as the use of vinegar based electrolytes such as that hypothesized to have been used in the original Baghdad battery or the use of common salt solutions such as NaCl.[10]

14.4 Outlook for Multifunctional Structural Energy Storage Composites

My work has demonstrated the feasibility of truly developing multifunctional structural energy storage composites using traditional manufacturing techniques for fiber based composites. Although our initial work is very promising, probably the most exciting aspect of our work is it opens up the door to an entire range of possibilities. First in the realm of structural supercapacitors, two areas of research could drastically improve the device performance. The first and biggest challenge is developing an electrolyte that doesn't compromise the stiffness of the electrolyte while still reaching a high ionic conductivity.[11-13] The second grand challenge is the improvement of the energy density of the devices. This could be improved by reducing the overall weight by growing CNT or another active material on conductive carbon fibers[14] and by increasing the density of the CNT, or by growing single walled CNT as opposed to multi-walled CNT.[15]

A second major area that could change the world is the development of structural batteries. Although there was some initial work in structural batteries by Liu et al.[16] showing that a traditional battery design could be implemented in a structural configuration, there has been almost no follow-up work to bring this type of battery to fruition. Adapting a similar approach to that used in my work where conductive carbon fibers or metal fiber meshes could be used as current collectors and traditional battery electrodes with graphite, $LiCoO_2$ carbon black and polymer glue could be cast around these current collectors and incorporated into a multifunctional design. One innovation that would be necessary for this architecture would be the development of a multifunctional solid state electrolyte that can function as Li ion battery electrolyte. Another possibility is the coating of entire batteries onto carbon fiber or metal mesh current collectors using sputtering and other deposition methods and then integrating these full cell wire batteries into a full composite design.

Finally because of the versatility of the composite design process it would be feasible that photovoltaics such as dye sensitized solar cells and perovskites, and a whole range of electronics could also be incorporated into the multifunctional design creating a whole new class of functional composite materials that reach far above and beyond just the development of structural energy storage.

14.5 Conclusion

The future of energy storage is bright. Innovation has constantly reinvented this community and will continue to do so. I have presented here three ideas which all represent possible innovations that can again reinvent the community of energy storage. Although each of the specific projects that I completed may not end up completely change the way we use energy storage, each project presents a foundation upon which future research can build, and with continued innovations such as paired battery electrodes integrated with Si photovoltaics, the development of different scrap metal battery chemistries, and the development of structural battery composites, these ideas may indeed reach commercial viability and come to completely change the future of energy storage.

References

1. Salkind, A. J.; Israel, P. *J Power Sources* **2004,** 136, (2), 356-365.

2. Goodenough, J. B.; Park, K.-S. *J. Am. Chem. Soc.* **2013,** 135, (4), 1167-1176.

3. Anjos, D. M.; McDonough, J. K.; Perre, E.; Brown, G. M.; Overbury, S. H.; Gogotsi, Y.; Presser, V. *Nano Energy* **2013,** 2, (5), 702-712.

4. Jaffe, A.; Saldivar Valdes, A.; Karunadasa, H. I. *Chemistry of Materials* **2015,** 27, (10), 3568-3571.

5. Douglas, A.; Muralidharan, N.; Carter, R.; Share, K.; Pint, C. L. *Nanoscale* **2016,** 8, (14), 7384-7390.

6. Ban, C.; Xie, M.; Sun, X.; Travis, J. J.; Wang, G.; Sun, H.; Dillon, A. C.; Lian, J.; George, S. M. *Nanotechnology* **2013,** 24, (42), 424002.

7. Chakkaravarthy, C.; Waheed, A. A.; Udupa, H. *J Power Sources* **1981,** 6, (3), 203-228.

8. Graetz, J.; Reilly, J.; Yartys, V.; Maehlen, J.; Bulychev, B.; Antonov, V.; Tarasov, B.; Gabis, I. *Journal of Alloys and Compounds* **2011,** 509, S517-S528.

9. Li, Q.; Bjerrum, N. J. *J Power Sources* **2002,** 110, (1), 1-10.

10. Nestoridi, M.; Pletcher, D.; Wood, R. J.; Wang, S.; Jones, R. L.; Stokes, K. R.; Wilcock, I. *J Power Sources* **2008,** 178, (1), 445-455.

11. Shirshova, N.; Bismarck, A.; Greenhalgh, E. S.; Johansson, P.; Kalinka, G.; Marczewski, M. J.; Shaffer, M. S.; Wienrich, M. *The Journal of Physical Chemistry C* **2014,** 118, (49), 28377–28387.

12. Shirshova, N.; Bismarck, A.; Carreyette, S.; Fontana, Q. P.; Greenhalgh, E. S.; Jacobsson, P.; Johansson, P.; Marczewski, M. J.; Kalinka, G.; Kucernak, A. R. *Journal of Materials Chemistry A* **2013,** 1, (48), 15300-15309.

13. Westover, A. S.; Baer, B.; Bello, B. H.; Sun, H.; Oakes, L.; Bellan, L. M.; Pint, C. L. *Journal of Materials Chemistry A* **2015,** 3, (40), 20097-20102.

14. Sharma, S.; Lakkad, S. *Composites Part A: Applied Science and Manufacturing* **2011,** 42, (1), 8-15.

15. Zhao, X.; Chu, B. T.; Ballesteros, B.; Wang, W.; Johnston, C.; Sykes, J. M.; Grant, P. S. *Nanotechnology* **2009,** 20, (6), 065605.

16. Liu, P.; Sherman, E.; Jacobsen, A. *J Power Sources* **2009,** 189, (1), 646-650.